Designing Scalable Biological Interfaces

Designing scalable biological interfaces

A DISSERTATION PRESENTED
BY
ADAM H. MARBLESTONE
TO
THE COMMITTEE ON HIGHER DEGREES IN BIOPHYSICS

IN PARTIAL FULFILLMENT OF THE REQUIREMENTS
FOR THE DEGREE OF
DOCTOR OF PHILOSOPHY
IN THE SUBJECT OF
BIOPHYSICS

HARVARD UNIVERSITY
CAMBRIDGE, MASSACHUSETTS
APRIL 2014

Thesis advisor: Professor George Church Adam H. Marblestone

Designing scalable biological interfaces

Abstract

This thesis presents the analysis and design of biological interfacing technologies in light of a need for radical improvements in scalability. It focuses primarily on structural and functional neural data acquisition, but also extends to other problems including genomic editing and nanoscale spatial control. Its main contributions include analysis of the physical limits of large-scale neural recording, experimental development of a screening platform for ion-dependent molecular recording devices, characterization of the design space for molecularly-annotated neural connectomics, and new designs for high-speed genome engineering and bio-nano-fabrication. Articulating governing principles and roadmaps for these domains has contributed to the initiation of multi-institutional projects that are strategically targeted towards scalability.

Contents

Listing of figures

To my parents

Acknowledgments

First of all, I would like to thank George Church. George has shown me how to push technology forward, but he has also given me an unforgettable glimpse of how to conduct oneself as leader and as a deeply ethical person. George's way of life makes me optimistic about the future. I hope to remain in his circle of influence, and to try, as best I can, to spread its spirit wherever I go.

I could not have made it here without William Shih, who first brought me to Harvard when I was an enthusiastic but naive college sophomore, at another institution, with little in the way of relevant experience. From our first meeting, he understood my motivation and became my mentor. As an undergraduate, he gave me a first experience of the excitement of developing radically new technologies; the intellectual outlook of his 3D origami team, at a time when these sorts of things were widely regarded as impossible, has profoundly influenced me. Always looking out for my best interests, he helped me come to Harvard as a graduate student, and welcomed me as a joint member of his lab, even as I explored divergent ideas, projects and institutional contexts throughout graduate school. I will never forget William's support, aspiring only to pay it forward to the next generation. I have also benefitted greatly from William's technical advice, notably his ability to hone in on the core experimental questions underlying nearly every project I attempted.

I am very grateful to my mentor Peng Yin, who brought me into his lab when it was only one or two members strong, and helped me to make it a "home base" for the subsequent four years. Sitting at a desk or bench in his ever-more-bustling lab was somehow where I felt most comfortable testing out nascent (or still embryonic) ideas. It has been a thrilling experience to watch as Peng has catalyzed a thriving community at the Wyss Institute, expanding to include many new minds and ideas, and producing shocking demonstrations of what innovation in biomolecular technology can look like.

I would also like to thank my committee member Ed Boyden for continual and profound inspiration and intellectual provocation over the years, and more recently for involving me in extremely exciting emerging projects and relationships. Ed has already taught me much more than he realizes. I'm truly excited to be embarking on joint adventures.

I am thankful to Joe Jacobson for his willingness to take an interest in my work, at several stages, and to serve on my defense committee.

I am deeply grateful to Lowell Wood, Tom Weaver, David Galas, Louis Lerman, Ray Sidney, Jay Davis, Paul Young and to the *Fannie and John Hertz Foundation* as a whole, for providing me not only with funding but, more importantly, with a big confidence boost and a truly unbelievable network.

The fellowship emphasizes not only the "freedom to innovate" but also a sense of "responsibility to innovate", and the community of fellows is humbling, inspiring and enabling. I can think of no other institution that I would be more proud to associate with. The signs of this community's influence, direct and indirect, are literally written all over this thesis. I hope the Hertz directors will be pleased in a few years to see the impact of all the other "side projects" that have recently emerged inside this group.

Lowell Wood, in particular, wrote me a series of eloquent letters, in response to queries at some of the more difficult and formative moments in graduate school, which have fundamentally shaped my perspective on being a scientist. Lowell also contributed decisively to the ideas about fiber optic multiplexing described at the end of Chapter 3, and it is an honor to be able to include some of Lowell's arguments here.

I am deeply grateful to Paul Young for the financial support of my Hertz fellowship, which is named after Lowell.

I am incredibly lucky to have had a series of amazing mentors stretching back many years. They have truly made everything possible. In high school, Benton Minks was, in a way, my first research advisor, helping me to see how powerful writing could be as a way of thinking. While still a middle-school and high-school student, I got exposed to the wonder of cutting edge science in the Bose Einstein condensation lab of David Hall at Amherst College and the robotics lab of Rod Grupen at UMass Amherst. Mary McCarthy taught my AP biology class and made sure I didn't fail it. Susan Caporello helped me skip a grade in math. Early in college, letting me in despite a distinct lack of pre-requisites on my part, James McBride taught the freshman organic chemistry course that showed me what it means to communicate clearly about scientific ideas, why the history of science is an essential and under-appreciated lens on the present, and what a dunce I was in the organic laboratory.

Michel Devoret introduced me to real research, helping me engage with the abstract and philosophical subject of quantum entanglement and Bell's inequalities. The many hours spent in his office, going deeper and deeper into quantum information theory, were invaluable to my learning. More than that, they acquainted me with a form of intellectual beauty and elegance that has made an indelible impression on how I think. To this day, I can hardly believe that Michel was willing to engage so closely with an inexperienced undergraduate, always patiently waiting for me to catch up with his stream of insights and intuitive leaps, and allowing me to be involved in the process. I hope that one day I will be able to influence even one student as profoundly as Michel has influenced me. Also during those days, Steve Girvin's mentorship and teaching were inspiring and confidence building, allowing me to get to the heart of what makes physics such a deep and powerful subject. Archana Kamal was very generous and patient as a graduate student mentor, amidst working at a furious rate of progress on her own projects, and was a pleasure to work with.

During summers at Dana-Farber, Shawn Douglas took me under his wing, taught me much about software, science and design, and provided a fantastic role model. At times, his advice proved crucial in setting my direction, including the decision to go to Harvard Biophysics and to make my home at the Wyss Institute. He also set the stage for me to choose George Church as an advisor. It was a privilege to be able to help out on a project as important and downright cool as caDNAno, and I couldn't imagine a more capable person to have learned from in that process. Through his example and by

starting BIOMOD, Shawn also helped me get involved in mentoring and team leadership, which has been a privilege.

At the very beginning of graduate school, I was lucky to learn molecular biology from Harris Wang, an extremely capable and meticulously organized experimenter who was nevertheless remarkably patient. Mike Jewett was another one of these who put up with me at this stage and helped a lot. As preparation for that experience, I must also send a heartfelt thanks to Joseph Wolenski at Yale – one of my most enthusiastic and supportive teachers – for getting me involved in, and excited about, real biology experiments despite being a clueless theoretical physicist. I could not have made that transition without you.

Neil Gershenfeld brought me into the Center for Bits and Atoms for a life-changing nine-month-long rotation. The intellectual and experimental environment he has created, and his divergent, integrative thinking about problems, have truly expanded my horizons and shaped my sense of possibility. While it took me a while to get up to speed on fabrication, his How To Make (Almost) Anything course ultimately crystallized for me the ability to truly enjoy building and experimenting, greatly deepening and concretizing my knowledge of technology.

Manu Prakash was my one-on-one mentor and friend for that CBA rotation. Manu is a singularly talented and creative experimenter. Yet he was kind enough to let me tag along and experience a kind of figurative preschool or kindergarten of laboratory explorations. He helped me – at first – merely to take things apart and muck with the hundreds of items on his shelves (an activity which continues to this day, whenever I spend time in the CBA). Then later, to fiddle with lasers, test out simple circuits with the oscilloscope, dip one liquid metal into another with an AFM we dug up from a closet, spin coat a polymer, spend hours entranced in front of an SEM, put together fluidic contraptions with 3D printed interconnects, build an AFM prototype that looked at first like a huge telescope (the very opposite of good mechanical design) and a second prototype that looked like it might possibly just work, attempt our own molecular threader, collimate a xenon lamp, measure a DNA melting curve, and many other "firsts". During this time, Peter Schmidt-Nielsen, a prodigious high-school-age programmer, let me learn from him about micro-controllers and software, as we learned together about spectroscopy, electronics, RF and other topics. Yael Maguire and Rehmi Post mentored both of us during this time, presumably with some degree of amusement. Max Lobovsky, one of the best engineers I know, was also a patient and inspiring lab partner. It is remarkable that my personal life survived this period of time, as I was in the lab at 4:00 am on many nights, enthralled by this new type of direct contact with reality.

Among many other things, Robert Barish showed me how to get serious about doing a proper job of nanotechnology, actually getting an AFM to finally work at the requisite resolution, and from there we engaged in a partnership that led to some exciting results, and to many deeply thought-provoking conversations. Rob has been a trusted friend, and a thoughtful guide to the complexities of science and graduate school. I have learned much from him and the brilliant ideas he has generated. I wish him the best of luck on his next phase, in Japan, and will miss him while he's over there.

Adam Cohen generously brought me in for an unexpected exploratory research rotation, which was a fantastic experience – Joel Kralj and Daniel Hochbaum were kind enough to let me tag along with their exceptional rhodopsin work during that time.

Kevin Esvelt helped get me into biology for real, engaging in a series of deep dialogues about fundamental problems, and also bringing me finally fully up to speed on things as basic as PCR and cloning. Kevin has taught me about what it really means to understand and engineer a natural system shaped by evolution, and has helped me bootstrap to become at least a semi-competent biology experimenter. He has also greatly influenced some of the philosophies behind my research and encouraged me in certain non-traditional ways of thinking. Kevin has thus dually mentored me in some of the most concrete, and some of the most philosophical, aspects of being a scientist.

Brad Zamft was my partner in molecular tickertape research, patiently tutoring me on many of the keys to a successful experiment and project. His energy, organization and enthusiasm have shown me how to get "on track" with a project, and how exciting things can be when we're making fast progress. I greatly appreciate his open-mindedness and friendship in helping me to be involved in these advances. Reza Kalhor was another important lab mentor on the tickertape work and beyond.

Evan Daugharthy, Jay Lee, Seth Shipman, Ian Peikon and Justus Kebshull were critical in the strategy / design work on connectomics and in the exciting activities growing out of that.

Prashant Mali and Dave Zhang helped decisively on several occasions in getting experiments to work better.

Konrad Kording has been a wonderful mentor from afar. He has been another of those who appear to see my many interests as a strength rather than a weakness, seeking to help me deepen any and all of them.

I would like to thank Tony Zador as well as Yuriy Mishchenko for their generosity in explaining to me some of the principles behind new possibilities for connectomics and allowing me to expand upon and champion these and related ideas in our future-oriented white-papers. They have helped me to become somewhat less of an outsider to the richness of neuroscience.

Charles Fracchia has been a tirelessly enthusiastic co-conspirator on several projects, introducing me to new and more entrepreneurial ways of making progress. Shuguang Zhang, an unbelievably generous and supportive mentor, has been instrumental to our efforts.

I would like to thank Tom Dean for hosting me in a fascinating visit at Google/Stanford, for being an inspiring teacher in the broadest sense, and for his recent collaboration and support on several projects.

It has been a true pleasure recently to work with Gary Marcus, who has involved me in fascinating projects and expanded my horizons in the theoretical and cognitive aspects of brain science. It means a lot to me that Gary has been so generous and patient in helping me move into new areas.

I would like to thank Erik Winfree, Lulu Qian, Paul Rothemund, Kent Kemmish, Tom Dean, David Dalrymple and Danielle Fong for hosting me on mind-expanding visits to the West Coast and Drew Klein, Cathy Jan and Madeleine Udell for providing housing, food, entertainment, good conversation, friendship and considerable jealously as far as the weather, while I was there.

David Dalrymple, Semon Rezchikov, Dario Amodei, Juan Batiz-Benet, Zak Stone, Jonathan Gootenberg and Riley Drake have been wonderful co-conspirators in thinking about how science as a whole could make more progress, and about the remarkable times we find ourselves in. Our many fascinating discussions make me optimistic about where the world can go. It is an honor to be able to share the journey with you.

I am grateful to Fatih Yanik for engaging me in inspiring discussions early in graduate school.

I am profoundly thankful to my own students: Evan Wu, Sherrie Wang, Nick Perkons, Shwinn Ricci, Ian Choi, In Young Cho, Valentina Lyau, Wesley Chen, Jacob Pritt, Andrew Payne and Noah Donoghue, and to the students in the BioPhysics and SynBio classes who asked thought-provoking questions and did great projects.

Other friends in the lab(s) have taught me much, and provided a great deal of fun in the process. These include Mingjie Dai and Ralf Jungmann, Luvena Ong, Bryan Wei, Cameron Myrhvold, Johannes Wohrstein, Maier Avendano, Poyi Huang, Luhan Yang, Max Lobovsky, Nadia Cheng, Nadya Peek, Rehmi Post, Daniel Martin-Alarcon, Daniel Schmidt, Dan Goodman, Sri Kosuri, Vatsan Raman, Alex Chavez, John Scheiman, Noah Jakimo, Henry Lee, Marc Lajoie, Gleb Kuznetsov, Lisa Nip, Danny Levner, Ido Bachelet (and thanks Ido for an amazing trip to Israel), Fei Chen, Paul Tillberg, Josh Glaser, Ted Cybulski, Ylaine Gerardin, Anjali Datta, Jon Russell, Jacob Steinhardt, Steve Perrault, Wei Sun, Ben Stranges, Christian Wentz, Scott Greenwald, Jamie Rogers, John Aach and others.

Tom Lutz, John DiFrancesco and Martin Montoya made it possible for me to use lab equipment that I would have been quite properly afraid to use otherwise, and did so patiently and with great kindness.

I am grateful to Yveta Masarova and Meghan Radden for putting up with me in the Church lab, for enabling so many of the things we did through your diligent efforts to keep the show running, and for being genuinely nice people. Similar comments are in order for Elizabeth Haney and Danielle Pastuszak in the Yin lab, Joe Murphy at the CBA, Jermaine Reid, Susan Kelly and Alison Reggio at the Wyss, Sara Vassallo at the Church lab and several others.

Don Ingber, Mary Tolikas and others do a great job making the Wyss Institute an exciting place, where remarkable things seem to appear every few weeks.

It is difficult to find sufficient words to thank Michele Jakoulov and Jim Hogle for their unfailing support – far over and above that of any academic call of duty – during my time in the Harvard Biophysics program. You really make Biophysics the gem that it is, enabling things that would otherwise be at best very difficult. I will be singing the program's praises and yours for years to come.

Moving towards the end of this long list, I would like to thank my amazing friends outside of science for making life both enjoyable and meaningful.

I am so grateful to my grandmother Shirl Marblestone for her unconditional love, as well as to the rest of the Marblestone and Seeger families, to my Wermer cousins, Alex and Ariana, aunt and uncle Margaret and Steve, and Marie, Salome, Krysia and Pierre across the ocean.

Most of all, I owe any successes to my parents, Hedy Wermer, Ben Branch (including the nights at our rooftop telescope, robotics demos, model rockets, astrophysics classes, article discussions, books, magazine subscriptions, trips, math camps and many many other influences that got me involved in science from an early age), and Robert Marblestone. Words cannot express your love and sacrifice or what it has meant to me. A big thanks also to the cats, dogs, lizards, beta fish and rats.

Finally, I thank Adrienne for making every day wonderful and for your profound support during these years of intense learning.

...the space systems community taught me a way of thinking that harnessed creative vision to physical, quantitative reasoning, in order to explore what could be achieved in new domains of engineering... Satellite launchers and moonships grew out of quantifiable engineering visions: system-level concepts that could be sketched, assessed, and discarded at a rapid pace, evolving through a kind of Darwinian competition. The best concepts would win the resources of time and attention needed to fill in more details, to optimize designs, to apply closer analysis, and after this refinement and testing, to compete again. The prize at the end would be a design refined into fully detailed specifications, then metal cut on a factory floor, then a pillar of fire rising into the sky bearing a vision made real...

K. Eric Drexler[169]

1 Introduction

This thesis presents the analysis and design of biological interfacing technologies in light of a need for radical improvements in scalability. It focuses primarily on large-scale structural and functional neural data acquisition, but also extends to other problems including genomic editing and nanoscale spatial control. Its unifying aspiration is to derive scalable technology architectures from first principles, irrespective of current practice.

Technology architecting: The efforts described here often take the form of cross-disciplinary "road-mapping", i.e., systematic identification of the constraints shaping a range of alternative pathways towards scalability. This in turn gives rise to proposals for technologies quite distinct from those used today, in acute sub-scale. For example, techniques practical for recording the activities 100-1000 neurons may need to be abandoned in the design of systems scalable to 100-1000 *million* neurons. Because of the complexity of biological science and its stratification into specialized experimental sub-fields driven by the constant production of concrete scientific results, we reasoned that cross-disciplinary architecting of long-term technology strategies may be under-explored relative to its potential payoffs.

Anticipated outcomes: While the early-stage concepts developed here are not yet fully validated experimentally, we hope that these analyses and prototype experiments can serve to re-orient aspects of research towards new platforms whose benefits will outweigh the costs and risks associated with "starting from scratch". The best-case outcome is the initiation of profitable new research directions and systematic development projects; the worst-case outcome is a renewed appreciation of the challenges of interfacing with biological complexity at scale.

From architectures to teams and projects: Reflecting the focus on initiating new experimental directions, we have catalyzed the formation of multi-disciplinary teams. These teams have applied for collaborative research grants (each spanning $\geq$ 3 institutions) – on molecular signal recording, in-situ readout of neuronal connectivity barcodes, and vascular delivery of neural recording and stimulation devices – which are based in part on the ideas explored here.

In Chapter 2, an essay co-written with Gary Marcus and Tom Dean, we begin with a high-level discussion of the assumptions underlying the extant approaches to reverse engineering the computational architecture of the neocortex. We highlight a scientific strategy based on classifying "mesoscale" computational elements via their putative origins in distinct molecularly-specified developmental and plasticity rules. These ideas provide one possible scientific context for our efforts to design scalable means of neural data acquisition incorporating rich molecular information.

In Chapter 3, we study the problem of recording the electrical "spiking" of a significant fraction of the neurons in a mammalian brain. Despite many proposals for incremental improvements on existing neural recording techniques, and despite much recent interest in the problem [21,20], the limiting factors and governing principles for brain activity mapping have not been systematically described, and there are few detailed technical proposals for cellular-resolution recording methodologies which could apply at whole-brain scale. To address this challenge, we mobilized the intellectual efforts of more than 17 collaborators across many disciplines and institutions, asking what it would take to record from all neurons in a mouse brain at millisecond resolution, based on an analysis from first principles of physics and from the known biophysics of the brain [434]. This analysis has been featured in a number of subsequent white-papers [144,585,136] and was highlighted in *Nature Physics* [86].

We structured the analysis around three problems: (1) All neurons must be probed at a sufficient rate, (2) the energy transmitted into the brain must not cause thermal damage and (3) the volume of instrumentation introduced into the brain must not cause physical damage. We found that all existing approaches require orders of magnitude improvement in key parameters in order to scale to whole brain observations. Electrical recording is limited by the low multiplexing capacity of electrodes and their lack of intrinsic spatial resolution, optical methods are constrained by the scattering of visible light in brain tissue, magnetic resonance is hindered by the diffusion and relaxation timescales of water protons, and the implementation of molecular recording is complicated by the stochastic kinetics of enzymes.

We also studied the physics of powering and communicating with microscale devices embedded in brain tissue and found that, while radio-frequency electromagnetic data transmission suffers from a severe power–bandwidth tradeoff, communication via infrared light or ultrasound may allow high data rates due to the possibility of spatial multiplexing. The use of embedded local recording and wireless data transmission would only be viable, however, given major improvements to the power efficiency of microelectronic devices.

The purpose of exploring the physical limits of brain activity mapping is to *identify assumptions whose strategic, purposeful violation could create opportunities* for novel solutions. With Brad Zamft, Michel Maharbiz and Konrad Kording, we have organized a series of meetings among researchers from several fields, in order to architect solutions to the problem of scalable neural recording. This has led to several theoretical proposals which are now being actively vetted at a preliminary design stage. One of these, sensor multiplexing via fiber-optic reflectometry, is briefly described in a supplemental note to Chapter 3.

In Chapter 4, we report preliminary experimental steps toward a novel platform for massively parallel neural recording[123,373,735,227]: molecular recording devices, also known as molecular ticker-tapes. We reasoned that the ideal recording device would be a nanoscale machine capable of quantitatively transducing a wide range of variables into a molecular recording medium suitable for long-term storage and facile readout in the form of digital data. In one potential implementation of such a device, cation concentrations would modulate the misincorporation rate of a DNA polymerase (DNAP) on a known template, allowing DNA sequences to encode information about the local cation concentration[735]. This approach is a significant conceptual departure from existing methods for physiological signal recording. We (with collaborators from MIT and Northwestern University) have received a grant from the National Institutes of Health (NIH), totaling more than $9 million, to further explore this idea, based on our preliminary data.

We (with Brad Zamft and others) published the first experimental paper in the molecular recording field[735]. It describes the development of a high-throughput screening methodology for ion-dependent molecular recording devices, leveraging massively parallel DNA sequencing technology. We quantified the cation sensitivity of DNAP misincorporation rates using a sequencing machine, making possible the indirect readout of cation concentration by DNA sequencing. Using multiplexed deep sequencing, we quantified the misincorporation properties of two DNA polymerases – Dpo4 and Klenow exo- – obtaining the probability and base selectivity of misincorporation at all positions within

the template. We found that Dpo4 acts as a DNA recording device for Manganese with a misincorporation rate gain of 2%/mM. Modulation of misincorporation rate is selective to the template base: the probability of misincorporation on template T by Dpo4 increases >50-fold over the range tested, while the other template bases are affected less strongly. Furthermore, cation concentrations act as scaling factors for misincorporation: on a given template base, Manganese and Magnesium change the overall misincorporation rate but do not alter the relative frequencies of incoming misincorporated nucleotides.

In work led by Josh Glaser[227], we also published the first theoretical paper on the molecular recording device concept. This paper establishes limits on the temporal resolution of recording that arise from molecular stochasticity, and derives the need for molecular clocking mechanisms to achieve single-spike resolution. A brief summary of this theoretical analysis is included in Chapter 3.

In Chapter 5, we analyze the design space for large-scale cellular-resolution mapping of synaptic connectivity ("connectomics") by evaluating the economic and scaling constraints on all previously proposed cellular-resolution connectomics architectures[433]. We discuss technology options that could potentially reduce the costs of neural connectivity mapping by orders of magnitude compared to the standard electron microscopy methods.

In Chapter 6, we describe a proposed strategy, termed *FISSEQ-BOINC*, for the simultaneous readout from a single brain of multiple distinct structural and functional signatures including transcriptome, connectome, cell lineage and activity history – i.e., for the construction of a *Rosetta Brain* readout as defined in[122]. This strategy leverages the recently developed technology of fluorescent in-situ sequencing (FISSEQ)[396] in an optical microscope as the primary mode of information-extraction, coupled with the use of cell-identifying DNA barcodes as proposed by Zador[734,532] and earlier authors[239,685].

Specifically, we derive strategies, based on optical microscopy and in-situ DNA sequencing, that could lead to at least a 10× – 100× cost reduction for whole-mouse-brain structural connectomics,

relative to the existing electron microscopy approaches, while also providing a natural route to integration with diverse molecular annotations. Efforts are now underway in the Church, Boyden and Zador labs to move towards experimental implementation of these and related ideas, e.g., through integration of FISSEQ with novel high-speed super-resolution optical microscopies.

In Chapter 7, we describe broader applications of DNA as an "informational substrate". We (joint with Kevin Esvelt) experimentally demonstrate a simple system for arbitrary-sequence single-stranded DNA (ssDNA) production inside the *E. coli* bacterium, a tool which may find application in genome engineering and in the development of molecular recording devices optimized for *slow* timescales (rather than the fast timescales characteristic of neural spiking).

In addition, we study the problem of constructing integrated bio-molecular nano-assemblies, in which diverse functional elements are arranged in programmable patterns. We (joint with Robert Barish) report initial experimental investigations into a novel scheme for chip-scale bio-molecular fabrication (i.e., "nanometer-to-centimeter" or "nm2cm" integration) via top-down organization of self-assembled DNA nanorods on custom DNA micro-arrays via hybridization. Using structural DNA nanotechnology, we (joint with Mingjie Dai and Ralf Jungmann) also demonstrate a system to "stretch out" a single DNA double-helix or ssDNA strand of arbitrary sequence and to display it for high-resolution microscopy.

Chapter 8 is a brief addendum describing an experiment in biological interfacing at the human scale.

1.1 Citations to published work and acknowledgements to co-authors

Collaboration was essential to all of the work described here, and I am pleased to acknowledge the following co-authors and our associated joint publications:

- A modified version of Chapter 2 will appear as: Marcus, Marblestone and Dean. *Computa-*

tional Diversity and the Mesoscale Organization of the Neocortex: A Hypothesis Inspired by Digital Circuit Design. Submitted. (2014).

We thank Rafa Yuste, Xiao-Jing Wang, Rick Granger, Blaise Aguera y Arcas, Nuno de Costa, Clay Reid, Ed Lein, Stefan Mihalas, and Amy Bernard, for helpful discussions, Jennifer Goldman, David Heeger, Sebastian Seung, Christof Koch, Chris Eliasmith, Sean Hill, Randy Gallistel, Konrad Kording, Shawn Olsen, Jeremy Freeman, and Doug Bemis for detailed comments, and Shawn Olsen, Jennifer Goldman and Ed Boyden for many useful references.

- Chapter 3 appeared as[434]: Marblestone [co], Zamft [co], Maguire, Shapiro, Cybulski, Glaser, Amodei, Stranges, Kalhor, Dalrymple, Seo, Alon, Maharbiz, Carmena, Rabaey, Boyden, Church and Kording. *Physical Principles for Scalable Neural Recording*. Frontiers in Computational Neuroscience (2013) and one figure in this chapter is modified from Glaser, Zamft [co], Marblestone [co], Moffitt, Tyo, Boyden, Church and Kording. *Statistical Analysis of Molecular Signal Recording*. PLoS Computational Biology (2013).

  We thank K. Esvelt for helpful discussions on bioluminescent proteins; D. Boysen for help on the fuel cell calculations; R. Tucker and E. Yablonovitch (`http://www.e3s-center.org`) for helpful discussions on the energy efficiency of CMOS; C. Xu and C. Schaffer for data on optical attenuation lengths; T. Dean and the participants in his CS379C course at Stanford/Google, including Chris Uhlik and Akram Sadek, for helpful discussions and informative content in the discussion notes (`http://www.stanford.edu/class/cs379c/`); and L. Wood, R. Koene, S. Rezchikov, A. Bansal, J. Lovelock, A. Payne, R. Barish, N. Donoghue, J. Pillow, W. Shih, P. Yin and J. Hewitt for helpful discussions and feedback on earlier drafts.

- The supplemental note to Chapter 3 may appear as: Marblestone, Amodei, Wood, Church and Boyden. *Multiplexed Neural Interfacing via Optical Micro-Fibers: Theory*. Many of the ideas in this section were originally suggested by Lowell Wood in response to a draft of[434].

- Chapter 4 appeared as [735]: Zamft [co], Marblestone [co], Kording, Schmidt, Alarcon, Tyo, Boyden and Church. *Measuring Cation Dependent DNA Polymerase Fidelity Landscapes by Deep Sequencing*. PLoS ONE (2012).

  We thank Zach Herbert at the Dana-Farber Cancer Institute Molecular Biology Core Facility for providing expert assistance with MiSeq sequencing; Sriram Kosuri for providing barcode sequences and for helpful discussions; Roger Woodgate for helpful discussions; and A. Michael Sismour for helpful discussions. We thank Noah Donoghue for assistance with micro-fluidic device design and fabrication and Prashant Mali for guidance on automation and surface chemistry.

- Chapter 5 appears as [433]: Marblestone, Daugharthy, Kalhor, Peikon, Kebschull, Shipman, Mishchenko, Lee, Dalrymple, Zamft, Kording, Boyden, Zador and Church. *Conneconomics: The Economics of Large Scale Neural Connectomics*. bioRxiv (2013).

  We thank Josh Glaser and Ben Stranges for discussions on barcodes, Todd Huffman for discussions on serial sectioning, and Ken Hayworth and Richard Schalek for discussions on EM automation. Dario Amodei, Juan Batiz-Benet, Ted Cybulski, Tom Dean, Noah Donoghue, Kevin Esvelt, Russell Hanson and Jason Pipkin for discussions.

- Chapter 6 will appear as: Marblestone, Daugharthy, Kalhor, Peikon, Kebschull, Shipman, Lee, Mishchenko, Kording, Boyden, Zador and Church. *Rosetta Brains: Towards Scalable, Annotated Connectomes*. Many of these individuals contributed important aspects of the proposed designs, and experimental efforts aimed broadly in these directions are now proceeding across three labs; my role in this project has been primarily that of a synthesizer of ideas, quantitative analyst and catalyst of collaborations.

  We thank Fei Chen, Paul Tillberg, Ian Choi, Gary Marcus, Dario Amodei, Ted Cybulski, David Dalrymple, Tom Dean, Noah Donoghue, Kevin Esvelt and Brad Zamft for discussions.

- Chapter 7 has not been published. It represents joint work with a number of key people. The structural DNA nanotechnology experimental work was conducted with Robert Barish, Mingjie Dai, Ralf Jungmann, Richard Terry, Frederic Vigneault, Dave Zhang and Shawn Douglas, among others.

  The nm2cm design is based on a proposal by George Church, created following discussions with the author and others in early 2010, and refined through interactions with Robert Barish, Peng Yin, Rich Terry and William Shih. The nm2cm concept is also described in a 2010 report of invention by Church and colleagues, on which the description given here is based.

  The in-vivo work on ssDNA production and continuous MAGE was done in close partnership with Kevin Esvelt and led to further collaborations with Alex Chavez.

  The design work on slow timescale recorders was also done in collaboration with Kevin Esvelt and Alex Chavez, inspired by general discussions with Jonathan Gootenberg, Sasha Rayshubskiy, George Church and Konrad Kording.

- Chapter 8 represents unpublished joint work with Charles Fracchia.

With the instruments of the time so weak, there seemed little chance to understand brains, at least at the microscopic level. So, during those years I began to imagine another approach. Perhaps we could work the other way; begin with the large-scale things minds do and try to break those *processes down into smaller and smaller ingredients... Then, perhaps we could combine what we learned from both "top down" and "bottom up" points of view - and eventually close in on the problem from two directions.*

Marvin Minsky

2

Computational Diversity and the Mesoscale Organization of the Cortex

The human neocortex participates in a wide range of tasks, yet superficially appears to adhere to a relatively uniform six-layered architecture throughout its extent. For that reason, much research has been devoted to characterizing a single "canonical" cortical computation[135,164,482], repeated mas-

sively throughout the cortex[557], with differences between areas presumed to arise from their inputs and outputs rather than from "intrinsic" properties[714,163,61]. There is as yet no consensus, however, about what such a canonical computation might be[145], little evidence that uniform systems can capture abstract and symbolic computation (e.g., language)[437,438,440] and little contact between proposals for a single canonical circuit and complexities such as differential gene expression across cortex[397,266], or the diversity of neurons and synapse types[507].

Here, we evaluate and synthesize diverse evidence for a different way of thinking about neocortical architecture, which we believe to be more compatible with evolutionary and developmental biology[435,439,436], as well as with the inherent diversity of cortical functions. In this conception, the cortex is composed of an array of configurable computational blocks, each capable of performing a variety of distinct operations, and possibly evolved through duplication and divergence[435,55]. The computation performed by each block depends on its internal configuration. Area-specific specialization arises as a function of differing configurations of the local logic blocks, area-specific long-range axonal projection patterns and area-specific properties of the input. This view provides a possible framework for integrating detailed knowledge of cortical microcircuitry with computational characterizations.

According to a classic hypothesis of Mountcastle[482], "all parts of the neocortex [might] operate based on a common principle, with the cortical column being the unit of computation"; along similar lines, Creutzfeldt[135] suggested that the "functional role of a circumscribed cortical area depends exclusively on its position within a certain functional circuit and is defined by it" rather than on any intrinsic, between-area differences in wiring. Wyss et al[714] similarly suggested that "functionally heterogeneous cortical areas can be generated by only a few computational principles" with "the variability of the input signals [yielding] functional specialization", a view often associated with notion of a "canonical cortical microcircuit"[135,164,218]. (Two versions of this hypothesis might be distinguished, one in which the cortical micro-circuitry itself is taken to be identical or nearly identical across areas, and a second in which a single common learning rule applies throughout the cortex, potentially giving

rise to different micro-circuits in different areas as a function of input.)

There is, however, as yet no consensus about what the putative common microcircuit, or common learning rule, might be. Although suggestions have been made for how a single pattern recognition algorithm could underlie the operations of the various primary sensory areas[61], whether the rest of cortex can be characterized in similar terms remains highly controversial[145]; there are also clear limits on the capacities of such systems to generalize beyond a space of training examples[437,438], raising in-principle concerns about the capacity of currently-popular pattern recognizers to capture language, planning and other aspects of higher-level cognition.

Although the "uniform micro-circuit" and "uniform learning rule" views remain popular in some computational circles[714,61,218,385], and have recently been influential in artificial intelligence[385], they have arguably lost favor over time within empirical neuroscience[461,291,674]. Indeed, as discussed below, recent experimental work has often emphasized the importance of structural and functional diversity in the brain at all developmental stages and at multiple levels[507,248,201], as well as heterogeneity between cortical areas[236,490,185,184,720,146]. As van Hooser recently[674] put it, "the diversity found in cortical architecture suggests that there may be no single algorithm for cortical processing."

Against the background of longstanding "uniformist" vs. "specialist" debates, and in contrast to accounts under which functional specialization derives principally from differences in input[135,714,61], we argue for a conception of the cortex as a computationally heterogeneous array of configurable computational blocks (CCBs), configured partly on the basis of local molecular cues, rather than purely as a function of input. Systems of this structure might be taken as loosely analogous to Field-Programmable Gate Arrays (FPGAs) or other Programmable Logic Devices (PLDs) used in digital circuit design, which also consist of arrays of configurable elements, each of which is capable of executing a number of distinct functions such as AND, XOR, or more complex functions like addition or multiplication, depending on its configuration.

The CCB view, which we believe to be consistent with the implicit beliefs of many neuroscien-

tists[674,248,223,104,328,103], though rarely explicitly articulated, offers a natural account of how neural "wetware" with superficially similar physical and anatomical properties can compute a wide diversity of functions. Strictly uniform architectures, such as Hierarchical Temporal Memory[218], offer little purchase on why faculties such as language and vision have such different characters, beyond the true – but likely inadequate – observation that areas can functionally differentiate based on their respective sensory inputs. On the present account, the basic architecture of the individual blocks is shared across the entire cortex, but the local logic performed by each block can be individually tuned to specific kinds of problems. This approach also fits naturally with the "tinkering", rather than bespoke customization, that is typical of evolution by natural selection[435,314,610], the general trend of complex systems to evolve specialized modules at multiple levels of functional organization[564], and the repeat-with-variation character of much of biology that stems from the adaptive versatility of processes such as duplication and divergence[435,55]. It is conceivable for example, that reusable cortical logic blocks might have descended with modification from ancestral central pattern generators[732,249].

2.1 How configurable computational blocks might be realized

2.1.1 Physical instantiation

Individual blocks might be instantiated at multiple structural scales. Some might correspond to networks of multiple neurons, such as interconnected cell assemblies[92,272] or cortical columns[482]. Perin, Berger, and Markram[519] have found "synaptic organizing principles" leading to strongly connected neuronal groups at the scale of 10-100 neurons. It also possible that single neurons could form configurable computational blocks; as Koch and Segev[362] noted, "[the individual neuron] has evolved conceptually from that of a simple integrator of synaptic inputs... to a much more sophisticated processor with mixed analog-digital logic and highly adaptive synaptic elements". Different logical blocks could also overlap or be "superposed" physically, toggling between logical states either on-line (e.g., through

electrical signals or neuromodulation [45,44]) or off-line (e.g., through enduring wiring changes).

Even within a single computation, such as divisive normalization, there may be considerable differences in biophysical implementation across species and across systems [104]; likewise, even within a single low-level process, such as visual search, more than one computational element may be involved (e.g., both divisive normalization and quadratic nonlinearity) [418,539].

2.1.2 Range of computations

In principle, CCBs might be flexible enough in their configurability to compute essentially arbitrary functions [420,719,181,180]. Alternatively, CCBs might be relatively restricted – perhaps by the stereotyped micro-anatomy, connectivity and molecular composition of the cortex – to a smaller set of operations. Our default presumption is that individual logical blocks would consist of reusable circuits that stand in between top-level cognitive processes and the fine-grained anatomical elements, perhaps even individual neurons, that perform only small parts of a computation. Blocks might consist, for example, of circuits that instantiate processes such as variable binding, memory retrieval, copying, and routing. More elementary operations such as multiplication, dot product, temporal integration and linear superposition [180,360] might also be realized in individual blocks. A multi-leveled hierarchy of feature detectors might consist of a set of blocks that provide for processes such as pooling and normalization [28]. Complex systems that perform language or scene understanding would presumably depend on a combination of many logic blocks. Figure 2.1 presents some candidate computations that might plausibly be realized by individual configurable blocks or by sets of blocks, and potential ways those computations might be implemented physically and algorithmically. Our commitment here is not to the specific, but to the broader strategy that is implied, namely one in which the central emphasis is on cataloguing a heterogeneous set of building blocks that could unify bottom-up considerations from neurophysiology with candidate computations derived from top-down analysis [26,27,438,104,528,446].

Importantly, complex computations such as those involved in language may also rely on tight-knit

Computation	Algorithmic/ representational realization	Neural implementation(s)	Brain location(s)
Rapid perceptual classification	Receptive fields, pooling and local contrast normalization [58,61]	Hierarchies of simple and complex cells[62]	Visual system
Complex spatiotemporal pattern recognition	Bayesian belief propagation [19,63]	Feedforward and feedback pathways in cortical hierarchy[19]	Sensory hierarchies
Learning efficient coding of inputs	Sparse coding[64]	Thresholding and local competition[65]	Sensory and other systems
Working memory	Continuous or discrete attractor states in networks[66,67]	Persistent activity in recurrent networks[68]	Prefrontal cortex
Decision making	Temporal-difference reinforcement learning algorithms[69,70]; actor-critic models[71]	Cortically implemented Bayesian inference networks combined with temporal difference reinforcement learning via the dopamine system and action selection systems in the basal gangla[72]	Prefrontal cortex
	Winner-take-all networks[73]	Recurrent networks coupled via lateral inhibition[73]	Prefrontal cortex
Gating of information flow	Context-dependent tuning of activity in recurrent network dynamics[74]	Recurrent neural networks implementing line attractors and selection vectors[74]	Prefrontal cortex
	Shifter circuits[64,75]	Divergent excitatory relays and input-selective shunting inhibition in dendrites[76]	Visual system
Gain control	Divisive normalization[35]	Shunting inhibition in networks or balanced background synaptic excitation and inhibition [77]	Common across many cortical areas
Sequencing of events over time [78]	Feed-forward cascades; Serial working memories[79]	Synfire chains[80-82]; Thalamo-cortico-striatal loops[83,84]	Common across many cortical areas
Representation and transformation of variables	Population coding [85]	Time-varying firing rates of cosine-tuned neurons representing dot products with encoding vectors	Motor cortex
Variable binding	Holographic reduced representations [56,86]	Circular convolution of vectors represented by neural population codes	Cortical areas involved in sequential or symbolic processing
	Dynamic binding[87,88]	Neural synchronization[89]	

Figure 2.1: A sample (not intended to be comprehensive) of computations that might be associated with cortical blocks, and their potential "algorithmic" and physical realizations (ref. numbers refer to those in forthcoming ArXiv preprint).

interactions with brain areas outside the neocortex[404,618] such the basal ganglia[141] and hippocampus[141,263]. Connections to the cerebellum, basal ganglia and thalamus could contribute to sequential or recursive processing capabilities, e.g., by underwriting a form of short term memory that could support neural implementations of push-down automata or simple register machines. The prefrontal cortex / basal ganglia system, for example, has been suggested to implement pointer-like mechanisms to enable symbol processing and cognitive control[381]. Indeed, some theories posit a multi-regional "global workspace"[138,589] or "dynamically partitionable auto-associative network (DPAAN)"[270] as an essential enabler of variable binding and symbolic processing.

Some blocks might be mere quantitative variants of others, with important parameters (e.g., degree of recurrence[689] or sheer size of circuitry (Granger, p.c.), modified through the process of duplication and divergence. For example, simple cell / complex cell modules may recur with variation at all levels of the sensory hierarchies[28]. Other blocks might, over evolutionary time, become qualitatively distinct, perhaps via the emergence of new axonal pathways or local synaptic connectivity and plasticity rules. It is also possible, of course, that some blocks take on multiple functional roles, e.g., memory and decision-making might be subserved by variants on a single recurrent circuit[689,30].

2.1.3 Configuration mechanisms

Gross structural differences, such as the lack of granular cells in layer 4 of the motor cortex[83] may contribute to important differences between block configurations in different areas, but blocks might be differentially configured in more subtle ways as well. One possibility, which we will refer to as the molecularly-specified synaptic connectivity hypothesis is that statistically stereotyped geometric templates (e.g., cortical columns), that are defined by canonical neuron morphologies and their laminar placements[282], may be largely invariant across the cortex, but with specific local synaptic connectivity fine-tuned by a mixture of plasticity and area-specific molecularly-guided developmental rules. Such rules, by hypothesis, would guide the "last mile" of neural wiring in different blocks, by, for example,

directing the local formation, removal or change in size of synapses "on top" of otherwise stereotyped arborization. For instance, layer 5 pyramidal cells with molecular tag α might seek a specific molecular cue α' in a transiently connected cell to drive synapse growth or pruning, whereas layer 5 pyramidal cells with molecular tag β might adjust synaptic weights with their neighbors via Hebbian plasticity mechanisms. This molecularly defined heterogeneity could allow different circuit configurations to emerge from circuitry that superficially appears, without knowledge of the detailed local connectivity, to be stereotyped.

More generally, at least two classes of biological mechanism could assign computational configurations to CCBs. First, genetically guided processes of developmental biology, such as cell division, cell migration and axon guidance could differentially shape local circuitry. Such processes can be extremely precise. For example, families of molecules exhibiting combinatorial molecular recognition, such as cadherins[299,383] or the many RNA splice isoforms of Dscam in the fly[264], may endow neurons with locally unique "identity tags" to constrain their connectivity. Conjunctions of axon-guidance gradients and competition between axons can also yield highly precise structures, such as topographic maps[660,611]. Biologically plausible developmental rules could also generate certain types of precise connectivity, such as perfectly reciprocal connections between areas, by "sharpening" connections[130]. At the same time, single neurons can make different types of synapses on different types of target cells[637], new connections between neurons can form in a manner dependent on the nature of the existing connections[728], and the formation of electrical connections can be influenced by the molecular profiles of the participating neurons[214]. It is even possible that the molecules of the extracellular matrix shape synaptic connectivity and provide a substrate for long-term memory[664].

Second, activity-dependent changes in synaptic connectivity or strength could lead to internal reconfigurations of the logic blocks and hence modify their computational functions in response to input. Combinations of spike-timing-dependent Hebbian plasticity and heterosynaptic competition, for example, could contribute to the sculpting of connectivity underlying precise sequencing of neural

activity[197]. Importantly, both the resulting block configurations (microcircuits) and also the mechanisms of their configuration (e.g., learning rules) may differ across areas, due to heterogeneity at the molecular level.

Crucially, synaptic plasticity can lead to qualitative changes in the functions of circuits, not just quantitative tuning of parameters. In cultured cells, molecular changes at one synaptic connection can be communicated to other parts of the cell[202] and changes in the expression of ion pumps at synapses can lead not only to changes in synapse strength, but also to inversions in the "sign" (excitatory vs. inhibitory) of a synaptic connection[712]. Synapses can even change which neurotransmitter they use for signaling, in response to experience[175]. Developmentally, activity may even be able to transform one type of cell (e.g., pyramidal) into another (e.g., stellate)[98].

Computational reconfiguration could also occur on shorter timescales. Molecular modulators such as dopamine could serve to activate or recruit distinct sub-circuits within a fixed anatomy [45,44,230], thus toggling between different input-output mappings. Similarly, different states of dynamical activity in a sub-population of neurons (e.g., different limit cycle oscillations in recurrent networks[732]) could change the input-output function of a block[125,87,200]. "Gating" mechanisms at the level of electrical activity might also vary the functional connectivity between blocks.

2.2 Evidence for cortical heterogeneity

Although it is not yet technologically feasible to fully resolve the longstanding debates over the fundamental building blocks of cortical circuitry, a number of considerations point to the possibility of important cortical heterogeneity that could underlie both qualitative and quantitative differences between CCBs as well as the learning rules which give rise to those differences.

At a coarse level, there are several well-known cytoarchitectonic differences such as the agranularity of motor cortex layer 4, and a rostral-caudal gradient in supra-granular (II-IV) layer neuron numbers

per unit of cortical surface[115]. Likewise the distribution of different types of interneurons can differ sharply between areas: in V1, PV-containing interneurons (including fast-spiking basket cells) are prevalent (75%) relative to (CB- and CR-containing) interneurons, whereas in the prefrontal cortex CR-containing neurons (about 45%) outnumber both PV and CB-containing interneurons[689]. Likewise, canonical structural features such as ocular dominance columns appear in some places of cortex but not in most others, and are present in some closely-related species but not in others[291].

Local microcircuitry also differs between cortical areas. For example, motor cortex is dominated by "top-down" layer 2 to layer 5 local connections[699], while primary sensory areas have prominent "ascending" local connections L4 to L2/L3 and L5 to L2[601]. Synaptic connectivity and synaptic properties differ between frontal cortex and primary visual cortex. The probability of recurrent connections between neurons in frontal cortex is substantially higher than in the primary sensory cortex[689]. Pyramidal cells in prefrontal cortex have, on average, up to 23 times more dendritic spines than those in the primary visual areas[185] and cells in visual association areas are larger and have more spines than those in primary visual areas[184]. Whereas most excitatory cortical synapses exhibit short-term synaptic depression, some excitatory synapses in the frontal cortex exhibit short-term synaptic facilitation, perhaps contributing to the generation of sustained activity that is characteristic of prefrontal processing[690]. Recent work suggests there can also be important microcircuit-level differences within an area, such as a 2.5 fold difference in the number of neurons per cortical barrel column from dorsal to ventral in rodent S1[461].

At a finer-grained level, several recent observations seem consistent with a molecularly-specified synaptic connectivity hypothesis. First, molecular properties of cells with the same morphological cell type can differ even within a single cortical layer[346], making it possible in principle that local synaptic connectivity might be mediated not just by activity-driven plasticity[732] but also by different molecularly defined cell sub-types of the traditionally recognized, chemo-morphologically defined cell types.

Second, there is evidence that some neuronal morphologies and placements may have evolved such

that they are consistent with many potential patterns of synaptic connectivity[330].

Third, there are small but statistically reliable differences between gene expression in different areas of the cortex such that "the spatial topography of the neocortex is strongly reflected in its molecular topography-the closer two cortical regions, the more similar their transcriptomes"[266] – allowing the possibility, in principle, for different cortical areas to wire in different ways, perhaps prior to experience, so that some such differences emerge early in development. Data from the Allen Mouse Atlas shows that specific genetic markers, such as RAR-related orphan receptor beta, potassium voltage-gated channel, subfamily H (eag-related) member 7, ephrin A5, and activity regulated cytoskeletal-associated protein (Arc) are expressed at markedly higher levels in primary sensory areas (V1, S1, and A1) than elsewhere in the cortex (Stefan Mihalas, personal communication). Stansberg et al[626] review 65 genes, mainly participating in signal transduction, that are enriched in specific cortical regions. Other recent work points to selective gene expression in primates[718] and humans[266]. At the same time, recent studies of DNA copy number variants in single neurons[240] and retrotransposons[38,189] suggest other molecular mechanisms that could potentially contribute to the configuration of computational blocks. Slight molecular differences, such as the alternative splicing of GPR56, may have profound consequences in human development and evolution, by selectively altering stem cell proliferation and gyral patterning in the vicinity of Broca's area[36].

Fourth, there are important functional differences between areas that may, in the final analysis, not be attributable to activity alone, but rather to prewired differences in the configuration of individual blocks; neural activity in frontal areas, for example, tend to be less immediately stimulus-driven and more persistent than primary sensory areas[689]; at the same time, primary sensory areas differ significantly from one another in their sensitivity to brief temporal offsets[721].

Fifth, recent investigations of mouse primary somatosensory cortex[620] combining in situ hybridization data mining, marker gene co-localization, and retrograde tracing suggest that particular subsets of cell types, such as subsets of layer 5 pyramidal cells, project differently to distal targets – in a fashion

that is systematically governed by a molecular, combinatorial code. (Whether such a combinatorial code applies at the local microcircuit level remains unknown.)

Sixth, specific molecular cues can, at least in some instances, be used to reprogram circuit connectivity, even in post mitotic cortical neurons. De le Rossa et al[143] for instance showed that "the molecular identity, morphology, physiology and functional input-output connectivity of layer 4 mouse spiny neurons could be specifically reprogrammed during the first postnatal week by ectopic expression of the layer 5B output neuron- specific transcription factor Fezf2". As noted above, sensory input can also lead to important resculpting[98], and there is considerable evidence that endogenously-generated waves can drive local fine-tuning, at least in primary sensory areas[353], even before the onset of vision[11].

Finally, recent evidence suggests that genes such as SAM68[302] can govern the activity-dependent alternative splicing of neurexin molecules[659] that play important functions in the formation, maturation, and maintenance of synapses. The state of pre-synaptic neurexin splicing can even influence post-synaptic receptor trafficking[29], potentially allowing for a configurational code that could integrate intrinsic and extrinsic cues; crucially, such neurexins are represented differentially across the brain, and across developmental stages[302]. Neurexins also interact with neuroexophilin ligands, which are differentially expressed in sub-populations of synapses[74], to influence synaptic function.

Collectively, this evidence makes it plausible that different areas of cortex might be wired in importantly different ways, despite a shared six-layered substrate, potentially supporting a broad array of computationally distinct blocks and block configurations.

2.3 Road Map

Many strategies for reverse engineering neural computation have been suggested, ranging from whole brain cellular-resolution functional imaging and large-scale data analysis[21], to whole-brain biophysically realistic simulation using models extrapolated from diverse datasets[443,312], to intensive studies

of a single system[361] (e.g., visual cortex). The present viewpoint points to a complementary strategy (Figure ??): leveraging emerging possibilities for co-registering[734,396,532] molecular data[532,396], connectomics[734,586] and activity mapping[21,298,262,16], with the specific goal of creating a taxonomy of mesoscale computational elements and a characterization of how networks are differentially configured between cortical areas.

In principle, one could then seek a phylogenetic reconstruction of how distinct logic blocks (e.g., hierarchical pattern recognizers versus circuits that bind variables or those that orchestrate sequences of operations) arose over the course of evolution, perhaps descending with modification from precursors such as central pattern generators[250]. Using computational modeling, one might explore both quantitative change[689] (e.g., in tunable analog parameters such as strength or breadth of connectivity) and qualitative changes (e.g., in the development of new rules of synaptic modification, or in the introduction or loss of cell-type-specific short-range or long-range connections). For example, Kouh and Poggio have explored a biologically plausible circuit which generates diverse types of nonlinearity – including energy models, divisive normalization, gaussian-like operations and max-like operations – depending on its parameter tunings[378].

The CCB viewpoint also suggests an approach to modeling that contrasts with large-scale biophysically realistic simulations such as Blue Brain[442]. In the roadmap suggested here, cortical logic blocks would be identified and their computational functions would be abstracted. Then, the pattern of interconnections between logic blocks, at a scale above that of individual neuronal connections, would be determined. At this point, a mesoscale abstract simulation could be constructed. Rather than moving from neurons and networks directly to behavior, abstract computational building blocks could be identified at an intermediate scale[438,103,528] and associated with corresponding anatomical or physiological structures[103] to comprehensively map block-block connectivity, attributing computational functions to each block-block interaction. In effect, this could proceed in two directions, both upward from connectomics, cell type mapping and neural circuit modeling, and downwards from models that

aim to integrate functional anatomy with a diversity of cognitive representations[182,635].

2.4 Discussion

2.4.1 Some apparently conflicting evidence

One of the most commonly cited sources of evidence in favor of putative cortical uniformity comes a classic series of experiments by Sur and collaborators[558,597,429], based on earlier work by Frost[210,211], in which visual inputs to primary visual cortex (V1) were rerouted to the primary auditory cortex (A1), which in turn was shown to be capable of processing visual stimuli. While these studies are often taken to imply a "uniform" cortical substrate, several caveats are in order[435]. First, such results have only been demonstrated within primary sensory cortices, which might plausibly share a (somewhat) uniform pattern recognition architecture, whereas other areas (e.g., in frontal cortex) that are likely highly diverged from such pattern recognizers. Second, the "rewired" auditory cortex still retains some of its intrinsic properties[429] and the resulting "visual" system is not without defects. Visual input leads only to a partial re-structuring of A1 at an anatomical level[597]. Third, the areas were not (contra to a widespread characterization) directly "rewired"; rather intrinsic axon guidance mechanisms used in development were harnessed to guide rewiring, in part relying on molecular cues shared between visual and auditory areas, but which might not be equally effective if visual input were induced to connect to, e.g., prefrontal cortex[435]. In the subsequent decade, there appears not to have been any published report of successful attempts to reroute visual inputs to other areas that seem more different (e.g., prefrontal cortex), indirect evidence that cortical "interchangeability" may be far from general.

2.4.2 Relations with other proposals

While other authors have emphasized the importance of cataloging a basic inventory of the brain's computational primitives[438,103,245], the notion of construing the cortex as a heterogenous array of con-

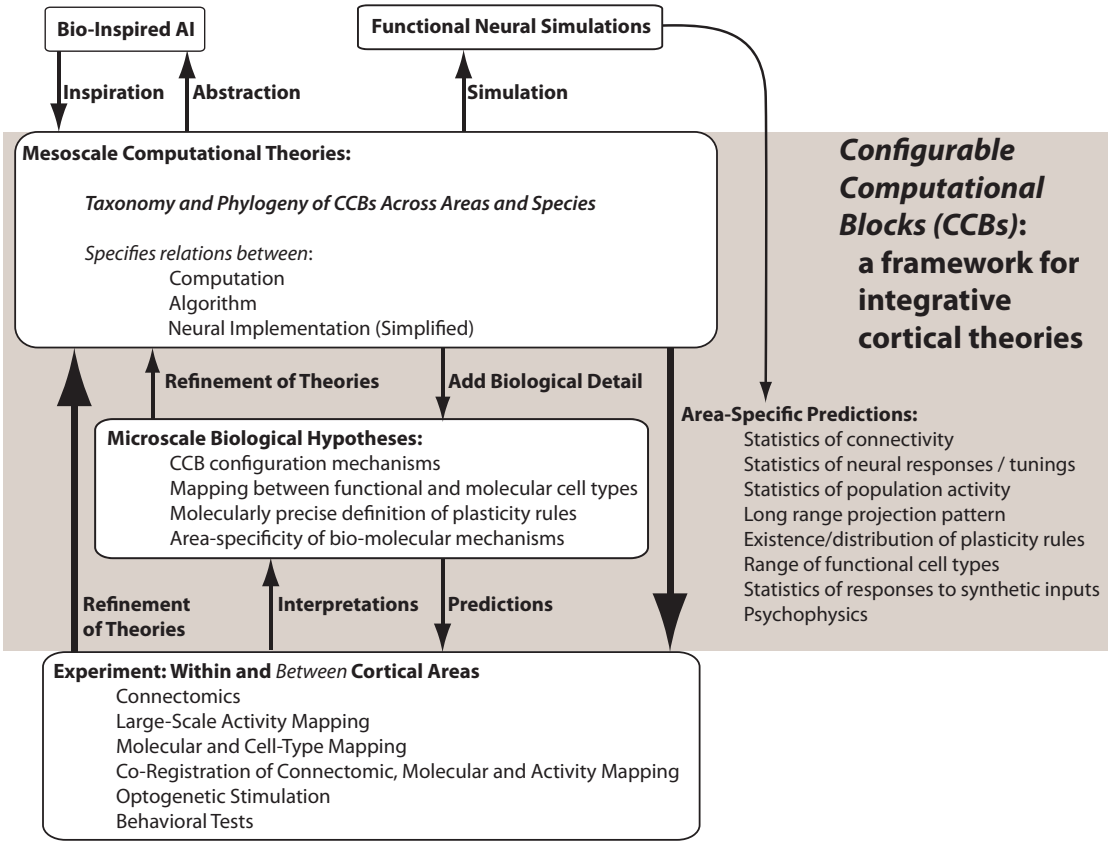

Figure 2.2: Strategy for constructing and validating integrative cortical theories, incorporating a taxonomy of distinct operations across areas. A mesoscale computational theory is an abstract specification of a set of configurable computational blocks, articulating an inventory of computational functions, and mapping these operations to specific cortical areas and neural implementations, as well as delineating the interactions between blocks. A microscale biological theory specifies the realization of these operations in neural wetware, including the biomolecular and input-driven determinants of CCB configurations. Simulations of the mesoscale computational theory predict the statistics of connection weights, tuning curves, population activity patterns and other variables as a function of cortical area. In turn, these signatures are empirically measurable through connectomic or activity mapping. The microscale biological theory also generates area-specific predictions about detailed structures measurable via molecular and cell type mapping. Co-registration of molecular, connectomic and activity mapping thus jointly constrains the nature of the CCBs and their configuration mechanisms, across many levels of description and as a function of cortical area.

figurable computational blocks has been given little explicit attention in the literature. Unpublished work by Rafael Yuste (personal communication) raised an analogy between brains and FPGA's in a different way, focusing primarily on their dense interconnectivity[200]. Douglas and Martin[162] describe a cortical microcircuit that might be taken to be similar to an unconfigured block, though they do not describe it in these terms, and do not emphasize the potential computational differences between differently configured blocks.

Several theories[61,218,28,529] aim to give a general account of a broad range of hierarchical sensory computations. For example Anselmi et al[28] offer a principled account of how rapid computation of transformation-invariant signatures of new inputs by the ventral visual stream could underlie recognition or category learning from small numbers of examples; it is unclear, however, whether these or similar mathematical principles would generalize beyond the sensory hierarchies, to other areas of the cortex (e.g., prefrontal) and aspects of cognition (e.g., language understanding).

Maass[419] studied the computational versatility of soft winner-take-all or soft-MAX operations, which were suggested by Douglas and Martin to be central to the operation of the putative canonical cortical microcircuit[162] and which also feature heavily in a variety of other models[553,546,497]. Recent work suggests that spike-timing dependent plasticity on top of a soft-MAX circuit structure can give rise to computations approximating simple Bayesian inference[491] as well as hidden Markov models[334,131]. Kouh and Poggio[378] have also suggested tunable circuits that approximate MAX-like operations for some parameter values but generalize to other nonlinear operations under different parameters.

"Liquid state machines" are tunable computational elements that are consistent with random internal wiring, and it has been suggested that this framework may provide a canonical, but highly configurable, cortical microcircuit model[597]. The basic idea is to exploit a randomly wired recurrent network of nonlinear elements, which will generate a rich internal repertoire of nonlinear functions. A subset of these elements is chosen and their outputs run through tunable linear decoders. Merely by tuning

the weights of the linear decoders, one can synthesize a wide range of computations on spatiotemporal input streams. These networks can be trained to perform multiple distinct functions simultaneously using Hebbian plasticity modulated by a simple global reward signal [285], suggesting the possibility that some computational logic blocks could be configured through reinforcement learning (though others may be prewired through the use of molecular cues). Nonetheless, their correspondence with real brain circuitry and with higher-level cognitive architectures remains uncertain.

The semantic pointer architecture unified network (SPAUN) system [182] is a single spiking neural network model which generates diverse functions and flexibly integrates these functions in a manner suggestive of the flexibility of primate cognition. SPAUN combines serial working memory (via a recurrent attractor neural network with a family of fixed points corresponding to stored values [612]), reinforcement learning, action selection [632], symbol manipulation via vector symbolic architectures [633], motor control [154], image recognition and various forms of pattern completion, and arguably comes closest, among existing models, towards attempting to provide an integrated mesoscale theory of cortical organization. SPAUN models visual cortex as a hierarchy of feature detectors (restricted Boltzmann machines), and prefrontal cortex as a separate working memory system based on neural integrators and convolution memories [421]. All these systems are implemented in spiking neurons through a common mathematical framework, the NEF, for representation and transformation of variables in neuronal populations. In principle, neural populations implementing functions via the NEF could provide a substrate for configurable computational blocks.

The HyperNEAT architecture [216] is not explicitly concerned with constructing configurable sets of basic instructions, but it provides a natural substrate for building structures that repeat with variation [554].

In short, the notion of using a taxonomy of configurable computation blocks for bridging between computational and neural descriptions has not been a core focus of theoretical and computational modeling efforts in neuroscience.

2.5 Recap

Historically, within the space of possible cortical models – from von Neumann architectures, to the Turing universality of networks of McCulloch and Pitts neurons, to random interconnectivity, to massively repeated canonical computational modules, to a uniform substrate shaped by one or many learning rules – comparatively little attention has been paid, in theoretical and computational neuroscience, to architectures that incorporate a rich set of basic instructions (as opposed to only one or a few "canonical" operations) via partially stereotyped yet systematically diversified neural structures. Such architectures are a natural choice given our knowledge of the brain's development and function, and they provide a conceptual framework for generating hypotheses about how diverse neural structures and activities relate to elementary computational functions implemented by the brain.

In the long run, the notion of configurable logic blocks might also help to make sense of human "uniqueness", to the extent that the repertoire of CCB configurations might differ across species. For example, even if most mammals manage with a limited form of cortical computation based only on motifs like pattern recognition and working memory, primates and humans might further re-purpose elements such as the cortical column, potentially providing for the capacity to concatenate arbitrary symbols [438] or represent recursive structures [658,265]. Future work might allow the comparison of inventories of CCBs across species.

Intriguingly, recent transcriptome analyses [266,369] show that the human frontal areas are marked by "a predominance of genes differentially expressed within human frontal lobe and a striking increase in transcriptional complexity specific to the human lineage in the frontal lobe" – exactly as one might expect if some new computational block configuration had recently evolved.

To understand in depth what is going on in a brain, we need tools that can fit inside or between neurons and transmit reports of neural events to receivers outside. We need observing instruments that are local, nondestructive and noninvasive, with rapid response, high band-width and high spatial resolution... There is no law of physics that declares such an observational tool to be impossible.

Freeman Dyson

3

Physical Principles for Scalable Neural Recording

Neuroscience depends on monitoring the electrical activities of neurons within functioning brains[21,43,219] and has advanced through steady improvements in the underlying observational tools. The number of neurons simultaneously recorded using wired electrodes, for example, has doubled

every seven years since the 1950s, currently allowing electrical observation of hundreds of neurons at sub-millisecond timescales[630]. Recording techniques have also diversified: activity-dependent optical signals from neurons endowed with fluorescent indicators can be measured by photodetectors, and radio-frequency emissions from excited nuclear spins allow the construction of magnetic resonance images modulated by activity-dependent contrast mechanisms. Ideas for alternative methods have been proposed, including the direct recording of neural activities into information-bearing biopolymers[735,227,373].

Each modality of neural recording has characteristic advantages and disadvantages. Multi-electrode arrays enable the recording of ~ 250 neurons at sub-millisecond temporal resolutions. Optical microscopy can currently record $\sim 100\,000$ neurons at a 1.25 s timescale in behaving larval zebrafish using light-sheet illumination[17], or hundreds to thousands of neurons at a ~ 100 ms timescale in behaving mice using a 1-photon fiber scope[739]. Magnetic resonance imaging (MRI) allows non-invasive whole brain recordings at a 1 s timescale, but is far from single neuron spatial resolution, in part due to the use of hemodynamic contrast. Finally, molecular recording devices have been proposed for scalable physiological signal recording but have not yet been demonstrated in neurons[735,227,373].

Figure 3.1 illustrates the recording modalities studied here. While further development of these methods promises to be a crucial driver for future neuroscience research[332], their fundamental scaling limits are not immediately obvious. Furthermore, inventing new technologies for scalable neural recording requires a quantitative understanding of the engineering problems that such technologies must solve, a landscape of constraints which should inform design decisions.

Our analysis is predicated on assumptions that enable us to estimate scaling limits. These include assumptions about basic properties of the brain, which are treated in section 3.1 (Basic Constraints), as well as those pertaining to the required measurement resolution and the limits to which a neural recording method may perturb brain tissue, which are treated in section 3.2 (Challenges for Brain Activity Mapping). Together, these considerations form the basis for our estimates of the prospects

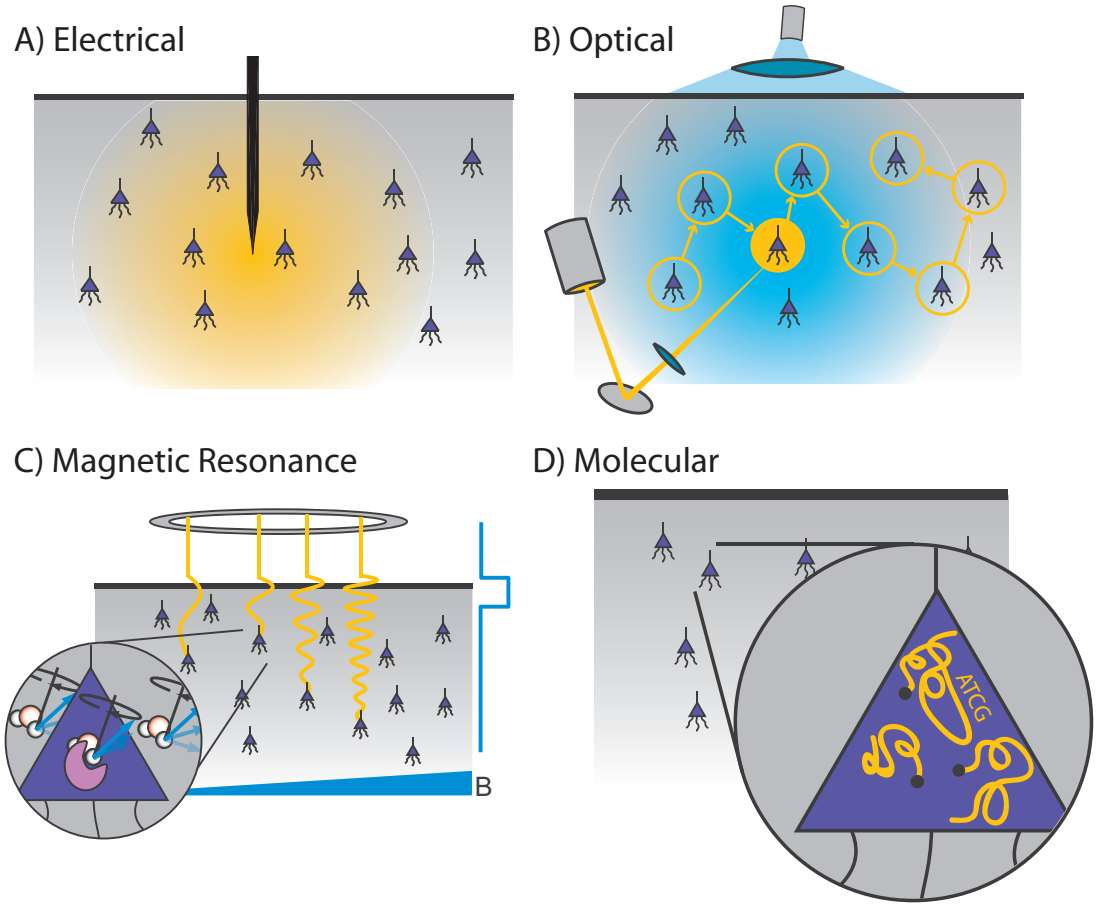

Figure 3.1: Four generalized neural recording modalities. (a) *Extracellular electrical recording* probes the voltage due to nearby neurons. (b) *Optical microscopy* detects light emission from activity-dependent indicators. (c) *Magnetic resonance imaging* detects radio-frequency magnetic induction signals from aqueous protons, after weak thermal alignment of the proton spins by a static magnetic field. Activity-dependent contrast agents are necessary to transduce neural activity into an MRI readout, whereas current functional MRI methods rely on blood oxygenation signals which cannot reach single-neuron resolution. (d) *Molecular recording* devices have been proposed, in which a record of neural activity is encoded in the monomer sequence of a biomolecular polymer – a form of nano-scale local data storage. This could be achieved by coupling correlates of neural activity to the nucleotide misincorporation probabilities of a DNA or RNA polymerase as it replicates or transcribes a known DNA strand.

for scaling of neural recording technologies. We analyze four modalities of brain activity mapping—electrical, optical, magnetic resonance and molecular—in light of these assumptions, and conclude with a discussion on opportunities for new developments.

Importantly, our assumptions, analyses and the conclusions thereof are intended as *first approximations and are subject to debate*. We anticipate that as much can be learned from where our logic breaks down as from where it succeeds, and from methods to work around the limits imposed by our assumptions.

3.1 Basic Constraints

Mouse brain The mouse brain contains $\sim 7.5 \times 10^7$ neurons in a volume of $\sim 420\,\mathrm{mm}^3$ [681] and weighs about 0.5 g. The packing density of neurons varies widely between brain regions. In the below, we will use a cell density of $\varrho_{\mathrm{neurons}} \approx 92\,000/\mathrm{mm}^3$, as measured for mouse cortex [78]. This corresponds roughly to one neuron per 22 µm voxel. The density of cortical synapses, on the other hand, approaches $10^9/\mathrm{mm}^3$, i.e., one synapse per $1\,\mu\mathrm{m}^3$ voxel. For comparison, the human brain has roughly 8×10^{10} neurons [34] in a volume of $1200\,\mathrm{cm}^3$ [22].

The human brain consumes ∼15 W of power (performing, at synapses, a rough equivalent of at least 10^{17} floating point computational operations per second on that power budget, according to one definition [572], although the analogy with digital computers should not be taken literally). Because power consumption scales approximately linearly with the number of neurons [279], the mouse brain is expected to utilize ∼15 mW. For comparison, the metabolic rate of the ∼20–30 g mouse is ∼ 200–600 mW depending on its degree of physical activity [622].

Neural activities Action potentials (spikes) last ∼2 ms. The rate of neuronal spiking is highly variable. Some authors have assumed an average rate of 5 Hz [572,261], but certain neurons spike at 500 Hz or faster [225], while many neurons spike much more slowly. For example, cerebellar granule cells, which

make up half of the neurons in the brain, have spontaneous firing rates of ∼0.5 Hz[109]. In neocortex, one analysis estimated 0.16 spikes per second per neuron (in primate) as energetically sustainable[398]. There may be as much as a two-fold change in metabolism and hence firing rate across brain states[294]. Certain neurons (possibly up to 90% for some neuron types in some brain areas) may be effectively silent[607,48], e.g., spiking less than once every ten seconds. Some studies have attempted to measure the *distribution* of neural firing rates in various cortical areas (as opposed to just the average rate), and have observed that these distributions are often long-tailed: a small minority of the neurons fires a majority of the spikes[563,500,295,588].

While these estimates of typical firing rates are useful numbers to have in mind, in the below we aim to sample all neurons at 1 kHz rates (or higher for techniques requiring observation of detailed spike waveforms). This choice is informed by several factors. First, measuring spike *timing* with millisecond precision is relevant for understanding network function, due to the possibilities for timing codes, spike-timing dependent plasticity mechanisms, and other effects relying on temporally-precise spiking patterns[444,35,650,224]. In this regard, it is also important for a recording method to maintain precise temporal phasing between measurements at different brain locations: activity measurements should be locked to precise global clocks, perhaps with a tolerable phase imprecision between any two measurements in the range of $\frac{1}{2} \times 1\,\text{ms} \approx 100\text{–}200\,\mu\text{s}$. Furthermore, the activities of neurons can be highly correlated locally or across large networks[577], suggesting that local activity sensors may be subjected to high instantaneous total firing rates due to simultaneously-active neurons.

Absorption and scattering of radiation All existing methods of neural recording utilize electromagnetic waves, from the near-DC frequencies of wired electrical recordings (∼1 kHz) to the radio-frequencies of wireless electronics and fMRI (MHz–GHz) to visible light in optical approaches (∼ 500 THz). These electromagnetic waves are attenuated in brain tissue by absorption and scattering. As an approximation to the electromagnetic absorption by brain tissue, we treat the absorption

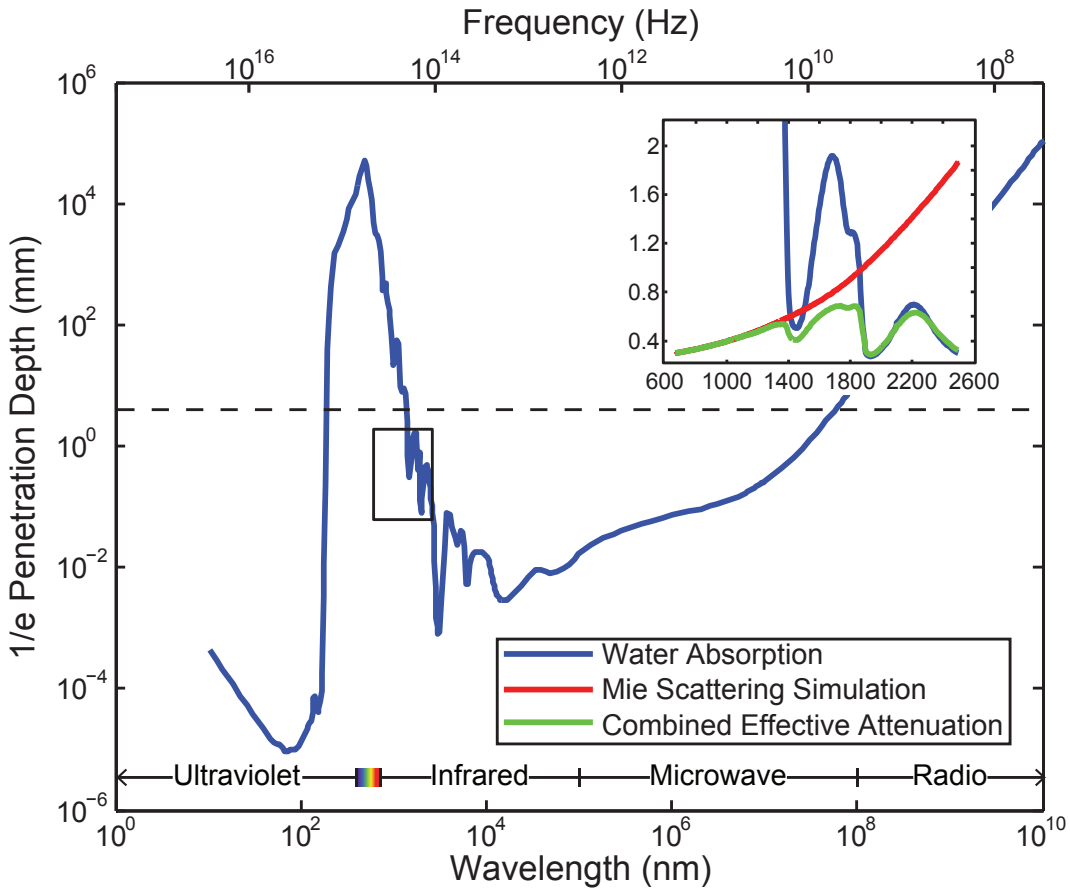

Figure 3.2: Penetration depth (attenuation length) of electromagnetic radiation in water vs. wavelength (data from [324]). The approximate diameter of the mouse brain is shown as a black dashed line. Inset: approximate tissue model based on Mie scattering and water absorption. Absorption length of water [377] (blue), approximate tissue scattering length in a Mie scattering model (red) and the resulting attenuation length (green) of infrared light (inset reproduced from [377], with permission).

by water, the brain's main constituent (68–80 % by mass in humans[157,191]). At visible and near-IR wavelengths, scattering dominates absorption: absorption lengths are in the ∼1 mm range, while scattering lengths are ∼25–200 µm[707]. The combined effect of absorption and scattering is measured by the attenuation length, the distance over which the signal strength is reduced by a factor of $1/e$ along a path. Figure 3.2 shows the absorption length of water[377], and the attenuation length in a Mie scattering model (from [292]) intended to approximate the scattering properties of cortical tissue (and see [213] for tissue skin depth measurements in the 10 Hz to 100 GHz range). This gives a preliminary indication of which wavelengths can be used to measure deep-brain signals with external detectors. Note that the attenuation length is only one of several relevant metrics: for example, scattering not only causes signal attenuation, but also causes noise and impairs signal separation, so the magnitude of the scattering is a key figure of merit.

3.2 Challenges for Brain Activity Mapping

Any activity mapping technology must extract the required information without disrupting normal neuronal activity. As such, we consider three primary challenges: spatiotemporal resolution and informational throughput, energy dissipation and volume displacement.

3.2.1 Spatiotemporal Resolution and Informational Throughput

A sampling rate of 1 kHz is necessary to capture the fastest trains of action potentials at single-spike resolution. A minimal data rate of 7.5×10^{10} bits processed per second is then required to record 1 bit per mouse neuron at 1 kHz.

In electrical recording, higher sampling rates (e.g. 10–40 kHz) are often necessary to distinguish neurons based on spike shapes when each electrode monitors multiple neurons. More fundamentally, one bit per neuron sampling at 1 kHz would likely not be sufficient to reliably distinguish spikes

above noise: transmitting ∼10 bit samples at ∼10 kHz (full waveform) or ∼10–20 bit time-stamps upon spike detection would be more realistic.

Conversely, it may be possible to locally compress measurements of a spike train before transmission. The degree of compressibility of neural activity data is related to the variability in the distribution of neural responses (e.g., such a distribution may be defined across time bins or repeated stimulus presentations)[640]. In the blowfly *Calliphora vicina*, the entropy of spike trains has been measured to be up to ∼ 180 bit/s, and the information about a stimulus encoded by a spike train was as high as ∼90 bit/s[640]. Extrapolating from fly to mouse, this would suggest that a compression factor of 5×–10× should be possible, relative to a 1000 bit/s raw binary sampling.

As a naïve estimate of the entropy as a function of firing rate, one can write the entropy H in bit/s, assuming 1 ms long spikes and $f =$ 1000 Hz sampling rate, as

$$H \approx \left(-P_{\text{spike}} \cdot \log_2\left(P_{\text{spike}}\right) - \left(1 - P_{\text{spike}}\right) \cdot \log_2\left(1 - P_{\text{spike}}\right)\right) \cdot f$$

where P_{spike} is the probability of spiking during the sampling interval (average firing rate/f). For an average firing rate of 5 Hz, $P_{\text{spike}} = 0.005$ and $H = 45$ bit/s, corresponding to a compression factor of ∼20×. However, at 500 Hz average firing rate, $P_{\text{spike}} = 0.5$ with $H \approx 1000$ bit/s, i.e., there is no compressibility. Therefore, compression could conceivably reduce the data transmission burden for activity mapping by 1–2 orders of magnitude, depending on the neurons and activity regimes under consideration. Note that these compressibility calculations have assumed that firing patterns are independent across cells; they represent the temporal compressibility of the spike train from each cell, treated individually. Patterns across cells could conceivably be compressed by a much larger amount, to the extent that there is redundancy between cells. Nevertheless, we use 1 bit/neuron/ms or 100 Gbit/s as a "minimal whole brain data rate" in what follows. In many cases, this likely constitutes a lower bound on what is feasible in practice.

3.2.2 Energy Dissipation

Brain tissue can sustain local temperature increases (ΔT) of 2C without severe damage over a timescale of hours. Indeed, changes of this magnitude may occur naturally in rats in response to varying activity levels[710]. Assuming that the brain is receiving a constant power influx $P_{\text{delivered}}$ and that the local thermal transport properties of mouse brains are similar to those of humans, we can approximate the temperature change in deep-brain tissue as a function of the applied power[621,392]:

$$\frac{\mathrm{d}T}{\mathrm{d}t} = \left(P_{\text{delivered}} + P_{\text{metabolic}} - \varrho_{\text{blood}} C_{\text{blood}} f_{\text{blood}} \Delta T\right) / \, C_{\text{tissue}}$$

where $P_{\text{metabolic}} = 0.0116\,\text{W/g}$ is the power per unit mass of basal metabolism, $C_{\text{tissue}} \approx 3.7\,\text{J/(K g)} \approx 0.88 \cdot C_{\text{water}}$ is the specific heat capacity of brain tissue, $\varrho_{\text{blood}} = 1.05\,\text{g/cm}^3$ is the density of blood, $C_{\text{blood}} = 3.9\,\text{J/(K g)}$ is the specific heat capacity of blood, $f_{\text{blood}} = 9.3 \times 10^{-9}\,\text{m}^3\text{/(g s)}$ is the volume flow rate of blood, and ΔT is the temperature difference between the brain tissue and the blood (at 37C). A steady-state temperature increase ($\mathrm{d}T/\mathrm{d}t = 0$) of 2C corresponds to dissipation of $\sim$40 mW per 500 mg mouse brain. Therefore, a recording technique should not dissipate more than $\sim$40 mW of power in a mouse brain at steady state.

This estimate of the power dissipation limit in mouse brains, based on such a simplified model of the brain's thermal transport mechanisms, is likely an under-estimate of the actual maximum steady-state power dissipation. Radiative heat loss was ignored here since infrared light emitted by deep-brain tissue is quickly re-absorbed by nearby tissue. We have also ignored cooling due to flows in the cerebrospinal ventricles[617] and in the glymphatic system[303]. We have further assumed that conductive heat loss from the brain surface is negligible compared to the heat extracted volumetrically by blood flow. While this may hold true locally in deep brain voxels and over short timescales (e.g., $<$ 1 min), further work (e.g., a whole-head model[392,642]) is needed to define the true limits of sustained volumetric heat production by neural recording systems distributed throughout the mouse brain. Indeed, the char-

acteristic length scale of temperature inhomogeneities in the brain is on the order of millimeters[644], whereas heat exchange with the flowing blood dampens the effects of local perturbations over longer length scales. For large brains, this means that sources and sinks of heat exert only local thermal effects; for a mouse brain on the scale of $<$ 10 mm, however, surface and volumetric effects likely combine to influence temperature changes at any site in the brain[643]. Experimentally, increasing the temperature gradient at the brain surface, via a cranial window exposed to ambient air at 25C (i.e., the common craniotomy technique used to access mouse neocortex), has been shown to dis-regulate brain temperature down to a depth of several millimeters[331]. For the above reasons, our estimates of the brain's capacity for heat dissipation should be treated only as first approximations.

Higher power levels, compared to the maximum steady state power, may be introduced into brains transiently. According to the above equation, if a neural recorder dissipates $\sim$40 mW per 500 mg mouse brain, then the brain approaches the steady-state temperature in 2–3 min, making shorter experiments potentially feasible. This is in agreement with the estimate from[644] of a $\sim$1 min time constant for brain temperature changes, as well as with experimental measurements showing similar time constants for temperature variations resulting from sustained neural stimulation[456,661]. Increasing convective heat loss from the brain by increasing blood flow (e.g. via increased heart rate) or cooling the brain (volumetrically or via its surface[643]), the blood, the cerebrospinal fluid (CSF), or the whole animal[530], could increase the allowable transient or steady-state power dissipation.

There are also limits on the power density of radiation applied to brain tissue. For radio-frequency electromagnetic radiation, the specific absorption rate (SAR) limit on the power density exposed to human tissue is $\sim$10 mW/cm^2 [2], while for ultrasound (which couples less strongly to dissipative loss mechanisms in tissue) the SAR limit is up to 72$\times$ higher[4]. The power density limit for visible and near-IR light exposures are also in the $\sim$10–100 mW/cm^2 range for $\sim$1 ms long exposures, decreasing as the exposure time lengthens (based on the IEC 60825 formulas[3]).

High local power dissipation (transient or steady-state) can modify the electrical properties of ex-

citable membranes, altering neuronal activity patterns. For example, heating of cell membranes and of the surrounding solution by millisecond-long optical pulses leads to changes in membrane electrical capacitance mediated by the ionic double layer[594]. Slower temperature changes (on a scale of seconds) resulting from RF radiation lead to accelerated ion channel and transporter kinetics[595]. Both of these effects are appreciable when the temperature changes are on the order of 1–10C.

For comparison with current practice, common guidelines for chronic heat exposure from biomedical implants[710] use upper limits of 2C temperature change, 40 mW/cm² heat flux from the surface of implanted brain machine interface (BMI) hardware, and an SAR limit of

$$\frac{\sigma E^2}{2\varrho} < 1.6\,\mathrm{mW/g}$$

for electromagnetic energy absorbed by tissue, where E is the peak electric field amplitude of the applied radiation, $\sigma \approx 0.18$ S/m is the electrical conductivity of grey matter and $\varrho \approx 1\,\mathrm{g/cm^3}$ is the tissue density[392] (this corresponds to an irradiance of $\varepsilon_0 c E^2/2 \approx 2.4\,\mathrm{mW/cm^2}$). A 96-channel BMI system demonstrated in living brains had dissipated areal power density approaching 40 mW/cm²[555].

3.2.3 Sensitivity to Volume Displacement

To prevent damage to the brain, we assume that a recording technique should not displace $> 1\,\%$ of the brain's volume. *The appropriate damage threshold is not yet established, however, so this constitutes a first guess.* It is possible to insert large numbers of probes throughout multiple brain areas without compromising function. In rats, 96 electrodes of 50 µm diameter were simultaneously inserted across four forebrain structures (cortex, thalamus, hippocampus and putamen)[551]. In rhesus macaque, 704 electrodes of diameter 50 µm and average depth 2.5 mm were chronically implanted in cortex[494]. Note, however, that the total volume displacement in these experiments was below 0.1 %, and below 0.01 %, respectively. Furthermore, these studies used a low density of electrodes. Thus,

detailed limits on the amount and density of inserted material are unknown.

Furthermore, the nature of the volume displacement is important—sheets of instrumentation that sever long-range connectivity, for example, would disrupt normal brain function regardless of the degree of volume displacement. Conversely, higher volume displacement might be possible if introduced gradually, or during early development, insomuch as the brain can adapt without disrupting natural computation. One important consideration in this regard would be the disruption of blood circulation by inserted material; a high density of implanted material in a brain region could cause stroke due to widespread vascular damage. Recent studies have defined in microscopic detail the complete vascular network of the mouse cortex using high-throughput histology[66]; this type of information could be used to enumerate key vascular pathways which could be spared from damage. To apply this in a particular animal, however, would require a non-destructive method to image the vasculature at a similar resolution; otherwise, only a broad statistical view can be obtained, since the detailed vascular geometry will vary from animal to animal.

Secondary effects like glial scarring may also pose obstacles to the long-term implantation of large numbers of probes[531,692], although methods are being developed to alleviate this[652,548,547]. In the context of electrical recording, the impact of glial scarring may vary depending on geometry. For example, the recording sites at the tip of a Utah or Duke multi-electrode array are typically viable in chronic recordings of up to 18 months in primates[494,649], whereas in array formats with multiple electrodes along each shaft, such as the Michigan array, chronic recordings of up to 4 months have been reported in rats[679]. Differences in recording lifetime may be due to differences in the pattern of glial encapsulation of the contacts.

3.3 Evaluation of Modalities

We next evaluate neural recording technologies with respect to the above challenges, using the mouse brain as a model system. Table 1 lists the modalities studied, the assumptions made, the analysis strategies applied, and the conclusions derived.

In the oldest strategy for neural recording, an electrode is used to measure the local voltage at a recording site, which conveys information about the spiking activity of one or more nearby neurons. The number of recording sites may be smaller than the number of neurons recorded since each recording site may detect signals from multiple neurons. As a note for practitioners, we use the term "electrode" interchangeably with the terms "recording site" or "contact", meaning a point-like voltage sensing node: many multi-electrode arrays in common use (e.g., the Duke and Utah arrays) are conductive only at the tip, whereas other designs (such as the Michigan array) have multiple contacts along the shaft. Each shaft in a Michigan array would thus constitute multiple "electrodes" or "recording sites" in our parlance. Traditional electrical recording techniques keep active devices such as amplifiers outside the skull and therefore do not pose a heat dissipation challenge; this may change if amplifiers are brought closer to the signal sources to reduce noise.

Slowly varying (e.g., < 300 Hz) extracellular potentials (LFPs)[54,93] on the order of 0.1–1 mV, and fields[24] on the order of 1–10 mV/mm, are generated by neural activity. While LFPs can be filtered from the higher-frequency signals associated with extracellular voltage spikes, these and other effects necessitate maintaining precise potential references (i.e., ground levels) for voltage measurements distributed widely across the brain.

Spatiotemporal Resolution

Limits assuming perfect spike sorting We begin with an idealized estimate of the number of electrodes required to record from the entire mouse brain, neglecting the difficulty of assigning

observed spikes to specific cells (spike sorting), and focusing only on what is needed to detect spikes from every neuron on at least one electrode. The key variable here is the maximum distance between an extracellular electrical recorder and a neuron from which it records spikes. In a first approximation, this is determined by two factors: the decay of the signal with distance from the spiking neuron and the background noise level at the recording site. We assume that for an electrode to reliably detect the signal from a given neuron, the magnitude of that neuron's signal must be larger than the electrode's noise level. Note, however, that knowledge of spike shape distributions could potentially be used to extract low-amplitude spikes from noise.

The peak signals of spikes from neurons immediately adjacent to an electrode are in the 0.1–1.0 mV range and scale roughly as e^{-r/r_0}, where r is the distance from the cell surface and the $1/e$ falloff distance, r_0, has been experimentally measured at ~28 μm in both salamander retina[582] and cat cortex[246], and computed at ~18 μm in a biophysically realistic simulation[238,23]. However, this decay is strongly influenced by the detailed geometry of neuronal currents and the properties of the extracellular space (e.g., its inhomogeneity, which may lead to a frequency-dependent falloff of the extracellular potential[54]), making analytical calculation of the decay rate difficult (at large distances, a much slower $1/r^2$ dipole falloff is expected).

Several sources of background noise enter the recordings. Johnson noise, which arises from thermal fluctuations in the electrode, is

$$V_{\text{johnson}} = (4k_B TZ\text{BW})^{1/2}$$

which for physiological temperature, electrodes of impedance $Z = 0.5\,\text{M}\Omega$, and $\text{BW} = 10\,\text{kHz}$ bandwidth is $V_{\text{johnson}} \approx 9\,\mu\text{V}$. The recordings are also affected by interference from other neurons, which has been reported to exceed the Johnson noise, and is non-stationary due to changes in the cells' firing properties[567]. The noise and interference from these sources realistically produces $>$ 10–20 μV of voltage fluctuations[100]. Current recording setups thus have signal to interference-plus-noise

ratios (SINRs) of < 100, where the SINR is defined as the ratio of the peak voltage from immediately adjacent neurons to the voltage fluctuation floor of the electrode.

A limit on the maximum recording distance is the distance at which the signal from the farthest neuron falls below the noise floor, $r_{\max} \approx r_0 \ln(\text{SINR})$. For SINR ≈ 100, $r_{\max} \approx 130\,\mu\text{m}$. For comparison, recent experimental data from multi-site silicon probes has shown few detectable neurons beyond $\sim 100\,\mu\text{m}$ and none detectable beyond $160\,\mu\text{m}$[172]. Recordings in the hippocampal CA1 region could not detect spikes from cells farther than $140\,\mu\text{m}$ from the electrode tip[277], even after averaging over observations triggered on an intracellularly recorded spike; in hippocampus, this corresponds to a detection volume containing approximately 1000 neurons[94]. Furthermore, in many studies (in monkeys, rats and mice) using multi-electrode arrays with 150–300 μm inter-electrode spacings, no neuron is seen by more than one electrode[700,105,372,323].

Due to the steep local falloff, even improving the SINR by a factor of 10 only extends the maximal recording distance to $r_{\max} \approx 190\,\mu\text{m}$. Assuming packing of the brain into equal sized cubes of side length $d = \frac{2\sqrt{3}}{3} r_{\max} \approx 150\,\mu\text{m}$ gives $N > 130\,000$ electrodes for whole brain recording using recording sites with $r_{\max} \approx 130\,\mu\text{m}$. Note that N varies as the third power of $r_{\max}$ and is therefore highly sensitive to variations in the assumed maximal recording distance; the number of required recorders can range from 38 000 to 210 000 as $r_{\max}$ varies from $190\,\mu\text{m}$ to $110\,\mu\text{m}$.

These calculations, by assuming perfect spike sorting, greatly underestimate the required number of electrodes in practice. First, signals from the weakest cells are far weaker than those from the strongest cells and the signals from some cells decay much faster than others[246]. Second, because of neuronal synchronization, the local noise produced by nearby neurons may sometimes be large. Third, spike waveforms can vary over the course of a recording session[193,638]. Finally, with many neurons per electrode or at high firing rates, spikes from detectable neurons will often temporally overlap, making spike sorting difficult.

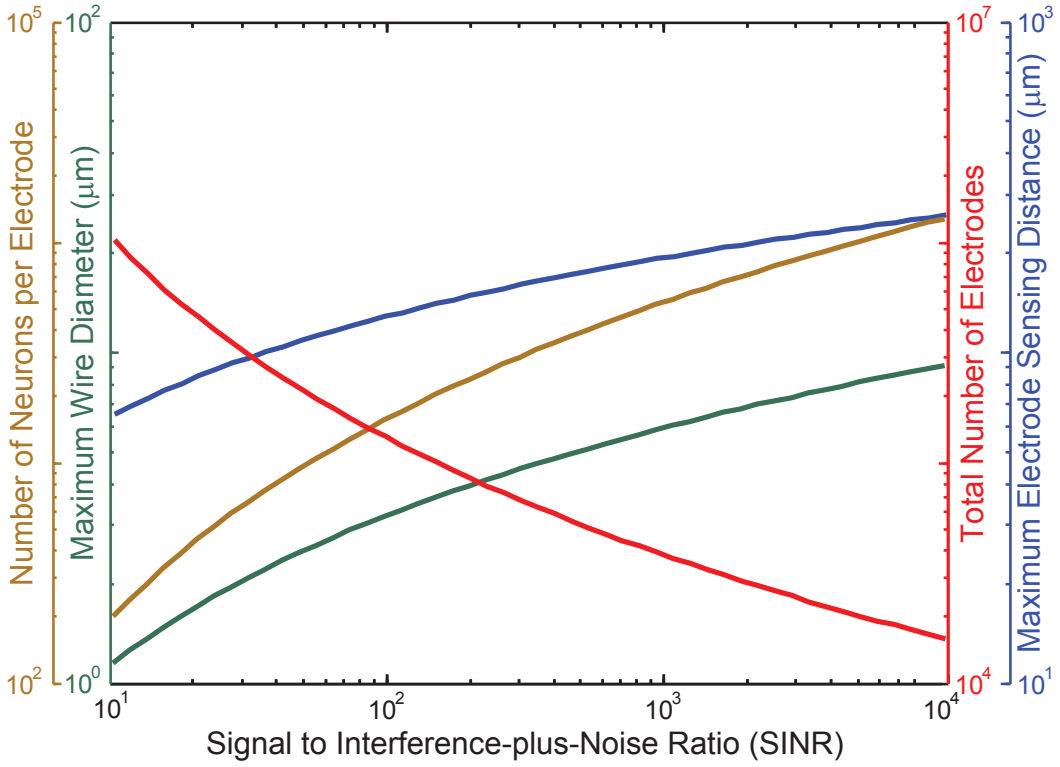

Figure 3.3: The voltage signal to interference-plus-noise ratio (SINR) for neurons immediately adjacent to the recording site sets an approximate upper bound on the distance, $r_{\max}$, between the recording site and the farthest neuron it can sense (blue), due to the exponential falloff of the voltage SINR with distance. Assuming at least one electrode per cube of edge length $\frac{2\sqrt{3}}{3} r_{\max}$ in turn limits the number of neurons per recording site (gold), the total number of recording sites (red) and the maximal diameter of wiring consistent with $< 1\,\%$ total brain volume displacement (turquoise). SINR values for current recording setups are $< 10^2$. In practice, the number of neurons per electrode distinguishable by current spike sorting algorithms is only ~ 10, with an estimated information theoretic limit of ~ 100, so these curves *greatly under-estimate* the number of electrodes which would be required based on realistic spike sorting approaches in a pure voltage-sensing scenario.

Limits from spike sorting The previous calculations have assumed that any spike which is visible above the noise on at least one electrode can be detected and correctly assigned to a particular cell, i.e., that the problem of spike sorting can be solved perfectly. However, perfect spike sorting is far beyond current algorithmic capabilities and in fact may not be possible in principle.

To achieve the scenario described above, with $N = 130\,000$ recording sites per mouse brain, would require each electrode to sort spikes from all $\frac{4}{3}\pi r_{\max}^3 \varrho_{\text{neurons}}$ neurons in a sphere of radius $r_{\max} \approx 130\,\mu\text{m}$ surrounding the recording site, where $\varrho_{\text{neurons}} \approx 92\,000/\text{mm}^3$ is the density of neurons. This assigns ~800 neurons to a single electrode. Roughly half (i.e., 400) of these neurons will lie at $> 100\,\mu\text{m}$ distance from the electrode, and their signals on the electrode will therefore have voltage SINRs of $< 100e^{-100\,\mu\text{m}/28\,\mu\text{m}} \approx 2.8$, assuming as above that extracellular spike amplitudes decay exponentially in space.

Electrical recording can be viewed as a data transmission problem, with the electrode playing the role of a communication channel (see section 4.4). According to the Shannon Capacity Theorem[134], the information capacity C of a single analog channel (with additive white Gaussian noise) is

$$C = \text{BW} \log_2(1 + S/N)$$

where BW is the bandwidth, S is the signal power (proportional to the square of the voltage), and N is the noise power. Here the bandwidth is $\text{BW} \approx 10\,\text{kHz/s}$, and the ratio of peak signal power to noise power of a single spike for the outer 400 cells is no more than 2.8^2, or 0.5×2.8^2 using the RMS signal power instead of the peak. With 400 cells emitting 2 ms spikes at 5 Hz, there will be an average of 4 cells spiking at a time, for $S/N \approx 0.5 \times 4 \times 2.8^2 \approx 15.7$ counting the signal power from all the spikes. The channel capacity is then $C \approx 40\,\text{kbit/s}$. This represents the maximum amount of information (e.g., about which neuron spiked when) that the population of spiking neurons can transmit via the electrode which measures them. To transmit *uniquely identifiable* signals from all 400 neurons at

millisecond temporal precision, however, requires 1 kbit/s $\times$ 400 $=$ 400 kbit/s, which is $>$ 10$\times$ greater than the channel capacity and is therefore not achievable. Even with optimal temporal compression of $\sim$5 Hz spikes (see section 2), we would need to transmit $\sim$400/20 $=$ 20 kbit/s, which is strictly less than the channel capacity and thus possible in principle, but barely so. Furthermore, the channel capacity given here is an overestimate, since 2.8 is an upper bound on the SINR of the outer cells. On the other hand, note that the use of a nominal 5 Hz average firing rate here (in the estimates of signal to noise ratio and of temporal compressibility) greatly oversimplifies the distribution of firing rates across neurons, as discussed in section 2 above, so this analysis can only be treated as a first approximation.

Based on these rough estimates, perfect spike sorting may not be possible at $\sim$800 neurons per electrode, in a sphere of radius 130 μm surrounding a recording site, and at the noise levels typical of current electrodes. In essence, there may not be enough room on the electrode's voltage trace to discriminate such a large number of weak, noisy signals. Note that these information-theoretic limits still apply even if it is possible to resolve temporally overlapping spikes. In fact, the channel capacity is what ultimately limits the ability of a spike sorting algorithm to resolve such overlapping spikes.

To see the regime in which spike sorting becomes feasible, suppose that each electrode is only responsible for spike sorting from the population of $\sim$100 neurons nearest to the electrode, i.e., in a sphere of radius $r \approx 64\,\mu$m, assuming the 92 000/mm^3 cell density from mouse cortex. The outermost 50% of these neurons are then positioned $>$ 50 μm from the recording site. For these outermost 50 neurons, the voltage SINR is $< 100e^{-50\,\mu\text{m}/28\,\mu\text{m}} \approx 17$ and $S/N < 0.5 \times 17^2 \times (2\text{ ms} \times 5\text{ Hz} \times 50) \approx 72.3$. The channel capacity is therefore $<$ 62 kbit/s, whereas 50 kbit/s is needed for signal transmission from 50 neurons without temporal compression versus $\sim$2.5 kbit/s with temporal compression. Even 100 neurons per electrode may therefore still be close to the limits of information transmission through the noisy channel corresponding to a single electrode.

In practice these limits are likely to be highly optimistic, since the set of spikes emerging from a neuronal population is far from an optimally designed code from the perspective of multiplexed signal

transmission through a voltage-sensing electrode: the waveforms for different neurons are similarly-shaped rather than orthogonal, the spikes emitted by a given neuron vary somewhat in amplitude and exhibit shape fluctuations (signal-dependent noise), and it is not known in advance what the characteristic signal from each neuron looks like (or even how many neurons there are).

Indeed, current practice is far from the above information-theoretic limits. At present, spike sorting algorithms operating on data from large-scale (250-500 electrodes), densely spaced ($\sim$30 µm), 2D multi-electrode arrays can reliably identify and distinguish spikes from nearly all of the 200-300 retinal ganglion cells[447,524] in a small patch of retina, and can also infer approximate cell locations through spatial triangulation of spike amplitudes. This represents a roughly 1 : 1 ratio of cells to electrodes. Electrodes with up to 4 single units can be found in chronically implanted multi-electrode arrays (in both mouse and primate)[133,494], where the electrodes are sparse, although the average yield of cells per electrode is closer to 1 : 1; if only electrodes with at least one cell are counted, the average rises to $\sim$1.5–1.7 cells per electrode. Optimistically, simulations of neural activity suggest that 5-10 neurons per electrode may be distinguishable using current spike sorting algorithms[517,567,100]. A limit of $\sim$10 neurons per electrode would imply $N = 7.5 \times 10^6$ electrodes to record from all neurons in the mouse brain, which could be accomplished by positioning recording sites on a cubic lattice with $\sim$40 µm edge length.

Future algorithmic improvements could enable sorting from more than $\sim$10 cells per electrode, but this becomes increasingly challenging. One simple estimate of a reasonable practical limit, for the regime of many neurons per electrode, would be the largest number of neurons that can be sorted without requiring the frequent resolving of temporally overlapping spikes: if the average neuron fires at $\sim$5 Hz and spikes last $\sim$2 ms, then at most roughly 100 neurons per electrode can be sorted without requiring overlaps to be resolved. Note that while some present-day algorithms can successfully resolve overlapping spikes[447,524,582,217,534], they typically do so only in the case where electrodes are densely spaced and any given spike appears on many electrodes, such that spatial information can be used to

resolve the overlap. Resolving overlaps when spikes appear on only one or a few channels is more difficult due to noise and spike-shape variation.

Overall, ∼100 cells per electrode may be taken as a rough estimate of the limits of spike sorting, and would imply $N = 750\,000$ electrodes and an edge spacing of ∼80 μm if a cubic lattice of recording sites were used. However, we should not exclude the possibility of game-changers which could alter the nature of the recorded data to improve the available information. For instance, CCD cameras could be attached to multi-electrode arrays to aid in the identification and localization of cells, or directional information on the source of spikes could be obtained at each recording site, for example by measuring the directions of gradients in voltage. Systems that capture such additional information could circumvent the above information-theoretic limits and improve spike sorting.

Volume Displacement

We require $< 1\,\%$ total volume displacement from N recorders. Wires from each electrode must make it to the surface of the brain, which implies an average length $\ell \approx 4$ mm for the mouse brain (depending on assumptions about the wiring geometry).

As a rough approximation, consider each recorder to produce a volume displacement associated with a single cylindrical wire, with length ℓ and radius r. Thus r must satisfy

$$\pi r^2 \ell N_{\text{min,rd}} < 0.01 V_{\text{brain}}$$

Using $N_{\text{min,rd}} = 210\,000$ or $38\,000$ recording sites (lower and upper limits from the perfect spike sorting case from above) and $\ell \approx 4$ mm requires wires of radius $r_{\text{max}} \approx 6.0\,\mu$m, or $2.5\,\mu$m, respectively. Alternatively, if 7.5×10^6 electrodes must be used (current spike sorting case from above), the required wire radius is ∼200 nm. While these dimensions are readily achievable using lithographic fabrication, there would be a challenge to produce *isolated* wires of such dimensions at scale (perhaps

suggesting the use of wire bundles). Still, volume constraints per se are unlikely to fundamentally limit whole-mouse-brain electrical recording even in the most pessimistic scenario.

Figure 3.3 illustrates the above considerations as a function of the electrode SINR.

Implanting Electrodes in the Brain

There are several technology options for introducing many electrodes into a brain. For example, flexible nanowire electrodes could, in theory, be threaded through the capillary network[412], as was proposed by Llinas and Hunter. Capillaries are present in the brain at a density of 2500–3000 per mm^3[1], which equates to one capillary per 73 μm, with each neuron lying within ∼ 200 μm of a capillary[413]. The minimum capillary diameter is as small as 3–4 μm, although the average diameter is ∼8 μm, comparable to the non-deformed size of the red blood cells[208]. Blocking a significant fraction of capillaries could lead to stroke or to unacceptable levels of tissue necrosis/liquifaction.

The cerebrospinal ventricles may also provide a convenient location for recording hardware. Furthermore, neural tissues could be grown around pre-fabricated electrode arrays[316], or silicon probes arrays with many nano-fabricated recording sites per probe[172] could be inserted into the brain.

Mechanical forces during insertion and retraction of silicon and tungsten microelectrodes from brain tissue have been measured in rat cortex at ∼1 mN for electrodes of ∼25 μm radius[322]. These forces are comparable to the Euler buckling force F of a 2 mm long cylindrical tungsten rod of r =5 μm radius

$$F = \frac{\pi^2 EI}{(KL)^2} \approx 1\,\text{mN}$$

where $E = 411$ GPa is the elastic modulus of tungsten, $I = (\pi/2)r^4$ is the moment of inertia of the wire cross-section, $L \approx 2$ mm is the length of the wire, and K is the column effective length factor which depends on the boundary conditions and is set to $K = 1$ here for simplicity.

This suggests that it may be possible to push structures of < 10 μm diameter into brain tissue (see[487]

for related calculations). It might be advantageous to pull rather than push wires into the brain (e.g., using applied fields, or perhaps even cellular oxen[698] to carry the wires), since the thinnest wires could withstand tension forces much higher than the compressive force at which they buckle (although there may also be ways to circumvent buckling, e.g., via rapid vibration).

Conclusions and Future Directions

Electrical recording has the advantage of high temporal resolution, but the large number of required recording sites poses challenges for delivery mechanisms. Ongoing innovations in electrical recording that could be leveraged for dramatic scaling include the development of highly multiplexed probes, multilayer lithography for routing electrical traces, novel methods to implant large numbers of electrodes, smaller electrode impedances to reduce the Johnson noise, amplifiers with lower input-referred noise levels, spike sorting algorithms capable of handling temporally overlapping spikes and adaptively modeling the noise, and hybrid systems integrating electrical recording with implantable optics or other methods.

One challenge for a purely-electrical recording paradigm pertains to the ability to relate the measured electrical signals to specific cells within a circuit. As the set of neurons recorded by each electrode grows to encompass a large volume around the electrode, it will become more difficult to attribute the recorded spikes to particular neurons. Furthermore, given the complex geometries of neuronal processes, it is not obvious how to determine the spatial position or layout of a neuron from its electrical signature on a nearby electrode. A given electrode will be positioned near the axons or dendrites of some neurons, and near the cell bodies of other neurons, complicating data interpretation. If the spatial density of recording sites is increased such that many electrodes sample the same neuron, however, this could enable imaging of neuronal morphology and signal propagation via voltage signals across multiple electrodes[39]. Currently, extracellular electrical recording also does not allow extraction of molecular information on the cells being recorded, although intracellular electrophysiological record-

ing methods (e.g.,[363]) might enable this for a limited number of cells.

3.3.1 Optical Recording

Optical techniques measure activity-dependent light emissions from neurons, typically generated by fluorescent indicator proteins, although activity-dependent bioluminescent emissions are an emerging possibility. Current genetically encoded calcium indicators can only distinguish spikes below ∼50–100 Hz firing rates without averaging[616] due to slow intra-molecular kinetics and indicator saturation at high firing rates, although significant improvements in speed are ongoing[647]. Intracellular calcium rises and drops can occur within 1 ms and 10–100 ms respectively[280], which sets the ultimate speed limit for calcium imaging. The field of genetically-encoded high-speed fluorescent voltage indicators is also advancing quickly[47,379,243,636,102,19] and these may find particular use in monitoring sub-threshold events[574].

Spatiotemporal Resolution

Multiplexing strategies For optical approaches, the light originating from the activity of each neuron must be separated from emissions originating from other points in the brain: this can be accomplished in many ways, leading to a variety of architectures for 3D imaging. *Epi-fluorescence microscopy* images a plane in the specimen (i.e., with depth of field DOF $= \frac{2n}{NA^2}$, where n is the refractive index, λ is the wavelength and NA is the numerical aperture of the imaging system[540]) onto a spatially-resolved two-dimensional detector (e.g., a CCD camera). The focal plane is then scanned in order to reconstruct 3D images; because the entire 3D volume is illuminated during image acquisition, out-of-focus neurons cause background emissions. *Light sheet imaging* is similar to epi-flourescence imaging, except that only neurons near the focal plane are illuminated, reducing out of focus noise. Unfortunately, this requires transparent brains[17]. Volumetric imaging can also be performed in a single

snapshot using *lightfield microscopes*[399,84], which capture the directions of incoming light rays, trading in-plane resolution for axial resolution, or by using multi-focus microscopes[10]. In *multi-photon microscopy*, nonlinearities result in fluorescence excitation occurring only near the focal point of the excitation laser, which is scanned across the sample. In *confocal scanning microscopy*, only photons from a point of interest are measured due to geometric constraints (e.g., pinholes). Alternatively, 3D imaging can be performed via *wavefront coding*, which extends the depth of field by creating an axially-independent point-spread function using known optical aberrations, in combination with computational deconvolution[168]. With a known 3D pattern of excitation light, wavefront coding can be applied to 3D fluorescence microscopy without scanning using a 2D detector array[540]. Emerging, alternative strategies rely on *tagging* emissions from different sources with distinguishable modulation patterns[691,155,173,724,713], or precisely controlling and tracking the timing of light emissions[114]. Optical techniques thus achieve signal separation by multiplexing spatially (e.g., direct imaging) or temporally (e.g., beam scanning), or often by a combination of the two.

While optics might seem to require a number of photodetectors comparable to the number of neurons (or a similar number of sampling events in the time domain, e.g., for scanning microscopies), new developments suggest ways of imaging with fewer elements. For example, compressive sensing or ghost imaging techniques based on random mask projections[683,641,654,646] might allow a smaller number of photodetectors to be used. In an illustrative case, an imaging system may be constructed simply from a single photodetector and a transmissive LCD screen presenting a series of random binary mask patterns[297], where the number of required mask patterns is much smaller than the number of image pixels due to a compressive reconstruction.

Effects of light scattering Single-photon techniques limit imaging to a depth of a few scattering lengths at the excitation and emission wavelengths of activity indicators: up to ∼1–2 mm for certain infrared wavelengths[292,358,359] vs. a few hundred microns for visible wavelengths[707]. Activity

dependent dyes are currently available only in the visible spectrum; indicators operating in the infrared (see[199,598,599] for far-red fluorescent proteins) could improve imaging depth.

Multi-photon excitation takes advantage of the deeper penetration of infrared light. Two or more infrared photons may together excite a fluorophore with an excitation peak in the visible range, leading to the emission of a visible photon. If only one neuron is illuminated with sufficient intensity to generate multi-photon excitation, all photons captured by the detector originate from that neuron, regardless of the scattering of the outgoing light. Hence, the emission pathway is limited less by scattering than by absorption. This has resulted in imaging at $>$ 1 mm depth[292,358,359].

There are at least five options for overcoming visible light scattering to enable signal separation from deep-brain neurons[21,20]:

1. Infrared light can excite multi-photon fluorescence in an excitation-scanning architecture.

2. Fluorophores with both excitation and emission wavelengths in the infrared could be developed.

3. By knowing the precise form of the scattering, it can be possible to correct for it. Emerging techniques based on beam shaping allow transmission of focused light through random scattering media by inverting the scattering matrix[128]. Because the scattering properties change over time, this must be done quickly, possibly faster than the imaging frame rate, necessitating high-speed wavefront modulation. This can currently be achieved with digital micro-mirror devices (DMDs), but not with the phase-only spatial light modulators (SLMs) that are used to prevent power losses in the excitation pathways for nonlinear microscopies, although GHz switching of phase-only modulators appears feasible in principle[20]. High speed focusing through turbid media is also achievable using all-optical feedback in a laser cavity[495], and it is even possible to measure the scattering matrix non-invasively[110] using a photo-acoustic technique, or

via all-optical approaches based on speckle correlation[59]. Similar techniques are available for incoherent light[338].

When using short optical pulses, scattering can lead to temporal distortions that degrade the peak light intensity at a focal spot. The $<$ 100 fs pulse durations used in two-photon microscopy, for example, are comparable to the time it takes light to travel 30 μm in vacuum. Fortunately, wavefront shaping techniques can correct for scattering-induced temporal distortions as well[455,337].

4. Light sources and/or detectors could be positioned close to the measured neurons, necessitating the use of embedded optical devices. This could be done using optical fiber[425] and/or waveguide[740,741] technologies, which are developing rapidly. For example, single-mode fiber cables can support $>$ 1 TB/s data rates[505,77] with low light loss over hundreds of kilometers[472]. It is possible to directly image through gradient index of refraction (GRIN) lenses[486] or optical fibers[425,333,203], which provides one way to multiplex multiple observed neurons per fiber.

5. Light emissions from distinct locations can be tagged with distinguishable time-domain modulation patterns, and the emission time-series for each source can later be decoded from the summed signal resulting from scattering[691,155,173,724,713,114]. For example, ultrasound encoding[691,326], which frequency-tags light emissions from a known location via a mechanical Doppler shift of the emitter[426], provides a generic mechanism to sidestep problems of elastic optical scattering, although it requires distinguishing MHz frequency modulations in THz light waves (part per million frequency discrimination). Radio-frequency tagging of light emissions via a digitally synthesized optical approach is also an option and may be applicable to combatting the problem of emission scattering in deep-tissue, multi-point, multi-photon imaging[155].

Speed of beam scanning The speed of scanning microscopes is currently limited by beam repositioning times (~0.1 µs for spinning disk [425,333,203], ~3 µs for piezo-controlled linear scan mirrors, ~10 µs for acousto-optic deflectors [682], ~8 kHz line scans for resonant galvanometer mirrors). The 10 µs repositioning time for acousto-optic deflectors is set by the speed of sound in the deflector crystal, while scanning mirrors and spinning disks are limited by inertia. Note that 0.1 µs repositioning time for current spinning-disk confocal techniques would require 10 seconds per frame for whole mouse brain imaging with a single scanned beam (10^{-7} s/site $\times$ 10^8 sites/brain). There is therefore a need for a 10^4 fold improvement in beam repositioning time and/or beam parallelization in order to achieve 1 kHz imaging frame rates for whole mouse brains.

One strategy to implement parallelization would exploit (yet to be developed) fast, high-resolution phase modulator arrays to arbitrarily re-shape coherent optical wavefronts for multisite holographic multi-photon excitation in 3D [20,512,675]. With fast phase modulation (e.g., ~1 GHz), beating each excitation spot at a different frequency could allow a single detector to probe multiple sites in parallel, despite arbitrarily-large scattering of the outgoing light [20]. Emerging optical techniques may provide alternative means to implement similar strategies [155]. Temporal multiplexing of excitation pulses at distinct locations (e.g., via few-nanosecond beam delays) also allows parallelization of the excitation beam while combatting scattering ambiguity of the emitted light [114]. Furthermore, temporal focusing techniques in two-photon microscopy (depth-dependent pulse duration) can excite an entire plane or line within the sample [506,651,583,511], as well as arbitrary patterns of points [512], potentially allowing fast axial scanning (somewhat analogous to light-sheet techniques used with transparent samples). This method intrinsically corrects for scattering of the excitation light [513], although not of the emission light. Like other multi-photon techniques, however, all these methods remain highly dissipative, as discussed below.

Fluorescence lifetimes in the 0.1–1 ns range [639] ultimately constrain the design of scanning fluorescence microscopies. A delay of 0.1 ns per mouse neuron per frame corresponds to only 100 Hz frame

rate without parallelization, implying that parallelization into at least 10 to 100 beams is essential. The fluorescence lifetime also limits the achievable modulation frequencies in beat-frequency-multiplexed parallelization strategies[155], bit lengths in encoded strategies[173], and temporal offsets in temporally-multiplexed strategies[114], suggesting that parallelization of detectors may be necessary in a strongly scattering environment. Depending on the degree of parallelization, which constrains the achievable dwell times given a fixed frame rate, photon counts may also become a limiting factor for high-speed scanning in some approaches.

Diffraction Using the small angle approximation, the diffraction-limited angular resolution of an aperture is $\vartheta \approx \frac{\Delta x}{y} \approx \frac{}{D}$, where Δx is the spacing which must be resolved, y is the imaging depth, λ is the wavelength, and D is the aperture diameter. Thus distinguishing neurons which are 10 µm apart and at a depth of 10 mm requires a lens aperture D of $>$ 1 mm when $\lambda \approx 1\,\mu$m. Diffraction therefore does not appear to be a limiting factor for cellular resolution imaging, except in the context of microscale apertures that might find use in embedded optics approaches.

Energy Dissipation

Light that does not leave the brain is ultimately dissipated as heat. The total light power requirements for optical measurement of neuronal activity using fluorescent indicators depend on factors including fluorophore quantum efficiency, absorption cross-section, activity-dependent change in fluorescence, background fluorescence, labeling density, activation kinetics, detector noise, scattering and absorption lengths, and others. Unfortunately, many of these variables are unknown or highly dependent on particular experimental parameters.

A statistical analysis of photon count requirements for spike detection (in the context of calcium imaging) can be found in [708], which derived a relationship between the number of background photon counts (N_{bg}) and the number of signal photon counts required for high fidelity spike detection given

photon shot noise. This scales roughly as $N_{\text{signal}} > 3\sqrt{2N_{\text{bg}}}$, even at low absolute photon count rates. While this analysis governs the number of detected photons, the number of emitted photons will be higher due to losses. In one example using two-photon excitation, 5 % of the emitted photons were captured by the photodetector[351]. One implication of photon shot noise is that faster-responding indicators (e.g., voltage indicators which respond in near-real-time to the membrane potential) must be brighter.

MULTI-PHOTON EXCITATION Multi-photon experiments rely on short laser pulses with high peak light intensities at a focused excitation spot to excite nonlinear transitions[351]. This imposes an experimentally relevant physical limit: at least one excitation pulse of sufficient intensity per neuron per frame is required in order to excite multi-photon fluorescence during each frame. Assuming 1 kHz frame rate and 0.1 nJ pulses[114], delivering only one pulse per neuron per frame would dissipate roughly ($10^8 \times 1\,\text{kHz} \times 0.1\,\text{nJ}$) 10 W in the mouse brain, which is clearly prohibitive. This is a lower bound because, in general, more than one excitation pulse per neuron per frame may be required to excite detectable fluorescence (e.g., one reference reported 12 pulses per spot[351]). For three-photon excitation, the situation will be even worse as higher peak light intensities are required to excite three-photon fluorescence.

Could the single-pulse energy be reduced while maintaining efficient two-photon excitation? The number of two-photon (2P) transitions excited per fluorophore per pulse is $n_a = F^2 C/t$, where F is the number of photons per pulse per area in units of photon/cm^2, C is the two-photon cross-section in units of cm^4 s/photon, and t is the pulse duration in seconds. This can be approximated as

$$n_a = \left(\frac{\frac{E}{hc/\lambda}}{\left(\frac{\lambda}{2(\text{NA})}\right)^2} \right)^2 \frac{C}{t} = \left(\frac{4E\,(\text{NA})^2}{hc\lambda} \right)^2 \frac{C}{t}$$

where NA is the numerical aperture of the focusing optics, E is the pulse energy and λ is the stim-

ulation wavelength. For a 2P experiment with 100 fs, 0.1 nJ pulses, assuming a 2P cross section[453,171] of 10^{-48} cm^{4}s/photon (i.e., 100 Goeppert-Mayer units[237], comparable to that of DsRed2[171]), $\lambda = 900$ nm and NA $= 1.0$, $n_a \approx \frac{1}{2}$. Thus, a few pulses are likely necessary and sufficient to excite 2P fluorescence by each fluorophore within the focal spot. With a 2P cross section above 10^{-47} cm^{4}s/photon (1000 Goeppert-Mayer units, higher than that of any fluorescent protein that we are aware of[171]), one could reduce the pulse energy by an order of magnitude (and hence n_a by two orders of magnitude) while maintaining $n_a > \frac{1}{20}$, i.e., one in twenty fluorophores excited by each pulse. Reducing the pulse energy much further might lead to unacceptably low excitation levels. Alternatively, shorter pulse durations could increase the light intensity, and hence 2P excitation probability, at fixed pulse energy.

Quantum dots can have 2P cross sections much higher than those of fluorescent proteins: water-soluble cadmium selenide–zinc sulfide quantum dots have been reported with 2P cross sections of 47000 Goeppert-Mayer units and are compatible with in-vivo imaging[389]. These would allow excitation efficiencies of $n_a > \frac{1}{20}$ at pJ pulse energies, bringing whole-brain 2P imaging into the $\sim$100 mW range. Thus, the use of quantum dots or other ultra-bright multi-photon indicators could be decisive for supporting the energetic feasibility of multi-photon methods at whole brain scale; there are also plausible strategies for coupling quantum dot fluorescence to neuronal voltage[448]. However, some quantum dots have long fluorescence lifetimes[137], which may constrain scan speed.

For comparison to current practice, in a typical multi-photon experiment on mice, $\sim$50 mW of time-averaged laser power at the sample was used with a dwell time of $\sim$3 µs[706], corresponding to $\sim$150 nJ energy dissipation per spot per frame. This dwell time would allow imaging only $\sim$300 neurons at millisecond resolution with a single scanned excitation beam. The average excitation power here is likely already close both to whole-brain thermal dissipation limits, and to photo-damage limits for pulsed two-photon excitation[288,368].

Bioluminescence

To work around the requirement for large amounts of excitation light, bioluminescent rather than fluorescent activity indicators could be used[488,452,451]. Consider a hypothetical activity-dependent bioluminescent indicator emitting at ∼1 700 nm (IR), in order to evade light scattering. As a crude estimate, assuming that 100 photons must be collected by the detector per neuron per 1 ms frame, and 1 % light collection efficiency by the detector relative to the emitted photons, ∼ 100 μW of bioluminescent photons emissions are required for the entire mouse brain (using $E_{\text{photon}} = hc/\lambda$). This would be feasible from the perspective of heat dissipation. By contrast, in a 1-photon fluorescent scenario, if 100 excitation photons must be delivered into the brain to generate a single fluorescent emission photon, the power requirement becomes 10 mW, which is on the threshold of the steady-state heat dissipation limit. Therefore, bioluminescent indicators could potentially circumvent problems of heat dissipation even in the 1-photon case.

The widely used bioluminescent protein firefly luciferase is ∼80 % efficient in converting ATP hydrolysis coupled with luciferin oxidation into photon production, yielding ∼0.8 photons per ATP-luciferin pair consumed[584], and has ∼90 % energetic efficiency in converting free energy to light production. Heat dissipation associated with the luciferase biochemistry itself is therefore not a significant overhead relative to the 100 μW of emitted photons calculated above. In the same scenario, however, each neuron would consume $\sim 6 \times 10^8$ additional ATP molecules per minute in order to power the bioluminescence, which is within the limits of cellular aerobic respiration rates (∼1 fmol O_2 per minute per cell[475], with ∼30 ATP per 6 O_2, hence 3×10^9 molecules ATP synthesized per minute from ADP via glucose oxidation), but not by a large margin. Transient increases in metabolic rate are possible: energy dissipation more than doubles in the mouse during high physical activity[622]. Therefore, whole-brain activity-dependent bioluminescence, at speeds high enough to achieve millisecond frame rates, may be metabolically taxing for the cell but is nevertheless plausible as a light generation strategy.

Note that we have not treated the energy required to bio-synthesize the luciferin compound, which may create additional overhead (though conceivably luciferin could be provided exogenously).

Conclusions and Future Directions

Scattering of visible light in the brain creates a problem of signal-separation from deep-brain neurons. Multi-photon techniques, which scan an infrared excitation beam, can work around this scattering problem. However, current multi-photon techniques using fluorescent protein indicators, when applied at whole brain scale, would dissipate too much power to avoid thermal damage to brain tissue. Systems (such as plasmonic nano-antennas[63] or subwavelength metallic gratings[260]) that could locally excite multi-photon fluorescence without the need for high-energy laser pulses could conceivably ameliorate this issue. Importantly, quantum dots show promise as ultra-bright multi-photon indicators, if they can be targeted to neurons and optimized in terms of fluorescence lifetime. New methods besides multi-photon techniques could also work around the scattering of visible light in the brain. For example, fluorophores or bio-luminescent proteins could be developed which operate at infrared wavelengths. A compelling example from nature is the black dragonfish, which generates far red light ($\sim$ 705 nm) via a multi-step bioluminescent process (using this light to see in deep ocean waters)[703,99]. A large set of activity indicators with distinguishable colors, generated through a combinatorial genetic recombination mechanism such as BrainBow[410], could also improve signal separation. Targeting, via protein tags, of activity indicators to specific locations — such as the axon, soma, soma and proximal dendrites, distal dendrites, pre-synaptic terminals, post-synaptic terminals, or intact synapses — could also aid in signal discrimination[31,179,132,315,672,70,194,717]. In addition, implanted optical devices, which place emitters and detectors within a few scattering lengths of the neurons being probed, could potentially obviate the negative effects of scattering and allow visible-wavelength indicators to be used without a need for multi-photon excitation. In principle, excitation and detection do not need to make use of the same modality. For example, photoacoustic microscopy[198] uses pulsed laser excita-

tion to drive ultrasonic emission, leading to optical absorption contrast. Such asymmetric techniques impose fundamentally different requirements from pure-optical techniques relative to fluorophore properties, required light intensities and other parameters.

3.3.2 Embedded Active Electronics

The preceding sections have assumed that electrical or optical signals from the recorded neurons are shuttled out of the brain before digitization and storage, but it is also conceivable to develop embedded electronic systems that locally digitize and then store or transmit (e.g., wirelessly) measurements of the activities of nearby neurons. This could allow for shorter wires in electrical recording approaches, and for shorter light path lengths in optical recording approaches, as well as for more facile (e.g., non-surgical) delivery mechanisms for the recording hardware.

Integrated circuits have shrunk to a remarkable degree: in about 3 years, following the Moore's law trajectory, it will likely be possible to fit the equivalent of Intel's original 4004 micro-processor in a 10 μm × 10 μm chip area. Functional wirelessly powered radio-frequency identification (RFID) chips as small as 50 μm in diameter have been developed [671] and tags with chip-integrated antennas function at the 400 μm scale [7]. Integrated neural sensors including analog front ends are also scaling to unprecedented form factors: a 250 μm × 450 μm wireless implant – including the antenna, but not including a ∼1 mm electrode shank used to separate signal from ground – draws only 2.5 μW per recording channel [62]. The system operates at ∼1 mm range in air, powered by a transmitter generating ∼50 mW of transmitted power. Note that for a single such embedded recording device, the heat dissipation constraint is set not by the device's own dissipation (10 μW for four recording channels) but rather by the RF specific absorption rate limit associated with the 50 mW transmit power.

Possibilities may exist for non-surgical delivery of embedded electronics to the brain: remarkably, cells such as macrophages (∼13 μm in size) can engulf structures up to at least 20 μm in diameter [101] and have been studied as potential delivery vehicles for nano-particle drugs [329], suggesting that they might

be used to deliver tiny microchips. T-cells and other immune cells can trans-migrate across the blood brain barrier[186] and ghost cells (membranes purged of their contents) engineered to encapsulate synthetic cargo[126] can fuse with neurons[281]. It might even be possible to engineer such cell-based delivery vehicles to form electrical gap junctions[624] with neurons or to act as local biochemical sensors[493].

The real-time transmission bandwidth requirements for neural recording could be significantly reduced if it is only desired to take a "snapshot" of neural activity patterns over a limited period of time, but this would require a large amount of local storage. For example, flash memory can store $>$ 10 Mbit of data in a device 100 μm on a side: a 64 giga-byte microSD card with 1.5 cm^2 area corresponds to 34 mega-bits per (100 μm)^2 area. Even denser forms of memory storage are under development and could perhaps be used in a one-time-write mode in the context of neural recording long before they become commercially viable for use as rewritable media in the electronics industry.

Here we consider the power dissipation associated with embedded electronic recording devices, as well as the constraints on possible methods to power them. In the next section, we describe how physics constrains the data transmission rates from such devices.

Power Requirements for Recording

Any embedded system needs to process data, in preparation for either local storage or wireless transmission. Physics defines hard limits on the required power consumption associated with data processing (neglecting the possibility of reversible logic architectures[56]), arising from the entropy cost for erasing a bit of information[387]:

$$E_{\text{Landauer}} = \ln(2)\, k_B T \approx 3 \times 10^{-21}\,\text{J/bit} \qquad \text{(the Landauer limit)}$$

Ambitious yet physically realistic values for beyond-CMOS logic lie in the tens of $k_B T$ per bit processed[716]. Scaling 40 $k_B T$/bit to record raw voltage waveforms at a minimal 1 kbit/s/neuron (e.g. 1 kHz

sampling rate, 1 bit processed per neuron per sample), the total power consumption for whole mouse brain recording could in principle be as low as ∼16 nW. While this leaves $> 10^6$-fold more room (energetically) for increased data processing (more required bit flips per second), or energetic inefficiency of the switching device (greater dissipation per bit), realistic devices in the near-term may in fact require this much overhead, if not more. This necessitates a more detailed consideration of limiting factors for today's microelectronic devices.

In the context of electrical recording, the first step that must be performed by an embedded neural recording device is digitization of the voltage waveform. Until mV-scale switching devices are developed (see discussion below), it is necessary to amplify the ∼10–100 μV spike potential in order to drive digital switching events in downstream gates. During this sub-threshold amplification step, a CMOS (or BJT) device will dissipate static power (associated with a bias current). Importantly, in order to decrease the input-referred voltage noise of this amplification process, it is necessary to increase the bias current and hence the static power dissipation. For a simple differential transistor amplifier, the minimal bias current scales as

$$I_\mathrm{d} = \frac{\pi}{2}\frac{4k_\mathrm{B}T}{V_\mathrm{noise}^2}\frac{k_\mathrm{B}T}{q}\mathrm{BW}$$

where V_noise is the input-referred voltage noise of the amplifier and q is the electron charge. For an extracellular recording with $\mathrm{BW} = 10\,\mathrm{kHz}$ and $V_\mathrm{noise} = 10\,\mu\mathrm{V}$, this implies a minimal bias current $I_\mathrm{d} \approx 60\,\mathrm{nA}$ or a minimal static power of $(I_\mathrm{d}V_\mathrm{dd}) \approx 6 \times 10^{-8}\,\mathrm{W}$ at $V_\mathrm{dd} \approx 1\,\mathrm{V}$ operating voltage. Assuming 10 neurons per recording channel, there are then 7.5 million recording channels for a mouse brain, which gives a power dissipation associated with signal amplification of ∼ 500 mW. Note that realistic analog front ends (which are subject to $1/f$ noise and require multiple gain stages) draw 6×–10× greater bias current, quantified by the noise efficiency factor (NEF) [634], to achieve the same input-referred noise levels.

Local on-chip digital computation also incurs an energy cost. Current CMOS digital circuits con-

sume 5–6 orders of magnitude [667,370,716,666] more energy per switching event (∼1 fJ/bit including charging of the wires [667]) compared to the Landauer limit (e.g., for a digital CMOS inverter, and ignoring the static power associated with the leakage current). This corresponds to a ∼1 fF total load capacitance at 1 V operating voltage. For 100 GHz switching rates (10^8 neurons × 1 kHz) as above, this corresponds to 0.01–0.1 mW. Realistic architectures, however, will incur overhead in the number of switching events required to store, compress and/or transmit neural signals, likely bringing the power consumption into an unacceptable range (e.g., 1000 bits processed per sample would be 100 mW here). To take a concrete example, commercial RFID tags consume ∼10 μW [9]. At a chip rate of 256 kbit/s (with a Miller encoding of 2), this yields 7.8×10^{-11} J/bit, which is ∼10 orders of magnitude higher than the Landauer limit. Applying current RFID technology to whole mouse brain recording at 1 kbit/s/neuron would thus draw ∼8 W of power. Therefore, at least 2–3 orders of magnitude reduction in power consumption will be necessary in order to apply embedded electronics for whole-brain neural recording.

Until recently, the energy efficiency of digital computing has scaled on an exponential improvement curve [370]. This was a consequence of Moore's law and Dennard scaling, where both the capacitance of each transistor and its associated interconnect, as well as the operating voltages, were reducing with the device dimensions. Unfortunately, issues related to device variability and the 3D structures needed to maintain the on-to-off current ratio have largely stopped the reduction in effective capacitance per device; current devices are stuck at ∼ 100–200 aF for a minimum sized transistor. Furthermore, the exponential increase in leakage current that comes along with the scaling of the threshold voltage in this scenario has precluded substantial further decreases in voltage at a given performance level. Indeed, for the past several technology generations (since about 2005), CMOS devices have operated at a supply voltage of ∼1 V.

While neural signal processing does not demand very stringent transistor speeds and so reductions below ∼1 V are certainly feasible, a fundamental limitation in scaling the supply voltage still remains.

Specifically, CMOS has a well-defined minimum-energy per bit and an associated minimum-energy operating voltage that is defined by the tradeoff between static (leakage) and dynamic (switching) energy: as the operating voltage is decreased, the capacitive switching energy decreases, but the ratio of currents in the on and off states, $I_{\text{off}}/I_{\text{on}}$, increases exponentially, increasing the energy associated with leakage (this effect is independent of the threshold voltage in the sub-threshold regime). For practical circuits, the supply voltage that leads to this minimum energy is on the order of 300–500 mV, and thus supply voltage scaling will at most provide 3×–10× improvement in energy over today's designs.

Thus, a paradigm shift in microelectronic hardware is needed to reduce power by several orders of magnitude if we are to approach the physical limits. Developing a switching device operating in the mV range, rather than the 1 V range of current transistors, would allow $(1\,\text{V}/1\,\text{mV})^2 = 10^6$ fold reduction in power consumption[716]. Electronic circuits constructed using analog techniques[571], which sometimes rely on bio-inspired computational architectures, show promise for reducing energy costs by up to five orders of magnitude[544,571,431], depending on the nature of the computation and the required level of precision.

Figure 3.4 shows the power consumption per bit processed for several technology classes as well as the corresponding total power consumption required for whole brain readout, assuming a minimal whole-brain bit rate of 100 Gbit/s.

Powering Embedded Devices

Embedded systems need power, which could be supplied via electromagnetic or acoustic energy transfer, or could be harvested from the local environment in the brain.

There are two key regimes for wireless electromagnetic power transfer: non-linear device rectification and photovoltaics. If the single-photon energy is sufficient to allow electrons to move from the valence to the conduction band—that is, band gap $< h\nu/q$, where q is the electron charge, h is Planck's constant, and ν is the frequency of the photon—a photovoltaic effect can occur. Otherwise,

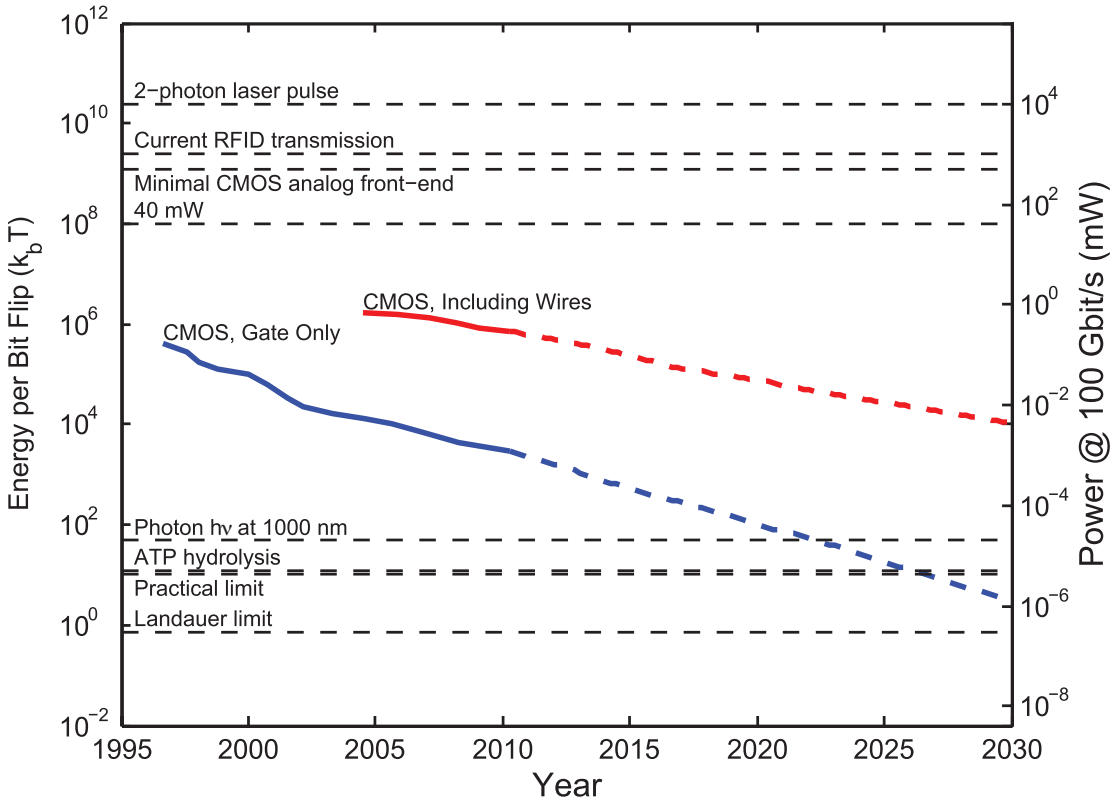

Figure 3.4: Energy cost of elementary operations across a variety of recording and data transmission modalities, expressed in units of the thermal energy (left axis) and as a power assuming 100 GHz switching rate (right axis). The Landauer limit of $k_B T \ln 2$ sets the minimum energy associated with a logically irreversible bit flip. The practical limit will likely lie in the tens of $k_B T$ per bit [716], comparable to the free energy release for hydrolysis of a single ATP molecule (or addition of a single nucleotide to DNA or RNA). The energy of a single infrared photon is $\sim 50\, k_B T$. Single gates in current CMOS chips dissipate $\sim 1 \times 10^5$–$10^6\, k_B T$ per switching event, including the capacitive charging of the wires interconnecting the gates (red curve). The switching energy for the gate, not including wires, is $\sim 100\times$ lower (blue curve). The power efficiency of CMOS has been on an exponential improvement trend due to the miniaturization of components according to Moore's law (data re-digitized from [667]), although power efficiency gains have slowed recently. Current RFID chips compute and communicate at $\sim 1 \times 10^9$–$10^{10}\, k_B T$ (> 10 pJ) per bit transmitted, while the total energy cost per floating point operation in a 2010 laptop was $\sim 1 \times 10^{12}\, k_B T$. The power associated with a minimal low-noise CMOS analog front end for signal amplification corresponds to ~ 500 mW at whole mouse brain scale. A single two-photon laser pulse at 0.1 nJ pulse energy corresponds to $\sim 1 \times 10^{10}\, k_B T$. For comparison, the 40 mW approximate maximal allowed power dissipation, according to section 3.1 (Basic Constraints) above, with its equivalent per-bit energy of $\sim 1 \times 10^8\, k_B T$ at the minimal 100 Gbit/s bit rate.

electromagnetic energy is converted to voltage by an antenna and non-linear device rectification may occur.

When photon energies are much lower than the band gap, power conversion is governed by the total RF power and by the impedances of the antenna and the rectifier, rather than by the individual photon energy. For a monochromatic RF source, there is no thermodynamic or quantum limit to the RF to DC conversion efficiency, other than the resistive losses and threshold voltages for a semiconductor process. For rectification, when the input voltage to the rectifier is much higher than a semiconductor process threshold, conversion efficiencies of 85 % have been achieved[648]. At low input voltages relative to the semiconductor process threshold, efficiencies as high as 25 % and 2 μW load have been achieved (see[431] for an analysis of power efficiency). Ultimately, rectification improvements are dependent on the same improvements which will be needed for next-generation low-power computing: mV scale switching devices (promising research directions include tunnel FETs[305], electromechanical relays[408] and other options).

While efficient rectification is thus not a fundamental issue, capturing sufficient RF energy in the first place becomes increasingly challenging as microchips become smaller and more deeply embedded in tissue. Wireless electromagnetic power transfer imposes range constraints due to the loss in power density with distance. For directional power transfer, placing the receiver at the edge of the transmitter's near field (the Rayleigh distance $\frac{D^2}{4}$ where D is the transmitter aperture) has advantages in terms of energy capture efficiency[510], whereas for omni-directional antennas it is advantageous to place the receiver as close as possible to the transmitter. If embedded chips are oriented randomly with respect to the transmitter, the radiation patterns of their antennas cannot be highly directional, i.e., their gains G_r (a measure of directionality) must be close to one. In the far field, this lack of directionality limits power capture by the antenna (due antenna reciprocity[221]): the maximal power P_A available to the chip is

$$P_A = \frac{G_r P_{\text{rad}} \lambda^2}{4\pi}$$

where P_{rad} is the power density of radiation around the antenna, λ is the wavelength and $G_r \approx 1$ for a non-directional antenna[431].

It may be possible to power devices with pure magnetic fields (which are highly penetrant) via near-field (non-radiative) inductive coupling, which is widely used in systems ranging from biomedical implants to electric toothbrushes, or conceivably by using magneto-electric materials[354,536,730,196]. For the case of simple inductive coupling, however, the tiny cross-sections of micro-devices limit the amount of power which can be captured: a loop of 10 µm diameter in an applied field of 1 T switching at 1000 Hz produces an induced electromotive force of only 0.1 µV. Assuming a copper loop (~17 nΩ m resistivity) with 1 µm × 1 µm cross-section and 40 µm length (around the outer edge of the chip) gives a power (V^2/R) of only ~15 fW associated with the induced current. In general, the use of coupled high-Q resonators can increase the range and efficiency of near-field electromagnetic power transfer by orders of magnitude[335] compared to non-resonant inductive power transfer and may be particularly relevant for implanted devices[284]. Unfortunately, at the ~10 µm length scale, the achievable on-chip inductances and capacitances are severely limited, which restricts the operating range of any resonant device to high frequencies $\left(f_{\text{resonant}} = \left(2\pi\sqrt{LC}\right)^{-1}\right)$ which will be attenuated by tissue. Electromagnetic near-field power transfer though tissue to ultra-miniaturized microchips may thus be inefficient, again due to low capture efficiency of the applied fields by tiny device cross-sections.

Alternatively, if the photon energy is above the silicon band gap ($\lambda < \frac{hc}{qV_{\text{th}}} \approx 3$ µm or less for silicon), the chip is essentially acting as a photovoltaic cell. There is no thermodynamic or quantum limit to the conversion efficiency of light to DC electrical power for monochromatic sources, other than resistive losses and dark currents in the material (86 % in GaAs for example[60]). Again, however, capturing sufficient light becomes difficult for tiny devices. To supply 10 µW (typical of current wirelessly-powered RFID chips) photovoltaically to a 10 µm × 10 µm (cell sized) chip at 34 % photovoltaic efficiency requires a light intensity of ~ 300 kW/m² at the chip, which is prohibitive. Furthermore, in the use of infrared light for photovoltaics, the penetration of the photons through tissue is

decreased compared to radio frequencies.

Piezoelectric harvesting of ultrasound energy by micro-devices is a possibility[585]. The efficiency of electrical harvesting of mechanical strain energy in piezoelectrics can be above 30 % for materials with high electromechanical coupling coefficients (e.g., PZT)[5,715]. The losses in the piezoelectric transduction process are well described by models such as the KLM model[382,107].

An alternative to wireless energy transmission is the local harvesting of biochemical energy carriers. Implanted neural recording devices could conceivably be powered by free glucose, the main energy source used by the brain itself. The theoretical maximum thermodynamic efficiency for a fuel cell in aqueous solution is equal to that of the hydrogen fuel cell: $\Delta G^\circ/\Delta H^\circ = 83\,\%$ at 25C. Furthermore, if glucose is only oxidized to gluconic acid, the Coulombic (electron extraction) efficiency is at most 8.33 %[543], which bounds the thermodynamic efficiency. The blood glucose concentration in rats has been measured at ∼7.6 mM, with an extracellular glucose concentration in the brain of ∼2.4 mM[609]. A hypothetical highly miniaturized neural recorder with a device area of 25 µm × 25 µm and efficiency of 80 %, processing a blood flow rate of ∼1 mm/s[310] could extract

$$(80\,\%)(7.6\,\text{mM})(25\,\mu\text{m})^2(1\,\text{mm/s})(2880\,\text{kJ/mol}) \approx 11\,\mu\text{W},$$

which is sufficient for low-power device such as RFID chips[116]. Unfortunately, current non-microbial glucose fuel cells obtain only ∼ 180 µW/cm² peak power and ∼3.4 µW/cm² steady state power[543]. Thus there is a need for 10^4- and 10^6-fold improvements in peak and steady state power densities, respectively, for non-microbial glucose fuel cells to power brain-embedded electronics of the complexity of today's RFID chips (or for the corresponding decrease in power requirements, as emphasized above).

Conclusions and Future Directions

The power consumption of today's microelectronic devices is more than six orders of magnitude higher than the physical limit for irreversible computing, and 2–3 orders of magnitude higher than

would be permissible for use in whole brain millisecond resolution activity mapping, even under favorable assumptions on the required switching rates and neglecting both the power associated with noise rejection in the analog front end and the CMOS leakage current. Thus, the first priority is to reduce the power consumption associated with embedded electronics. In principle, methods such as infrared light photovoltaics, RF harvesting via diode rectification, or glucose fuel cells, could supply power to embedded neural recorders, but again, significant improvements in the power efficiency of electronics are necessary to enable this. Other potential energy harvesting strategies include materials/enzymes harnessing local biological gradients such as in voltage, osmolarity, or temperature. An analysis of the energy transduction potential of each of these systems is beyond the scope of this discussion. Fortunately, with many orders of magnitude potential for improvement before physical limits are reached, we may expect that embedded nano-electronic devices will emerge as an energetically viable neural interfacing option at some point in the future.

3.3.3 Embedded Devices: Information Theory

Most recording methods envisioned thus far rely on the real-time transmission of neural activity data out of the brain. Physics and information theory impose fundamental limits on this process, including a minimum power consumption required to transmit data through a medium. The most basic of these results hold irrespective of whether the data transmission is wired or wireless, and regardless of the particular physical medium (optical, electrical, acoustic) used as the information carrier.

A communication "channel" is a set of transmitters and receivers that share access to a single physical medium with fixed bandwidth. The bandwidth is the range of frequencies present in the time-varying signals used to transmit information. In wireless communications, information is transmitted by modulating a carrier wave. To allow modulation, the frequency of the carrier wave must be higher than the bandwidth: for example, a 400 THz visible light wave may be modulated at a 100 GHz rate. The physical medium underlying a channel could be a wire (with a bandwidth set by its capacitive RC

time constant), an optical fiber, free space electromagnetic waves over a certain frequency range, or other media.

As a concrete example, consider a police department with 100 officers, each possessing a hand-held radio. The radios transmit vocalizations by modulating an 80 MHz carrier wave at ∼10 kHz. This constitutes a single shared communications channel with 10 kHz bandwidth. Simultaneously, the fire department may communicate via a separate channel, also with a bandwidth of ∼10 kHz, by modulating a 90 MHz carrier wave. The channels are separate because modulation introduced into one does not affect the other. If the neighboring town's police department makes the mistake of also operating at 80 MHz carrier frequency, then they share a channel and conflicts will arise.

Power Requirements for Single-Channel Data Transmission

We first treat the case in which there is a single channel for transmitting data out of the brain. As discussed above in the context of electrical spike sorting, the Shannon Capacity Theorem[134] sets the maximal bit rate for a channel (assuming additive white Gaussian noise) to

$$R_{\max} = \mathrm{BW} \log_2 (1 + \mathrm{SNR})$$

where BW is the channel bandwidth and SNR is the signal-to-noise ratio. If there is only thermal noise the $\mathrm{SNR} = P/(N_0 \mathrm{BW})$, where N_0 is the thermal noise power spectral density of $k_B T$ W/Hz and $P = (\mathrm{PL}) P_0$ is the power of the transmitted signals P_0, weakened by path loss PL. Therefore the transmitted power P_0 is lower-bounded:

$$P_0 > k_B T \, \mathrm{BW} \, \frac{2^{R\mathrm{max}/\mathrm{BW}} - 1}{\mathrm{PL}}$$

as shown in Figure 3.5 (bottom). In a minimal model of a transmitter-receiver system, there thus exists a tradeoff between the required signal power and the bandwidth of the carrier radiation, due to the thermal noise floor, even in the absence of path loss (PL = 1).

Path loss weakens the proportion of the power that can reach the detector. Using the above equation, we can calculate, as a function of bandwidth, the power necessary to transmit a target whole-brain bit rate of 100 Gbit/s through a medium with path loss dependent on the carrier wavelength, as shown in Figure 3.5 (top).

For RF wavelengths, the radiation penetrates deeply but the achievable data rates are low without excessive power consumption, due to the limited bandwidth. For wavelengths intermediate between RF and infrared, the penetration depth is low and power must be expended to combat these losses, despite the high carrier bandwidth. Only in the infrared and visible ranges do the tradeoffs between power, bandwidth and penetration depth allow transmission of $>$ 100 Gbit/s out of the brain through a single channel without unacceptable power consumption.

The analysis above has ignored the effects of noise sources other than thermal noise, but many additional noise sources will increase the amount of power needed to transmit data, via a decrease in the SNR at fixed input power. For optical transmission in the brain, the noise is dominated by time-correlated "speckle noise" below 200 kHz, which arises mostly from local blood flow[Carp et al.]. This correlated noise, which cannot be filtered by simple averaging, could be avoided by modulating optical signals at frequencies above 200 kHz.

Spatially Multiplexed Data Transmission

As discussed above, transmitting information through a single channel imposes direct limits on bit rate, carrier frequency and input power. However, it is conceivable to divide the data transmission burden over many independent channels, i.e., over many pairs of transmitters and receivers, each operating at lower bandwidth (e.g., at radio frequencies). Indeed, this would be optimal in a scenario

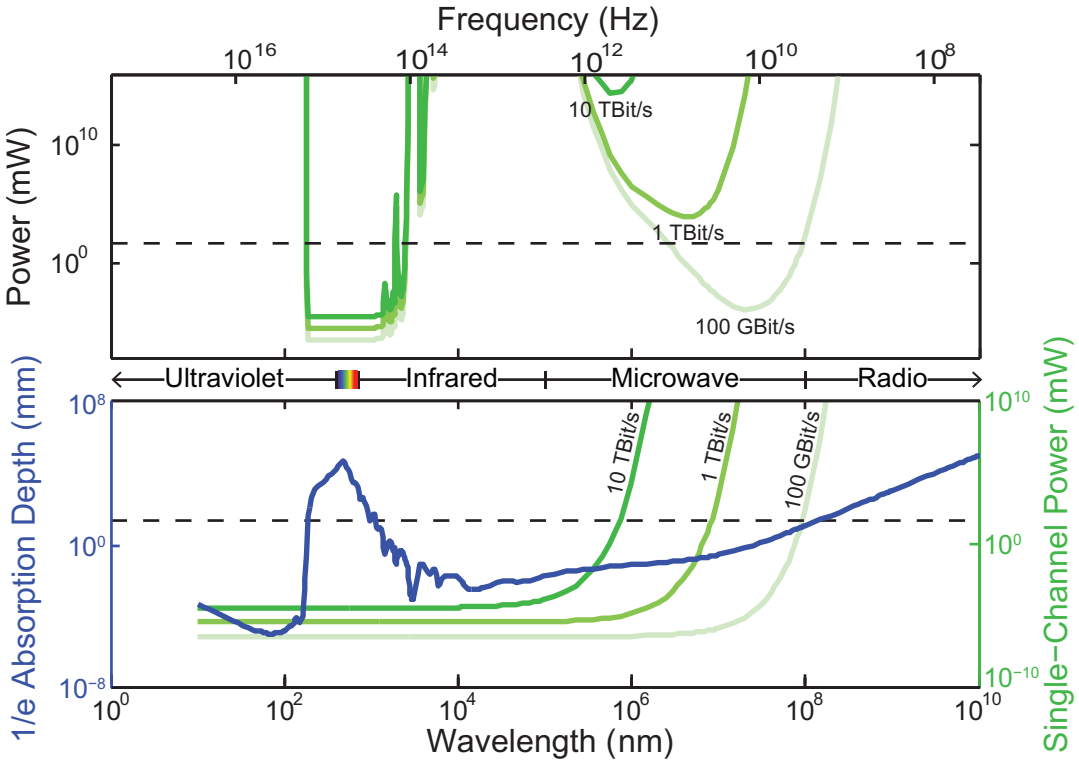

Figure 3.5: Power requirements imposed by information theory on data transmission through a single (additive white Gaussian noise) channel with carrier frequency ν (an upper bound on the bandwidth), given thermal noise and path loss. Bottom: absorption length of water as a function of frequency (blue), minimal power to transmit data at 100, 1000 and 10 000 Gbit/s (green) as a function of frequency, assuming thermal noise but no path loss. Top: minimal power to transmit data at 100, 1000 and 10 000 Gbit/s as a function of frequency, assuming thermal noise and a path loss corresponding to the attenuation by water absorption over a distance of 2 mm. While formulated for a single channel, at certain wavelengths (e.g., RF) these factors also constrain multiplexed data transmissions between many transmitters and many receivers, depending on capacity of the system for spatial multiplexing. Horizontal dashed lines: 40 mW, the approximate maximal whole-brain power dissipation in steady state.

where many embedded devices measure and then transmit the activities of nearby neurons. As a concrete example of such "spatial multiplexing," an effective capacity of 1 Tbit/s could conceivably be obtained by splitting the data over 1000 transmitter-receiver pairs each operating at 1 Gbit/s, with the transmitters arranged in a $10 \times 10 \times 10$ grid. Importantly, in order to exceed the above limits for single-channel data transmission, it must be possible for these transmitter receiver pairs to share the same bandwidth and operate simultaneously without conflicts, for example by modulating distinguishable carrier waves or by transferring data over separate wires. The conditions under which this may occur, however, can be counter-intuitive. For example, for antennas to operate independently, they must be spaced apart from one another by roughly a wavelength. For 10 GHz microwaves, the wavelength is $\sim$3 cm, so no more than a handful of microwave transmitters (e.g., operating at frequencies in the 100 GHz–1 THz range) can co-occupy the mouse brain while operating independently.

Even with many non-independent transmitters co-occupying the brain and operating simultaneously over the same frequency spectrum, it may be possible under some conditions to "factor out" the effects of the coupling and allow an increase in channel capacity relative the single-channel result. To treat such scenarios, a generalization to Shannon's capacity theorem to multi-input-multi-output (MIMO) channels has shown that the maximal total data rate is

$$R_{\text{max}} = \text{BW} \cdot \log_2 |\boldsymbol{I} + (\text{SNR})\boldsymbol{H}\boldsymbol{H}^*|$$

where $\boldsymbol{I}$ is the identity matrix, $|\cdot|$ denotes the matrix determinant, $\boldsymbol{H}$ is the ($\mathcal{M} \times N$ for N transmitters and $\mathcal{M}$ receivers) channel matrix giving[668] the coupling between the vector of transmitted signals and the vector of received signals and $\boldsymbol{H}^*$ denotes the matrix adjoint of $\boldsymbol{H}$. The vector of received signals is then $\boldsymbol{y} = \boldsymbol{H}\boldsymbol{x} + \boldsymbol{n}$ where $\boldsymbol{x}$ is the vector of transmitted signals and $\boldsymbol{n}$ is a noise vector. Any matrix can be written as $\boldsymbol{H} = \boldsymbol{U}\boldsymbol{V}^*$ where $\boldsymbol{U}$ and $\boldsymbol{V}$ are unitary matrices, and is a diagonal matrix whose

elements are the *singular values* λ_i. One can re-write the above equation as

$$R_{\max} = \mathrm{BW} \cdot \sum_{i=1}^{\min(M,N)} \log_2 \left(1 + \mathrm{SNR} \cdot \lambda_i^2\right)$$

If the matrix $\boldsymbol{H}$ is of full rank, then the capacity for the multi-channel system can increase over the single-input-single-output (SISO) result by $\min(\mathcal{M}, \mathcal{N})$ times[606]. Note that the rank of the matrix corresponds to the number of non-zero singular values, so an analysis of the singular values of channel matrices can inform us about the multiplexing capacity of the channel. Furthermore, this multiplexing capacity can in principle be achieved even when the transmitters are not in communication with each other, which could potentially be important for scenarios involving many brain embedded transmitters[623].

Transmission through a medium with negligible scattering is the simplest situation to analyze. In this case, evaluating the matrix $\boldsymbol{H}$ requires knowledge of the transmitter-transmitter, transmitter- receiver, and receiver-receiver distances, as well as the orientations and radiation patterns of the antennas (e.g., high gain antennas will have a highly directional radiation pattern). Depending on these factors, the beam from each transmitter will spread to impinge upon multiple receivers and the effective number of spatially independent beams will be reduced. With transmitter-transmitter and receiver-receiver distances larger than the wavelength, and highly directional antennas with appropriately chosen orientations, it is possible to increase the channel capacity linearly with $\min(\mathcal{M}, \mathcal{N})$.

Random scattering, in a coherent disordered medium where the mean free-path ℓ is much larger than the wavelength λ and much smaller than the size of the disordered medium, is another condition where the matrix $\boldsymbol{H}$ is a random scattering matrix of full rank[483,533]. Intuitively, for the case of two transmitters and two receivers separated by a disordered medium larger than the mean free path: if transmitter 1 is at least a mean-free path from transmitter 2 (or potentially as close as a few wavelengths[57]), the path from transmitter 1 to receiver 1 and the path from transmitter 2 to receiver 2 would

be uncorrelated with respect to one another (in terms of physical path, phase, amplitude fluctuations, and other properties). The rank of the matrix $\boldsymbol{H}$ would then be 2. Devising a code on the transmitter such that the receivers can distinguish between these two uncorrelated streams results in a doubling of the capacity, rather than simply averaging the noise floor, which would provide only a logarithmic capacity gain due to the increased SNR.

Thus, contrary to intuition, a high degree of random scattering can potentially be useful for data transmission, by enabling spatial multiplexing of channels. This idea has been demonstrated experimentally in the context of ultrasound transmissions[153]. Biological tissue in the infrared range is well described as such a random scattering medium (e.g., mean free path $\sim 200\,\mu m$ at ~ 800 nm *in vivo*). Therefore infrared light could be used for spatially multiplexed data transmission out of the brain. At wavelengths λ comparable to critical brain dimensions in the mouse, however, an insufficient number of scattering events will occur to create multiple independent pathways for N transmitters. Mathematically, the matrix $\boldsymbol{H}$ will have one highly dominant singular value and a number of much smaller remaining terms, such that the signals appearing at a receiver from two separate transmitters will be highly linearly dependent, differing by only a small phase angle. Therefore, there will be no capacity gain from multiple transmitters, and distinct transmitters will effectively share a single channel (reducing to the SISO result).

Little is known about the biological interaction with electromagnetic fields at wavelengths much shorter than the critical brain dimensions but beyond the infrared, approximately 100 GHz ($\sim$3 mm) to 100 THz ($\sim 3\,\mu m$) in the mouse. If multiple scattering occurs and the absorption is low, this may also be a regime conducive to MIMO communications[40]. Efficiently generating and processing radiation in this regime by embedded devices is an outstanding problem, however. The so-called "THz-gap"[656] exists because (moving towards higher frequencies starting from DC electronics), parasitic capacitances and passive losses limit the maximum frequency at which a field-effect transistor (FET) may oscillate and on the other hand (moving downward in frequency starting from optics), the band-

gaps of opto-electronic devices limit the minimum frequency at which quantum transitions occur. Thus there is no high-power, low-cost, portable, room temperature THz source available. Advances in THz light generation, e.g. through the use of tunneling transistors, could be enabling.

Ultrasound as a Data Transmission Modality

An important caveat to these conclusions on wireless data transfer occurs if we consider the use of ultrasound rather than electromagnetic radiation. Because the speed of sound is dramatically slower than that of light, the wavelength of 10 MHz ultrasound is only $\sim 150\,\mu m$ (approximating the speed of sound in brain as the speed of sound in water, $\sim$1 500 m/s). Thus, many 10 MHz ultrasound transmitters/receiver could be placed inside a mouse brain while maintaining their spatial separation above the wavelength, and a linear scaling of the MIMO channel capacity with the number of devices is likely possible in this regime, assuming that appropriate antenna gains and orientations can be achieved inside brain tissue. Beam orientation could present a challenge if micro-devices are oriented randomly after implantation. With an attenuation of 0.5 dB/(cm MHz)[6], the attenuation at 10 MHz is only 5 dB/cm. Thus ultrasound-based transmission of power and data from embedded recording devices may be viable[585].

In contrast, direct imaging of neural activity by ultrasound (e.g., using contrast agents which create local variations in tissue elastic modulus or density) may be more difficult. While the theoretical (diffraction-limited) and currently practical resolutions of 100 MHz ultrasound are $\sim 15\,\mu m$, and 15–60 µm[206], respectfully, at these frequencies, power is attenuated by brain tissue with a coefficient of $\sim$50 dB/cm[6] (10^5-fold attenuation per cm), which imposes a penetration limit (e.g., for measurements with a dynamic range of 80 dB[206]). Attenuation of ultrasound by bone is stronger still, at 22 dB/(cm MHz)[6]. Attenuation could therefore limit the use of ultrasound as a high-resolution neural recording modality in direct imaging modes, but multiplexed transmission of lower-frequency ultrasound from embedded devices could sidestep this issue.

Physics and information theory impose a tradeoff between bandwidth and power consumption in sending data through any communication channel. Considering only thermal noise and no path loss, achieving 100 Gbit/s data rates through a single channel necessitates either a bandwidth above a few GHz or a transmitted power above $\sim$100 mW, the latter of which may be prohibitive from a heat dissipation perspective if the signals are to be generated by dissipative microelectronic devices. Researchers have proposed to use thousands or millions of tiny [241] wireless transmitters embedded in the brain to transmit local neural activity measurements to an external receiver via microwave radiation [176]. However, based on the above power-bandwidth tradeoff, this will require a bandwidth above a few GHz. At the corresponding carrier frequencies, the penetration depth of the microwave radiation drops significantly, requiring increased power to combat the resulting signal loss. While one might hope that multiple independent channels could be multiplexed inside the brain, reducing the bandwidth and power requirements for each individual channel, the long wavelengths of microwave radiation compared to the mouse brain diameter suggest that such channels cannot be independent, as is confirmed by an analysis of the multi-input-multi-output (MIMO) channel capacity for this scenario. Therefore, radio-frequency electromagnetic transmission of whole brain activity data from embedded devices does not appear to be a viable option for brain activity mapping.

On the other hand, an analysis of the channel capacity for IR transmissions in a diffusive medium suggests that, because of its high frequency and decent penetration depth, infrared radiation may provide a viable substrate for transmitting activity data from embedded devices. For example, data could be transmitted via modulating the multiple-scattering speckle pattern of infrared light by varying the backscatter from an embedded optical device, such as an LCD pixel [365], in an activity-dependent fashion. Because the speckle pattern is sensitive to the motion of a single scatterer [57,514], coherent multiple scattering could effectively act as an optical amplifier and as a means to create independent communi-

cation pathways. Furthermore, multiplexed data transmission via ultrasound is likely possible because of its short wavelength in tissue at reasonable carrier frequencies. It may also be of interest to explore network architectures[88] in which data is transmitted at low transmit power over short distances via local hops between neighboring nodes capable of signal restoration.

3.3.4 Magnetic Resonance Imaging

Magnetic resonance imaging (MRI) uses the resonant behavior of nuclear spins in a magnetic field to non-invasively probe the spatiotemporally varying chemical and magnetic properties of tissues. Although originally conceived as a means to image anatomy, MRI can be used to observe neural activity provided that correlates of such activity are reflected in dynamic changes in local chemistry or magnetism.

In an MRI study, a strong static field ($B = 1$–15 T) is applied to polarize nuclear spins (usually ^{1}H), causing them to resonate at a field-dependent Larmor frequency

$$f = \frac{\gamma}{2\pi} B$$

where γ is the gyromagnetic ratio of the nucleus (e.g., ^{1}H has a gyromagnetic ratio of 267.522 MHz/T[474] and therefore resonates at 42.577 MHz in a 1 T field). To obtain positional information, spatial field gradients are applied such that nuclei at different positions in the sample resonate at slightly different frequencies. Sequences of RF pulses and gradients are then applied to the sample, eliciting resonant emissions that contain information about spins' local chemical environment, magnetic field anisotropy and various other properties.

Most functional studies rely on dynamic changes in two forms of relaxation experienced by RF-excited spins. The first form results from energy dissipation through interactions with other species (e.g. other spins or unpaired electrons), causing the spins to recover their lowest energy state on a

timescale, T_1, of 100–1000 ms[559]. The second form of relaxation reflects the dephasing of spin signals in a given sampling volume (voxel) over a timescale, T_2, of 10–100 ms[147] due to non-uniform Larmor frequencies caused, e.g., by the presence of local magnetic field inhomogeneities.

In blood-oxygen level dependent[501] functional MRI (BOLD-fMRI), the most widely used form of neural MR imaging, increased neural activity in a given brain region alters the vascular concentration of paramagnetic deoxy-hemoglobin, which affects local magnetic field homogeneity and thereby alters T_2. Although the existence of this paramagnetic reporter of oxygen metabolism is fortuitous, the data it provides is only an indirect readout of neural activity[614,414,327], which is limited in its spatial and temporal resolution to the dynamics of blood flow in the brain's capillary network (1–2 s). The spatial point-spread function of the hemodynamic BOLD response is in the 1 mm range, although sub-millimeter measurements, revealing cortical laminar and columnar features, have been obtained by filtering out the signals from larger blood vessels[42]. A significant area of current and future work is aimed at developing new molecular reporters that can be introduced into the brain to transduce aspects of neural signaling such as calcium spikes and neurotransmitter release into MRI- detectable magnetic or chemical signals[596,374,296], as described in section 4.5.3, below.

Spatiotemporal Resolution

The temporal resolution of MRI is limited by the dynamics of spin relaxation. For sequential MR signal acquisitions to be fully independent, spins must be allowed to recover their equilibrium magnetization on the timescale of T_1 (100–1000 ms). However, if local T_1 is static its pre-mapping could enable temporally variant T_2 effects to be observed at refresh rates on the faster T_2 timescale (10–100 ms)[147]. It may also be possible to detect events that occur on a timescale shorter than T_1 and T_2, if the magnitude of the resulting change in spin dynamics overcomes the lack of independence between acquisitions. Note that these limitations on the repetition time of the underlying pulse sequence are not eliminated by "fast" pulse sequences such as echo-planar imaging (EPI)[628] and fast low-angle shot

(FLASH)[257] or by the use of multiple detector coils[705]. These techniques accelerate the acquisition of 2D and 3D images, but still require spins to be prepared for readout.

The spatial resolution of current MRI techniques is limited by the diffusion of water molecules during the acquisition time[229], since contrast at scales above the diffusion length will be attenuated by diffusion. The RMS distance of a water molecule from its origin, after diffusing in 3D for a time T_{acq}, is

$$d_{\text{rms}} = \sqrt{6 D_{\text{water}} T_{\text{acq}}}$$

where $D_{\text{water}} = 2300\,\mu\text{m}^2/\text{s}$ is the self-diffusion coefficient of water. For $T_{\text{acq}} \approx 100\,\text{ms}$, $d_{\text{rms}} \approx 37\,\mu\text{m}$, which sets the approximate spatial resolution. For ultra-short acquisitions at $T_{\text{acq}} \approx 10\,\text{ms}$, $d_{\text{rms}} \approx 12\,\mu\text{m}$.

More technically, as described above, MRI uses field gradients to encode spatial positions in the RF frequency (wavenumber) components of the emitted radiation. The quality of the reconstruction of frequency space thus limits the achievable spatial resolution. The sampling interval of the detector Δt, and the field gradient G, determine the wavenumber increment as

$$\Delta k = \gamma G \Delta t$$

The spatial resolution (here considering only one dimension) is then given by[229]:

$$\Delta x_{k\text{-space}} = \frac{\pi}{\frac{T_{\text{acq}}}{\Delta t}\Delta k} = \frac{\pi}{T_{\text{acq}}\gamma G}$$

Note that it is the gradient field, not the polarizing field B_0, which determines the resolution. For a gradient field of 100 mT/m and an acquisition time of 100 ms

$$\Delta x_{k\text{-space}} = \frac{\pi}{(100\,\text{ms})\,(267\,\text{MHz/T})\,(100\,\text{mT/m})} \approx 1.17\,\mu\text{m}$$

Due to relaxation, however, the emissions from a spin at a given position do not constitute a pure tone with a well-defined frequency. Instead, each spin exhibits a frequency spread, which gives rise to another limit on the spatial resolution[229]:

$$\Delta x_{\text{relaxation}} = \frac{2}{\gamma G T_2^*}$$

where T_2^* is the shortest relaxation time. Assuming $T_2^* = 5\,\text{ms}$ and $G = 100\,\text{mT/m}$, gives

$$\Delta x_{\text{relaxation}} \approx 14\,\mu\text{m}$$

Therefore, for water protons, the resolution limit is set by diffusion over ~ 100 ms acquisition timescales, rather than by k-space sampling or relaxation. For other spin species (e.g., with lower diffusion rate), it may be possible to achieve resolutions limited by frequency discrimination.

Notably, there exists a practical trade-off between spatial resolution, temporal resolution, and sensitivity (SNR). In particular, to achieve high spatial resolution, it is necessary to densely sample *k*-space. Fast sampling sequences such as FLASH and EPI achieve speed by sampling each point of *k*-space using less signal and often at a lower resolution. Even at high field strengths (11.7 T), this tradeoff results in practical EPI-fMRI with a spatial resolution of $150\,\mu\text{m} \times 150\,\mu\text{m} \times 500\,\mu\text{m}$ and a temporal resolution of 200 ms[729]. Achieving much higher spatial resolutions requires longer acquisitions and/or lower temporal sampling. For example, achieving a $20\,\mu\text{m}$ anatomical resolution in MRI of *Drosophila* embryos required 54 minutes for a small field of view of $2.5\,\text{mm} \times 2.5\,\text{mm} \times 5\,\text{mm}$[498]. Furthermore, the flies were administered paramagnetic gadolinium chelates to shorten T_1 and thereby the acquisition time. Separately, frame rates of 50 ms have been obtained for dynamic imaging of the human heart, but required the use of strong priors to reduce data collection requirements[736].

Energy Dissipation

Energy is dissipated into the brain when the excited spins relax to their equilibrium magnetization in the applied field. The energy associated with this relaxation is of order the Zeeman energy:

$$\Delta E_{\text{Zeeman}} = \frac{\gamma}{2\pi} h B_0$$

To obtain an upper bound on the heat dissipation of MRI, we first assume that the brain is entirely water, that every proton spin is initially aligned by the field and then excited by the RF pulse, and that all spins relax during a T_1 relaxation time of ~ 600 ms. In this scenario, even an applied field of as high as ~ 200 T would generate dissipation within the $\sim$50 mW energy dissipation limit. In reality, the energy dissipation is 4–5 orders of magnitude smaller, because only a tiny fractional excess of the spins are initially aligned by the field ($\sim 1 \times 10^{-5}$ for fields on the order of 1 T). Therefore, thermal dissipation associated with spin excitation in MRI is unlikely to cause problems unless field strengths much greater than the largest currently used fields ($\sim$20 T) are invoked, or spins with much higher gyromagnetic ratios are used.

Practically, the main energy consideration in MRI is the absorption by tissues of RF energy applied during imaging pulse sequences and the switching of magnetic field gradients. Such absorption is often calculated through numerical solutions of the Maxwell Equations taking into account the precise geometry, tissue properties and applied fields for a particular experimental setup[127]. The typical specific absorption rate (SAR) is well under 10 W/kg (or 5 mW per 500 mg), and is restricted by the FDA to less than 3 W/kg for human studies.

Imaging Agents

All the preceding discussion about spatiotemporal resolution presumes the existence of local time-varying signals (e.g., changes in T_1 or T_2) corresponding to the dynamics of neural activity. The hemodynamic BOLD response is the most prominent such signal, the limitations of which are discussed above. There have been studies working towards direct detection of minute (e.g., ∼0.2 nT) magnetic fields associated with action potentials through their effects on MRI phase or magnitude contrast [69,522], but reliably detecting these fields above the physiological noise will likely require novel strategies [709,259] and estimates of the feasibility of these methods have been complicated by the lack of a realistic model for the local distribution of neuronal currents. MRI detection of the mechanical displacement of active neurons due to the Lorentz force in an applied magnetic field [560] has also been explored, as has the detection of activity-dependent changes in the diffusion of tissue water [665,393], possibly due to neuronal or glial [355] cell swelling [307,287], although strongly diffusion-weighted scans may have disadvantages in terms of SNR [318]. Manganese influx through voltage-gated calcium channels [406,673] generates MRI contrast, but exhibits slow uptake kinetics and even slower efflux, such that manganese monotonically accumulates in the neurons over time. Conceivably, over-expression of manganese efflux pumps such as the iron transporter ferroportin [423] could allow time-dependent activity imaging using manganese contrast.

In the past 15 years, efforts have been undertaken to develop chemical and biomolecular imaging agents that can be introduced into the brain to produce MRI detectable signals corresponding to specific aspects of neural function (analogously to fluorescent dyes and proteins). One critical advantage of using genetically encoded indicators would be the ability to target these indicators to specific cell types [424,417] and/or cellular compartments [31,179,132,315,672,70,194,717]. Notable examples of engineered molecular MRI contrast agents include T_1 and T_2 sensors of calcium [32,403] and a T_1 sensor of neurotransmitter release [596]. Depending on their mode of action, these imaging agents can provide temporal

resolutions ranging from 10 ms to 10 s[593]. However, a major current limitation for fast agents is the requirement that they be present in tissues at µM concentrations, posing major challenges for delivery and genetic expression. Model organisms lacking hemoglobin (e.g., the blowfly), and hence lacking a hemodynamic BOLD response (as is also the case for ex-vivo brain slices), may be particularly useful for in-vivo testing of novel activity-dependent contrast mechanisms, and specialized setups have been constructed to perform MRI at near-cellular spatial resolution in this context (though still requiring several hours to generate whole-brain anatomical images at this resolution)[320].

Figure 3.6 shows the achievable temporal resolution for various classes of activity-dependent MRI contrast agents as well as the spatial resolution limit due to water proton diffusion.

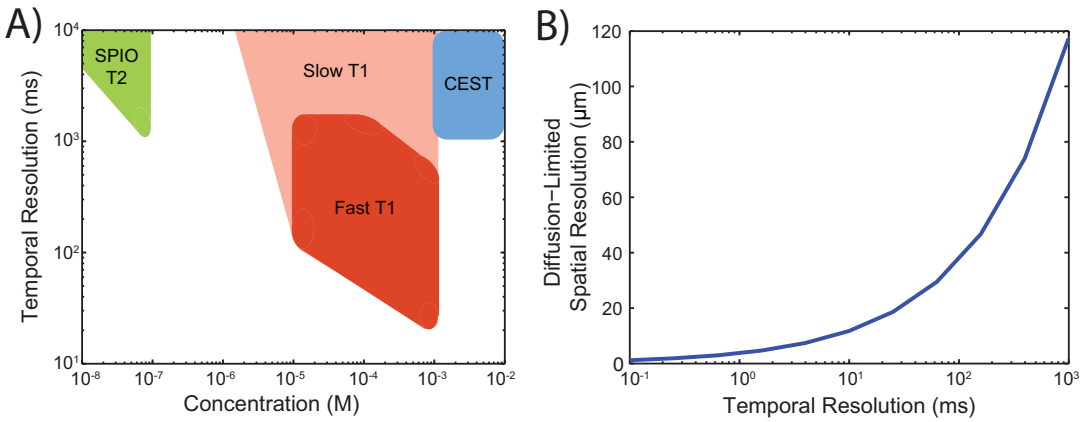

Figure 3.6: Key factors determining the spatiotemporal resolution of dynamic MRI imaging. (a) Temporal resolution and contrast agent concentration allowing $>$ 5 % contrast, for different classes of dynamic MRI contrast agent (reproduced from [593], with permission). (b) Diffusion limited spatial resolution for water proton MRI as a function of temporal resolution.

Conclusions and Future Directions

Moving beyond hemodynamic contrast is crucial for improving the spatiotemporal resolution of fMRI, and several avenues may be available for doing so, especially through the use of novel molecular contrast agents and/or genetic engineering. More fundamentally, current MRI techniques rely on the

excitation of proton spins in water: this limits imaging to $>$ 100 ms timescales, unless SNR is severely compromised, due to the low polarizability and long T_1 relaxation times of proton spins. There is also a spatial resolution limit of tens of microns over these timescales due to water's fast diffusion. Methods which couple neural activity to non-diffusible, highly polarized spins could, in principle, ameliorate this situation.

3.3.5 Molecular Recording

An alternative to electrical, optical or MRI recording is the local storage of data in molecular substrates. Each neuron could be engineered to write a record of its own time-varying electrical activities onto a biological macromolecule, allowing off-line extraction of data after the experiment. Such systems could, in principle, be genetically encoded, and would thus naturally record from all neurons at the same time.

One proposed implementation of such a "molecular ticker tape" would utilize an engineered DNA polymerase with a Ca^{2+}-sensitive or membrane-voltage-sensitive error-rate[735] to record time-varying neural activities onto DNA[227] as patterns of nucleotide misincorporations relative to a known template DNA strand (for alternative local recording techniques see[209,73]). The time-varying signal would later be recovered by DNA sequencing and subsequent statistical analysis[227]. DNA polymerases found in nature can add up to $\sim$1 000 nucleotides per second[343], and certain non-replicative polymerases such as DNA polymerase iota have error rates of $>$ 70 % on template T bases[207]. Similar strategies could be implemented using RNA polymerases or potentially using other enzyme/hetero-polymer systems.

Spatiotemporal Resolution

Polymerases proceed along their template DNA strands in a stochastic, thermally driven fashion; thus, polymerases that are initially synchronized will de-phase with respect to one another over time, occupying a range of positions on their respective templates at the time when a neural impulse occurs. The rate of this de-phasing is a key parameter governing the temporal resolution of molecular recording. By averaging over many simultaneously replicated templates, it is theoretically possible to associate variations in nucleotide misincorporation rate with the times at which these variations occurred, and thus to obtain temporally resolved recordings of the cation concentration [227].

An analysis of the projected temporal resolution of molecular ticker tapes as a function of polymerase biochemical parameters can be found in [227]. This work suggests that molecular ticker tapes require synchronization mechanisms if they are to record at $<$ 10 ms temporal resolution for durations longer than seconds, even when 10 000 templates per cell are recorded simultaneously, unless engineered polymerases with kinetic parameters beyond the limits of those found in nature can be developed. Recording at lower temporal resolutions, however, appears feasible using naturalistic biochemical parameters, even in the absence of synchronization mechanisms. This situation is summarized in Figure ??

The development of mechanisms to improve synchronization of the ensemble of polymerases within each cell, or to encode time-stamps into the synthesized DNA (e.g., molecular clocks), could improve temporal resolution and decrease the number of required template strands per neuron. Mutation-based molecular clocks over evolutionary timescales are widely used in the field of phylogenetics [499], and new tools from synthetic biology [183] and optogenetics or thermogenetics [58] also suggest strategies for building molecular clocks on faster timescales. As an example sketch of a possible synchronization mechanism, optogenetic methods (e.g., similar to [367]) could be used to halt, and thus re-phase, a subpopulation of polymerases at a light-dependent pause site in the template DNA, while another sub-

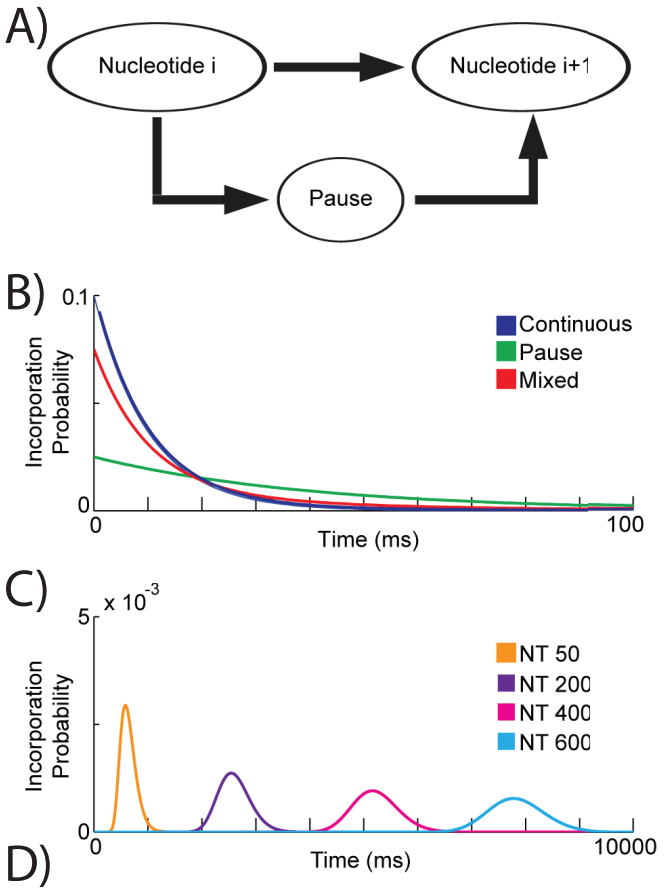

Misincorporation Probability at High Concentration (δ_b = δ_0+m)	Baseline Misincorporation Probability (δ_0)			
	0.5%	1.5%	5%	15%
1%	75 sec			
3%	325 sec	125 sec		
10%	700 sec	475 sec	250 sec	
30%	1275 sec	1000 sec	750 sec	425 sec

The maximum recording duration at which decoding at 100 ms temporal resolution is possible with 95% decoding accuracy. An optimal DNAP with an elongation time of 1 ms and no pausing is used, along with 10000 DNA templates. The search for maximal achievable recording durations was performed at 25 second intervals.
doi:10.1371/journal.pcbi.1003145.t001

Figure 3.7: Simulations of the dephasing of unsynchronized molecular ticker-tape ensembles, and its impact on the achievable temporal resolution of recording, modified from [227]. A) The polymerase can directly extend a base, or transition into and out of a paused state before extending. B) Even with no paused state, dwell times are stochastic, here assuming an exponential distribution. C) Because of the stochasticity of dwell times, the polymerase ensemble dephases over time. D) Table of parameter dependences for unsynchronized recording at 100 ms temporal resolution, reproduced from [227]. With 10000 templates, 1000 nt/sec average speed, and no pausing, recording for several minutes for a range of misincorporation parameters. Recording at 10 ms resolution is significantly more difficult: even in the limiting case of 100% misincorporation rate at high ion concentration and 0% misincorporation rate at low ion concentration, an average speed of 3500 nt/s would be needed to sustain 1 minute of recording at 10 ms temporal resolution and 95% decoding accuracy.

population of polymerases reads through this pause site to maintain temporal continuity of recording; then the second population could be re-synchronized at an orthogonal light-dependent pause site while the first population reads through. Alternatively, some form of optogenetics could be used to directly write bit strings encoding time stamps into the synthesized DNA. These strategies would require one or two, sufficiently strong global clock signals to be optically broadcast to all neurons. The optics involved would be comparatively simple: this could be done using far fewer optical fibers than would be required for fiber-based activity readout, for instance. Alternatively, if the brain could be flash-frozen at a precisely known time, this could serve as a global time-stamp corresponding to the termination of DNA synthesis (e.g., the DNA 3' end).

Spatial resolution for molecular recording would naturally reach the single cell level. To determine which nucleic acid tape originated from which neuron, static cell-specific DNA barcoding could be used[734] to associate the synthesized DNA strands with nodes in a topological connectome map obtained via DNA sequencing. Fluorescence in-situ DNA sequencing (FISSEQ)[396] on serially-sectioned or intact tissue (fixed post-mortem)[120] could be used to obtain explicit geometric information.

Energy Dissipation

Nucleotide metabolism DNA polymerization imposes a metabolic load on the cell. Replication of the 3 billion bp human genome takes approximately eight hours in normally dividing cells, which equates to a nucleotide incorporation rate of $\sim$ 100 kHz. Therefore, in order not to exceed the metabolic rates associated with normal genome replication, molecular ticker tapes operating at 1 kHz polymerization speed[343] would be limited to approximately 100 simultaneously replicated templates per cell. Even more recordings would be possible for RNA ticker tapes. The mammalian cell polymerizes at least 10^{11} NTPs per 16-hour cell cycle[313]. Therefore, $\sim$1 700 RNA tickertapes, each operating at 1 kHz, could be placed in a cell before generating a metabolic impact equal to that of the cell's baseline transcription rate. While these comparisons to baseline physiological levels are reasonable guide-

lines, it is likely that a neuron can support higher metabolic loads associated with larger numbers of templates. The maximal rate of neuronal aerobic respiration is ∼5 fmol of ATP minute via oxidative respiration (see the section on bio-luminescence). Assuming ∼1 ATP equivalent consumed per nucleotide incorporation, if neuronal metabolism were entirely dedicated to polymerization, it could support the incorporation of up to 6×10^9 nucleotides per minute, or 10^5 simultaneously replicated DNA templates at 1 kHz.

Power dissipation Normal DNA and RNA synthesis do not produce problematic energy dissipation and molecular tickertapes will likewise not be highly dissipative, at least in the regime where nucleic acid polymerization rates do not exceed those associated with genome replication or transcription.

Volume Displacement

The nucleus of a neuron occupies ∼6 % of a neuron's volume ($(4\,\mu m)^3/(10\,\mu m)^3$). Ticker tapes operating at 1 kHz with 10 000 simultaneously replicated templates could record for 300 seconds before the total length of DNA synthesized equals the human genome length. In the case of RNA polymerase II-based transcription, 2.75 h of recording by 10 000 recorders is required to reach the net transcript length in the cell. Therefore, with appropriate mechanisms to fold/pack the nucleic acids generated by molecular ticker tapes, they would not impose unreasonable requirements on cellular volume displacement over minutes to hours.

Conclusions and Future Directions

Molecular recording of neural activity has the advantages of inherent scalability, single-cell precision, and low energy and volume footprints. Making molecular recording work at temporal resolutions approaching 1 kHz, however, will require multiple new developments in synthetic biology, including

protein engineering to create a fast polymerase ($>$ 1 kHz) that strongly couples proxies for neural activity to nucleotide incorporation probabilities. Synchronization mechanisms would likely be required to perform molecular recording at single-spike temporal resolution. An attractive potential payoff for molecular approaches to activity mapping is the prospect of seamlessly combining—within a single brain—the readout of activity patterns with the readout of structural connectome barcodes[734,466], transcriptional profiles[396] (e.g., to determine cell type) or other (epi-)genetic signatures[569] which are accessible via high-throughput nucleic acid sequencing.

3.4 Discussion

We have analyzed the physical constraints on scalable neural recording for selected modalities of measurement, data storage, data transmission and power harvesting. Each analysis is based on assumptions – about the brain, device physics, or system architecture – which may be violated. Understanding these assumptions can point towards strategies to work around them, and in some cases we have suggested possible directions for such workarounds. Even valid assumptions about natural brains may be subject to modification through synthetic biology or external perturbation. For example, methods for rapidly removing heat from the brain could work around our assumptions about its natural cooling capacity, supporting a range of highly dissipative recording modalities. Likewise, assumptions about the necessary bandwidth for data transmission could be relaxed if some information is stored locally and read out after the fact.

In some cases, theoretical extensions of our first-order analyses could reveal important insights. The power-bandwidth tradeoffs identified in section 4.4 for electromagnetic data transmission may place limits on the informational throughput of fMRI, for example, or a realistic simulation of heat fluxes in the brain could reveal the true limits of power dissipation. In many other cases, new experiments will be required to move beyond crude estimates of feasibility.

The analysis of physical limits illustrates challenges and opportunities for technology development. While the opportunities can only be touched upon here, and some directions have been treated elsewhere[144,20,21], we anticipate further analyses which could explore design spaces in detail. Here we briefly summarize a sampling of new directions suggested by our analysis.

Electrical recording The signal to noise ratio for a voltage sensing electrode imposes limits on the number of neurons per electrode from which signals can be detected and spike-sorted, likely requiring roughly one electrode per 100 neurons. To go beyond this, pure voltage sensing nodes could be augmented with the ability to directionally resolve distinct sources. For example, the 3D motion of a charged nanoparticle in an electric field, or of a dielectric nanoparticle in an electric field gradient, could be monitored at each recording site[711].

Optical recording While light scattering creates severe limitations on optical imaging, embedded optical microscopies could overcome these limits. Embedded optical imaging systems with high signal multiplexing capacity would be desirable, to minimize the required number and size of implanted optical probes.

One option might be to use time-of-flight information to multiplex many sensor readouts into a single optical fiber: this could potentially be realized using time-domain reflectometry techniques, commonly used to determine the positions of defects in optical fibers, coupled to neural activity sensors arranged along the fiber, which would modulate the fiber's local absorption or backscatter[711]. Time-domain reflectometry techniques have already reached 40 μm resolution[386].

Alternatively, novel fluorescent or bio-luminescent activity indicators could in principle relax the limits associated with light scattering, either by enabling efficient two-photon excitation at lower light dosages, or through all-infrared imaging schemes. Infrared bio-luminescence may be a particularly high-value target.

Delivery For both embedded optical and electrical recording strategies, new delivery mechanisms will be needed to scale to whole mammalian brains. Many of the basic parameters for scalable delivery mechanisms are still unknown. For example, can a large number of ultra-thin nano-wire electrodes or optical fibers be delivered via the capillary network? Can cells such as macrophages engulf ultra-miniaturized microchips and transport them into brain tissue? Can the blood brain barrier be locally opened (e.g., using ultrasonic stimulation[301]) to allow targeted delivery of recording probes?

Intrinsic signals The ideal technique would not require exogenous contrast agents or genetically encoded indicators, instead relying on signals intrinsic to neurophysiology. Neurons exhibit few-nano-meter scale[311] membrane displacements (e.g., in response to Maxwell stresses from large local electric field variations) during the action potential[502]. These can be measured using optical interferometry[190], but in principle they could also be monitored acoustically (and related activity-associated membrane swellings have been directly observed by atomic force microscopy[348] in cultured neurons). Sensors could be embedded in or around tissue to transduce the resulting acoustic vibrations into an electrical or optical readout. This could potentially allow recording at larger distances than the $\sim 130\,\mu m$ maximum recording radius for a voltage sensing node. Other intrinsic signals include changes in refractive index associated with neural activity, which will modulate the reflection and scattering of light[629]. These intrinsic changes in optical properties can be measured with optical coherence tomography (OCT)[391]. Local metabolic and hemodynamic signatures are also detectable optically, such as hemoglobin oxygenation (e.g., via functional near-infrared spectroscopy[293]) and the partial pressure of oxygen[515,395]. For minimal invasiveness, diffuse optical tomography uses near-infrared light (600–950 nm), which passes sufficiently-readily through the skin and skull to allow imaging of hemodynamics in cortex[283,325,300], although currently with limited spatial and temporal resolution.

Data transmission through diffusive media Unlike radio-frequency electromagnetics, infrared wavelengths may allow spatially multiplexed data transmissions from embedded recording devices, creating multiple independent channels by taking advantage of the stochasticity of light paths in strongly-scattering tissue. Alternatively, techniques are emerging to dynamically measure and invert the optical scattering matrix of a turbid medium, using pure-optical or hybrid techniques.

Ultrasound Certain wavelengths of ultrasound exhibit potentially-favorable combinations of wavelength (spatial resolution), bandwidth (frequency) and attenuation compared to radio-frequency electromagnetics. Ultrasound could be used as a mechanism for powering and communicating with embedded local recording chips[585]. Novel indicators[592] would likely need to be developed to perform neural activity imaging using pure ultrasound. Hybrid techniques such as photo-acoustic[198] or ultrasound-encoded optical[691] microscopies are also of interest.

Molecular recording For local recording, molecular recording devices could sidestep power constraints on embedded electronics, at the cost of increased engineering complexity. For molecular recording to become practical at temporal resolutions approaching the millisecond scale, sophisticated protein and viral engineering would likely be required to create a high-speed polymerase-based recorder operating in the neuronal cytoplasm. This would also necessitate molecular synchronization or time-stamping mechanisms to maintain phasing between multiple polymerases within a single cell, as well as between different cells.

On the other hand, molecular recording devices operating at slower timescales (e.g., seconds) could perhaps be engineered via more conservative combinations of known mechanisms, such as CREB-mediated signaling to the nucleus[148] or nuclear-localized calcium sensing[578]. In either case, the nucleic acid strands resulting from such molecular recorders could be space-stamped with cell-specific viral connectome barcodes[734] for later readout by bulk sequencing. Alternatively, the ticker tapes could be

read within their anatomical contexts by in-situ sequencing, i.e., nucleic acid sequencing performed inside intact tissue[396].

Combining static and dynamic datasets Combining dynamic activity information with static structural or molecular information could allow these datasets to disambiguate one another. For example, a diversity of colors for fluorescent activity indicators (i.e., a form of BrainBow[410] calcium imaging) could ease requirements on spatial separation of optical signals, and the color pattern across cells could be mapped post-mortem at single-cell resolution using in-situ microscopy. Generalizing further, in-situ sequencing enables the extraction of vast quantities of molecular data from fixed tissue, in effect allowing observations with a palette of 4^N colors, where N is the length of the nucleic acid polymer. It may be possible to harness this exponential informational resource to enhance the readout of dynamic activity information as well, e.g., through molecular recording.

MRI Current MRI is limited by its reliance on intrinsic hemodynamic contrast mechanisms and on rapidly diffusing aqueous protons. Indicators coupling neural activity to spin relaxation rates are being developed to move beyond hemodynamic contrast. Novel excitation and detection schemes that could sensitize MRI to fast, local, intrinsically activity-dependent mechanisms (e.g., cell swelling, neuronal magnetic fields), while filtering out the slower BOLD response, are also of interest and should initially be tested in organisms or slice preparations lacking hemodynamic responses. Detailed computational models of neuronal currents within a tissue voxel (e.g., in the spirit of[549]), and of the resulting mechanical and chemical changes, could be useful for evaluating potential new methods. In principle, MRI could also abandon the use of water protons as the signal sources, although this would pose significant implementation challenges.

Readout methods New signal processing frameworks such as compressive sensing could reduce bandwidth requirements and inspire new microscope designs exploiting computational imaging prin-

ciples[545,677,349,527]. Fast readout mechanisms[390] applied to giga-pixel arrays (e.g., the 3.2 giga-pixel CCD camera planned for the Large Synoptic Survey Telescope, which will have ∼1 s readout time) might be adapted to large-scale electrical or optical recording methods. Linear photodiode arrays can achieve 70 kHz line readout rates[8], and many such linear arrays could be read out in parallel. Optoelectronic methods that convert between time, space and frequency representations of signals[231,234,235,233,427,663,232] could inspire designs for even faster readouts (e.g., ∼10 MHz frame rates have been demonstrated in brightfield imaging). Although these methods are not directly compatible with fluorescence measurements due to their use of spectral dispersion, related ideas (e.g., beat frequency multiplexing) may enable fluorescence microscopy at rates above that of CCD-based imaging[155,173], limited ultimately by fluorescence lifetimes, while also exhibiting favorable properties with respect to scattering.

Alternative modalities X-ray imaging has been used on live cells[478] and might find use in neural recording if suitable contrast agents could be devised. X-rays interact with electron shells via photoelectric absorption and Compton scattering and with band structure in materials. X-ray phosphors utilize substitutions in an ionic lattice to generate visible or UV light emission upon X-ray absorption[309]. In principle, some of these mechanisms could be engineered as neural activity sensors, e.g., in an absorption-contrast mode suitable for tomographic reconstruction[388]. While tissue damage due to ionizing radiation would ultimately be prohibitive (e.g., on a timescale of minutes[711]), very brief experiments might still be possible.

Likewise, electron spin resonance (ESR) operates at ∼100× higher Larmor frequency compared to proton MRI, which improves polarizability of the spins. Due to Pauli exclusion, use of this technique requires an indicator with unpaired electrons. These can be found in nitrogen vacancy diamond nanocrystals[290] (nano-diamonds), which are also sensitive to voltage[159] and to magnetic fields[258], and are amenable to optical control and fluorescent readout of the spin state (although the 2P cross-section of the $(N-V)^-$ center appears to be relatively low[694]).

Hybrid systems New mergers of input, sensing, and readout modalities can work around complex engineering constraints. Electrical or acoustic sensors could be used with optical[566] (e.g., fiber) or ultrasonic readouts and power supplies. An MRI machine could interact with embedded electrical circuits powered by neural activity[319]. Linking electrical recording with embedded optical microscopies or other spatially-resolved methods could circumvent the limits of purely electrical spike sorting. Optical techniques such as holography or 4D light fields could generalize to ultrasound or microwave implementations. Consideration of analogies and synergies between fields suggests a combinatorial space of possibilities.

Our goal here has not been to pick winning technologies (which may not yet have been conceived), but to aid a multi-disciplinary community of researchers in analyzing the problem. The challenge of observing the real-time operation of entire mammalian brains requires a return to first principles, and a fundamental reconsideration of the architectures of neural recording systems. We hope that knowledge of the constraints governing scalable neural recording will enable the invention of entirely new, transformative approaches.

3.5 Supplemental: Detailed modeling of the extracellular spike

3.5.1 Modeling the extracellular potential from a firing neuron

To calculate the extracellular electric field gradients felt by the sensing particles, we began with a compartmental model[238] of the extracellular voltage from a firing neuron. We ran the model of[238] using cell d151 and parameter set B, at a fine grid spacing of 2 μm, and computed the decay of the extracellular spike amplitude with radial distance from the soma. Figures ??–?? show the spatial pattern of decay of the extracellular potential in the vicinity of the dendritic tree. We fit the falloff profile near the soma to a monopole-like ($V(r) \approx 1/r$) model, and the falloff profile far from the soma to a dipole-like

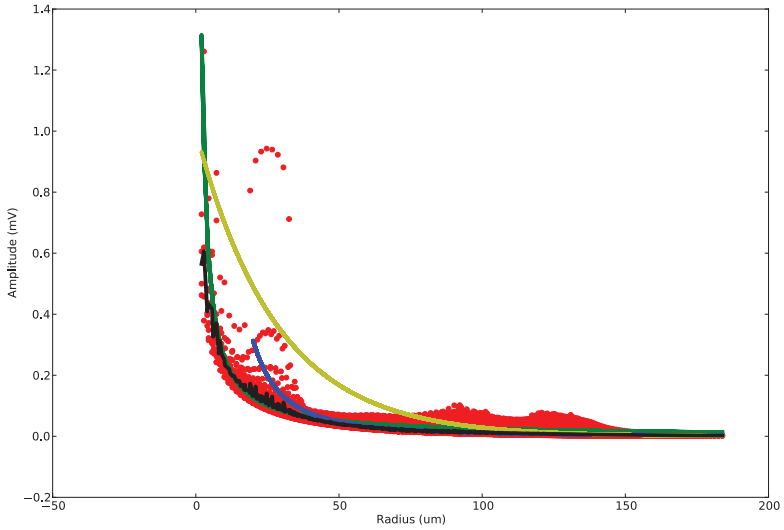

Figure 3.8: Calculated decay of extracellular potential from a compartmental neuron model [238], as a function of radial distance from the soma (red). The black curve is the average potential at each radial distance. Monopole fit to local decay (green), dipole fit to far-away decay (blue) and exponential model (yellow). The monopole model works well near the soma, while the dipole model works well farther away from the soma. The exponential model appears to help capture the effects of proximity to local dendrites, since a perfectly-spherical soma would generate a perfect monopole model, while a current-conserving, elongated neuron would generate an approximate dipole model at large distances.

$(V(r) \approx 1/r^2)$ model. The resulting models take the forms

$$V_{\text{mono}}(r) \approx \frac{2.65}{r}\text{mV}$$

and

$$V_{\text{dip}}(r) \approx \frac{146}{r^2}\text{mV}$$

where r is measured in microns. We also compared an exponential model (yellow)

$$V_{\text{exp}}(r) \approx 1\,\text{mV} \cdot \exp(-\frac{r}{28\,\mu\text{m}})$$

for the falloff. The full falloff pattern in a 2D plane is shown in Figure 3.11.

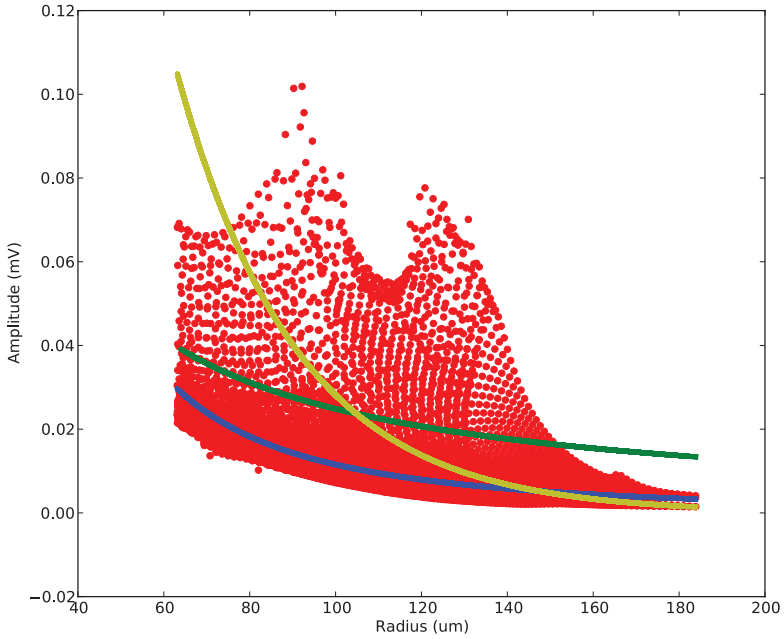

Figure 3.9: Zoom-in on calculated decay of extracellular potential from a compartmental neuron model [238], as a function of radial distance from the soma. Monopole fit to local decay (green), dipole fit to far-away decay (blue) and exponential model (yellow). The monopole model overshoots the data at large distances, while the dipole model accurately captures the shape of the long-distance falloff.

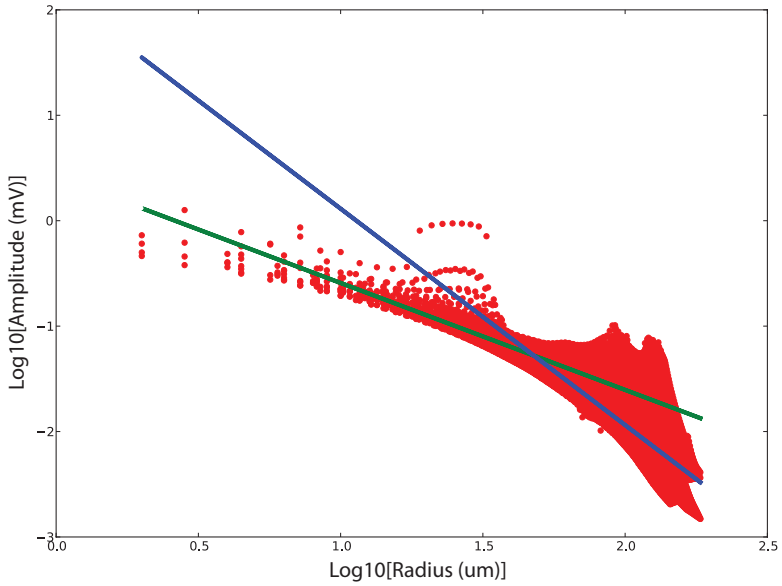

Figure 3.10: Log-log plot illustrating the transition between the monopole and dipole falloff regimes of the extracellular potential from a spike. The falloff is monopole-like below $\sim 45\,\mu m$ radius (green) and dipole or multipole-like above $\sim 60\,\mu m$ radius (blue).

3.5.2 Calculating the electric field gradient

Assuming a purely radial electric field, the field strengths in the three models (see Figure 3.12) are given by

$$E_{\text{mono}}(r) \approx \frac{-2.65}{r^2}\,\text{mV}/\mu\text{m}$$

$$E_{\text{dip}}(r) \approx \frac{-292}{r^3}\,\text{mV}/\mu\text{m}$$

$$E_{\text{exp}}(r) \approx -\frac{1\,\text{mV}}{28\,\mu\text{m}} \cdot \exp\left(-\frac{r}{28\,\mu\text{m}}\right)$$

so that

$$\frac{dE_{\text{mono}}}{dr}(r) \approx \frac{5.3}{r^3}\,\text{mV}/\mu\text{m}^2$$

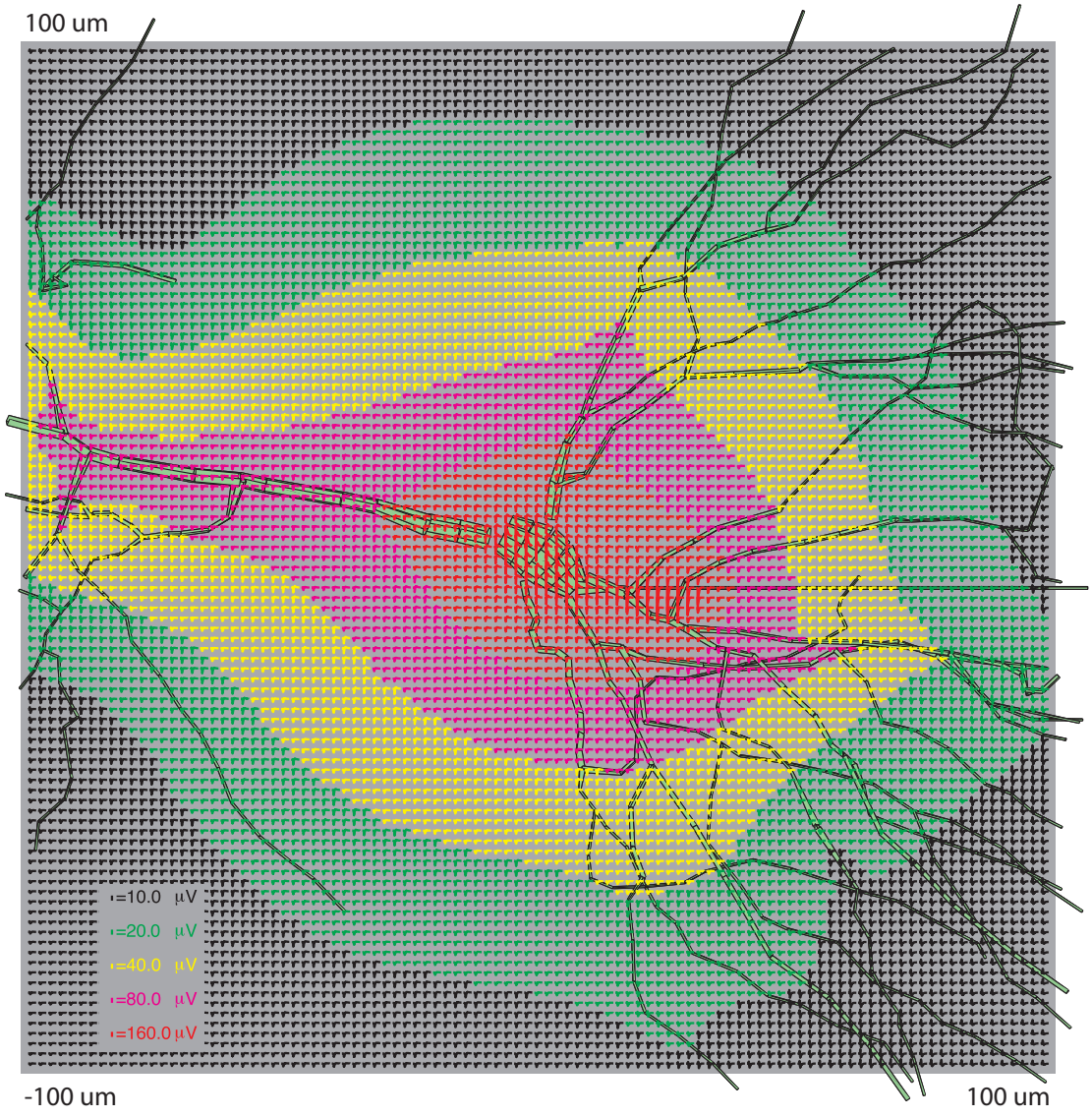

Figure 3.11: Extracellular action potential amplitudes and shapes on a 2 µm grid of width 130 µm × 130 µm, from the cell d151[238], assuming uniform extracellular conductivity of 0.3 Siemens / meter (red). Model generated using Matlab and NEURON software and cell model from[238].

$$\frac{dE_{\text{dip}}}{dr}(r) \approx \frac{876}{r^4}\,\text{mV}/\mu\text{m}^2$$

$$\frac{dE_{\text{exp}}}{dr}(r) \approx \frac{1\,\text{mV}}{(28\,\mu\text{m})^2} \cdot \exp(-\frac{r}{28\,\mu\text{m}})$$

are the corresponding electric field gradients. Thus, at reasonable sensing distances (e.g., 20–100 μm) from the soma, we can expect fields of order 1–10 μV/μm and field gradients on the order of 0.1–1 μV/μm².

3.6 Supplemental: Prospects for fiber-optic multiplexing

In later chapters, we present a detailed study of the molecular recording approach, but for now we briefly consider an example of a potential "hybrid" *optoelectronic* architecture for performing whole-brain activity mapping. With Lowell Wood and colleagues, we contemplated laying optical fibers bearing periodically spaced activity sensors throughout the entirety of a mammalian brain, and continuously monitoring signals elicited from these sensors by using time-delay reflectometry of optical pulses sent along the fibers. The idea is to *sense* neuronal activations electrically, acoustically or magnetically from a *short* standoff (maximizing SNR and removing a need for genetic manipulation), but to *probe* the apparatus optically (maximizing bandwidth). Optical fibers are used to contain optical probe pulses, such that photons largely remain inside the fibers and do not enter the brain tissue itself, minimizing tissue heating.

3.6.1 Thin Optical Fibers as Volume-Efficient, Low-Loss Conduits for Signal Transmission from the Brain

The fibers under consideration would be high-index-glass optical fibers of $< 1\,\mu$m diameter (i.e., "photonic nanowires"[657]), with unusually thin metal jackets on the order of ∼10–100 nm. Ultra-thin fibers with lengths of at least 1 cm and diameters as small as 100 nm can be fabricated by tapering of commer-

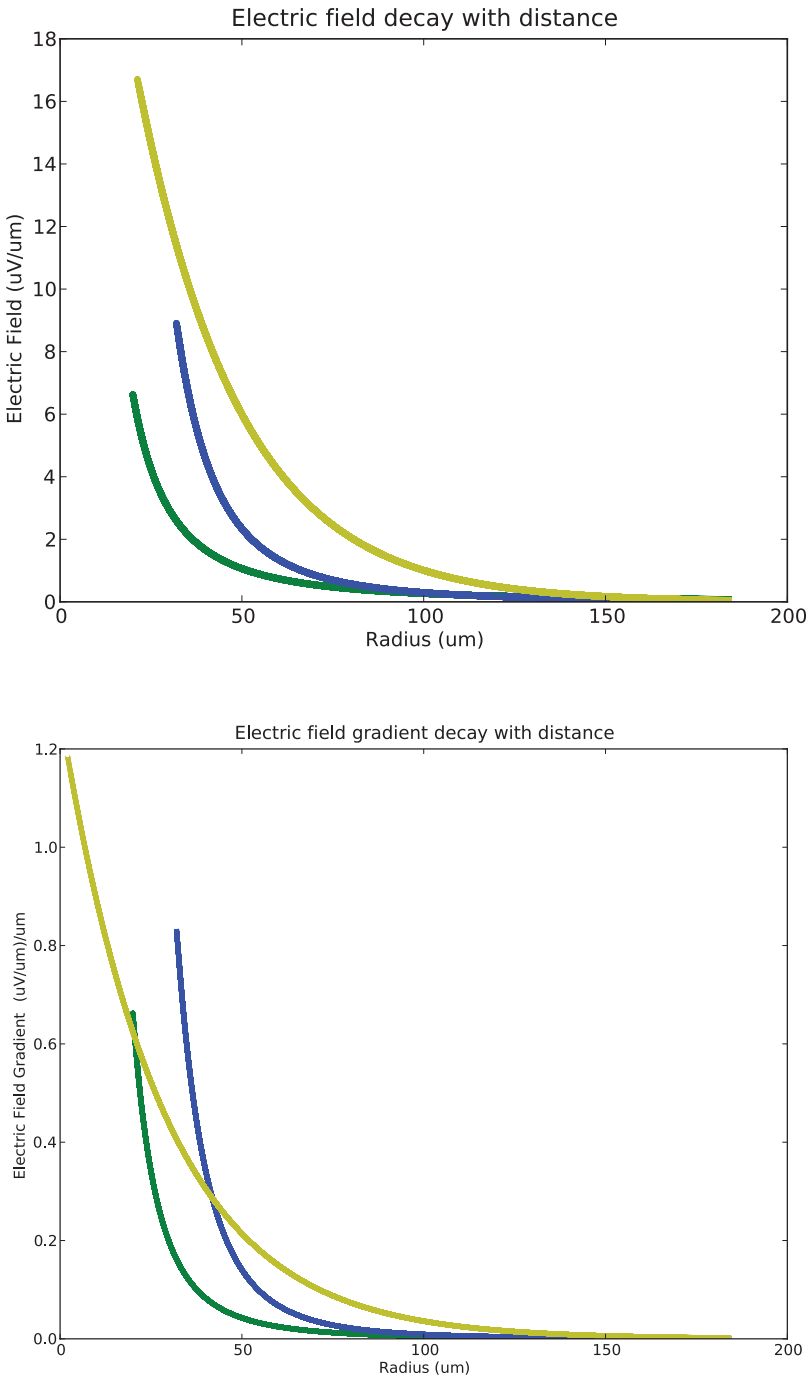

Figure 3.12: Decay of the electric field magnitude (top) and field gradient (bottom) with radial distance from the soma, for the monopole (green), dipole (blue) and exponential (yellow) falloff models.

cial optical fibers. Blue light (450–500 nm) probe pulses of sub-picosecond durations (e.g., 0.1–0.2 ps) would be repeatedly sent through each fiber via a pulsed laser.

Due to the thin jacket, these fibers are lossy by telecommunications standards: over short distances (∼1 cm), however, these losses are negligible. The losses arise from evanescent wave leakages out the fiber walls: the non-propagating, evanescent optical field extends out from the fiber by a distance on the order of a fraction of the wavelength (i.e., 100–200 nm for blue light).

3.6.2 Local neural activity sensors

In order to probe neural activity with ∼10 μm spatial resolution, we would need to attach ∼1000 local activity sensors along the ∼1 cm length of each fiber. These sensors would each locally modulate the optical transmission, reflection or loss properties of the fiber. The sensors would themselves be 1–10 μm in size. They could, for example, be fabricated lithographically and attached at defined positions along the fiber using a pick-and-place robot. The sensors could respond to either of two intrinsic signals from the action potential: electrical potential or mechanical displacement. Figure ?? tabulates a selection of possible sensing mechanisms, which are discussed in detail below.

3.6.3 Interaction with the evanescent field

A sensor-element external to the fiber could modulate the fiber's transmission properties by interacting with the evanescent fields leaking out radially from the fiber's walls. Prior work used micro-mechanical cantilevers to modulate the evanescent wave scattering from a fiber[49], leading to an optical sensor of the cantilever displacement: in this study, a 1 mm long tapered fiber with 1 μm outer diameter (and mechanical stiffness 1 mN/m = 1 pN/nm) was able to detect cantilever displacements on the scale of tens of picometers.

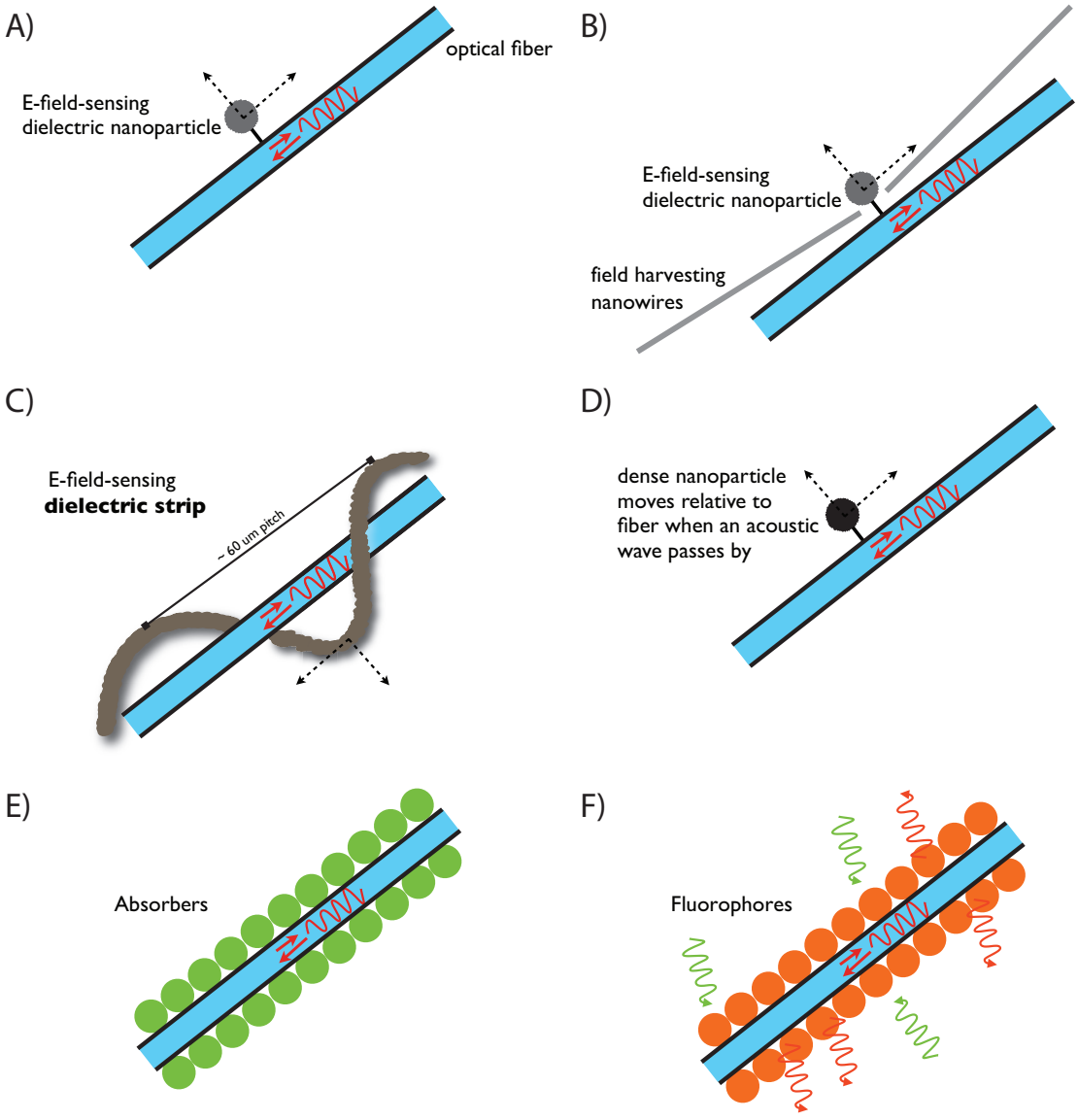

Figure 3.13: Selected options for coupling neural of activity measurements into a time-resolved reflectometric readout via interaction with the evanescent field from an optical fiber. **A)** Electric field gradient sensing dielectric nanoparticle. **B)** Electric field gradient sensing dielectric nanoparticle with metal nanowires for field focusing. **C)** Electric field gradient sensing dielectric strips. **D)** Acoustic vibration-sensing nanoparticle. **E)** Dyes with absorption contrast, e.g., sensitive to electric or magnetic fields. **F)** Fluorescent dyes.

3.6.4 Multiplexed sensor readout

The total number of required fibers would be on the order of $(1\,\text{cm}/100\,\mu\text{m})^2 \approx 10000$ and each such fiber would bear 1000 sensors. Thus we would have 10M sensors to read out 75M mouse neurons, which appears feasible from the perspective of electrical spike sorting. This readout would need to occur at a rate of 10 kHz. We thus require a highly parallelized readout and digitization scheme that would enable real-time digital storage of this data.

Time-delay reflectometry measurements of activity sensors

Time-delay reflectometry (TDR) involves sending laser pulses down each fiber and measuring their return-times, due to reflection off of "defects" in the fiber: 100 μm/ (speed of light) = 0.3 ps, which sets the temporal width of the required optical pulses. TDR measurements using pulsed lasers have already achieved a spatial resolution of $< 20\,\mu\text{m}$ [204,386].

The displacement of each of the ∼1 000 such sensor-modules deployed along the ∼1 cm active length of the fiber-in-capillary, would be read-out by a probing optical pulse every few dozen microseconds, whose variable return waveform would encode the position of each of the sensing crystals relative to the fiber's axis.

Alternatively, fiber Bragg grating sensors [252,704,376] with different wavelength tunings at different sensing positions could lead to a spectrally-resolved readout. Other reflectometric techniques such as optical low-coherence reflectometry have reached micron spatial resolutions [140].

3.6.5 Compatibility with engineering constraints

We briefly remark here on the compatibility of this architecture with the basic constraints outlined in [434]: < 50 mW power dissipation, < 1% volume displacement and the ability to sample all neurons at > 1 kHz rates.

Energy dissipation Assume that a probing optical pulse of ten million blue light photons is launched into each of 10000 fibers every microsecond. This corresponds to $10000 * (10^7$ photons per $\mu s) *$ (Planck's constant) $*$ (speed of light)$/500$ nm $= 40$ mW, which is within the $\sim$50 mW bound. In any case, only a fraction of this energy would be dissipated in brain tissue (most would be reflected inside the fiber).

Sampling rate If pulses are repeated every microsecond, the system could average over 100 pulses per frame and still sample at 10 kHz rates.

Volume displacement With 10000 fibers, each 1 um in radius and 1 cm long, we have a volume displacement of 0.3 mm^3 which is less than 0.1% of the 420 mm^3 mouse brain volume. Furthermore, this system could conceivably be deployed via the micro-vasculature with no brain tissue volume displacement whatsoever. The fraction of brain grey matter taken up by capillaries is roughly 1%[336].

3.6.6 Electric field sensing

Electric field gradient sensing dielectric particles

To implement electric field sensing in this approach, the fiber jacket could be thinned at defined locations. At these locations, a dielectric nanoparticle could be attached via an elastomeric "glue". Then, the nanometer-scale motions of the dielectric particle in the extracellular electric field gradient from a firing neuron would re-position the particle with respect to the fiber axis, modulating its degree of interaction with the evanescent optical field. The interaction with the evanescent field would, in turn, modulate the probability of backscatter at this location by the optical pulse traveling along the fiber.

A set of these sensors could, for example, be deployed in helical symmetry about the fiber-optic line, with a pitch of $\sim$10 μm and a period of $\sim$60 μm. The axially-dependent depth-of-modulation of the fiber's optical transmission properties – induced by the nanometric-scale differential motions of

the nanoparticles relative to the fiber's axis, under the action of the time-varying electric field gradient from the proximate neurons – would then encode not only the distance to but also the direction of the depolarizing neuron.

Calculating the dielectrophoretic force The force on a dielectric particle in an electric field gradient is

$$F_{\text{dielectrophoretic}} = 4\pi * r^3 * \varepsilon_{\text{sol}} * K * \frac{d\|E\|^2}{dr} \approx 8\pi * r^3 * \varepsilon_{\text{sol}} * K * E * \frac{dE}{dr}$$

where r is the particle radius, ε_{sol} is the dielectric constant (permittivity) of the surrounding medium and K is the Clausius-Mosotti factor, which approaches K = 1 for particles with dielectric constants much greater than that of the surrounding solution[480]. We will assume that K = 1, i.e., that we are using particles with high dielectric constant*.

Some studies assume a value for the permittivity of brain tissue similar to that of water, i.e., $\varepsilon_{\text{sol}} \approx 80 * \varepsilon_o \approx 8 \times 10^{-10}$ F/m, or slightly lower, i.e., $\varepsilon_{\text{sol}} \approx 10 * \varepsilon_o \approx 10^{-10}$ F/m[54], where $\varepsilon_o \approx 10^{-11} F/m$ is the permittivity of free space. On the other hand, measurements in the 10 Hz frequency range reported relative permittivities as high as 10^7 [213], or 10^5 at 1 kHz[579], and these values have been used in some subsequent studies[286]. It has been suggested that this anomalously-high apparent permittivity at low frequencies may be due to the cable properties of local dendrites[473,477,476]. We believe that it is very unlikely, however, that the effective microscale permittivity value anywhere inside a biological

*Barium strontium titanate ($BaSrTiO_4$) is a ferroelectric material above its Curie temperature, exhibiting a spontaneous electric polarization in the absence of an applied field. Below the Curie temperature, ferroelectric materials undergo a structural change to become paraelectric, and just below the Curie Temp, the dielectric constant (polarizability) becomes large. Importantly, in $BaSrTiO_4$, the Ba:Sr ratio can be adjusted to set the Curie temperature just above the working temperature (e.g., 37C in a physiological experiment). At this setting, $BaSrTiO_4$ exhibits a dielectric constant much greater than that of the surrounding solution. Each of the electric field gradient sensors may thus be a metal-jacketed $BaSrTiO_4$ crystal, doped to have its Curie temperature just above the cerebral temperature. The high dielectric constant of the nanocrystal then allows for comparatively large dielectrophoretic forces in the E-field gradient from the firing neuron.

organism – i.e., the permittivity value which enters into the calculation of the dielectrophoretic force – would be many orders of magnitude higher than that of water. We thus use $\varepsilon_{sol} \approx 10^2 * \varepsilon_o \approx 10^{-9}$ F/m, only slightly higher than that of water, in what follows.

Using $r = 170$ nm particle radius, our expressions for the electric fields then give dielectrophoretic forces on the order of $F_{\text{dielectrophoretic}} \approx 10^{-11}$–$10^{-9}$ pN for distances on the order of 50–100 μm from the neuron soma. These forces will last roughly 1 ms or less.

Comparison with thermal forces For comparison, a force sufficient to overcome thermal fluctuations over 1 nm displacements must satisfy

$$F \cdot 1\,\text{nm} > kT_{\text{room}} \approx 4 * 10^{-21}\,\text{J}$$

or in other words, $F > 4$ pN. Over 100 nm displacements, we require $F > 0.04$ pN forces to overcome thermal noise. Therefore, the endogenous electric field gradients are grossly too small to exert forces on individual sub-micron dielectric nanoparticles that would be detectable above the thermal noise. We therefore require strategies to either a) enhance the dielectrophoretic force, or b) suppress thermal noise. We consider these options in turn below.

Electric field focusing

To increase the dielectrophoretic force, one strategy would be to increase the local electric field gradient applied across the nanoparticle. For example, it would be possible to "harvest" the line-integrated electric field over much larger distances, and then to "focus" this integrated field across a smaller distance (e.g., across the 100 nm nanoparticle). This means that the local voltage swing of ∼1 mV could be applied over a ∼ 100 nm scale distance, rather than over the natural 10–100 μm decay distance.

This could be achieved with long, thin (albeit not 'quantum wire') strands of metal, acting as

'antennae', in order to focus the ambient neural electric fields down to the sensor-stations. These strands would be most naturally deployed on the outside of the fiber-optic lines: we contemplate 100 nm × 100 nm coaxial cross-sections of e.g., Au metal (possibly overcoated with a thin dielectric-insulating layer). These could be applied with lithographic means, but could perhaps also be subtractively defined by coaxial ion-milling of an initially-uniformly-applied metallic overcoating of the optical fiber.

Thus, let's assume that 1 mV is "focused down" by the nanowires to a $\sim$ 100 nm separation across our dielectric nanoparticle, leading to an electric field strength of $E = \frac{dV}{dr} = 1\,\mathrm{mV}/100\,\mathrm{nm}$ inside the particle and an electric field gradient of $\frac{dE}{dr} = \frac{d^2V}{dr^2} = 1\,\mathrm{mV}/(100\,\mathrm{nm})^2$. The same formula for the dielectrophoretic force, above, then gives $F_{\text{dielectrophoretic, field-focusing}} \approx 0.02$ pN, which is still not sufficient to overcome thermal noise. We thus turn to an alternate strategy for enhancing the SNR relative to thermal fluctuations.

Electric field gradient sensing dielectric strips

We have determined above that small dielectric nano-particles are highly sensitive to thermal noise, leading to a SNR limitation. This may be partially overcome by electric field focusing, but it would be more desirable to use an inherently noise-robust architecture. Thus, instead of a single tiny 'dot', one should employ a continuous, relatively 'fat' helical 'stripe' of dielectric, wound around the outer surface of the fiber with e.g. $\sim$60 μm pitch – e.g., with a stripe-width and stripe-thickness each of $<$ 1 μm thickness. There is then $\sim$10–20 μm of such stripe *coherently* 'flexing' in the fiber's evanescent field – which happens to nearly coincide with the demonstrated resolution of optical time-domain reflectometry.

This coherent distortion of the optical waveguide leads to an improvement in the signal-to-noise ratio: this is because actually-interfering noise sources now are required to be coherent over distances of dozens of microns and thus will have comparatively modest amplitudes. As a first-order estimate,

we can consider each 20 μm segment of the dielectric helix to move as a single, rigid particle under the endogenous electric field gradient. The force is then equivalent to that which would be obtained by scaling one of the dimensions of our dielectric particle, above, from roughly 200 nm to roughly 20 μm, i.e., a factor of 100 improvement. Unfortunately, this is still not sufficient to bring the applied forces reliably above the level of thermal fluctuations.

Conclusions on electric field gradient sensing

A continuous helical pattern of micron-thick Curie-doped $BaSrTiO_4$ crystal may allow cancellation of thermal noise due to its extended length, while simultaneously maximizing the harvesting of the local electric field gradient forces. Metal jacketing could enhance the interaction of these sensing strips with the evanescent field of the optical fiber probe, and patterning of metal structures around the fiber could support electric field focusing and plasmonic resonance effects, increasing the achievable modulation of the fiber's optical transmission properties. Due to the extremely weak fields emanating from the firing neuron, a *combination* of these methods would likely be necessary to achieve sufficient signal to noise ratio.

3.6.7 Acoustic sensing

During the action potential, neuronal membranes displace by a few nanometers, corresponding to a brief ~1 kHz acoustic vibration[311,190,348]. This displacement will propagate through the tissue to reach a sensor module, with the propagation occurring at roughly the speed of sound in water: ~1 500 m/s. These nanometer displacements are large compared to the picometer displacements to which the bony structures of the middle ear routinely respond usefully – and their attenuation over 1 cm distances in brain tissue is negligible. Therefore, detection means very modest compared to cochlear ones should suffice to sense them. Furthermore, arrays of such detectors can in principle phase-difference in order

to position-locate signal sources to high angular (and, with enough detectors, also range) accuracy – again, just as pairs of cochlea do, in human audition. Disambiguation of signals from distinct sources should be quite feasible with high-rate, high-precision readouts from acoustic sensors.

Similar to the above scheme for electric field sensing, a micro-lever placed close to the fiber would scatter evanescent optical waves in a manner sensitively dependent on the fiber-cantilever distance, as in [49] above, thereby acting as a vibration sensor. The micro-lever could consist of a heavy-metal nanoparticle attached to the jacket-thinned fiber via an elastomeric glue. The differential motion of the heavy-metal nanoparticle relative to the fiber in an acoustic vibration field would then modulate the evanescent field scattering.

Acoustic sensing particles

We can perform an order-of-magnitude estimate of the sensitivity of such a system. The membrane velocity is $v = \sim 5$ nm/ms $= 5\,\mu$m/s leading to a pressure $p = Zv \approx 1$–10 Pa where $Z = 1.6 \times 10^6$ kg s/m^2 is the acoustic impedance of brain tissue. The acoustic power density is then $p \cdot v = 5\,\mu$W/m^2.

Assuming that the neural soma undergoing vibration has area $(10\,\mu\text{m})^2$, the neuron radiates 5×10^{-16} W of acoustic power during an action potential. The total energy radiated per AP is thus 5×10^{-16} W $*$ 2 ms $= 10^{-18}$ J $= 200$ kT.

The ultrasound attenuation in brain tissue is roughly 0.5 dB/cm MHz, which we'll assume is negligible here, i.e., at kHz frequencies. During the 2 ms action potential, we thus have at most 10^{-20} J delivered to our 1 μm^2 transducer, whereas $kT = 4 \times 10^{-21}$ J. A tentative conclusion from this is that acoustic sensing is difficult for a sensor particle with sub-micron sensor cross-section.

Acoustic sensing strips

Similar to the argument above for dielectric particles vs. dielectric strips, it is likely that a continuous strip of deforming material would be preferable to small, isolated particles. As in the electric field sensing case, transforming to a strip geometry increases the effective volume of the sensor particle by a factor of roughly 100: this may be sufficient to capture as much as 10^{-18} J per action potential, as compared to $kT = 4 \times 10^{-21}$ J.

3.6.8 Alternative sensing modalities

Field sensing vs. voltage sensing

While many voltage-sensing dyes exist, these always operate on a voltage differential, e.g., across a membrane: voltage itself is not physically meaningful, only voltage differences. Hence our use of field-gradient-sensing nanoparticles, above, rather than "voltage sensors". Measuring voltage differences requires a ground reference, as in conventional extracellular electrical recording. Without sampling over large distances (e.g., with electric field-focusing nanowires), there is no way to obtain such a ground reference in the fiber OTDR setup. Thus, in the below, we assume that the sensing particles/dyes are sensitive to electric or magnetic fields, or to propagating acoustic waves, rather than the extracellular potential per se.

Fluorescent dyes

Unfortunately, the 0.1–1 ns fluorescence lifetimes of typical fluorescent dyes imply that fluorescence resulting from evanescent wave excitation of fluorescent indicators by the optical probe pulses is not an option in an OTDR scenario, since the corresponding spatial uncertainty is at least speed of light $*$ 0.1 ns $=$ 3 cm, which is larger than the entire mouse brain. There may exist plasmonic or stimulated

emission strategies which could dramatically decrease the fluorescence lifetime. An example of such an effect has been shown for NV diamond, although the lifetimes are still too long[575].

Absorption dyes

On the other hand, absorption is instantaneous, so neural activity sensors which modulate the absorption probability of a probe-pulse would be conceivable. Absorption measurements in OTDR appear as a drop in the reflected signal power at distances beyond the position of an absorber, so absorption can be spatially resolved[573,645]. On the other hand, absorption-based measurements dissipate much more power in the tissue.

In particular, optical absorption measurements on nitrogen vacancy nano-diamonds, attached to the fiber inside its evanescent field, could perhaps measure the local *magnetic* fields[394] produced by neuronal currents[258]. While these systems are typically operated in a fluorescence-detected NMR mode, absorption-based detection would also be possible[14]. A preliminary demonstration of optically-detected magnetic resonance from an NV diamond nanocrystal has been implemented in a tapered optical fiber system[409].

Prior work We expect a local neuronal magnetic field strength of ∼0.1 nT at ∼10 μm sensor standoff. Current NV diamond magnetometer systems (using ensembles of NV centers[653]) have achieved sensitivities of $\mathrm{nT/Hz^{1/2}}$[604], i.e., 100 nT over a 10 kHz bandwidth, but it has been suggested that sensitivities could reach $\mathrm{fT/Hz^{1/2}}$[12], i.e., sub-pico-tesla over 10 kHz bandwidth. Individual NV diamond spins have achieved few-nano-tesla sensitivity for kHz-frequency AC fields at room temperature, but required tens of seconds of averaging to do so[454]. The demonstrated electric field sensitivity of individual NV diamond spins is much lower, at roughly 100 $\mathrm{V/cm/Hz^{1/2}}$[158], orders of magnitude too small to detect 1–10 μV/μm fields at kHz bandwidths.

Detection limit The ultimate detection limit for a spin-based magnetometer with spin density n in volume V, due to quantum fluctuations, is[14]

$$\delta B_q \approx \frac{1}{\gamma} \frac{1}{\sqrt{nVt_m T_2^*}}$$

where $\gamma = 1.76 \times 10^{11}\,\mathrm{s}^{-1}\mathrm{T}^{-1}$ is the gyromagnetic ratio of the nitrogen vacancy center, t_m is the measurement duration and T_2^* is the dephasing time.

The system of[14] reported $T_2^* = 0.15\,\mu\mathrm{s}$ at room temperature. Optimistically, we can imagine extending the dephasing time to $T_2^* = \sim 1\,\mathrm{ms}$ (e.g., for isotopically enriched ultra-pure diamond samples[627]). Then for $n = \sim 1 \times 10^{18}\,\mathrm{cm}^{-3}$ (there are roughly 10^{23} carbon atoms per cubic centimeter of diamond, so that this corresponds to a defect density of 10 ppm) and $t_m = 1\,\mathrm{ms}$ (i.e., 1 kHz bandwidth), we have $\delta B_q \approx 1.3 * 10^{-10}\mathrm{T}$ for $T_2^* = 0.15\,\mu\mathrm{s}$ and $\delta B_q \approx 1.6 * 10^{-12}\mathrm{T}$ for $T_2^* = 1\,\mathrm{ms}$, where we have assumed a continuous 200 nm thick shell around the 1 um diameter fiber, extending over a distance of 20 um, and with volume $V = 2 * \pi * 500\,\mathrm{nm} * 200\,\mathrm{nm} * 20\,\mu\mathrm{m}$.

Thus, at the quantum limit, ensemble nitrogen vacancy diamond absorption sensors, packed densely on the outside of the fiber, could exhibit more-than-sufficient magnetic field sensitivity to detect neuronal magnetic fields from a distance of tens of microns. Current NV spin magnetometers, however, exhibit 2-3 of magnitude higher detection limit even at a reduced temperature of 75K[14], which would likely bring neuronal magnetic fields to the threshold of detectability.

Increasing the density above 15 ppm in diamond of natural isotopic abundance causes increased decoherence due to spin-spin coupling – within the NV spin bath and via coupling of NV centers to spin-1/2 carbon-13 impurities (at roughly 1% natural isotopic abundance) – and thus no net benefit to sensitivity[13]. Thus, without isotopically pure diamond, the spin density is saturated in the above calculation. Thus, the available options appear to be to increase the total volume of NV-doped diamond around the fiber, or to use isotopically pure diamond. It may also be of interest to explore other spins,

such as color centers in doped silicon carbide[364].

3.6.9 Modulation of fiber transmission properties through evanescent field interactions

The evanescent field around an optical fiber takes the form $E(r) = E_0 \exp(-r/d_p)$ where r is the radial distance from the fiber wall and $d_p \approx \lambda/3$ is the penetration depth, although the exact penetration depth is highly dependent on the geometry of the fiber and the thickness of the fiber wall (by using a very thin metal cladding, one could create as much field leakage from the fiber as desired). Thus, for a first order model, we use $d_p \approx 200$ nm.

If the sensor-particle or sensor-strip was displaced by 10 nm, we could expect a change on the order of a few percent in integrated evanescent electric field contained *inside* the particle or strip:

$\int_{10}^{110} e^{-x/200}\,dx / \int_{20}^{120} e^{-x/200}\,dx \approx 1.05$, for example. Whereas the 0.01 dB detection sensitivity of OTDR corresponds to a fraction of a percent change in the reflection coefficient at a sensor site: 0.01 dB $= 10^{0.001} = 1.0023$ for example.

The metal jacket of the sensor-particle or sensor-stripe is intended to maximize interaction with the evanescent field of the fiber. Indeed, lithographic resolutions have improved so drastically over the past several years that this metal jacket could be patterned so as to support plasmonic resonances, which could increase the interaction strength with the fiber's evanescent fields by another factor of Q (of the order of 10-20, for high-quality optical-plasmonic metals such as Ag in such geometries), if necessary.

3.6.10 Delivery and source localization

Sequential delivery to the capillary bed

According to textbook neuroanatomy, every neuron is 20–100 μm away from a capillary. One recent study in mouse cortex found a mean distance between the center of a neural soma and the nearest micro-vessel of ∼15 μm[662]. It has previously been suggested that a network of nanoscale electrical wires (e.g., conductive polymer nanowires, insulated except at their tips) could be deployed in the capillary bed, in principle permitting a highly scalable and minimally invasive brain interface[412]. In the case of the optical fiber sensors discussed above, delivery might be performed simply by "playing out (fiber-optic) lines" into the arterial side of cerebral blood-flow, and letting them drift into the capillary bed under the influence of viscous drag. In principle, a scheme can be imagined wherein, if light leaking from an already-deployed line is sensed by the line currently being deployed, it could be auto-withdrawn by a short distance and allowed to stochastically seek an alternative route, i.e., one involving a capillary that is not already occupied (although it should be noted that the vascular network contains many loops[65]).

It has yet to be determined whether embedding sub-micron fibers *of any kind* deep into the capillary network would cause stroke[602], excessive clotting or other damage (e.g., platelet adhesion due to turbulence, activation of the coagulation and complement systems). These concerns are heightened because the minimal capillary diameter in mouse vibrissa primary sensor cortex can be as small as ∼2.5–4 μm, although with an average of ∼4–6 μm[67]. There might also need to be a biocompatible coating on the fiber to prevent blood clotting or other effects.

Delivery to the brain parenchyma via biodegradable supports

Another option would be to push the fiber-probes directly into brain tissue, much as is currently done for multi-electrode arrays. Because the fibers are deliberately thin (to maximize evanescent field

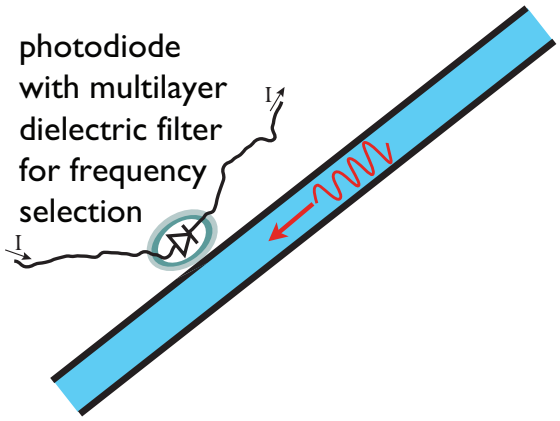

Figure 3.14: Conceptual diagram of an architecture for optically-powered and wavelength-multiplexed deep brain electrical stimulation, delivered minimally-invasively via the vasculature.

effects), it would be necessary to sheath them in a structural support, which is later removed, e.g., via bio-degradation.

3.6.11 Multiplexed fiber optic stimulation

Similar structures could be used for high-bandwidth brain stimulation. For potential application to deep brain stimulators, a slender catheter bearing one-or-more fiber-optic lines could be thread via the vasculature from the wrist up into locales of choice in the cerebrum. These lines could be used to deliver optical pulses of arbitrary 'formats' to micro-photodiodes in the vicinity of the tips of each fiber (or along their lengths, for multiplexing) which in turn could source current, upon demand into the walls of immediately-adjacent vasculature – with the other electrical end of the photodiodes being slender wires embedded in insulated segments of the fiber-optic line's jacket – which can sink the sourced current at locations-of-choice 'elsewhere.' A sketch of this system is shown in Figure 3.14.

One standard method for common-mode use of a single fiber to realize multiple channels is frequency/wavelength multiplexing. For neural stimulation, this would involve using a multi-layer dielectric filter over each of potentially dozens of photodiodes suspended on a single fiber-optic line.

This arrangement would be wasteful of optical power but efficient from the standpoint of mass and volume – which is likely the system-level optimum for the intra-vasculature situation.

Without digital storage, you can't have life. With digital storage, you don't exactly have a rock any more.

John Walker

4

Molecular Recording: Experimental Progress

Traditional approaches to signal recording rely on electromagnetic radiation or electronic hardware to couple the signals of interest to an external data storage device. These approaches become cumbersome, however, when signals reside deep within complex tissues, as is the case in func-

tional neural connectomics, where simultaneously accessing millions of neurons is currently not feasible[68,91]. In contrast, molecular approaches to information transfer are by nature ubiquitous, massively parallel, and inexpensive. We have recently proposed that information could be recorded onto DNA[37,123], arguably the most robust molecular information storage mechanism in nature. Recording systems based on DNA can leverage scientific and industrial interest in technologies for manipulating and sequencing nucleic acids, as well as advances in protein design.

A DNA polymerase could be repurposed as a nano-scale recording device, bypassing many of the hurdles of sensing technologies by locally measuring and storing information rather than requiring it to be rapidly transmitted, digitized and stored elsewhere. In a simple encoding scheme, an environmental signal of interest is coupled to the base misincorporation rate of the DNA polymerase (Figure 4.1A). Then, as the polymerase copies a known DNA template, the level of misincorporations produced in the copied strand will represent the amplitude of the environmental signal present. If the environmental signal varies over time, those changes could in principle also be reflected by changes in the misincorporation rate over time, enabling the DNA data storage idea to be extended to the time domain.

DNA polymerases are complex biochemical machines[90]. To establish them as molecular recording devices, it is necessary to quantify how environmental variables affect their copying fidelity. Of central importance is the transfer function associated with a particular DNAP, which maps the amplitude of the environmental signal to the misincorporation rate of the DNA sequence data. This transfer function is not only shaped by the biochemical properties of the polymerase, but also by other aspects of the experimental setup; it reflects the entire sensing pathway from environmental variable to filtered and processed sequence data. Therefore, the design of DNA recording devices requires the identification of any uncontrolled variables (such as local sequence context or secondary structure of the source template) that could alter the shape of this transfer function.

Cation concentrations are logical choices as the input signals for a DNA recording device because

they are affected by many physiological variables, and some are known to modify DNAP fidelity[178]. Ca^{2+}, for example, is involved in many signaling pathways, including neurotransmission[432] and immune activation[552], and can also be modulated by external stimuli[625]. Mg^{2+} and Mn^{2+} concentrations have been shown to strongly modulate DNAP misincorporation rate[79]. Quantifying the transfer function between cation concentration and DNAP fidelity is a useful step towards elucidating the principles of a DNA recording device.

There are a large number of known DNAPs with varying properties[51] that impact their usability as recording devices. A DNAP appropriate for DNA recording of environmental signals should ideally have a wide dynamic range of misincorporation rates and be active at mesophilic temperatures. Dpo4 (Sulfolobus solfataricus)[75] is a member of the Y-family of polymerases[568,85], which are implicated in translesion bypass[15] and somatic hypermutation[504] and have high misincorporation rates. Klenow exo- is the D355A, E357A mutant[152] of the Klenow Fragment of the E. coli DNA Polymerase I[384], which lacks 3'-5' proofreading activity, and, unlike most commercially available DNAPs, is compatible with the 37C extension temperature used for the Y-family enzymes. These two DNAPs seem particularly interesting in the context of recording device development.

Here we have developed a strand-specific deep sequencing method to measure the transfer function between divalent cation concentration and polymerase misincorporation rate in a highly multiplexed format. We performed barcoded, error-prone primer extensions using Dpo4 and Klenow exo-, at varying cation concentrations, and analyzed the products by deep sequencing. Analysis of the measured transfer functions reveals strong cation, template base, and sequence-context dependent effects on the misincorporation rate, which differ dramatically between the polymerases, and resolves the bulk misincorporation rate into its underlying transition probabilities. Our method for quantifying DNAP transfer functions will facilitate the development of engineered molecular recording devices that utilize DNA as a storage medium.

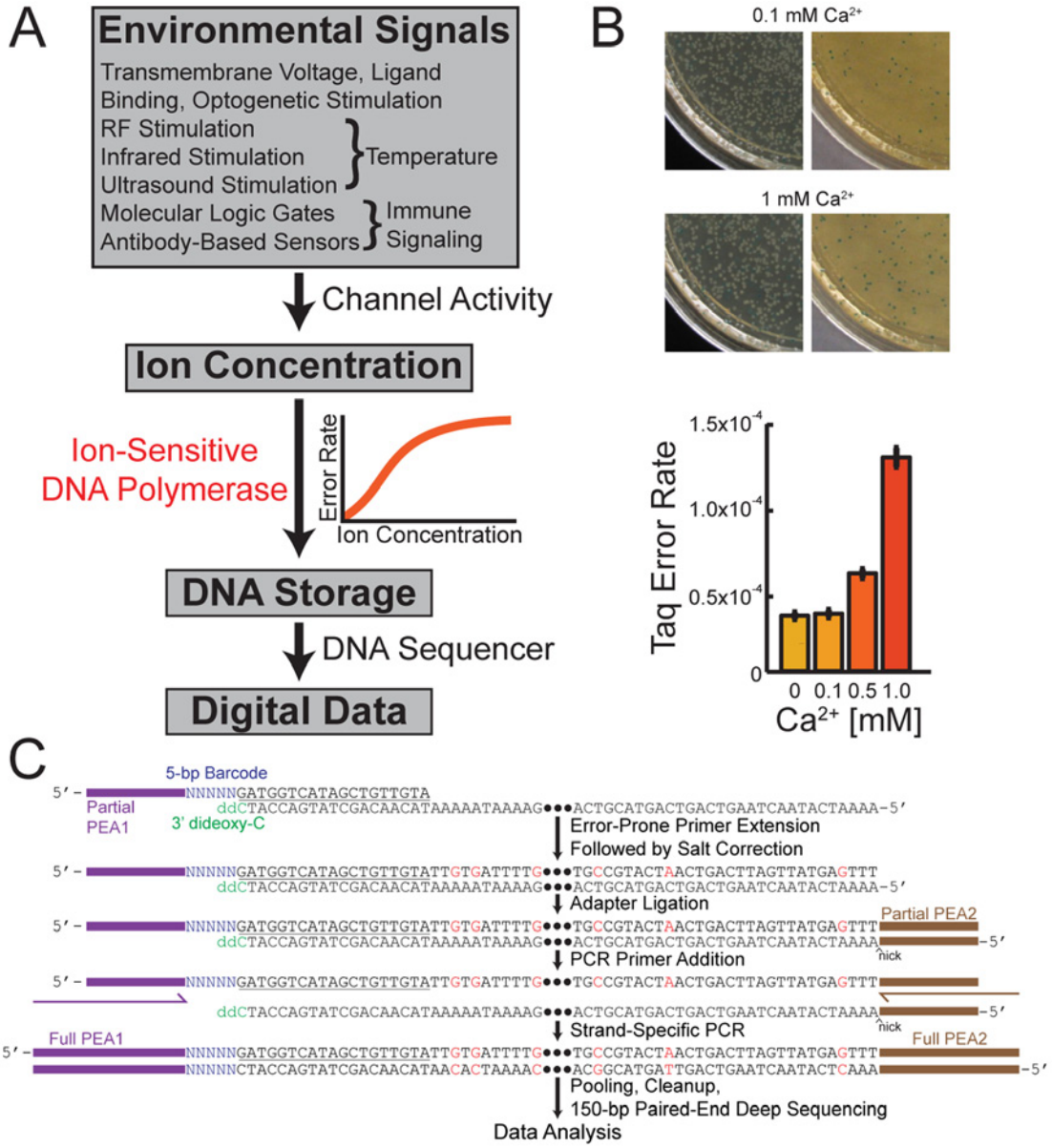

Figure 4.1: DNA polymerase (DNAP) as a molecular signal recorder. (A) Overview of a strategy for using DNA polymerases as signal recording devices. Signals (top) are coupled to intracellular or extracellular cation concentration through direct or indirect modulation of an ion channel activity. Cation concentration is in turn coupled to DNA polymerase fidelity on a known template according to a known transfer function (orange curve), generating a DNA recording, in which data is represented by the density of misincorporated bases, and which can be read by DNA sequencing (bottom). (B) Modulation of Taq polymerase by Ca^{2+} concentration, measured by a traditional blue-white colony counting assay. (C) Biochemical steps of the multiplex deep sequencing assay for measuring the transfer functions of error-prone DNAPs.

4.1 Results

To verify that physiologically relevant ions, such as Ca^{2+}, can in principle modulate DNAP fidelity, we checked the Ca^{2+} dependence of the fidelity of Taq DNAP using a lacIq-based PCR fidelity assay (Figure 4.1B). We constructed a derivative of pUC19 containing the lacIq repressor allele and the partial gene encoding for the colorimetric enzyme beta-galactosidase (lacZα). The plasmid was linearized, and PCR-amplified by Taq DNAP in buffers containing varying concentrations of Ca^{2+}. Subsequently, the amplified DNA was circularized and transformed into an α-complementing strain of E.coli. Replication by Taq DNAP introduces mutations in lacIq resulting in the de-repression of lacZα, whose activity after complementation is detected on X-Gal indicator plates. The ratio of blue to white colonies can be used to calculate the bulk Taq error rate if the number of DNA duplications, and mutations yielding non-functional protein, are known. There are 349 single-base substitutions at 179 codons that will result in a blue phenotype in the lacI gene[580]. Our assay recapitulates previously reported error rates for Taq ($2.6 * 10^{-5}$ per bp[46]) in the absence of added Ca^{2+}, and demonstrates that increasing divalent cation concentration monotonically increased the bulk error rate.

While Ca^{2+} modulated Taq fidelity, Taq is unable to serve as a recording device, because it requires high temperatures for extension and has a low misincorporation rate (<0.015% per nt) across the physiological range of Ca^{2+} concentrations[538]. We therefore focused our analysis on DNAPs that have high baseline misincorporation rates and operate at physiological temperatures.

4.1.1 Multiplexed Assay for Polymerase Misincorporation

To characterize DNAPs at varying cation concentrations, we developed a multiplexed primer extension assay with deep sequencing readout (Figure 4.1C). Barcoded primers were first annealed to a known DNA template, followed by primer extension by the error-prone polymerase. Using a 96-well plate format allowed simultaneous testing of many cation concentrations. Subsequently, all wells

were normalized to equal cation concentrations (salt correction) to eliminate ion-dependent bias in downstream biochemical steps. To eliminate bias against error-rich primer extensions, a partial Illumina adapter was then ligated downstream. Ligated products were amplified via high-fidelity PCR using primers that completed the Illumina adapter sequences. The template contained a dideoxy-C 3' modification, preventing extension by the polymerase along the upstream primer. Consequently, the template strand did not contain the primer-binding site for PCR amplification; only strands of non-template origin were amplified, and therefore contained the full Illumina adaptors used for sequencing.

Diversity in the initial sequenced bases is required for proper cluster identification during Illumina sequencing. We therefore positioned the 5-base barcodes indexing the 96-well plate wells such that these barcodes comprised the first five bases sequenced. Following deep sequencing using the Illumina MiSeq platform, individual reads were filtered in silico and compared with the template sequence to quantify misincorporation rates as a function of ion concentration and base position along the template (see Materials and Methods).

This method generated hundreds to thousands of reads per cation condition, some of which were not full length (the result of abortive extensions and/or extensions containing base deletions). Duplicate plate wells with nominally equal cation concentrations and different barcode sequences were analyzed independently and used to generate misincorporation rate estimates and errors (standard error of duplicate means).

4.1.2 Measurement of the Mean Transfer Function between Cation Concentration and Misincorporation Rate

We observed misincorporation rates for each reaction condition by comparing filtered sequencing reads with the known template sequence (Table S1). We first analyzed the cation dependence of Dpo4's mean misincorporation rate, and found it to be positively correlated with both Mg^{2+} and Mn^{2+} con-

centrations (Figure 4.3A-B, top). We found that Dpo4 acts as a Mn^{2+} sensor with a gain of 2%/mM. Dpo4 also acts as a sensor with a gain of 0.01%/mM for Mg^{2+} (Table S1). Dpo4 is therefore a far better sensor for Mn^{2+} than Mg^{2+}.

While the misincorporation rate for Klenow exo- is also positively correlated with Mn^{2+} (top of Figure 4.3C), it exhibits a weak negative correlation with Mg^{2+} (top of Figure 4.3D). Klenow exo- is a sensor for Mn^{2+} with a gain of 0.6%/mM and a sensor for Mg^{2+} with a gain of −0.01%/mM. Thus two cations may differ in the direction by which they modify the kinetics of misincorporation.

Note that in all cases, the measured mean misincorporation rates are much higher than the noise floor (shaded regions). This noise floor is defined as the mean plus the standard error of the mean of the misincorporation rate obtained by performing an identical protocol with the high-fidelity Phusion DNAP in HF buffer Figure 4.2), and is in agreement with previous studies that measured the substitution rate of phosphoramidite synthesis[352]. Therefore, the noise floor likely results from substitution impurities in the synthetic template strands. Our measurement of the noise floor is. Deep sequencing is therefore a reliable method to characterize DNAPs with high misincorporation rates.

We further measured the transfer function for mean misincorporation by Dpo4 and Klenow exo- with respect to Ca^{2+} concentration. Because the kinetics of primer extension in buffers containing Ca^{2+} alone are at least 50 fold slower than in either Mg^{2+} or Mn^{2+} [306], we performed the primer extensions in a variety of physiologically-relevant Mn^{2+} and Mg^{2+} backgrounds. The misincorporation rate by Dpo4 in a 200 uM Mn^{2+} background increases 2.9-fold from 1 nM to 1 mM Ca^{2+}, the majority of which occurs between 100 nM and 1 mM (Figure 4.3I, Table S1). Conversely, the misincorporation rate of Dpo4 decreases by 42% between 1 nM and 1 mM Ca^{2+} in a 7 mM Mg^{2+} background, with virtually all of the change occurring between 100 nM and 1 mM Ca^{2+} (Figure 4.3J). Ca^{2+} has no effect on misincorporation rate with Klenow exo- in the same backgrounds (Figure 4.3K and Figure 4.3L) nor in most other enzyme/buffer combinations (Table S1). Therefore neither of the tested DNAPs is promising as a Ca^{2+} sensor without further modifications.

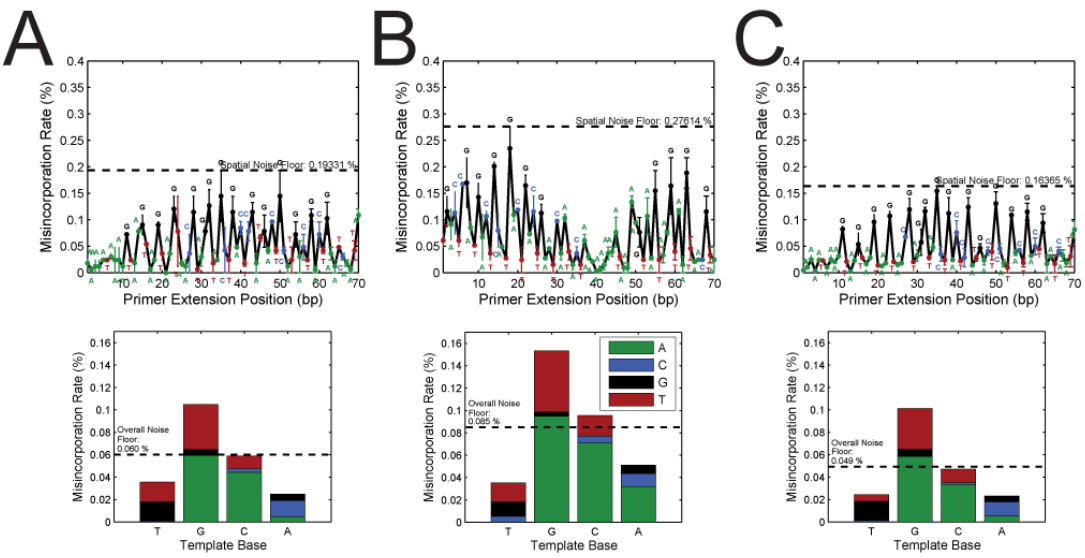

Figure 4.2: Measurement of the experimental noise floor. The spatial distribution (top) and template-base-specific (bottom) misincorporation rates for Phusion on the original (A) and swapped (B) templates. (C) Misincorporation rates for Phusion on the original template, using a modified protocol in which the ligation products were pooled and cleaned before high-fidelity PCR amplification. Dashed lines indicated the maximum peak, plus the error, of the spatially-distributed misincorporations (top) or the mean + SEM of misincorporations across all template bases (bottom) misincorporations, and served as the noise floors in the main text.

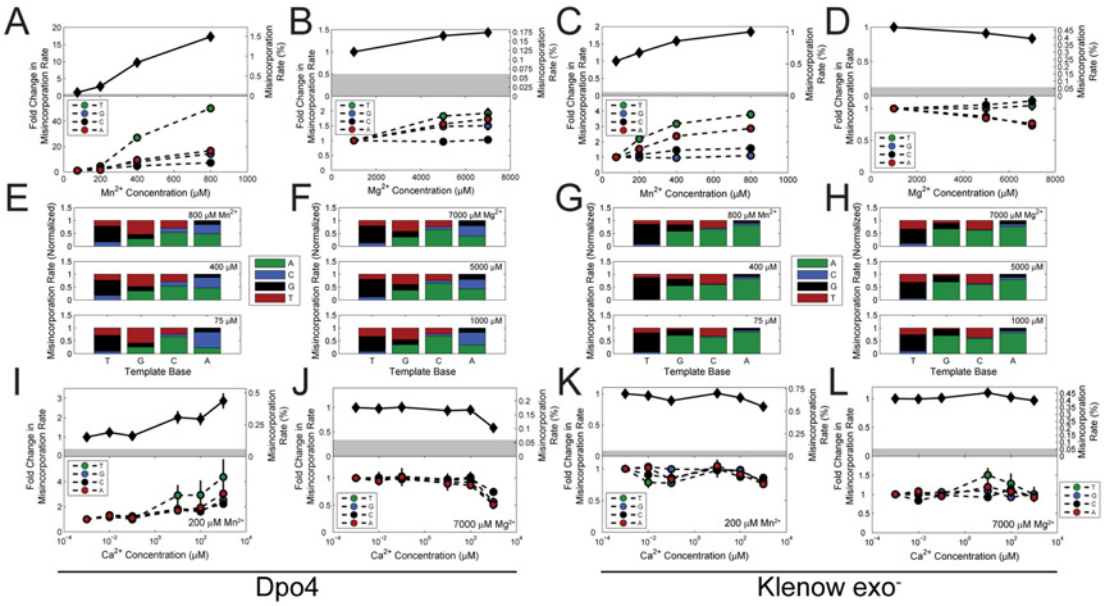

Figure 4.3: Ion-dependent misincorporation rates of Dpo4 and Klenow exo- polymerases. (A, B, C, D) Mean (top) and template-base-specific (bottom) misincorporation rates as a function of Mn^{2+} (A, C) and Mg^{2+} (B, D) concentrations. (E, F, G, H) Normalized distributions of misincorporated dNTPs for each template base. (I, J, K, L) Mean (top) and template-base-specific (bottom) misincorporation rates as a function of Ca^{2+} concentration at 200 uM background Mn^{2+} (I, K) and 7000 uM background Mg^{2+} (J, L) concentrations. Errors are given in Tables S1-2, and are shown as error bars in the line graphs when they are larger than the data symbol.

4.1.3 Base Specificity of Misincorporation

The misincorporation characteristics of DNAPs depend not only on cation concentrations, but also on the particular template base being copied. Deep sequencing allows quantification of the misincorporation rate at every position within the template (Figure 4.3A-D). Note that misincorporation by Dpo4 opposite a template T exhibits a >50-fold increase over the range of Mn^{2+} studied, while misincorporation rates opposite other bases show a comparatively weak dependence on Mn^{2+} (Figure 4.3B, Table S1). Thus the mean Mn^{2+} dependence of misincorporation rate of Dpo4 is largely driven by misincorporations opposite T. There is no obvious correlation of the misincorporation rate with the identity of the base preceding the template base (Figure 4.4).

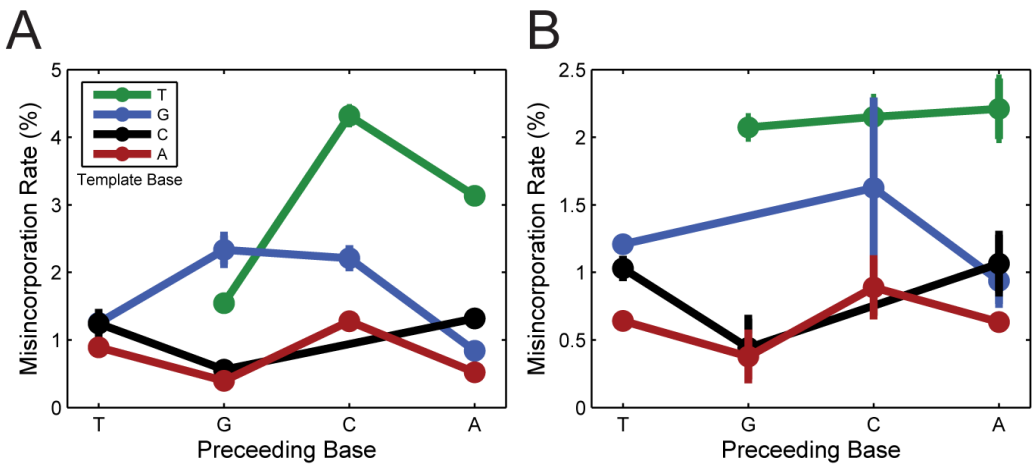

Figure 4.4: Analysis of misincorporation at two-base motifs in the template sequence. Misincorporation rate as a function of the template base and of the base preceding the template base, for Dpo4 at 800 μM Mn^{2+} on the original (A) and swapped (B) templates.

Deep sequencing also allows direct measurement of the 4x4 transition probability matrix between template base and incorporated base (Table S2, Figure 4.3E-H). For example, the disproportionate Mn^{2+} dependence of misincorporation by Dpo4 opposite template T is largely due to misincorporation of dGTP. Likewise, mutations caused by Klenow exo- are generally dominated by misincorpora-

tion of dATP, except on template T, which shows a >4-fold preference for misincorporation of dGTP. Misincorporation by Dpo4 of dGTP opposite template T increases 50-fold with Mn^{2+}. Note, however, that the relative proportions of the misincorporated bases on a given template base are largely insensitive to cation concentration for both Dpo4 and Klenow exo-. Rather, cation concentration acts as a scaling factor with respect to misincorporation opposite a given template base; it is the differential magnitude of this scaling factor between the template bases that underlies the template base dependence of misincorporation.

4.1.4 Misincorporation is Context-Dependent

Cations change misincorporation probabilities but not the distribution of misincorporations across incoming dNTPs. However, the template base itself is not, in general, sufficient to predict misincorporation rate; the sequence context is important as well (Figure 4.5A-C). For Dpo4, the shape of the graph is dominated by preferential misincorporations at template T (red dots). The dependency on the sequence, however, is complicated: switching the first half of the template (shaded blue) with the second half (shaded red) leaves some aspects of the misincorporation curve similar while changing others. Indeed, the swapped template leads to a more even distribution of misincorporations, indicating that template choice is an important design parameter for DNA recording.

There is no obvious sequence context dependence of misincorporation for Klenow exo- (Figure 4.5C), beyond the identity of the template base. Curiously, the misincorporation rate opposite template G, which dominates at 75 uM Mn^{2+}, stays relatively unchanged with increasing Mn^{2+} concentration, while misincorporations opposite template A increase, becoming the predominant peaks at 800 uM Mn^{2+}. Thus different DNAPs are differently affected by both cation concentrations and local sequence contexts.

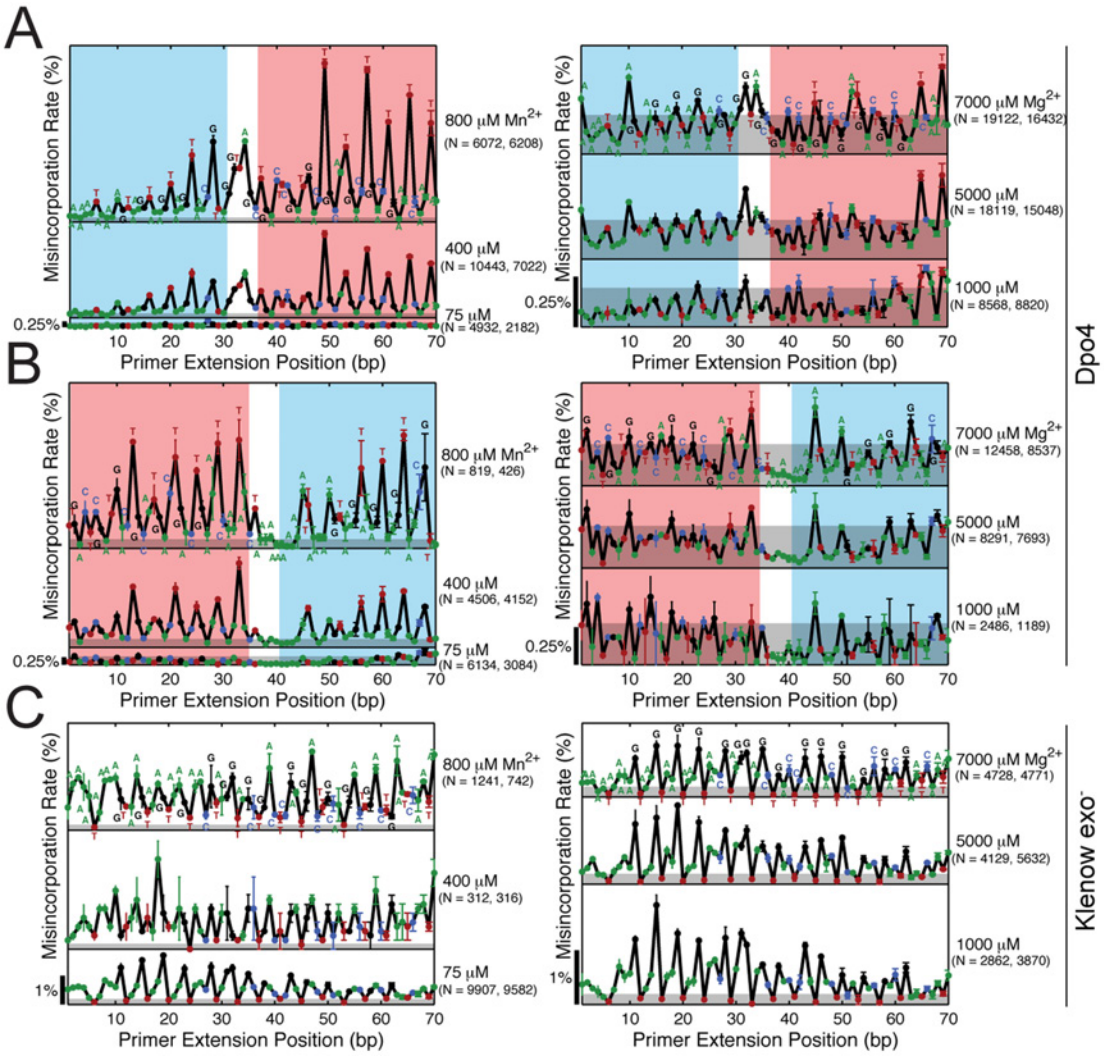

Figure 4.5: Template position dependence of misincorporation rates. (A) Template position dependence of Dpo4 misincorporation rates on the original template at varying Mn^{2+} (left) and Mg^{2+} concentration (right). (B) Template position dependence of Dpo4 misincorporation rates on the swapped template at varying Mn^{2+} (left) and Mg^{2+} concentration (right). (C) Template position dependence of Klenow exo- misincorporation rates on the original template at varying Mn^{2+} (left) and Mg^{2+} concentration (right). Letters above each data point denote the identity of the template base at that position. Grey shaded areas indicate the noise floor, defined as the maximum over positions of the misincorporation rate (plus SEM) observed in an identical experiment with Pfusion HF DNA polymerase (**Figure 4.2**). Red (blue) shaded areas in (A) and (B) correspond to shared sub-sequences between the original and the swapped template.

4.1.5 Statistical Analysis of Misincorporation Events

Our deep sequencing method produces large datasets that can be used to characterize the correlations within each strand of synthesized DNA, as well as the statistical distributions across strands. To test the hypothesis that DNAPs could tend to string errors together, we analyzed the lag-one correlations of misincorporations, asking if a misincorporation on one base makes it more likely that there is a misincorporation on the next base. After correction for bias due to correlations within the template itself (see Materials and Methods), there is a weak but statistically significant correlation of misincorporations across bases for Klenow exo- at 800 uM Mn^{2+} (0.047±0.002% excess misincorporations per base). For Dpo4, misincorporations at consecutive positions appear independent from one another (all excess errors <0.01% per base). Therefore, only for Klenow exo- is a misincorporation on a base associated with an increased probability of misincorporation on the next base.

It is unknown to what extent molecular heterogeneity plays a role in the generation of DNAP misincorporations. If each DNAP molecule performs misincorporations according to the same statistics, the distribution of the total number of misincorporations per read should be governed by a Poisson distribution. The variance is larger than the mean, however, for each DNAP/template combination tested, and the null-hypothesis of a Poisson distribution can be rejected for each of the datasets (χ^2 test, p<0.05). Thus the ensemble of nominally identical DNAP molecules is heterogeneous with respect to misincorporation rate.

To further study the determinants of misincorporation, we fit the misincorporation data set to a generalized linear model (GLM) containing sequence features that could plausibly impact misincorporation rates (Figure 4.6). Possible features included the identity of the template base and the predicted regional secondary structure. The models were able to fit the data (R^2 = 0.58±0.02 and 0.53±0.11 for the original and swapped templates, respectively, Figure 4.6A and Figure 4.6B). Interestingly, the models captured the interplay of sequence properties that determine the spatial depen-

dence of misincorporation. Fits to the original template data could predict the spatial dependence of misincorporation on the swapped template (R^2 = 0.49±0.06), and vice versa (R^2 = 0.50±0.01). Furthermore, the weights assigned to different features (Figure 4.6A, Figure 4.6C and Figure 4.6D) in the model point to potential determinants of the error rate. For example, the models identify the positive contribution of a template T to Dpo4's error rate and also suggest that local secondary structure may play a role (see Figure 4.7).

4.1.6 Information Content of Misincorporations

Because cation concentration modulates the number of misincorporations in the copied DNA, one can consider the sequenced data to store information about the cation concentration present during primer extension [422]. The information gain per base is related to the likelihood that the observed misincorporation rate at a given template position was produced at a particular cation concentration. For Dpo4 at high (800 uM) vs. low (75 uM) Mn^{2+}, the most informative template bases transmit 0.03 bits of information per base about Mn^{2+} concentration (Figure 4.6E), whereas only $5 * 10^{-4}$ bits per base are transmitted at high (7000 uM) vs. low (1000 uM) Mg^{2+}. Therefore, in the limit in which Mn^{2+} concentration could be modulated as each nucleotide is added, a Dpo4-based DNA recording device could in principle write 11 megabytes onto a template the length of a human genome ($3.2 * 10^9$ bases).

4.1.7 Alternate Misincorporation Analysis

The analysis described in the main text relies on sequence alignments to compare sequence reads with the known template. Alignments, however, require the sequenced read to be of sufficient length that the alignment algorithm can work reliably with respect to the full-length templates. We therefore imposed a length cutoff of 70 bp, as well as an alignment score cuttoff, to ensure that the sequenced reads could be properly aligned. As a control for analysis methodology, we also developed an alternate anal-

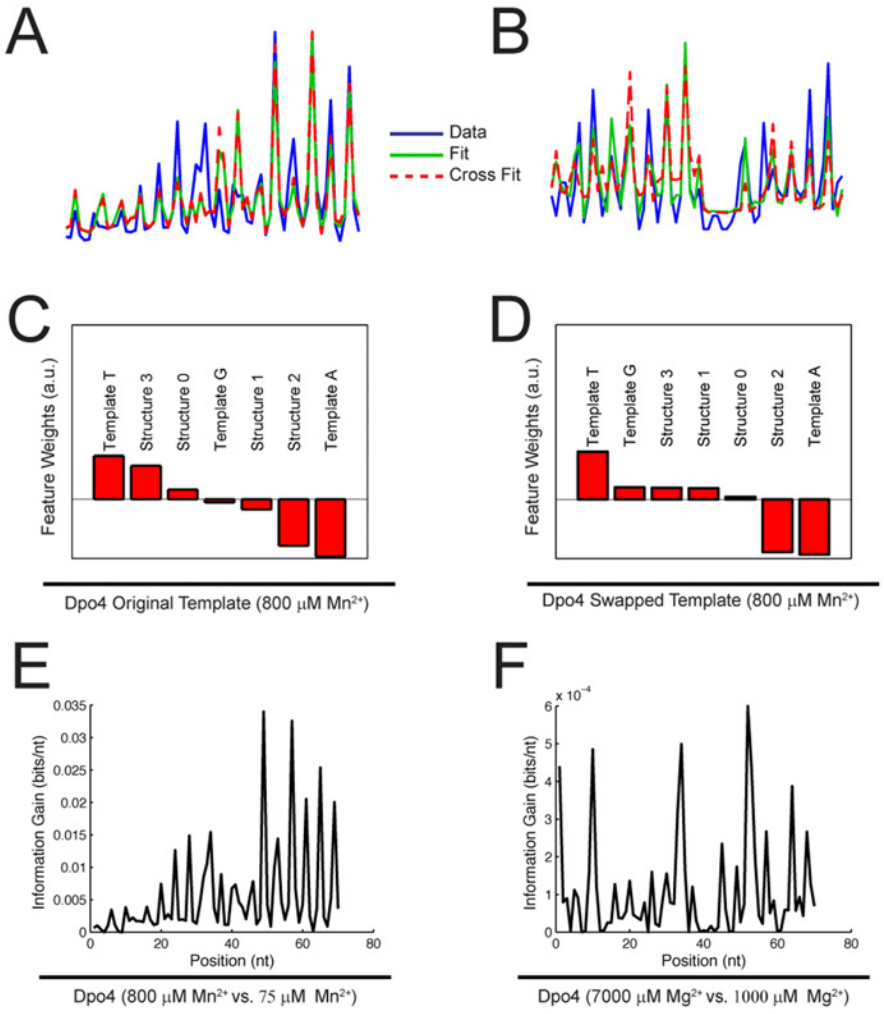

Figure 4.6: Statistical analysis of misincorporation by Dpo4. (A) Spatial dependence (un-normalized) of Dpo4 error rate at 800 uM Mn^{2+} on the original template (blue curve), and generalized linear model fits of this data set with respect to itself (green curve), and with respect to the swapped template data set (red curve). (B) Spatial dependence (un-normalized) of Dpo4 error rate at 800 uM Mn^{2+} on the swapped template (blue curve), and generalized linear model fits of this data set with respect to itself (green curve), and with respect to the original template data set (red curve). (C) Feature weights for generalized linear model fit to Dpo4 original template data. (D) Feature weights for generalized linear model fit to Dpo4 swapped template data. (E) Information gain per base as a function of template position, for discrimination between high (800 uM) and low (75 uM) Mn^{2+} by Dpo4. (F) Information gain per base as a function of template position, for discrimination between high (7000 uM) and low (1000 uM) Mg^{2+} by Dpo4.

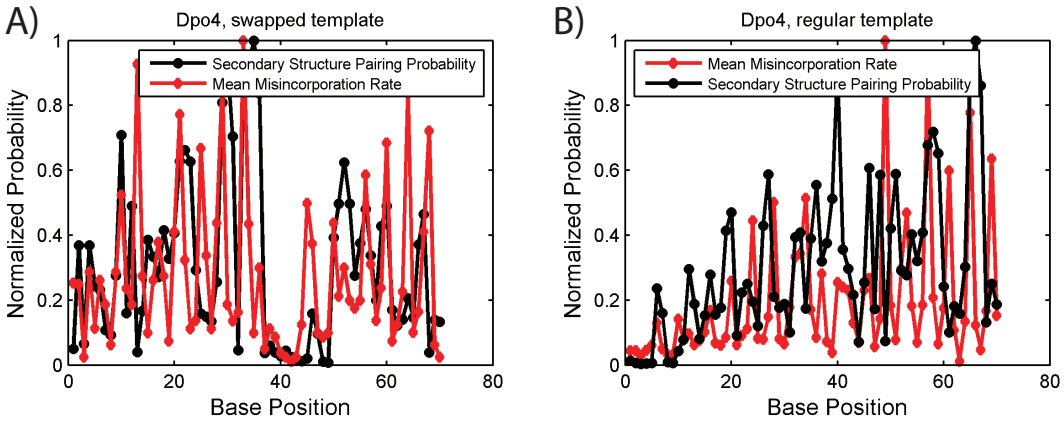

Figure 4.7: Overlay of Dpo4 misincorporation rates with NuPack-predicted secondary structure in the templates.

ysis method which does not make use of sequence alignments and which applies to both short and long sequences. Here, the filtered forward reads were compared with the perfect product sequence using a sliding window based on absolute position indexing. We counted a particular absolute base position in a particular read if the three bases before it and the three bases after it matched their respective template sequences. For such valid positions, misincorporation values were tallied with respect to the template. This method is not applicable to the first three bases and last three bases of the primer extension, and therefore the misincorporation rates at these six positions were set to zero for clarity in plotting. The results from such analyses on Dpo4 and Klenow exo- were consistent with the analyses given in the main text (Figure 4.8). This method, however, effectively removes most sequences with insertions or deletions from the analysis, and creates bias against sequences with multiple misincorporations within the sliding window.

All figures in the main text used the alignment based method.

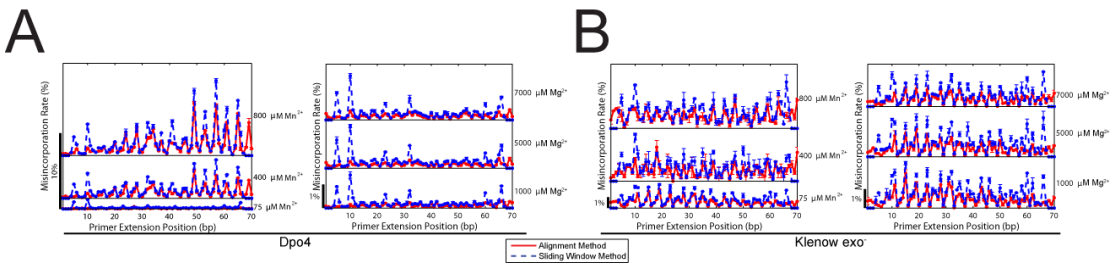

Figure 4.8: Comparison of alignment-based (main text) and sliding window-based (SI text) analyses of the spatial distribution of Dpo4 (A) and Klenow exo- (B) misincorporation rates at varying Mn^{2+} (left) and Mg^{2+} (right) concentrations.

4.2 Discussion

In this work, we have developed a method that can quantitatively map the misincorporation landscapes of error-prone polymerases as a function of environmental signals. Specifically, we quantified how the concentrations of environmental Mg^{2+}, Mn^{2+} and Ca^{2+} affect the fidelity of Dpo4 and Klenow exo-. Mn^{2+} has the strongest influence on misincorporation rates in comparison to the other cations. Our method resolves the misincorporation by spatial position and nucleotide-to-nucleotide transition. We find that, for Dpo4 and Klenow exo-, Mn^{2+} and Mg^{2+} change misincorporation rates but leave the distribution across incoming misincorporated nucleotides untouched. We have further shown that polymerase misincorporation rates exhibit sequence dependences. The development of a DNAP-based cation sensor, then, necessitates calibration of misincorporation rates at specific template positions, within specific sequence contexts, and at specific buffer conditions. The buffer-specificity of some DNAPs suggests that polymerase-based sensors might work best within controlled buffer environments, e.g. within living cells expressing ion channels, which can maintain buffer integrity, but selectively allow targeted ions to permeate. Our experiments quantify the transfer function of misincorporation from cations, through processing, all the way to DNA sequence data.

Our assay differs in important ways from the bacterial assays that have been used for the quantification of DNAP behavior[52,342,160]. Through deep sequencing we can readily observe polymerase trajec-

tories with single molecule and single base resolution while simultaneously generating large datasets, both of which are critical for achieving the comprehensive analyses necessary for establishing polymerase data encoding transfer functions. Single base pair resolution allows quantifying the template dependence of misincorporations, while single molecule resolution allows quantification of the correlation structure of misincorporations.

The method introduced here does have limitations, some of which can be mitigated. For example, the measured background noise level is likely dominated by errors introduced during the chemical synthesis of the oligonucleotides used as templates. The use of clonal isolates should dramatically lower that noise level and may prove necessary in adapting this method to the characterization of high fidelity DNAPs. In addition, GLM analysis indicates that the spatial dependence of the observed misincorporation rates may be in part due to the secondary structure of the ssDNA template. Using a nicked, double stranded template would reduce this source of variance, but would limit the applicability of the method to DNAPs with strand displacement or nick translation activity. While sophisticated molecular counting methods[605] and clonal substrates are necessary to quantify the low misincorporation rates of proofreading polymerases using sequencing[352], in this study, we have investigated error-prone polymerases, and are therefore readily able to measure strong effects despite the limitations of our method.

While we have demonstrated how a static ion concentration can be measured by a polymerase copying DNA, it would ultimately be useful to have polymerase-based sensors for time-dependent as well as static signals. To do so, it will be necessary to optimize the sensing polymerase for speed (for temporal resolution), processivity (for recording time), low pause probability (for linearity of temporal readout), total misincorporation rate (for information density) and dynamic range of misincorporation rate (for signal to noise ratio). We have shown that divalent ion concentration can be a potent, yet continuously tunable, modulator of polymerase misincorporation rates, and that such modulation can be restricted to particular template bases and base-to-base transitions. Based on its >15-fold

change in misincorporation rate over the Mn^{2+} range tested here, Dpo4 could act as a high resolution Mn^{2+} sensor. The fact that misincorporations are largely localized to certain template bases makes it possible in principle to preserve relevant features of the template (on the non-error-prone template bases) while transmitting information at the same time (on the other bases).

Advances in fields such as neuroscience impose spatial, temporal, and combinatorial challenges of unparalleled scope, associated with the three-dimensional recording and analysis of complex cellular systems. A molecular device capable of measuring and recording sub-cellular signals, which can be manufactured and delivered to target environments in a scalable fashion, may emerge as an optimal platform for biological signal recording. However, the basic principles for designing and testing such molecular recording devices in vitro have not yet been established. This study measures a static environmental signal – divalent cation concentration – by using DNA polymerases as molecular recording devices. The synthesized DNA strand can be considered as an archival medium, which stores the measured signal in the form of a misincorporation rate with respect to the known template. Indeed, the use of DNA as an information storage medium leverages the rapid improvement of sequencing technology, which is currently outpacing the Moore's law rate of improvement of microelectronic technology[106], and which promises to make DNA sequencing a preferred method for extracting data from biological and bio-molecular systems[509,734,304]. Extension of the techniques described here to time-varying signals and engineered polymerases could lead to molecular sensing technologies of unprecedented scalability.

4.3 Materials and Methods

4.3.1 Reagents

All primers were synthesized by IDT. All enzymes, dNTPs and buffers were from New England Biolabs (NEB) unless otherwise indicated.

4.3.2 Measurement of the Misincorporation Rate of Taq Polymerase

A derivative of pUC19 containing the lacZα and lacIq allele was linearized with DraII. Linearized DNA was purified and used as template in PCR reactions containing 5 U Taq DNAP, standard Taq buffer with 1.5 mM Mg^{2+}, 200 uM dNTPs (Invitrogen), $CaCl_2$ to indicated concentrations and 0.5 uM each of the primers

CLA55 (5'-AGCTTATCGATAAGCGATGCCGGGAGCAGACAAGC-3') and

CLA33 (5'-AGCTTATCGATGGCACTTTTCGGGGAAATGTGCG-3'). Reactions were cycled 30 times with 1 minute of annealing at 55C and 4.5 minutes extension at 68C. PCR products were purified using a DNA Clean and Concentrator-5 kit (Zymo Research). After determining the A260, the amplified DNA was digested at 37C for 4h with 10U ClaI, and purified. Ligation were performed using the NEB quick ligation kit with 50 ng of DNA, and directly transformed into DH5α E. coli and plated on LB-Carb containing 40ug/uL X-Gal. Blue and white colonies were counted after incubation at 37°C overnight. The error rate f was calculated as f = -ln(F)/(db)[344], where F is the fraction of white colonies, d is the number of DNA duplications and b = 349 bp is the effective target size of the 1080 bp lacI gene [19]. Error bars for the blue-white screening experiment were obtained using Poisson statistics where, for large n, the distribution is approximately Gaussian with a variance that is identical to the mean.

4.3.3 Primer Extension Assay

All reactions were performed in 96-well plates, on ice, unless otherwise noted. Annealing reactions were performed by mixing 100 nM barcoded primer N1.1.1.x (ACACTCTTTCCCTACACGACGCTCTTC-CGATCTNNNNNGATGGTCATAGCTGTTGTA), where the underlined region is the unique 5-mer barcode for each reaction, and x = 1 to 96; barcodes were composed with pairwise Levenshtein distances greater than one) with 150 nM PAGE-purified original template strand

N1.0.6 (AAAATCATAACTAAGTCAGTCAGTACGTCAGTAGCTCAGTCGA
TGGATGCAATGAATGAATGAATGAAAATAAAAATACAACAGCTATGACCAT-ddC)

or swapped template strand

N1.0.8 (CGATGGATGCAATGAATGAATGAATGAAAATAAAAAAAAATCATA
ACTAAGTCAGTCAGTACGTCAGTAGCTCAGTTACAACAGCTATGACCAT-ddC) in 1x annealing buffer (Table S3). The primer and template oligonucleotides were annealed by incubation at 95C for 5 min, followed by a -0.1C/sec ramp until reaching 25C. The PEA2 adapter dsDNA was made at the same time, by mixing N1.2.1 (P-AGATCGGAAGAGCGGTTCAGCAGGAATGCCGAG) and N1.2.2 (CTCGGCATTCCTGCTGAACCGCTCTTCCGATCT) to a final concentration of 300 nM each and annealing them via the same protocol.

Primer extensions were performed as per the manufacturer's instructions (Dpo4, Klenow exo-, Phusion) in 10 uL reactions containing 1 uL annealing reaction, 50 uM each dNTP, and 1 uL of a 1:1000 dilution of Dpo4 (Trevigen) in Dpo4 annealing buffer, 1 uL Klenow exo-, or 5 uL 2x Phusion Mastermix in HF buffer, in 1x extension buffer (Table S3). Primer extensions were initiated with the addition of divalent cation (chloride salt) to the reaction mixture and incubation at 37°C for 1h, except for Phusion, which was incubated at 95C for 10 minutes followed by 72C for 1h. After primer extension, a 10 uL mixture of divalent cations was added to each well such that the final concentration in each well was normalized to 800 uM Mn^{2+}, 7 mM Mg^{2+} and 1 mM Ca^{2+}. An automated liquid handling robot (Agilent) was used to create stocks of the divalent cations used for primer extension and salt correction in a 96-well plate format.

Ligations were performed in 10 uL volumes containing 6 uL salt-corrected primer extensions, 200U/uL T4 DNA ligase (New England Biolabs), 1 mM ATP, and 1.23 nM PEA2 adapter. Ligations reactions were incubated at 16C overnight. High-fidelity PCR of the ligation reactions was performed by adding 5 uL ligation reaction, 0.5 uM primer N1.3.1 (CAAGCAGAAGACGGCATACGAGATCG-GTCTCGGCATTCCTGCTGAACCGCTCTTCCGATCT) and 0.5 uM N1.3.2 (AATGATACGGC-

GACCACCGAGATCTACACTCTTTCCCTACACGACGCTCTTCCGATCT), in 1x HF Phusion mastermix, and incubating at 98C for 30s, followed by 30 cycles of incubation at 98C for 10 s and 72°C for 1 min, followed by a final extension at 72C for 10 in.

4.3.4 DNA Sequencing

Pooled PCR products were cleaned using a MinElute Cleanup Column (Qiagen) into 20 uL buffer EB, resulting in a final concentration of 300-400 ng/uL. Cleaned products were diluted to a nominal concentration of 12-14 nM, calculated using a droplet spectrophotometer (Qubit, Invitrogen), assuming a nominal average dsDNA length of 100 bp in the sample. The diluted sample (2 uL) was combined with 8 uL water, denatured with 10 uL NaOH and added to 980 uL HT1 buffer (Illumina). To introduce sufficient base diversity for baseline intensity correction during the sequencing run, 600 uL phiX paired-end library DNA (Illumina) was combined with 400 uL of the sample and loaded on a MiSeq (Illumina) for 150 bp paired-end sequencing. Approximately 4-5 pm of sample and at least 5 pm of phiX DNA were loaded in each sequencing run.

4.3.5 Data Analysis

Raw sequencing reads in the forward direction were filtered for the presence of the left primer binding sequence, the first 12 bp of the right adaptor sequence, and the presence of a correct barcode. Raw sequencing reads in the reverse direction were filtered for the presence of the left primer binding sequence and the barcode. Forward reads in which the sequence between the left and right adaptors did not exactly match the corresponding reverse paired end read were discarded. We also filtered out instances of a short spurious PCR product resulting from known primer dimer contamination. The forward reads thus filtered were aligned with the sequence of the theoretical error-free primer extension product (reverse complement of the template) using the BioPython function pairwise2.align.globalxs

with gap open and gap extend penalties of -10 and -2 respectively. Sequences with length greater than or equal to 70 bases between the left and right adaptors, and alignment scores greater than 60, were selected for further analysis. Misincorporations aligned to a given template position were counted towards the tally of misincorporations at that position and with respect to its corresponding template base. Misincorporation rates were measured as ratios of the number of misincorporations at a given position or template base to the total number of events counted at that position or template base. Insertions or deletions at a given position were not counted towards the misincorporation tally nor towards the tally of total events at a position. An alternative analysis method that did not rely on alignments was also used (SI Text). All data analysis was performed in Python and Matlab; code is available upon request.

4.3.6 Generalized Linear Model (GLM) Construction, Poisson Statistics and Auto-Correlations

Generalized linear models (GLMs) were constructed to predict the misincorporation probability at a given template position based on sequence context and secondary structure. To construct the variable to be fit (y), we took the filtered, aligned reads and removed those that contained insertions or deletions, resulting in a set of 70 nt long alignments to the first 70 bases of the template. We further ignored the first and last 3 bases of these alignments to enable the use of regional information on secondary structure. For each base in y, the regressor contained binary features representing the identity of the template base, a continuous feature representing the position in the template, and the regional secondary structure prediction at positions ranging from three bases before the template base to three bases after. Only three of the four template bases were used as explicit features, as the fourth is included in the bias term. The ensemble-averaged secondary structure of the original and swapped templates were calculated at 37C and standard salt conditions using NuPack software[733]. The secondary structure at a given template position was defined to be the sum of the ensemble pair probabilities of the

corresponding template base with respect to all other template bases, and was calculated as one minus the probability that the corresponding template base is unpaired, as evaluated by NuPack. The data sets used for GLM fitting corresponded to individual experimental replicates. GLM calculations were performed using the Matlab glmfit function with a binomial distribution. Excess lag-one errors were calculated by subtracting the error expected based on the misincorporation probability $(n_p/N_t)^2$, where n_p is the number of errors at a particular template position within the data set, and N_t is the total number of templates in the data set.

4.3.7 Calculation of the Shannon information Gain Per Base

Calculation of the information gain per base proceeded by a Bayesian framework. Initially equal prior probabilities were assigned to high and low cation concentrations, corresponding to one bit of missing information, i.e., $p(L) = p(H) = 1/2$, where $p(L)$ and $p(H)$ are the probabilities that the cation concentration is in the low state or high state, respectively. Observing the misincorporation rate updated the distribution. The expected information gain (conditional entropy) is

$$H_{\text{exp}} = p(I)H_{\text{incorrect}} + (1 - p(I))H_{\text{correct}}$$

where p(I) is the probability of misincorporation weighted by the prior over cation concentration (see below), and $H_{\text{incorrect}}$ and H_{correct} are conditional Shannon entropies, defined as

$$H_{\text{incorrect}} = -p(H|I)log_2(p(H|I)) - p(L|I)log_2(p(L|I))$$

and

$$H_{\text{correct}} = -p(H|C)log_2(p(H|C)) - p(L|C)log_2(p(L|C))$$

By Bayes' rule, $p(H|I) = p(I|H)p(H)/p(I)$, where $p(I|H)$ is the misincorporation rate per base

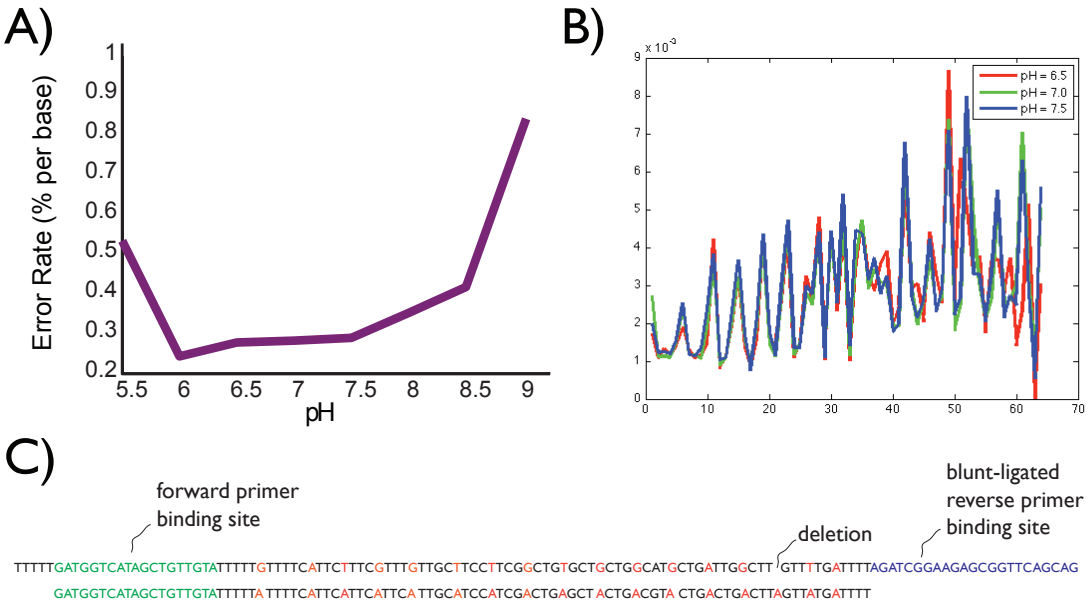

Figure 4.9: Additional sequencing results on ion dependent polymerase fidelity. A) pH dependence of Dpo4 misincorporation rate (experimental data from Daniel Martin-Alarcon, analysis joint with Brad Zamft). B) Template position dependence of the misincorporation rate of Dpo4 in several pH buffers, confirming the basic pattern observed in [735] (experimental data from Daniel Martin-Alarcon). C) Example sequencing read from misincorporation studies on polymerase *Iota*, which exhibits an exceptionally high error rate on template T bases.

at high cation concentration, as shown in Figure 4.5C. The other conditional probabilities ($p(H|C)$, $p(L|I)$, and $p(L|C)$) were calculated analogously. The misincorporation probability was then calculated through marginalization, e.g., $p(I) = p(I|H)p(H) + p(I|L)p(L)$. Inserting these expressions into the equation for expected information gain (H_{exp}) allowed for calculation of the number of bits of information gained per base.

4.4 Further experimental progress on molecular recording

We (with Brad Zamft and Noah Donoghue) also performed further experiments on molecular recording, in addition to those described in [735]. These included studies of the pH dependence of Dpo4 misincorporation and application of the sequencing-based screening system to the ultra-high error rate

polymerase *Iota*. These are illustrated in Figure 4.9. Finally, we developed a fluidic system and associated amine-epoxy surface chemistry for testing time-varying buffer conditions, as shown in Figure 4.10. Manual buffer exchanges with Dpo4 using this surface chemistry led to *preliminary* (not yet well-reproduced) data on two-bit time-coding, as shown in Figure 4.11. Due to low processivity, Dpo4 was pre-equilibrated with the first and second buffers before addition to the surface; thus, this represents only a *first premliminary step* towards true time-resolved molecular recording via error-rate modulation of a single processive enzyme as it continuously copies a template.

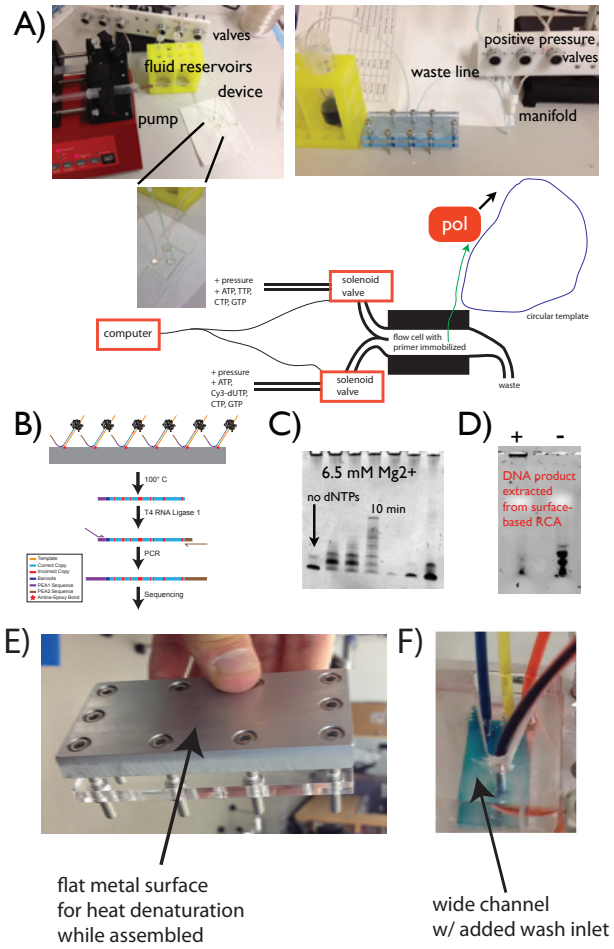

Figure 4.10: Fluidics and surface chemistry for molecular recording device prototyping. A) Microfluidic system constructed for testing time-dependent molecular recording reaction in-vitro. The DNA template is immobilized to a glass slide via amine-epoxy chemistry and reactions are conducted inside a PDMS flow cell, which is sealed to the slide with a laser-cut acrylic clamp. An automated valve system (controlled via an Arduino microcontroller) was constructed to facilitate research into time-dependent recording reactions. B) Scheme for surface-based primer extension, extraction of the product strand from the surface, and preparation for sequencing. C) Denaturing PAGE gel of products extracted from a Dpo4 surface-immobilized primer extension reaction, with varying extension times from 1 minute to 10 minutes. D) Agarose gel of products extracted from a phi29 surface-immobilized rolling circle amplification reaction, with and without template circularization by CircLigase. E) Updated design of a mechanical clamp for adhering PDMS fluidic channels to an epoxy coated, DNA functionalized glass slide. The bottom of the clamp is machined from aluminum to ensure good thermal conductivity during the heat denaturation step, used to extract the synthesized DNA from the surface. F) Updated design of the channel with a large surface area and a third input line for wash buffer.

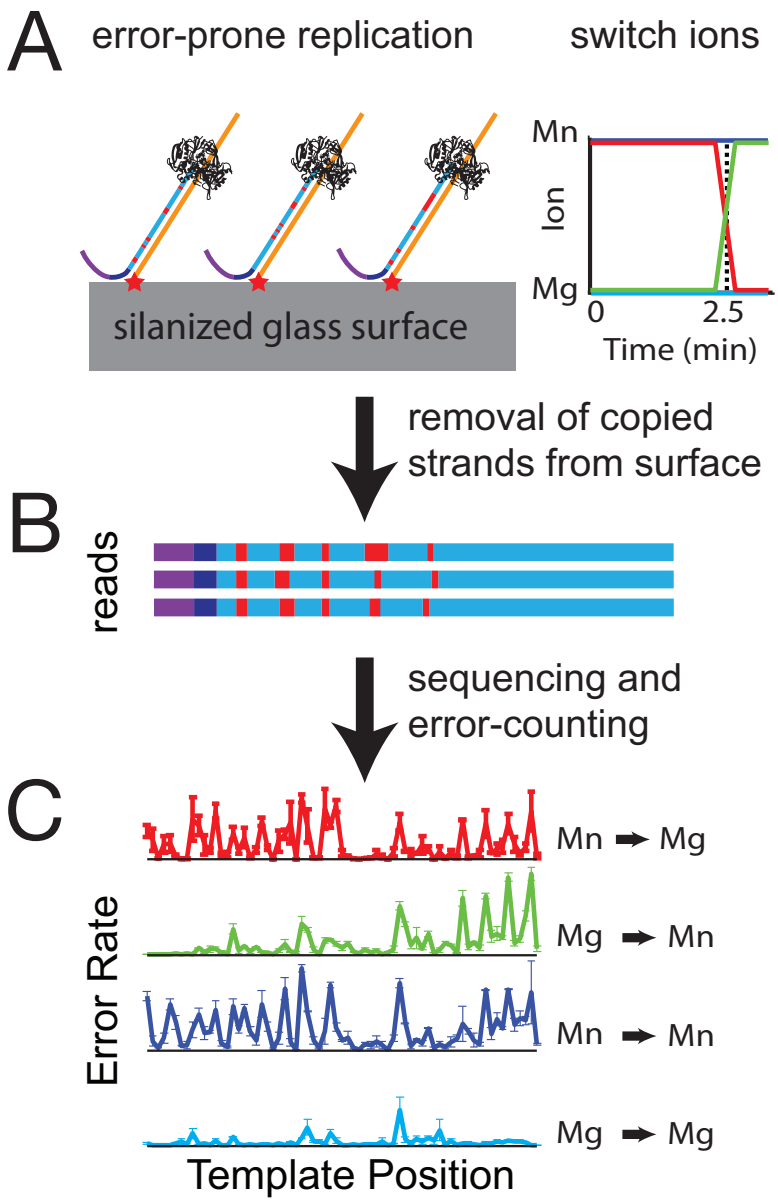

Figure 4.11: Preliminary results for manual buffer exchanges with Dpo4 on a BSA/SDS-passivated epoxy surface linked to the template DNA. DNA product was extracted and sequenced, and misincorporation rate was calculated as a function of template position. Two separate wells with surface-immobilized DNA template were subjected to the same series of buffer exchanges and the standard error of the mean misincorporation rate was used to generate error bars at each template position.

10X is easier than 10%.

Astro Teller

5

Conneconomics

We analyze the scaling and cost-performance characteristics of current and projected connectomics approaches, with reference to the potential implications of recent advances in diverse contributing fields. Three generalized strategies for dense connectivity mapping at the scale of whole mammalian brains are considered: electron microscopic axon tracing, optical imaging of combinatorial molecular markers at synapses, and bulk DNA sequencing of trans-synaptically exchanged nu-

cleic acid barcode pairs. Due to advances in parallel-beam instrumentation, whole mouse brain electron microscopic image acquisition could cost less than $100 million, with total costs presently limited by image analysis to trace axons through large image stacks. It is difficult to estimate the overall cost-performance of electron microscopic approaches because image analysis costs could fall dramatically with algorithmic improvements or large-scale crowd-sourcing. Optical microscopy at 50–100 nm isotropic resolution could potentially read combinatorially multiplexed molecular information from individual synapses, which could indicate the identifies of the pre-synaptic and post-synaptic cells without relying on axon tracing. An optical approach to whole mouse brain connectomics may therefore be achievable for less than $10 million and could be enabled by emerging technologies to sequence nucleic acids in-situ in fixed tissue via fluorescent microscopy. Strategies relying on bulk DNA sequencing, which would extract the connectome without direct imaging of the tissue, could produce a whole mouse brain connectome for $100k – $1 million or a mouse cortical connectome for $10k – $100k. Anticipated further reductions in the cost of DNA sequencing could lead to a $1000 mouse cortical connectome.

Wiring diagrams for neuronal microcircuits support efforts to reverse-engineer the brain and to identify structural contributors to neuropsychiatric pathologies[481,150,734]. Acquisition of large-scale connectivity data could, for example, help to guide efforts to simulate emergent network functions in mammalian brains[549], which are currently based on statistical extrapolations from small datasets[282,619]. Recently, the field of *connectomics* has sought to develop technologies to rapidly extract comprehensive cellular-resolution maps of synaptic connectivity[273].

Multiple toolsets could potentially support connectomics at the scale of entire mammalian brains or brain regions. These include automated electron microscopy and image analysis as well as newer techniques for DNA sequencing of cell-identifying molecular barcode tags[734]. It is unclear, however, to what degree these could be leveraged to create a scalable, integrated connectomics solution, and whether this could be done at a reasonable cost.

Here we analyze the design space for connectomics by considering the scaling and cost constraints on a range of solutions. We focus here on techniques for dense, cellular-resolution circuit mapping of individual brains: we do not consider sparse mapping (e.g., viral tracers), low-resolution mapping (e.g., diffusion MRI) or mapping based on functional measurements[470,219].

Approaches differ widely in the cost requirement for obtaining the complete connectome of an *individual mammalian brain*, such as the mouse brain, with 7.5×10^7 neurons in a volume of 420 mm^3 (a large fraction of these are in the cerebellum, roughly $3\times$ more than in cortex[278]). They also differ in the nature of the additional information which they provide, beyond the abstract cell-cell connectivity matrix.

In Sections 5.3 and 5.4, we review the existing electron microscopy approaches, as well as a recently proposed DNA sequencing approach called BOINC[734], focusing on their scalability towards the mapping of large volumes of mouse brain tissue. Finally, in Section 5.5, we discuss the prospects for connectomics solutions based on direct imaging by optical microscopy.

5.1 Challenges for connectomics

Generating microscale anatomical wiring diagrams is a major technological challenge[526]. To understand why this is the case, we begin by outlining some of the relevant structural features of neural circuits. As discussed in detail below in the context of specific methods, these features place stringent requirements on technologies for comprehensive measurement of synaptic connectivity. Depending on the method used to measure connectivity, different sets of features become critical in constraining the design space.

Packing density Neurons are packed densely in a three-dimensional jungle of wiring: there are roughly 100,000 neurons per mm^3 and 1–2 synapses per μm^3 on average inside mouse neocortex. In rat CA1 hippocampal neuropil, the spatial distribution of synapses appears to be consistent with a uni-

form random distribution on length scales above the synaptic size[466,565], with a mean synapse-synapse distance of $\sim$ 480 nm (see[565] for the measured distribution of distances). Measurements in rat layer III somatosensory cortex also suggested an approximate uniform distribution subject to the constraint that synapses cannot overlap in space[459], again with nearest-neighbor distances of $\sim$ 500 nm. If the locations of synapses are distributed uniformly, the number of synapses per cubic micron will conform approximately to a Poisson distribution, with mean density of 1–2 synapses per μm^3: 13%–37% probability of no synapses, 27%–37% one synapse, 18%–27% two synapses, 6%–18% three synapses, 1.5%–9% four synapses, 0.3%–4% five synapses and 0.05%–1% six synapses.

Spatial variability The spatial density and arrangement of synapses varies by region, cortical layer (see[89] for glutamatergic synapse density vs. layer in mouse neocortex), and so forth, although there appears to be a roughly universal number of neurons *beneath* a square of fixed area, say 1 mm^2, of the cortical surface, varying by a factor of less than 1.6 in rodents[111]. Furthermore, on some neurons, specific classes of synaptic contacts are spatially organized on the target dendrites[64,521]. Unfortunately, detailed measurements of these distributions are currently only available for a handful of brain locations.

Multiplicity There is a large variation in the *number* of synaptic contacts between any given connected *pair* of cells. In hippocampus, synaptically connected neurons are often linked by only one synapse, with higher level redundant connectivity occurring in a group of nearby neurons. In some areas of cortex there are only a handful of contacts between synaptically-paired cells[195], while in other areas there can be as many as a dozen or more, e.g., 6 ± 5 (mean $\pm$ standard deviation) among thick-tufted neurons in developing rat L5 neocortex[445]. In general these distributions are unknown. At some synapses outside cortex (e.g., the Calyx of held[276]) the effective number of "synapses" (i.e., vesicle release sites) is much higher.

Small feature sizes Relevant anatomical features of neurons are on the nanoscale, below the wavelength of light: dendritic spine necks and axons shrink in diameter down to tens of nanometers. Synapses can be as small as ~ 200 nm in diameter (including both pre- and post-synaptic compartments)[113].

Long projections Axons often travel several millimeters along complex paths, with *kilometers* of axonal wiring present in a cubic millimeter of cortex. Furthermore, at least a few cubic millimeters of reconstructed volume are likely needed to adequately define the connectivity of local cortical circuits, though smaller volumes may be sufficient to reconstruct canonical circuit patterns in other brain areas[273].

Diversity Mammalian connectomes are not identical across different individuals, so many connectomes should be mapped. Methods for statistical reconstructions of connectomes by combining partial reconstructions from multiple animals[469,467] can be useful for determining average connectomes as well as statistical variation around the average. To the greatest extent possible, however, multi-modality measurements should be integrated such that they can be simultaneously applied to each individual brain under study, rather than averaging or correlating across different brains. The ideal technique would be sufficiently low cost that many individual connectomes could be rapidly acquired. Post-hoc correlation across multiple single-brain connectomes could reveal insights at the level of mechanistic conservation: for example, there are likely connection motifs which are invariant across individuals, e.g. in the organization of cortical circuits.

Size of dataset The amount of data needed to store the abstract connectivity matrix of a mouse brain is roughly $N \cdot s \cdot \log_2(N) = 2.65 \times 10^{12}$ bits < 1 terabtye, where $N \approx 10^8$ is the number of neurons and $c \approx 10^3$ is the average number of synapses per neuron[697]. Including synaptic weights and molecular profiles has been estimated to increase this storage requirement by $< 100\times$[400].

5.2 Caveats for cost calculations

Below, we attempt to estimate the costs associated with hypothetical whole-mouse-brain connectomics projects – normalized to a three-year project – based on a variety of technology platforms. These estimates are intended as rough approximations and should not be taken literally as proposed figures for particular projects. Despite these caveats, it is of interest to explore how even crude estimates of project cost vary with changes to the technology architecture adopted, or with improvements to particular parameters, such as the speed of super-resolution optical microscopy or the number of parallel electron beams per electron microscope.

5.3 Electron microscopy (EM) connectomics

Electron microscopy is the most thoroughly developed approach for the dense reconstruction of neural circuits. Because the wavelength of an electron under 10 kV accelerating voltage is ~10 pm, imaging with electrons can (in principle) reach spatial resolutions in the sub-nanometer to nanometer range[37], more than sufficient to trace the finest morphological sub-structures of neurons. The basic strategy employed by the current EM approaches is to obtain many morphological images of thin tissue sections, segmenting those images into regions corresponding to distinct neuronal processes, and tracing individual axons from one image to another. Because axons are thin, long, and densely interspersed with other neuronal processes, tracing their entire lengths is a challenge.

5.3.1 EM data acquisition: basic properties

Beam current and bit precision The physical constraints on large-scale electron microscopy for neural circuit reconstruction were first studied in the 1980s[460], following the acquisition of the *C. elegans* connectome by electron microscopy[701]. The electron dose per pixel is one property which

constrains the resolution and speed of an imaging system. An exemplary recent connectomics study used roughly 14 electrons per nm^2 [275], or 3812 electrons per 16.5 nm $\times$ 16.5 nm pixel. Due to Poisson counting statistics, the fractional error in the estimate of the stain density in a voxel goes roughly as $1/\sqrt{N}$, where N is the number of electrons passing through the voxel [460], so the analog bit precision in that study was roughly $\log_2 \sqrt{3812} = 6$ bits at each pixel.

Merkle [460] used the number of electrons per voxel, the number of parallel electron microscopes available, and the total project time to estimate the beam current per microscope: imaging a whole human brain in 3 years at 10 nm $\times$ 10 nm $\times$ 10 nm voxel size, with 7-bit precision and 1000 parallel microscopes, would give 0.1 mA beam current, comparable with that of electron microscopes circa 1989.

TEM vs. SEM Transmission electron microscopy (TEM) involves passing electrons *through* a sample, whereas scanning electron microscopy (SEM) relies on back-scattered or secondary electrons emitted from the sample's surface. High-resolution EM analysis was originally limited to transmission electron microscopy, which necessitated the use of ultra-thin ($<$ 100 nm), grid-suspended sections to allow electron penetration through the slice. Although TEM sections cannot easily be made *thinner* than a few tens of nanometers, z-resolution can be improved by tilting the sample and performing a tomographic reconstruction [81]; only a handful of additional tilts are required if sparse reconstruction techniques are used [676]. Indeed, the first proposals for whole-mouse-brain electron microscopy circuit tracing [460] assumed a TEM tomography strategy.

Unfortunately, large-scale automation of transmission electron microscopy has been difficult in practice due to the need to isolate fragile ultra-thin sections which can be penetrated by the electron beam [269,267]. TEM is still used today, at rates approaching 10 megapixels per second using camera arrays [68], but in a recent study, $\sim$30 of $\sim$4 000 thin sections were lost in the preparation process [68]. Thus, improvements in TEM sample handling are needed to trace connectivity at whole-mouse-brain scale,

and we focus on scanning electron microscopy techniques below. Improvements in high-throughput, high-reliability automated TEM sample preparation, coupled with camera arrays[68], could make TEM viable for large-scale circuit reconstruction[81].

Maximum block size and the importance of lossless subdivision EM cannot take advantage of parallel imaging on multiple machines unless lossless subdivision of the tissue into "blocks" is performed prior to imaging: it must be possible to separately image two adjacent sub-blocks and stitch the resulting images together in software. The finest neuronal processes must be traceable from one sub-block to the other, and features localized at the block-block interface must be preserved. In one demonstrated technique for lossless subdivision[268,269], a hot diamond knife reduces the cutting stress locally and reversibly, and an oil film prevents damage due to scraping of the tissue block along the knife edge. This process appears amenable to large-scale automation.

Parallel beam instruments The speed of SEM can be increased by using multiple parallel beams in a single instrument. For example, Zeiss is developing a multi-beam SEM (mSEM) instrument with 61-fold parallelization. It is incorrect to assume, however, that the speed of a multibeam SEM scales proportional to the number of beams. Because of the limitations of electron optics and charge repulsion, the total current in each beam is typically much smaller than can be achieved in a single-beam system. A 10× speed improvement over an equivalent single-beam instrument would be a more conservative estimate, even though the system has 61 beams. Parallelization of a 40 mega-pixel per second SEM by a factor of 25 would lead to gigapixel per second rates, which appears to be a reasonable upper bound for the immediate future. More optimistically, advanced SEMs could potentially use thousands of parallel beams, and instrument costs could be reduced to the $100k regime via solid-state lithographic electron optics[269]; such systems may be a natural offshoot of the development of next-generation electron-beam lithography systems by the semiconductor industry.

Reliability and cost of sectioning Reliability of ultra-thin-sectioning is a key issue for SEM approaches. Empirically, it is currently difficult to knife-section a 300 µm × 300 µm × 300 µm block at 30 nm slice thickness, and usually takes multiple attempts; reliable sectioning becomes more difficult for larger block sizes. We highlight scenarios below where reliability of physical sectioning is likely to become the major limiting factor. Note also that at high electron doses, the mechanical properties of the block surface change in such a way to worsen the minimum section thickness and the sectioning reliability.

Diamond knives used in electron microscopy routinely perform 10k sections before incurring damage. Assuming that only 1000 sections are used per knife to keep damage rates conservatively low, and that each knife costs $2500, the cost of the knives for $420\,\mathrm{mm}^3/(1\,\mathrm{cm}^2 \times 25\,\mathrm{nm}) = 168000$ sections would be <$500k.

Another major challenge to whole brain imaging will be minimizing the material loss from vibratome section to vibratome section, and from the sub-sectioning of the brain either before or after embedding.

5.3.2 Approaches to automated SEM

Three strategies for large-scale electron-microscopy of brain tissue — SBEM, ATUM and FIB-SEM — are depicted in Figure 5.1.

Serial block face SEM (SBEM)

SBEM uses a diamond knife embedded in the SEM to serially remove an ultra-thin section of a pre-stained tissue block[464] after surface imaging, revealing the next layer to be imaged[151].

Resolution The z-resolution achievable with diamond knife sectioning is on the order of 25–30 nm, limited by the knife sharpness; note that the section itself can be destroyed in SBEM since

it is the block face that is imaged. The effective z-resolution of SBEM could be improved by using multi-energy deconvolution SEMs, allowing "virtual sections" thinner than the physical sectioning thickness of the diamond knife[76*]. SBEM also imposes a minimal lateral pixel size, since the higher electron doses associated with smaller pixels interfere with reliable physical scraping by the diamond knife when pixel densities surpass this limit[269].

Maximum block size Current implementations of SBEM are limited to tissue blocks ∼1 mm on a side, although there appears to be no block size limitation in principle[81].

Automated tape-collecting ultra-microtomy (ATUM)

ATUM[267,271] allows a block of tissue to be sliced into $>$ 25 nm ultra-thin sections which are arrayed on a tape reel for random-access imaging.

Resolution Empirically, the reliability of ATUM-SEM decreases considerably below ∼30 nm section thickness. As for SBEM, virtual sectioning techniques could potentially be used to achieve higher effective z-resolution.

Unlike SBEM, ATUM does not suffer from a minimal pixel size limit due to physical tissue damage at high electron doses, since the tissue sectioning occurs *before* imaging. This has allowed a lateral pixel size of 4 nm $\times$ 4 nm, such that a voxel size as small[†] as 4 nm $\times$ 4 nm $\times$ 25 nm appears to be possible[‡ 520].

[*] Virtual sectioning has particular application to reset sections (the first sections acquired after resetting the cutting arm of the ultra-microtome). ThruSight (FEI, Co) is a commercial application of this idea.

[†] The ATUM approach has been routinely applied to image at pixel resolutions down to 1 nm for the imaging of c-elegan neural processes; even sub-nanometer pixel resolutions are possible, but this is slow and in most cases can be considered as oversampling (Richard Schalek, personal communication).

[‡] Connectivity and synapses may be visible even with an 8–10 nm pixel size and proper staining (Richard Schalek, personal communication). In this case, imaging time and imaging cost decrease by a factor of 4. Furthermore, ATUM-based imaging has demonstrated the ability to perform multi-scale resolution (e.g., large axon tracts can be imaged at one pixel size and dwell time, while neuropil can be imaged at a smaller pixel size and dwell time); this further decreases the imaging time and cost.

Maximum block size ATUM-SEM can achieve large lateral slice sizes, e.g., 2.5 mm × 6 mm, and sufficiently-thin sectioning allows effectively lossless tracing along the axial dimension. Thus, ATUM-SEM appears to be suitable for whole-mouse-brain-scale automation[81].

Reliability Reliability of automated ultra-thin sectioning would likely be the key limiting factor for whole-mouse-brain EM imaging in this approach. One rough estimate gives success rate of 990 per thousand ATUM sections (Richard Schalek, personal communication). In addition, 10000 sections can be cut and collected for each fresh area of the knife (Richard Schalek, personal communication).

Focused Ion Beam SEM (FIB-SEM)

In FIB-SEM, a gallium ion beam, rather than a diamond knife, removes a thin layer of the tissue block by ablation[357], to expose a fresh surface for imaging.

Resolution FIB-SEM has achieved 5 nm × 5 nm × 5 nm voxel sizes[357], because it can a) tolerate large electron doses, eliminating the lateral resolution issues of SBEM and b) slice at a very fine z-resolution[269]. In fact, the z-resolution of FIB-SEM microscopy is limited by depth of electron penetration into tissue block[269], such that lower voltages and more sensitive electron detectors could in principle reduce the slice thickness even further.

Maximum block size The major limitation of FIB-SEM, which appears to be fairly fundamental, is that it can only apply to blocks at most 100 µm across along the direction of the milling beam (with an optimal size of ∼20 µm), due to the limited depth of focus within which the ion beam is thin and approximately collimated[269]. Automated FIB-SEM imaging of large volumes of brain tissue would thus involve lossless subdivision of the tissue into rectangular blocks, with one edge length of ∼20 µm and the other edges much longer: for example, blocks of dimensions ∼20 µm × 100 µm × 100 µm

might be a reasonable target.

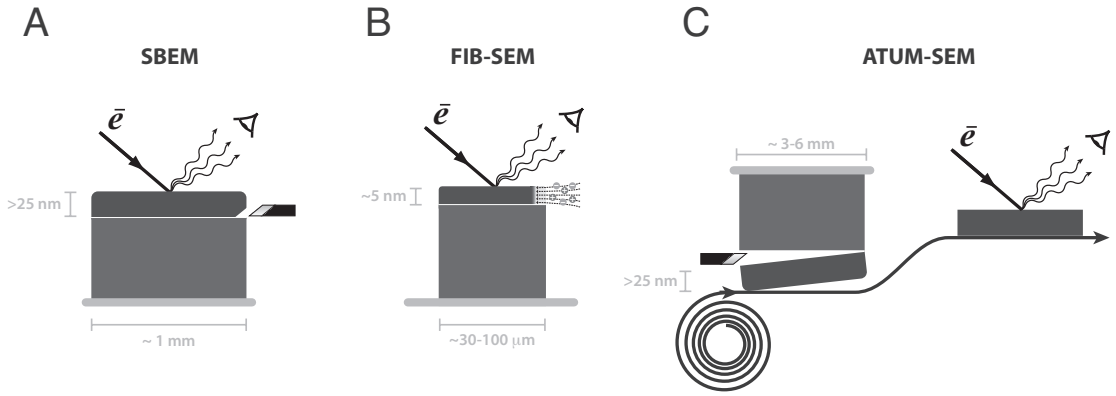

Figure 5.1: EM connectomics tools: A) Serial block face SEM (SBEM) images the top face of a pre-stained tissue block, then removes the imaged face with a diamond knife, revealing the next layer. B) Focused ion beam SEM (FIB-SEM) operates on a similar principle, but removes tissue layers by ablation with a focused beam of ions. This enables thinner sections and higher electron doses compared to SBEM, but the finite depth of focus of the ion beam limits the size of individual blocks. C) Automated tape collecting ultramicrotomy SEM (ATUM) sections tissue with a diamond knife and places the sections on a solid support, before loading samples into the electron microscope.

5.3.3 EM data acquisition: cost estimates

The image-acquisition cost for a 3-year project is given by

$$C_{3\,\text{year acq}} = \text{machine cost} \times \frac{T_{\text{imaging}}}{3\ \text{years}}$$

where T_{imaging}, the time it would take to acquire all the data on a single machine, is given by

$$T_{\text{imaging}} = \frac{1}{\text{pixels per second per beam}} \times \frac{\text{tissue volume/pixel volume}}{\text{number of parallel beams per SEM}}$$

In the below, we typically assume a machine cost of \$1M, and compute the imaging time for a 420 mm^3 brain at the highest achievable resolution on each machine type. Note that if pre-existing machines are used, or if the machine cost can be amortized over a longer duration (e.g., multiple projects),

then the effective image-acquisition cost would be lower.

SBEM

In one SBEM study, imaging a 325 μm × 325 μm × 60 μm tissue block at 16.5 nm × 16.5 nm × 25 nm voxel size took on the order of 7 weeks at ∼0.5 MHz pixel rate[82]. This is in order-of-magnitude agreement with the simplest calculation, based only on the pixel size and ∼2 μs dwell time: 2 μs × (325 μm × 325 μm × 60 μm)/(16.5 nm × 16.5 nm × 25 nm) ≈ 2 μs × 10^{12} pixels ≈ 517 hours ≈ 3 weeks. The estimated cost for a single whole mouse brain acquisition in 3 years is roughly $1B without parallelization and $20M–$100M with 60-fold parallelization. SBEM can likely be operated at lower pixel dwell times (e.g., 0.5 μs) without unacceptable loss of image quality, decreasing the cost proportionately.

ATUM

ATUM can achieve 40 megapixel per second imaging rate at 4 nm × 4 nm × 25 nm pixel size (or an effective imaging rate of 400–2400 megapixels per second with 10- to 60-fold parallelization). The estimated 3 year whole mouse brain imaging cost is then $300M and $5M–$30M.

FIB-SEM

FIB-SEM can achieve > 5 MHz pixel rate at 5 nm × 5 nm × 10 nm voxel size[269]. For a 3-year acquisition, we would need

$$\frac{1}{3\text{ years}} \times \frac{1}{5\text{ megapixels per second per beam}} \times \frac{420\text{ mm}^3}{(5\text{ nm} \times 5\text{ nm} \times 10\text{ nm per pixel})} \approx 3600\text{ beams}$$

Without parallelization, the estimated 3 year imaging cost is $3.6B, comparable to the estimate of $5B in[269] (which considers more than just imaging costs). At 60-fold parallelization, 60-360 machines would be needed, giving an estimated cost of $60-$360M.

Summary

Data *acquisition* costs for whole-mouse-brain automated EM approaches could lie in the range of $10M–$200M. These estimates do not include the costs of *developing* reliable systems for lossless tissue subdivision, thin-sectioning and sample handling.

5.3.4 EM data analysis: basic properties

A major outstanding challenge in SBEM connectomics is image analysis: reconstructing neuronal wiring from EM image stacks. Tracing thin axons over long distances is the key difficulty, as opposed to synapse detection[275,479].

Error propagation A critical issue is the reliability of the *analysis*. Each error affecting an axon can cause disproportionate damage to the reconstruction, by mis-labeling each of the hundreds of downstream synapses in the connectivity matrix. For example, if an error in an axonal trace occurs on average even once per the length of one axon, which is several mm in mouse brain, then 50% of all connections in the connectivity matrix will be incorrect. In practice, achieving one error per several mm of EM trace is challenging: in one study[465], the errors in the *manual* reconstructions from ssTEM data — i.e., the best reconstruction quality currently available, as compared with automated algorithms — were roughly 1 error per 1000 axonal slices, corresponding to roughly 1 error per ∼50–100 μm of axonal length, far below the ∼4 mm typical axonal length in mouse cortex. In that study, the slice thickness was 50 nm, so decreased error rates would be expected in the techniques studied here, which use $<$ 30 nm slice thickness.

Dependence on voxel size Currently, the ability of automated algorithms to trace the thinnest axons depends strongly on the imaging resolution. Given appropriate staining, a voxel size of

($< 10\,\text{nm}$) $\times$ ($< 10\,\text{nm}$) $\times$ ($< 10\,\text{nm}$) is sufficient to allow fully-automated axon tracing, whereas larger voxel sizes can lead to tracing ambiguities that are currently only resolvable through human-assisted image analysis. It is possible, though not proven[81], that a sufficiently small lateral pixel size — e.g., as is achievable in ATUM-SEM due to its tolerance of high electron doses, but not in SBEM — can allow for unambiguous automated neurite tracing even at relatively low z-resolutions.

Dependence on staining method The quality of EM data depends not only on the instrument resolution but also on the properties of the staining method. Staining of internal structures in axons and dendrites can lead to ambiguities in the resulting images. If only external surfaces are stained (e.g., along with a synapse stain) then even $25\,\text{nm} \times 25\,\text{nm} \times 25\,\text{nm}$ instrument resolution may be sufficient for unambiguous axon tracing in some cases. On the other hand, if many internal structures are heavily and non-specifically stained (i.e., the method produces large "blobs" of dense stain), then even $5\,\text{nm} \times 5\,\text{nm} \times 5\,\text{nm}$ instrument resolution may not be sufficient for axon tracing. Specific staining of the plasma membrane or other structures using genetically encoded contrast generators (e.g., APEX[450]) may be one option for programmable control of the staining properties. Genetically encoded contrast agents could be targeted to specific neuronal compartments, such as the axon (much as are certain ion channels)[31], in order to sparsify the scene. Reliable and uniform staining of entire mammalian brains prior to tissue sectioning is the subject of ongoing research[464].

Theoretical limits on the tracing error rate In EM tracing, the goal is to trace tube-like structures (axons) through a series of images using the fact that the tubes are hollow. The tubes are randomly oriented throughout the series of images, running perpendicular or parallel to the slice with roughly equal probabilities (in cortical neuropil). If the axon is perpendicular to the slice, then it appears as a "circle". If the axon is oriented parallel to the slice, then it appears as a "blob" of stain arising from its upper and/or lower membrane surfaces. The fundamental parameters are the largest

voxel dimension h and the smallest opening diameter d in the tubes. If two slice-parallel axons nearly overlap, and are heading in nearly the same direction, then their paths cannot be distinguished, even when using longer-range structure across multiple images or sections and even as judged by human experts. This led to a model of the frequency of such "true ambiguities"[465] per micron of axonal wires, as a function of the slice thickness h. Using the observed distribution of axon diameters $\varrho(d)$, the model predicts one expected true ambiguity per 100–1000 mm of axonal wire for 20–30 nm sections; recall that there are kilometers of axonal wire per mm^3 of tissue.

Data storage requirements Assuming 10 nm × 10 nm × 10 nm EM voxel size, there are $420\,mm^3/(10\,nm \times 10\,nm \times 10\,nm) \approx 5 \times 10^{16}$ voxels in a 420 mm^3 mouse brain. At 1 byte per pixel, this is ∼ 400 000 terabytes of EM image data, roughly the total amount of data transmitted over the internet during a 10 hour period circa 2013 (storage would cost $20M on $100 2TB hard drives).

5.3.5 EM data analysis: cost estimates

SBEM and ATUM

The standard z-resolution of SBEM and ATUM of 25–30 nm is not sufficient to allow fully-automated tracing of neuronal processes with currently available algorithms. Manual volume segmentation from SBEM image stacks by a trained human requires roughly 2 work-hours per μm^3. To get around this, Helmstaedter and colleagues[275] split the analysis pipeline into two separate stages: skeleton tracing and volume segmentation / contact detection.

For the skeleton tracing step, REdundant-Skeleton COnsensus Procedure (RESCOP)[274] is a human-assisted process for tracing the center of the axon. The software resolves disputes between users through redundancy and infers an estimate of the skeleton trace via a statistical model. A redundancy factor of 18 or 19 leads to roughly one tracing error per cell. This method achieved ∼0.0135 work-hours per

μm^3. At a labor rate of \$5 per hour, this corresponds to \$70M per mm^3; for the whole mouse brain the labor cost would be of order \$30B. To complete the analysis within 3 years using this method, assuming 2000 working hours per year, 945 000 laborers would be required.

The human-assisted skeleton tracing does not reveal synapses or detailed local morphology. This information is obtained via fully-automated volume segmentation algorithms, applied after the skeleton tracing[317,669]. The estimated volume error rate for this process is around 3%[275]. Note that this procedure currently does not reveal "ground truth" synapses as defined by the presence of a post-synaptic density (PSD) and pre-synaptic vesicles, but merely assesses the probability of connected neurons based on the pattern of contact between two cells (e.g., contact area, which is not a good predictor of actual synapses[468,275], except at very high contact areas[275]).

In an alternate workflow, segmentation can be performed automatically, followed by human proof-reading[526]. Assuming $(15\,nm)^3$ voxels, a recent review[526] estimated that current methods would require 4.5 million person years of proofreading for a whole mouse brain, similar to the $3 \cdot 945000 = 2.84$ million person years estimated above for manual skeleton tracing. Thus, either segmentation algorithms must be improved, or data quality must be improved to compensate, to allow a dramatic reduction in the need for either pre-segmentation manual skeleton tracing and/or post-segmentation manual proofreading.

Large-scale internet-based crowd-sourcing could play an important role in scaling up data analysis, since tens of thousands of users appear to be willing to participate in the process for "free"[587]. These players also collectively generate a large data-set for training machine learning algorithms[587]. Other crowd-sourcing approaches for image segmentation are also being developed[226].

Using today's tools, analysis costs would be in the tens billions of dollars for a whole mouse brain. The computational connectomics sub-field aims to reduce the analysis costs by orders of magnitude, ideally leading to full automation, and it is making progress towards this goal[339,556].

FIB-SEM

It is possible that the $(< 10\text{ nm}) \times (< 10\text{ nm}) \times (< 10\text{ nm})$ resolution of FIB-SEM will enable reliable, fully automated axon tracing and synapse identification from large volumes[269]. Automated synapse detection from FIB-SEM images has been demonstrated with error rates comparable to that of human experts (e.g., 0.92 recall at 0.89 precision)[53,380].

5.3.6 Annotation of EM connectomes

While stains have been developed to couple electron-imaging contrast to neuronal and vesicular membranes, there are few extant mechanisms to couple electron contrast to other forms of sub-cellular molecular information, such as specific genetic sequences or specific proteins. Recent attempts have been made to introduce multiplexed labeling capabilities into EM[228], as well as to create genetically encoded proteins which can serve as EM markers[450,608]. Furthermore, it may be possible to create nanoscale spatial patterns of heavy metals or other high-contrast elements which could serve as combinatorially-diverse EM labels (EM barcodes). Another option for obtaining multiplexed molecular information from a given cell body would be as follows: given the > 1000 sections that contain a single cell body, it would be possible to antibody-stain each section for a different molecular marker, and thus to assign a "molecular identity" to every EM-reconstructed cell, without requiring any single EM image to be "multi-colored". Nevertheless, EM currently lags behind optical microscopy in the ability to readily reveal biochemical information in a multiplexed fashion and in any neuronal compartment.

5.3.7 Summary

Electron microscopy imaging using serial block-face SEM (SBEM), automated tape-collection lathe ultramicrotomy (ATUM) or focused ion beam SEM (FIB-SEM) would cost hundreds of millions to billions of dollars for whole-mouse brain data acquisition using current instruments. Next-generation

parallel-beam SEMs — e.g., a 61-fold parallelized SEM under development by Zeiss — could reduce the data-acquisition costs into the range of tens of millions of dollars or below, depending on the degree and cost of parallelization.

FIB-SEM will likely allow fully-automated image analysis, due to its $<$ 10 nm z-resolution and compatibility with 5 nm in-plane resolution. However, due to its limited field of view per instrument ($\sim$20 μm along the milling axis), new instrumentation would be required to automate the sub-division of tissue into appropriate-sized blocks. Hayworth has demonstrated preliminary proof of principle that this sub-division could be achieved without information loss, to enable tracing of fine axons between blocks. SBEM and ATUM-SEM are more readily automated on the hardware side than FIB-SEM due to their compatibility with larger fields of view.

For SBEM and ATUM, which have z-sectioning limits of $\sim$25 nm, tracing of fine axons becomes more difficult for current image-segmentation software. Recent software advances, which separate skeleton-tracing (human-assisted) from subsequent volume segmentation and synapse identification (automated), have reduced the human labor requirements to roughly one work-minute per cubic micron (although current semi-automated image analysis methods mandate a staining protocol incompatible with "ground-truth" synapse identification, i.e., the presence of vesicles and PSD). At a labor rate of \$5 per hour, analysis of a whole mouse brain using this software would cost tens of billions of dollars and require nearly a million workers. Further advances in software are needed, therefore, to enable fully-automated analysis of image data generated from SBEM and ATUM. Importantly, the analysis costs could ultimately become negligible, in principle, through algorithmic advances. Also, the effective z-resolution of SBEM or ATUM could be improved through virtual sectioning.

Thus, given either a) construction of an automated tissue sub-division system for FIB-SEM or b) full software automation of SBEM or ATUM image analysis (e.g., via machine learning advances), *and* the emergence of multi-beam SEMs at a cost comparable to current single-beam SEMs, a whole mouse brain EM connectome project could be achievable for a cost of tens to hundreds of millions of dollars

and a duration of several years per mouse brain. A major advantage of EM connectomics is its ability to trace in detail the morphology and compartmental structure of neurons, which is tightly coupled to their electrochemical functions[428].

5.4 Trans-synaptic barcode pairing and bulk sequencing (BOINC)

A DNA barcode is a unique sequence of DNA used to "tag" an object of interest. Zador has suggested[734] an approach to connectomics, called Barcoding of Individual Neuronal Connections (BOINC), which leverages large numbers of DNA barcodes. First, each neuron is given a unique DNA barcode. Copies of each neuron's barcode are then exchanged with its immediate synaptic neighbors. A cell's own barcodes are then stitched together with barcodes received from its synaptic neighbors, forming a set of barcode pairs corresponding to synaptically connected neurons. Zador's original proposal suggested one potential implementation: using trans-synaptic tracer viruses (e.g., engineered pseudorabies replicons) to shuttle copies of the barcode from a given cell to its immediate pre-synaptic neighbors, whereupon a recombinase (e.g., phiC31 integrase) in the recipient cell would link donor and recipient barcodes into a single strand[734].

The barcode-pair DNA strings from all cells are extracted, pooled, amplified (i.e., creating many copies of each barcode pair) and sequenced on a bulk DNA sequencing machine, such as an Illumina HiSeq. This results in digital data specifying a set of "on" matrix elements, corresponding to barcode pairs (synaptic neighbors) which are observed, and a set of "off" matrix elements, corresponding to barcode pairs which are not observed (e.g., due to the absence of a synapse between the corresponding two neurons).

To allow "annotation" of the connectivity matrix, Zador and colleagues also suggested that additional information, encoded in nucleic acids, could be appended onto these barcode pairs, e.g., RNA sequences indicative of a cell's gene expression profile (cell type).

Note that the problem of determining the *spatial position* of each neuron is not solved by this approach, although coarse-grained positional information could be included by sectioning the tissue and appending additional, position-encoding DNA barcodes to the cell-barcode pairs extracted from each physical section, prior to bulk sequencing. The basic idea of BOINC is depicted in Figure 5.2.

Alternate molecular implementations of the same idea (e.g., which obviate the use of trans-synaptic viruses[532]) could be preferable from a practical standpoint. For example, synaptoneurosomes containing cell-specific barcode RNAs could be extracted from the tissue and their contents sequenced via a vesicle-barcoded emulsion PCR: synaptoneurosomes typically have some of the pre-synaptic and some of the post-synaptic membrane still attached and even re-sealed[680], although there would be an issue of synaptoneurosome collection efficiency in this scheme.

5.4.1 DNA barcodes

In one implementation, the DNA barcodes are contiguous strings of random nucleotides (random oligonucleotides)[685,415]. In another implementation, the barcodes correspond to an array of direct or inverted DNA sub-strings flanked by recombinase inversion sites[734,518] (e.g., with 19 nucleotide inversion sites for Rci recombinase[256,518]). The stochastic arrays could be generated in-vivo by recombinase activity, starting from a standard cassette present in all neurons. There is precedent for recombinase-based sequence diversity generation in biology: the Min system makes 240 distinct variants of its multiple-inversion site, leading to 240 different isomeric forms of a phage coat protein to evade bacterial defenses[366].

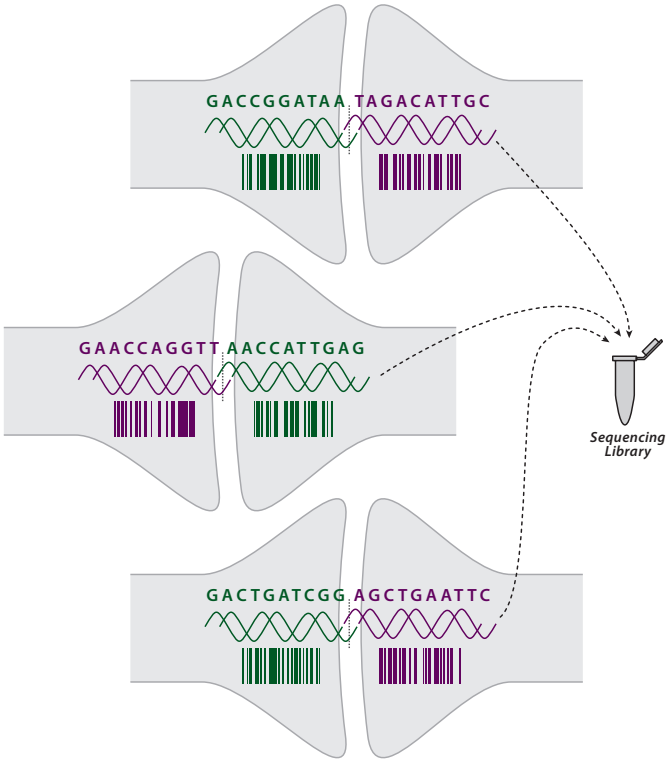

Figure 5.2: Reading out neuronal connectivity via bulk sequencing: cell-identifying nucleic acid barcodes from synaptically-neighboring cells are physically linked (e.g., via viral exchange and recombinase activity [734] or other methods [340]), and extracted from the neural tissue. The linked barcodes are then sequenced on a high-throughput DNA sequencer, such that each sequencing read corresponds to a barcode pair from a synaptically-connected pair of neurons.

In the first implementation, DNA barcodes consisting of only 20 DNA nucleotides (A, T, C or G) could in principle uniquely label $4^{20} = 10^{12}$ neurons, four orders of magnitude larger than the number of neurons in a mouse brain. When barcodes are generated (or chosen) randomly, there is a need to consider the probability of two neurons acquiring the same barcode. To uniquely identify a cell with a DNA barcode, the barcodes must be long enough to avoid the occurrence of duplicate barcodes in the population. The probability of no identical barcodes when n barcodes are chosen with replacement from a test-tube with 4^j barcodes (i.e., with all possible DNA oligonucleotides of length j) is

$$P(j, n) = n! \times \text{Binomial}(4^j, n)/(4^j)^n$$

where n is the size of the cell population and j is the DNA barcode length in nucleotides[457].

For $n = 7.5 \times 10^7$ neurons and $j = 31$ base-long barcodes, the probability of a duplication $1 - P(j, n) < 0.001$ (the per-neuron probability of duplication is then roughly 10^{-11}). This corresponds to a total barcode population size of $4^{31} \approx 5 \times 10^{18}$.

For the case of recombinase inversion barcodes, the number of barcodes generated from k segments is $k! \times 2^k$, as long as the recombinase inverts but only rarely excises on the relevant timescales[734,696,518]. To achieve a similar probability of barcode duplication, only $k \approx 16$ distinguishable segments are needed.

There are many other strategies to create cell-identifying barcodes besides the two just mentioned; the diverse mechanisms involved in generation of antibody diversity by the immune system provide a range of examples. Indeed, somatic (VDJ) recombination has been used as a form of in-vivo barcoding for tracing of lymphocyte lineages in the mouse[220].

Error sources PCR amplification and sequencing can introduce errors which would transmute one barcode into another. Fortunately, the recombinase-based barcode generation strategy leads to barcodes that are highly orthogonal at the sequence level (large minimal pairwise edit distance be-

tween barcodes, compared to the mutation probability), and synthetic barcode libraries introduced via viral transduction could be designed to be highly orthogonal. On the other hand, short barcodes strings which are generated stochastically in all cells by other methods will not necessarily be highly orthogonal.

Illumina paired-end sequencing can achieve error rates of roughly $p = 0.01^2 = 10^{-4}$ per base. Assuming a 100 bp template, the probability of two errors is then $p^2 \cdot \text{Binomial}(100, 2) = 5 \cdot 10^{-5}$. The error rate per cycle of PCR is much lower due to the high fidelities of proofreading polymerases: $f = 5 \cdot 10^{-7}$ per base for Pfusion[352]. The fraction of strands with ≥ 1 polymerase-induced error after d cycles of PCR on a template of length b nucleotides is then $F(\geq 1) = 1 - e^{-b \cdot f \cdot d} = 0.00125$[344] for $d = 25$ cycles and $b = 100$ nucleotides. On the other hand, in complex template libraries, errors due to mis-priming and chimeric products can occur at rates of 5% or higher. It is possible to reduce the effective PCR and sequencer error rates using "digital" sequencing methods like[352,605], which employ pre-amplification template barcoding and redundant sequencing to factor out these error sources.

Failure to capture any barcode pair corresponding to a given connection, leading to a false negative (missed connection) in the connectivity matrix, will likely be the dominant source of error in most implementations of BOINC. With highly orthogonal barcode sequences, false-positives due to sequencing errors can be minimized. Therefore, it is likely possible to implement BOINC in a regime where almost all errors are false-negatives, in contrast to the electron microscopic axon tracing approaches which are quite vulnerable to false-positives[734].

5.4.2 High-throughput DNA sequencing

The cost for a BOINC connectome is $C_{\text{BOINC}} = c \cdot r \cdot N_{\text{synapses}}$ where c is the cost per sequencing read, r is the number of sequencing reads per synapse and N_{synapses} is the number of synapses in the tissue under study. The fraction of un-sampled synapses is $f_{\text{unsampled}} = e^{-r}$[734] so that $1 - e^{-10} = 99.995\%$ of synapses are sampled at $r = 10$ and 95% of synapses are sampled at $r = 3$. Because many pairs

of neurons are connected by several synapses, the fraction of un-sampled connections (synaptically linked cell pairs) will be less than the fraction of un-sampled synapses.

The mouse brain contains roughly $N_{\text{synapses}} = 10^{11}$ synapses: an average of 10^3 synapses per neuron gives $N_{\text{synapses}} = 7.5 \times 10^{10}$, whereas an approximate average spatial density of 1 synapse per μm^3 gives $N_{\text{synapses}} = 4.2 \times 10^{11}$. Hence 10^{11}–10^{12} sequencing reads are required per mouse connectome, depending on the redundancy factor r.

With current sequencing technology, running 3 lanes of an Illumina HiSeq 2500 produces $> 10^9$ reads (of up to 100 bp each) in about 10 days for a cost of a few thousand dollars. Roughly 100 HiSeq runs would be required for a full mouse connectome, for a cost of a few hundred thousand dollars. An existing high-throughput genomics facility (with $>$ 50 HiSeq machines) could sequence a mouse connectome in 1-2 months.

The cost per base-pair (bp) of DNA sequencing has been decreasing rapidly: 2 bp per dollar in 2004, 10^6 bp per dollar in 2009 and 10^7 bp per dollar in 2011 [106,734]. The "$1000 human genome" corresponds to $\$1000/(3 \cdot 10^9 \text{ bp} \cdot 40\times) = \$10^{-8}$ per bp, assuming 40× coverage. At these rates, the cost per 100 bp read is $\$10^{-6}$. Thus the minimum cost at these rates is about $\$10^{-6}$/synapse, or about $100k for 10^{11} synapses. Three-fold and ten-fold oversampling ($r = 3$ or $r = 10$) raise the cost to $300k and $1M per whole mouse brain, respectively. Corresponding costs for the mouse cortex alone, which contains perhaps 10% of all synapses, range from $10k to $100k.

If these trends continue, it is not unreasonable to imagine that sequencing costs for a mouse brain connectome could drop by a further factor of 10 or more in the foreseeable future. At that point other expenses, including mouse and DNA processing costs, will dominate. Note that we have not included the cost of the bulk sequencing machines in this calculation: we are assuming that existing machines are used, e.g., at an existing genomics facility.

5.4.3 Annotation of BOINC connectomes

At 100–200 bp, each sequencing read would have enough room to include a minimal amount of transcriptomic information, in addition to just the connectivity matrix. This could take the form of RNA transcripts attached to the barcodes via RNA trans-splicing. Quantitating the relative proportions of just a few transcripts could be useful: for example, GAD67 and NeuN can be used to identify inhibitory neurons[461]. Sequencing and abundance-counting of a few dozen transcripts could be sufficient to identify known neurobiologically relevant cell types: PV, SOM and VIP to identify the major classes of interneurons, for instance, and DAT, CHAT and others to identify major classes of neurotransmitter-secreting cells. Reliably implementing such trans-splicing mechanisms may be difficult in practice, however, and the method does not scale to capture full transcriptomes. As an alternative, BOINC connectomes could be annotated with transcriptional information via cell-specific barcoding of ribosomes[532].

It is also possible that relative connection strength annotations could be incorporated into BOINC by counting the number of recovered barcode pairs corresponding to any given pair of cells. In many potential implementations of BOINC, the number of barcode pairs recovered from a given cell pair would scale approximately linearly with the total area of synaptic contact between the cells, which may be correlated with connection strength[371,187,731], although the precise extent to which this relation holds is not known and some potentially complicating factors have been identified[523]. Variability in the barcode pair collection efficiency across different cells could confound such measurements, however, and total contact area is likely not a perfect indicator of connection strength.

While BOINC can also be annotated with coarse-grained positional information, its major limitation is that it does not reveal the precise spatial position or morphology of each cell. Optical microscopy techniques incorporating BOINC barcodes could potentially ameliorate this, as discussed below.

5.5 Direct optical microscopy for connectomics

An optical microscopy approach to connectomics would be powerful, in principle, in that it could allow integration with a wide range of other biochemical measurements that are accessible through modern light microscopy, e.g, Fluorescent In-Situ Hybridization (FISH)[118,96] or serial histology[463,462]. It is widely believed, however, that electron microscopy is the only approach which can allow acquisition of connectomes by direct imaging. Indeed, there can be as many 10-40 neurites per diffraction-limited optical resolution volume[466], which creates severe difficulties with direct optical tracing of axons, even when neurites are tagged with distinct sets of fluorescent proteins through random genetic recombination (BrainBow)[410,321,95]. Nevertheless, there may be novel strategies which can work around this limitation.

5.5.1 Observing synapses vs. tracing axons

Because of the comparative sparseness — at 1-2 synapses per μm^3 — of synapses in 3D space, optical connectomics approaches could succeed by restricting their attention *only* to the synapses themselves[466]. Rather than directly tracing the paths of axons and dendrites through a series of images, cell-identifying molecules could be physically trafficked — via endogenous cellular processes — to the pre-synaptic and post-synaptic compartments[350,702,725]. Then, *observations of the synapses alone* could reveal the identities and/or properties of the pre-synaptic and post-synaptic cells.

Resolution requirement to resolve neighboring synapses Diffraction-limited 3D imaging ($\lambda/2\text{NA} \approx 200\,\text{nm}$ xy-resolution and $2\lambda/\text{NA}^2 \approx 533\,\text{nm}$ z-resolution for numerical aperture $\text{NA} = 1.5$ and wavelength $\lambda = 600\,\text{nm}$) is not sufficient to directly resolve a synapse from its neighboring synapses[466]. Simulations of synapse-labeled fluorescence microscopy based on EM reconstructed rat hippocampal neuropil have suggested, however, that $<$ 100 nm isotropic resolution

is sufficient to resolve >90% of synapses from their nearest neighbors[466]. These simulations assumed that fluorescence was limited to the pre-synaptic and post-synaptic densities (PSDs), as opposed to the entire axonal bouton or spine head.

Figure 5.3 shows a conservative estimate of the resolvability of nearest-neighbor synapses based on the dataset from[466], in which synapses are present at an average density of 1.85 per μm^3. A strict criterion for resolvability is applied: two synapses are considered to be non-resolved if any of their labeled points are separated by a distance smaller than the isotropic resolution. Since synapses are extended objects, it is often possible to separate them based on shape, even if they are not resolvable according to the strict criterion; the strict criterion gives a sufficient but not necessary condition for resolvability.

Labeling only of the PSDs allows resolution of >90% of synapses at isotropic resolution $<$ 125 nm, whereas labeling of the entire pre-synaptic and post-synaptic compartments gave poor performance even at $<$ 50 nm isotropic resolution. The poor performance for whole-compartment labeling is not surprising: synaptic boutons and spine heads often directly contact other nearby boutons and spine heads, leading to high confusion rates between nearby synaptic puncta, in the whole-compartment labeling scenario, even if the imaging resolution were to approach to zero. Therefore, to optically resolve individual synapses, it is essential that the labeling be highly specific to the PSDs, as could perhaps be achieved with a protein-tagging strategy.

Achieving the required resolution Experimentally, confocal microscopy in $<$ 100 nm thin sections and at roughly 200 nm diffraction-limited *xy* resolution — in the context of Array Tomography — appears to optically resolve most if not all synapses[463,462,356] via antibody staining of synaptic proteins such as synapsin. Isolated fluorescent puncta are observed, in numbers similar to those expected in the tissue based on EM measurements of synapse density[462]. In one recent study, the fluorescent puncta have been attributed to individual synapses[541] by comparison with EM imaging of the same serial sections.

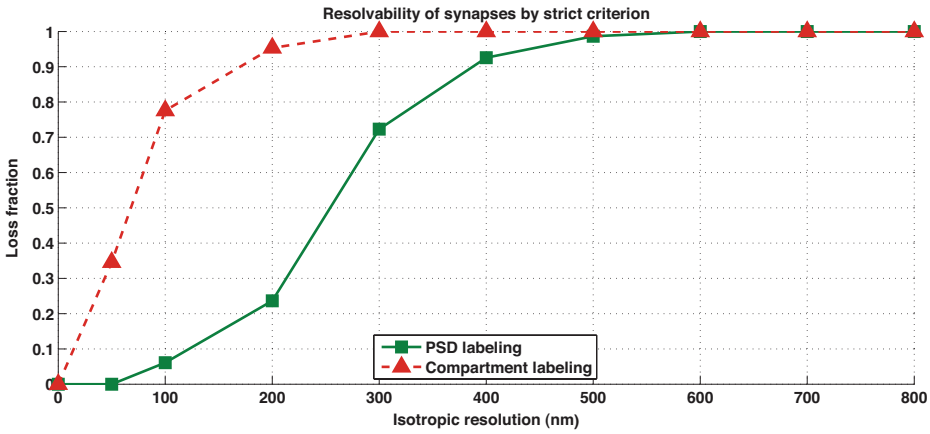

Figure 5.3: Optical resolution requirements for resolving nearest-neighbor synapses. The fraction of non-resolved synapses as a function of isotropic resolution for PSD labeling (green) and whole-compartment labeling (red), based on the dataset and analysis from [466]. A pair of synapses is considered unresolved here if and only if they contain labeled points separated by less than the isotropic resolution.

Advances in microscopy could minimize the need for ultra-thin 2D sections. The dual-objective imaging technique I^5M achieves 100 nm resolution axially and 200 nm resolution laterally in a wide-field mode [253], and multi-photon 4Pi-confocal microscopy gives similar axial resolution [177] in a parallelized beam-scanning mode.

A 10–100× improvement to the speed of linear structured illumination microscopy (SIM) has recently been reported [726]. Linear SIM exceeds the diffraction-limited resolution by a factor of 2 along all three axes, with commercial systems achieving 130 nm × 130 nm × 270 nm resolution voxels. Further improvement to the *axial* resolution of SIM could allow it to resolve most synapses. For example, I^5S two-objective detection [590] is a form of SIM with isotropic 100 nm resolution.

Other techniques offer even deeper levels of optical super-resolution. Nonlinear SIM – SIM performed at illumination intensities high enough to saturate the fluorophore – can improve resolution beyond that of linear SIM [254], and parallelized nanoscopies based on point-spread function engineering have been demonstrated [115]. Stochastic Optical Reconstruction Microscopy (STORM) achieves 30 nm × 30 nm × 50 nm voxel size in 3D [139], but at its current volume throughput of roughly 15 $\mu m^3/s$,

STORM of an entire mouse brain would take nearly 1000 imaging years.

Molecular methods could be used to increase the effective spatial resolution, relative to that of any given optical setup, by "stratifying" the observation of different synapses into different imaging frames[396]. This would increase imaging time proportionately. For a 2× cost in the imaging time, molecular stratification could also resolve the pre-synaptic and post-synaptic compartments of a given synapse: first activate pre-synaptic but not post-synaptic dyes, then switch to a new camera frame and reverse the activation pattern.

5.5.2 Strategies for optical connectomics

Fluorescent protein-based synaptic BrainBow A "synaptic BrainBow" strategy[466] has been proposed, in which each cell would express a distinct *combination* of fluorescent proteins, which would be targeted to the pre-synaptic and post-synaptic compartments. Then, by observing the spectrum of colors at each synapse, the corresponding pre-synaptic and post-synaptic cells could be identified, even if the pre-synaptic and post-synaptic compartments of a given synapse are not optically resolvable from one another. This could be combined with observation of the corresponding fluorescent protein color patterns expressed in the nuclei, thus labeling the locations of the corresponding somas.

This method could have favorable properties with respect to resolution of neighboring synapses, outperforming the conservative resolution requirements in Figure 5.3. Synaptic BrainBow relies on tagging synapses based on co-localization (spatial correlation) of fluorescence from pre-synaptic and post-synaptic markers: even if the fluorophores are not precisely localized to the pre-synaptic and post-synaptic densities, their emissions co-localize only over the synaptic cleft itself. Therefore, detection based on fluorescence co-localization can perform better than directly resolving single-colored synaptic puncta.

Unfortunately, the originally-proposed form of synaptic BrainBow[466] does not scale to entire mouse

brains because of the limited color palette of available fluorescent proteins: $2 \cdot \log_2(10^8) = 54$ spectrally distinguishable fluorophores would be required[466].

Fluorescent In-Situ Sequencing (FISSEQ) for 4^N-"color" synaptic labeling Novel methods could potentially allow variants of the synaptic BrainBow strategy to scale to mammalian systems. An alternative method could leverage Fluorescent In-Situ Sequencing (FISSEQ)[396,340], a recently-developed method for sequencing of DNA or RNA by optical microscopy in the context of intact tissue slices. In effect, FISSEQ constitutes a form of fluorescent microscopy in which there are 4^N distinguishable labels, corresponding to the 4^N possible nucleotide sequences of a DNA molecule of length N nucleotides. By leveraging FISSEQ, it may therefore be possible to create a 4^N-"color" variant of the synaptic BrainBow strategy, which would scale readily to whole mouse brains, despite using only four *actual* spectrally distinguishable fluorophores. In one possible implementation, cell-identifying RNA barcodes (similar to those used in BOINC) could be targeted to the pre-synaptic and post-synaptic densities, and their nucleotide sequences could be read out by fluorescent microscopy in-situ.

If the fluorescent sequencing frame rate of an Illumina HiSeq machine[§] were directly translated to in situ sequencing of 100 nm thick tissue slices in a diffraction-limited microscope, similar to the setup used in Array Tomography[463,462], the imaging time[¶] and imaging cost for a 3-year mouse brain

[§]Illumina machines can achieve cluster densities on the sequencing flow cell (essentially a glass microscope slide) of 1,000,000 clusters per mm^2, similar to the *areal* density of synapses in a 0.5–1 µm thick tissue section. Given that a HiSeq run takes roughly 250 hours (11 days) and generates 300 billion bases of sequence (e.g., 3 billion 100 bp reads), the time to sequence a 1 cm^2 area is

$$T_{\text{Illumina}} = 250 \text{ hours}/(3 \cdot 10^9 \text{ reads}) \times (10^8 \text{ clusters/cm}^2) \times (1 \text{ read per cluster}) = 8.3 \text{ hours}$$

[¶]For comparison, whole mouse brain fluorescence Micro-Optical Sectioning Tomography (fMOST) at 0.6 µm × 0.8 µm × 1 µm *xyz* voxel size took 19 days[242,737,508,401,117,119]. This is broadly consistent with the estimate given here for whole mouse brain FISSEQ at the Illumina scan rate and Array Tomography slice thickness: using 100 nm rather than 1 µm sections gives a factor of 10 relative to fMOST, and the 30 cycles of FISSEQ give an additional factor of 30, leading to 15 imaging years for whole mouse brain at the effective throughput of fMOST.

connectome would be

$$\frac{8.3 \text{ hours}}{100 \text{ nm} \times 1 \text{ cm} \times 1 \text{ cm slice}} \times 42000 \text{ slices} = 40 \text{ years}$$

and $13M respectively, assuming $1M per Illumina-rate machine.

5.6 Technology development pathways

These approaches could be validated in smaller brains. For example, the *Drosophila* brain, with 135k neurons, is roughly 1000× smaller than the mouse brain. In the electron microscopy approaches, only a few microscopes would be required for *Drosophila*, although image analysis would still pose significant challenges.

For BOINC, a single 11 day run on a HiSeq produces $> 10^9$ reads, more than sufficient for a *Drosophila* connectome (e.g., 10^8 synapses $\times\ r = 10$ reads per synapse). Reads of length 100 bp could include two 20-base barcodes, to uniquely label all neurons in the fly, as well as additional barcodes to provide spatial information. Indexing 10 sections along the x, y and z axes – forming blocks of $< 100\,\mu$m edge length – would require only $\log_4(10^3) = 5$ additional nucleotides, or < 10 additional nucleotides for a highly orthogonal set.

For an optical microscopy approach based on in-situ sequencing of synapse-localized RNA barcodes, roughly 5000 z-sections of 75 nm thickness and 400 μm × 1000 μm xy cross-section would be sufficient to cover the entire *Drosophila* brain. The totality of these sections would fit on a single standard microscope slide. If a 4-color 2D saturated SIM [254] image at 50 nm xy resolution takes 1 s to acquire and comprises a 50 μm × 50 μm field of view, then the time to image all the slices from a single fly is roughly 9 days. This is multiplied by a factor of 20 to account for 20 FISSEQ cycles. Therefore, ultra-thin-sectioning 2D SIM FISSEQ of an entire Drosophila brain at 50–100 nm × 50–100 nm × 75 nm resolution – likely sufficient to resolve nearly all synapses – could be performed in $<$ 6 months on a

single automated SIM microscope.

Once validated in a smaller model organism, extension to mammalian systems could be straightforward, although different model systems pose different obstacles for genetic engineering tasks like whole brain cellular-resolution barcoding. In addition, technologies like bulk EM staining may need to be adapted[464] to larger volumes. Due to its small brain size, with only a few million cortical neurons[489], the Etruscan shrew may be a desirable early target.

5.7 Summary

Several approaches for whole-mouse-brain connectomics may be nearly within reach for roughly $100M–$200M in a three-year project. For electron microscopy approaches, this would require dramatic improvements in the speed and accuracy of computerized axon tracing. Improvements to the reliability and automation of electron microscopy sample handling would also be essential.

Approaches leveraging a new "exponential resource" — nucleic acid sequence-space — appear to have the potential to further reduce the cost by a factor of 10–100 or more. For example, BOINC[734], a set of approaches based on bulk sequencing of nucleic acid barcodes that have been exchanged across the synaptic cleft and physically paired into a single sequencing read, could potentially obtain a mouse connectome for under $1M at today's sequencing costs. Further cost reductions are anticipated given the exponential improvement of DNA sequencing technology[106].

More speculatively, the ability to measure combinatorially-multiplexed molecular information (the 4^N possible RNA sequences of length N) in situ via optical microscopy, and to localize this readout specifically to synapses, could enable optical microscopy to directly acquire connectomes from fixed tissue samples. This approach could be feasible in the $10M range via a suitable combination of fast super-resolution microscopy[726,115,254], physical and/or optical thin-sectioning microscopy[463,462,117,485,590] and molecular stratification techniques.

The development of a whole mammalian brain connectomics capability will be a significant engineering challenge, regardless of the technology platform(s) adopted. Even once the component technologies are developed, there will be a need to integrate components into an automated pipeline for connectome acquisition. This is most likely to take place if technological innovations enabling significant cost reductions are introduced as early as possible.

Unfortunately, nature seems unaware of our intellectual need for convenience and unity, and very often takes delight in complication and diversity.

Santiago Ramón y Cajal

6

Rosetta Brain

We propose a neural connectomics strategy called Fluorescent In-Situ Sequencing of Barcoded Individual Neuronal Connections (FISSEQ-BOINC), leveraging fluorescent in situ nucleic acid sequencing in fixed tissue (FISSEQ)[396,340]. FISSEQ-BOINC exhibits different properties from BOINC[734,532], which relies on bulk nucleic acid sequencing. FISSEQ-BOINC could become a scalable approach for mapping whole-mammalian-brain connectomes with rich molecular annotations.

Scaling connectomics to whole mammalian brains is a challenge: the mouse brain has roughly 7.5×10^7 neurons and $> 10^{11}$ synapses in a volume of 420 mm^3, with kilometers of neuronal wiring passing through any cubic millimeter of tissue, and relevant anatomical features on the scale of < 100 nm [433]. We recently analyzed the design space for connectomics by studying the cost and scaling constraints on electron microscopy circuit tracing (EM) and bulk DNA sequencing of cell-identifying DNA barcode tag-pairs (BOINC) [734,433,532,518]. We also suggested using optical microscopy to map connectomes [433,122].

Here we elaborate on the potential of the optical approach, proposing a strategy called Fluorescent In-Situ Sequencing of Barcoded Individual Neuronal Connections (FISSEQ-BOINC), leveraging fluorescent in-situ nucleic acid sequencing (FISSEQ) [396,340]. FISSEQ-BOINC could determine the synaptic connectivity matrix, soma positions, and synapse positions, as well as diverse molecular annotations for cells and synapses.

In Section 6.1, we describe FISSEQ and propose FISSEQ-BOINC. In Section 6.3, we detail preliminary specifications for "Rosetta Brain" datasets – comprising joint, co-registered measurements of many cellular and molecular properties of a single brain – and explain how FISSEQ-BOINC could potentially meet them.

6.1 In situ sequencing of co-localized barcodes at synapses

Fluorescent in situ sequencing (FISSEQ) [396,340] is a method for sequencing DNA or RNA molecules via fluorescent microscopy, in the context of intact, fixed tissue slices. In FISSEQ, a series of biochemical processing steps, such as DNA ligations or single-base DNA polymerase extensions, are performed on a block of fixed tissue, interlaced with fluorescent imaging steps. Here we illustrate the case in which DNA polymerase extension is used – this is referred to as "sequencing by synthesis", because a copy of the *sequenced* strand is *synthesized* by the polymerase. The process is *conceptually* identical to the mechanism of fluorescent sequencing by synthesis in a commercial bulk DNA sequencing

machine[600], except that it is performed in fixed tissue.

Each DNA or RNA molecule in the sample is first "amplified" (i.e., copied) in-situ[471] via rolling-circle amplification[411] to create a localized "rolling circle colony" (rolony) consisting of identical copies of the parent* molecule[170]. A series of biochemical steps is then carried out. In the k^{th} cycle, a fluorescent tag is introduced, the color of which corresponds to the identity of the k^{th} base along the rolony's parent DNA strand. The system is then "paused" in this state for imaging. The entire sample can be imaged in each cycle. The fluorescent tags are then cleaved and washed away, and the next cycle is initiated. Each rolony – corresponding to a single "parent" DNA or RNA molecule in the tissue – thus appears, across a series of fluorescent images, as a localized "spot" with a sequence of colors corresponding to the nucleotide sequence of the parent molecule. The nucleotide sequence of each DNA or RNA molecule is thus read out in-situ via fluorescent microscopy.

The net result of this process is a form of fluorescent microscopy in which there are 4^N distinguishable "colors" or "labels", corresponding to the 4^N possible nucleotide sequences of a DNA molecule of length N nucleotides. Indeed, the FISSEQ-BOINC strategy for connectomics, presented below, can be roughly conceived as a "4^N-color synaptic BrainBow"[433,466,467,410,321,95], where N is the number of bases sequenced.

FISSEQ-BOINC In FISSEQ-BOINC, cell-identifying RNA barcodes[518,734,239,532,415] are targeted to the pre-synaptic and post-synaptic membranes, and FISSEQ is used to optically resolve and sequence the pre-synaptic and post-synaptic barcodes at a large fraction of synapses, thereby identifying connected pairs of cells in-situ. The idea of FISSEQ-BOINC is shown in Figure 6.1, and Supplemental Note 6.5.1 describes possible strategies for targeting nucleic acid barcodes to the pre-synaptic and post-synaptic membranes.

The key challenges for FISSEQ-BOINC are fourfold:

*In the case of RNA FISSEQ, a reverse transcriptase first creates a cDNA copy, which is then circularized and amplified to generate a local DNA rolony.

1) Biochemical cycling: the large number of biochemical and imaging cycles required, e.g., at least 30 images to in situ sequence a 30-base cell-identifying barcode

2) Resolution of distinct synapses: the need to optically resolve a given synapse from nearby synapses, which will require sub-diffraction-limited optical microscopy and/or molecular stratification if *most or all* synaptic contacts are to be observed (whereas synapses from a sparse subset of neurons are routinely resolved with diffraction-limited optics)

3) Resolution of pre-synaptic from post-synaptic barcodes: the need to distinguish barcodes on the pre-synaptic and post-synaptic sides of a synapse, despite their close apposition across the synaptic cleft[139], which will require further targeted resolution enhancements

4) Restriction of FISSEQ to synapses: barcode RNAs localized in axons or dendrites would often co-inhabit resolution voxels with pre-synaptic and post-synaptic barcodes, implying a need either for precise targeting of barcodes *only* to synapses (and nuclei), or for restriction of the FISSEQ biochemistry itself only to synapses – optical resolution considerations[433,466] further suggest that FISSEQ signal should be restricted as closely as possible to the synaptic cleft, rather than filling the entire pre-synaptic and post-synaptic compartments, i.e., the spine heads and axonal boutons

We next treat each of these challenges in turn.

6.1.1 Biochemical cycling

Cycle time Current FISSEQ biochemistry steps – based on sequencing by ligation – take 2.5 hours per base, but using Illumina-type sequencing chemistries – based on sequencing by synthesis – this can be reduced to 30 minutes per base. A variety of alternative chemistries have been developed for fast cyclic sequencing by synthesis in polymerase colonies[121].

Reagent cost Biochemical reagent costs are negligible compared to imaging costs (see below). Fluorescent ligation probes are the cost-limiting reagent in current FISSEQ protocols, available com-

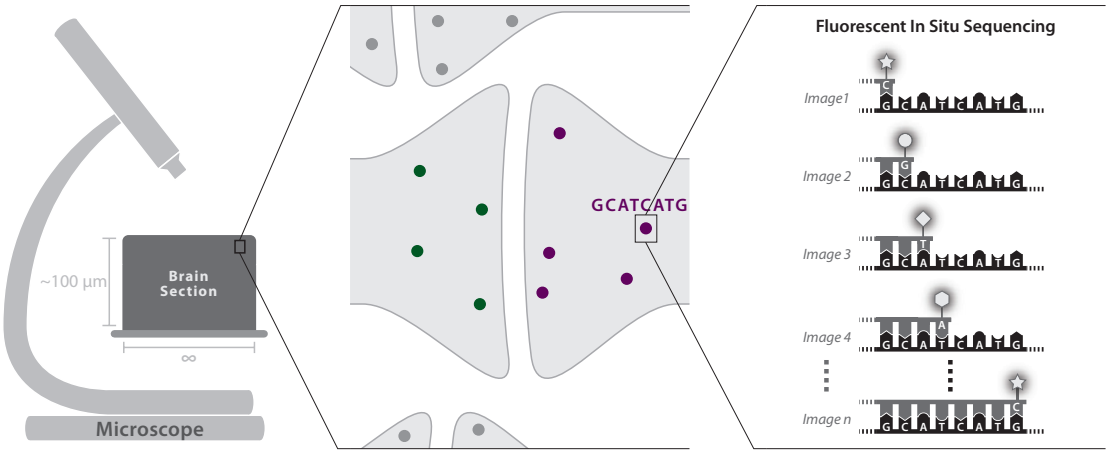

Figure 6.1: A fluorescent in-situ sequencing strategy for connectomics: cell-identifying nucleic acid barcodes are targeted to the pre-synaptic and post-synaptic membranes, where their sequences are read by FISSEQ in a high-resolution optical microscope. Resolving synapses from their neighbors, and distinguishing pre-synaptic from post-synaptic barcodes at a given synapse, requires strategies for sub-diffraction optical imaging.

mercially for roughly \$500 per 10^{17} molecules (and note that commercial biochemical reagents are often priced orders of magnitude above the synthesis cost). For comparison, we can estimate the number of ligation probe molecules required for whole-mouse-brain FISSEQ-BOINC as $n \cdot s \cdot m \cdot b \approx 10^{17}$ where $n \approx 10^8$ is the number of neurons, $s \approx 10^4$ is an upper bound on the average number of synapses per neuron, $m \approx 1000$ is the number of template copies per synapse, and $b \approx 100$ is the number of nucleotides per template. Thus, even if we require $100\times$ excess probe molecules, the reagent cost per whole mouse brain synaptic FISSEQ-BOINC is less than \$100k.

Error rates Sequencing by ligation has typical error rates of roughly $\varepsilon = 1\%$, such that a 30-base sequencing reaction has a success probability of $P_{\text{success}} = (1-\varepsilon)^{30} = 74\%$. If each base is sequenced three times, however, a majority voting scheme can be implemented: the sequencing-associated error rate could thus be reduced to $3\varepsilon^2+\varepsilon^3$, leading to $P_{\text{success}}^{\text{majority vote}} = (1-(3\varepsilon^2+\varepsilon^3))^{30} = 99.1\%$. This would triple the number of biochemical cycles. An alternative method to error-correct synaptic FISSEQ reads is discussed in Supplemental Note 6.5.4.

6.1.2 Resolution of distinct synapses

Resolution requirement Diffraction-limited 3D optical microscopy ($\lambda/(2 \cdot \mathrm{NA}) \approx 200$ nm *xy*-resolution and $2\lambda/\mathrm{NA}^2 \approx 533$ nm *z*-resolution for numerical aperture $\mathrm{NA} = 1.5$ and wavelength $\lambda = 600$ nm) is insufficient to reliably resolve nearby synapses, which are packed at an *average* density of 1-2 per μm^3 [433]. Prior theoretical studies [466,433], constrained by EM anatomical data from rat hippocampal neuropil, suggest that $> 90\%$ of synapses could be resolved at ~ 100 nm isotropic resolution. This conclusion is subject to the assumptions used in the simulations, including fluorescent labeling only of the pre-synaptic and post-synaptic protein densities (PSDs) rather than of the entire synaptic compartment [433].

Synapse-specific molecular labeling There exist multiple methods to optically label intact synapses via inter-cellular protein-protein interactions across the synaptic cleft, e.g., via neurexin-neuroligin interaction or split fluorescent protein complementation [194,717,407], or via immuno-staining against synapse-specific proteins [463,462]. These methods could be used to validate the ability of an optical setup to resolve distinct synapses, and/or to locate synapses before in-situ sequencing. Because close axon/dendrite contacts do not reliably predict the locations of individual synapses [468], it would be desirable to use such an independent molecular marker of valid synapse locations, although we also invoke other methods here to eliminate FISSEQ signal that does not originate from actual synapses.

Limits to spatial resolution from rolony size The rolling-circle nano-balls (rolonies) generated in FISSEQ are roughly 100–200 nm in diameter, in current protocols.

Strategies for resolution enhancement

We now consider strategies, which can be used alone or in combination, to ensure the resolution a given synapse from neighboring synapses: *super-resolution imaging*, *thin sectioning* and *molecular*

stratification. These strategies are illustrated in Figure 6.2.

SUPER-RESOLUTION IMAGING While much super-resolution microscopy research aims toward $<$ 10 nm resolution and live-cell compatibility, FISSEQ-BOINC gives rise to a different set of challenges: 50–100 nm resolution in four colors, in fixed tissue, using standard fluorophores, and at the *highest possible speed*. The speed/resolution tradeoff is likely to be favorable in an in-situ sequencing context: rolonies are brighter than single fluorophores, and the protocol is robust to photobleaching because new dyes are flowed in on each cycle[†].

To perform FISSEQ, a microscopy platform must ideally allow 4-color imaging, or at least 3-color imaging. On a 3-color microscope, the 4th base could be unlabeled such that absence of signal serves as the fourth color. A 2-color microscope, however, is insufficient[‡].

Among existing technologies, linear 3D structured illumination microscopy (SIM)[255] enhances resolution by a factor of 2 along all three axes, relative to the diffraction limit, and is naturally compatible with 4-color imaging using standard fluorophores. Analog SIM acquisition[726] can improve SIM speed and saturated SIM (SSIM)[254] can improve SIM resolution[§]. *I*^{5}*S* two-objective detection[590] is a form of SIM with isotropic $\sim$ 100 nm resolution. Other existing methods such as isoSTED can achieve $<$ 50 nm resolution along all three dimensions[576], but may be more difficult to adapt to high-speed, 4-color operation.

[†]Oxygen-radical scavenging buffers[18] can also be applied to minimize photobleaching and photodamage.

[‡]In theory, a scheme with 2$\times$ more fluorophore cleavage/removal cycles could be envisioned: flow on A and T, look with 2 colors, cleave and wash away the fluorophores without de-protecting the bases, flow on C and G, look with the same 2 colors, cleave and wash away the fluorophores, then de-protect and move to the next base. Unfortunately, in the current FISSEQ chemistry, fluorophore cleavage/removal is achieved via the same reaction as nucleotide de-protection. Use of a 2 color microscope would therefore require new FISSEQ chemistry.

[§]The light intensity of the sinusoidal illumination pattern needed for SSIM is >1 photon per cross-section per fluorescence lifetime; then the emission pattern is non-sinusoidal due to saturation and contains spatial information at higher harmonics.

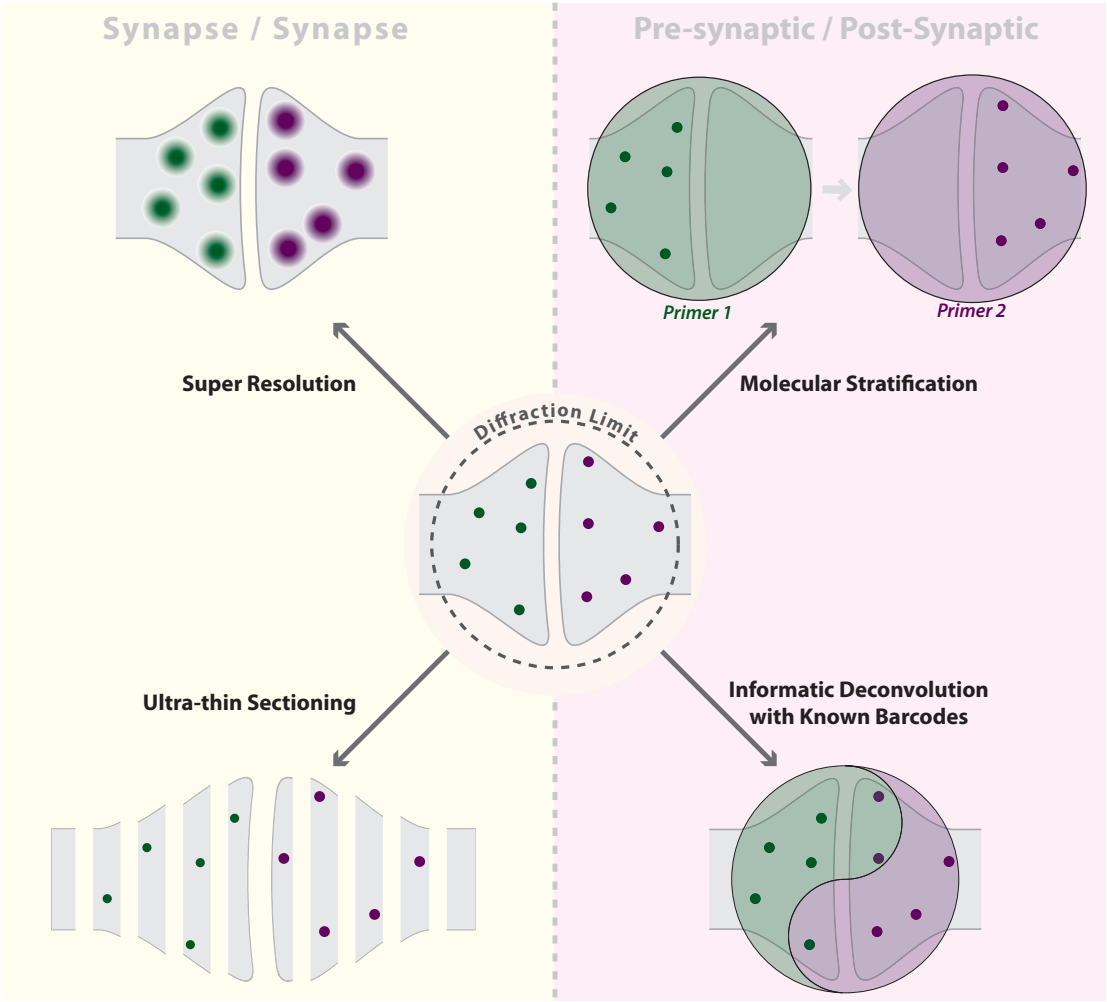

Figure 6.2: Resolution Enhancement Strategies for FISSEQ-BOINC: super-resolution, molecular stratification, thin sectioning, and informatic deconvolution from a known barcode pool. These techniques can be applied alone or in combination to improve the resolvability of nearest-neighbor synapses, and/or of barcodes on opposing sides of the synaptic cleft. Super-resolution microscopes overcome the traditional diffraction limited resolution limit ($\lambda/2\text{NA}$) via a variety of methods, such as patterned illumination, nonlinear optical effects, or stochastic single-molecule blinking. Molecular stratification initiates FISSEQ of only a (random or pre-programmed) subset of molecular barcodes in each imaging frame, e.g., activating only pre-synaptic or only post-synaptic barcodes. Thin sectioning (physical or optical) allows enhanced lateral resolution in a 2D plane by eliminating overlaps in the third dimension. Informatic deconvolution decodes mixed FISSEQ signals from a combination of distinct barcodes within a single resolution voxel, by relying on prior knowledge of the pool of individual barcodes.

Thin sectioning Thin sectioning below the intrinsic axial resolution of the imaging setup can improve the *effective* axial resolution, by physically separating otherwise unresolvable axial locations. It can also increase the effective lateral resolution, by decreasing the spot density in the *xy* plane within each section. Experimentally, Array Tomography – a form of thin-sectioning microscopy – appears to resolve most synapses in mouse brain tissue[463,462] using $<$ 100 nm tissue sections on a diffraction-limited confocal microscope. In Array Tomography, the process of diamond-knife sectioning is automated, and an array of tissue slices is generated on a strip of adhesive for subsequent random-access automated imaging. All-optical methods can also achieve axial sectioning down to the 100 nm level[253,177].

Molecular stratification Molecular stratification is a method leading to linear improvements in the *effective* spatial resolution of FISSEQ with linear increases in the number of imaging cycles, at *fixed* optical resolution of the microscope, by activating only a *subset* of the molecules in each cycle[396]. In one implementation, multiple distinct "primer" sequences are employed sequentially during the FISSEQ process, such that each primer initiates sequencing of a subset of the rolonies.

There are two broad types of molecular stratification – stochastic and deterministic. In stochastic stratification, an *arbitrary* subset of barcodes is activated in each step; for example, all barcodes beginning with the nucleotide "C". In deterministic stratification, a *defined* subset of the barcodes is activated in each step; for example, all barcodes at pre-synaptic but not post-synaptic terminals, or all barcodes in L5 pyramidal cells but not in other types of neurons.

Stochastic stratification could be implemented via random ligation of primer binding sites to the target nucleic acids before FISSEQ[396]. Up to 4x stratification can be obtained just by varying the last base of the primer binding site, since polymerase initiation is strongly dependent on correct homology at this position. Further stratification can be achieved by working backwards, gaining additional stratification by a factor of 4 at each step. Stratification factors of 10-100 should be readily achievable with this approach, albeit with the corresponding increases in imaging time. Stochastic molecular stratifi-

cation by a factor S should lead to an increase in the average point-point separation by a factor of $S^{1/3}$ along all three axes.

Molecular stratification could be used to reduce the effective density of synapses in each imaging frame. To do so, however, all of the rolonies at a *given* synapse are activated or inactivated together. For example, stratification could be performed using the first few bases of the cell-identifying barcode itself, which is cell-specific rather than rolony-specific.

6.1.3 Resolution of pre-synaptic from post-synaptic barcodes

To distinguish pre-synaptic from post-synaptic barcodes at a given synapse, further strategies must be employed for resolution enhancement of optical microscopy: barcodes positioned close to the pre-synaptic and post-synaptic membranes may be spaced apart by ∼10–50 nm across the synaptic cleft [466,139], well below the resolution of structured illumination microscopy and below the level where gains can be made through thin-sectioning. Molecular stratification and *informatic deconvolution* can solve this problem, as depicted schematically on the right side of Figure 6.2.

Molecular stratification In an elegant implementation of deterministic stratification, pre-synaptic and post-synaptic barcodes could be fused to distinct primer binding sites. A first primer would drive in situ sequencing only of pre-synaptic barcodes; then, in a subsequent set of biochemical cycles, a second primer would drive in situ sequencing only of post-synaptic barcodes. This would *eliminate the need to resolve pre-synaptic from post-synaptic barcodes in any single fluorescent image*. Supplemental Note 6.5.2 details a range of possible strategies to implement deterministic molecular stratification at the synapse.

To summarize: if a given synapse is already resolvable from *other* nearby synapses, then additional deterministic molecular stratification by a factor of 2 – by using distinct pre-synaptic and post-synaptic priming sequences – would be sufficient to resolve pre-synaptic from post-synaptic barcodes.

Informatic deconvolution So far, we have assumed that the pre-synaptic and post-synaptic barcodes must be optically resolved, either in the same imaging frame, or in separate imaging frames (via molecular stratification). This is not necessary, however, if the set of *possible* pre-synaptic and post-synaptic barcodes is already known, and is a small subset of the 4^n DNA strings of length n, where n is the barcode length.

For example, suppose that each cell's barcode is readable via FISSEQ in the cell's nucleus. In a first step, one can then perform FISSEQ on all the cell nuclei. One thereby determines all possible pre-synaptic or post-synaptic barcode sequences. Now suppose that both pre-synaptic and post-synaptic barcodes are contained within a single resolution voxel at each synapse, such that "mixed" fluorescent signals are obtained from the synapse during FISSEQ. Given the mixed signal, and the known set of possible barcode sequences obtained from nuclear FISSEQ, it is then possible to determine computationally which *combination* of the known barcode sequences gave rise to the observed mixed signal[¶].

We refer to this approach as *informatic deconvolution* of non-resolvable barcode combinations, given a pre-determined pool of individual barcode sequences. Supplemental Note 6.5.4 outlines options for informatic deconvolution in more detail.

6.1.4 Restriction of FISSEQ to synapses

Restricting the FISSEQ signal to synapses is critical to the implementation of FISSEQ-BOINC. Barcodes localized "part-way down" axons or dendrites would often co-inhabit FISSEQ resolution voxels occupied by genuine synapses. Furthermore, to achieve sufficient resolvability of neighboring synapses, the FISSEQ signal should be restricted as closely as possible to the synaptic cleft[433,466].

Methods to accomplish this restriction fall into two categories: barcode localization (trafficking RNA barcodes solely to the synapse) and location-restricted sequencing (restricting FISSEQ chem-

[¶] Additionally, synapse *locations* could be pre-labeled with an antibody (e.g., Anti-Synapsin I) and optically resolved, so that the microscope knows "where to look" for such mixed signals.

istry solely to the synapse). Supplemental Note 6.5.3 describes one strategy for restricting FISSEQ biochemistry to the synapse, even in the presence of barcode RNAs localized outside the synapse.

6.1.5 Cost estimate: Ultra-thin sectioning FISSEQ-BOINC

One approach would be to perform FISSEQ on $<$ 100 nm thin tissue sections in a standard diffraction-limited microscope, such as a confocal microscope. We treat this case here merely because it leads to a simple calculation of the estimated imaging cost; other methods allowing comparable degrees of super-resolution, which do not rely on thin sectioning, may be preferable in practice.

Spatial resolution Experimentally, this approach appears to resolve most synapses in the context of Array Tomography [463,462]. Resolution calculations [466] indicate that Array Tomography at 100 nm vertical slice thickness and 200 nm lateral resolution (via a standard confocal microscope) would resolve >90% of synapses from their nearest neighbors.

Imaging time A comparison with the rates of sequencing by fluorescent microscopy in commercial sequencing machines suggests that FISSEQ-BOINC in $<$ 500 nm thin sections could proceed at rates of 8 hours per cm^2 [433]. Assuming 100 nm sections, the total imaging time is

$$T^{\text{ultra-thin sectioning FISSEQ}}_{\text{mouse}} = \frac{8 \text{ hours}}{100 \text{ nm section}} \times 42000 \text{ sections} = 40 \text{ years}$$

to sequence >90% of mouse brain synapses at Illumina rates on a single machine [433].

Imaging cost With $1M in situ sequencing machines operating at Illumina speeds, and machine cost amortized over three years, the imaging cost would be $13M per whole mouse brain connectome[‖].

[‖] To distinguish pre-synaptic from post-synaptic barcodes, either a deterministic molecular stratification approach would be used – with distinct pre-synaptic and post-synaptic primer sequences, increasing the imaging cost by a factor of 2 – or informatic deconvolution could be applied based on a known barcode pool, such as

Additional costs The cost of instrumentation for whole mouse brain sectioning and section-handling, at 100 nm slice thickness, can likely be reduced below $1M [433].

Project cost The cost for a 3-year ultra-thin sectioning mouse brain FISSEQ-BOINC is therefore in the $10M-$20M range, subject to the prior experimental demonstration of the basic molecular mechanisms of FISSEQ-BOINC. This cost could be reduced if the individual microscopes were brought below $1M, or amortized over multiple projects.

Optical vs. physical sectioning Via all-optical techniques, I^5M microscopy achieves 100 nm axial and roughly 200 nm lateral resolution in a wide-field mode [253]. Parallelized multi-photon 4Pi-confocal microscopy leads to similar axial resolution [177]. Bessel beam plane illumination gives 2× improvement in the axial resolution and 1.5× improvement in the lateral direction relative to confocal microscopy, while allowing high speeds [215]. While we have focused on the physical sectioning approach here, because its ability to resolve densely labeled synapses has been demonstrated experimentally [463,462] and because it leads to a simple estimate of the imaging cost, optical sectioning may be preferable in practice, e.g., if auto-alignment methods for 4Pi interference are introduced.

6.1.6 Hybrid approaches

Hybrids between the bulk sequencing (BOINC) [734,532,433] and in situ sequencing (FISSEQ-BOINC) could lead to reduction of total costs, as well as potential experimental simplifications. For example, FISSEQ could be performed solely on each cell's self-barcode – localized in the nucleus – and BOINC bulk-sequencing could subsequently be used to determine the connectivity matrix. This would eliminate the requirement for high resolution direct observation of synapses by light microscopy, yet would

from nuclear FISSEQ, without any increase in the imaging cost.

still allow localization of each cell body in addition to determination of the connectivity matrix. Supplemental Note 6.5.5 discusses a potential hybrid strategy.

6.1.7 Summary

FISSEQ-BOINC leverages the recent development of fluorescent sequencing protocols for nucleic acids that have been locally amplified inside intact tissue[396,340]. This approach could have several advantages over other connectomics approaches such as axon tracing via large-scale serial-section electron microscopy. Most notably, like BOINC[734], it does not require error-prone morphological tracing of thin ($<$ 100 nm) neural processes over large ($\sim$1 cm) distances, instead relying on a digital representation of cell identity in nucleic acid strings for which *the fidelity of readout is independent of distance from the neuronal soma*.

FISSEQ-BOINC could allow the direct observation of synaptic connections in situ by reading the sequences of pre-synaptically and post-synaptically localized cell-identifying nucleic acid barcodes. Achieving the necessary spatial resolution in fluorescent microscopy, however, requires a suitable combination of: a) super-resolution microscopy, b) physical[463,462] or optical[253] sectioning of tissue into $\sim$ 100 nm slices, c) molecular stratification, and/or d) informatic de-convolution of multiple sequences within one optical resolution voxel using a known barcode pool.

A preliminary cost estimate suggests that FISSEQ-BOINC in 100 nm ultra-thin 2D sections may be achievable for roughly $10M per three year mouse connectome, using imaging equipment comparable to today's bulk fluorescent sequencing machines. The ultra-thin sectioning approach has been demonstrated experimentally to resolve densely labeled synapses in mouse cortex, and may integrate naturally with Array Tomography immuno-staining methods that report on the molecular diversity of synapses[463,462].

FISSEQ-BOINC integrates readily with other light-microscopy-based readouts, conferring high-dimensional, molecularly specific information: FISSEQ-BOINC is thus naturally suited to the acqui-

sition of Rosetta Brain datasets, as described below. In the simplest case, this includes integration with other FISSEQ readouts from the same tissue specimen, such as in situ transcriptomics[33] or in situ readout of cell lineage barcodes.

In the specific implementation proposed here, which sequences only synapse-localized and nuclear-localized barcodes – FISSEQ-BOINC does not trace the morphologies of neurons. It is possible that whole-cell FISSEQ could recover detailed morphology, however, if each neuron is filled sufficiently with barcoded transcript, in a manner somewhat analogous to current BrainBow approaches[410,321,95].

6.2 Preliminary experimental directions for FISSEQ-BOINC connectomics

6.2.1 Technology components

Given the prior experimental demonstration of FISSEQ[396,340], key experimental milestones on the way towards FISSEQ-BOINC include the following.

- Barcode each neuron with a unique RNA tag. For dense, whole-brain barcoding, the barcode generation mechanism should be genomically encoded rather than delivered virally. Mouse models may be readily accessible due to their ease of genetic manipulation, e.g., via embryonic stem cell implantation. A germline-competent transgenic encoding the barcoding mechanism must be developed, despite the fact that expressed barcodes pose potential issues of toxicity. Due to its small brain size, with only a few million cortical neurons[489], the Etruscan shrew may also be a desirable target.

- Find a set of RNA localization tags that can label all synapses regardless of cell type. This is discussed in Supplemental Note 6.5.1.

- Restrict the FISSEQ signal to the pre-synaptic and post-synaptic densities (PSDs): a FISSEQ enzyme such as phi29 could be targeted to the PSDs via an antibody (localization to entire

synaptic compartments is not sufficient[433] to allow good resolvability of neighboring synapses in a dense labeling scenario). This is discussed in Supplemental Note 6.5.3.

- Demonstrate optical resolution enhancement in the context of FISSEQ: to observe *nearly* 100% *of synaptic contacts* unambiguously, a 4-color (or at least 3-color) super-resolution microscopy with 50–100 nm *xy* resolution is needed, coupled with $<$ 100 nm thin sectioning or $<$ 100 nm axial resolution. Molecular stratification is a complementary tool for optical resolution-independent enhancement of the *effective* spatial resolution, and methods for molecular stratification are discussed in Supplemental Note 6.5.2.

- Achieve chemical compatibility of FISSEQ with appropriate tissue-embedding and immunostaining reagents: compatibility of FISSEQ with Array Tomography preparations would be valuable (OPTIONAL).

- Achieve biochemical compatibility of bulk BOINC with FISSEQ to allow hybrid strategies: BOINC could be used to obtain connectivity information via bulk sequencing while FISSEQ could be used on the same sample to obtain cellular positions and transcriptomes (OPTIONAL).

6.2.2 FISSEQ-BOINC projectomes

Simplified versions of FISSEQ-BOINC could be useful even while relaxing some of the above engineering requirements. For example, rather than mapping the precise synaptic connectivity, a first implementation could target FISSEQ-BOINC barcodes only to the pre-synaptic compartments and nuclei, thus obtaining the complete *projectome* of a single brain, i.e., the spatial locations to which all axons project. This would obviate the need to resolve pre-synaptic from post-synaptic compartments, requiring only FISSEQ of pre-synaptic compartments and donor nuclei / somas. Projectomes are powerful resources[205,503,620] of interest to many neuroscientists, and are useful for constraining

theories of brain architecture[441], yet current approaches require integrating many experiments across many brains and do not reach single-cell precision[71]. FISSEQ-BOINC would solve both problems.

Note that cellular-resolution, single-brain projectomes could also be achieved with BOINC through 3D sectioning of the tissue and subsequent section-specific barcoding; nuclear-localized DNA barcodes (revealing soma positions) could be distinguished from synapse-localized RNA copies of the barcodes (revealing projections) by observing the removal of introns or by other methods.

6.3 Toward Rosetta Brains

A key goal for neuroscience is to measure many biological variables simultaneously, in a co-registered fashion, within *single* brains[122]. Even co-registering just *two* variables at cellular resolution (e.g., activity and connectivity, or gene expression and projection pattern) has led to insights inaccessible to separate measurements[620,68], and it is important to extend such co-registration to as many relevant variables as possible. The results of such rich co-registration would constitute *Rosetta Brains*: integrative datasets that could constrain theoretical efforts to bridge across levels of structure and function in neural tissue.

Such integration could be enabled by the emerging ability to translate a variable of interest, such as synaptic connectivity, cell lineage[591], or perhaps even dynamic activity patterns[735,227,678], into a physical form that can be robustly stored, transported and measured – digitally-encoded nucleic acid strings, which can be read out in situ via FISSEQ as temporal patterns of colors.

6.3.1 FISSEQ-BOINC approach to Rosetta Brains

We can envision at least one route to Rosetta Brains, as follows[122]. Given a single brain, we would like to measure "A, B, C, D and E": Activity, Behavior, Connectome, Development and Expression of genes and proteins. All of these can be obtained via a FISSEQ-BOINC approach, as follows:

Activity can be measured via electrodes, optical microscopy, molecular recording[735,227,678] or other techniques[434,21], in a manner that allows co-registration[68] at the single-cell level with subsequent fixed-tissue optical microscopy.

Behavior can be monitored via video in the context of hypothesis-driven experimental paradigms or free behavior.

Connectomes can be obtained via FISSEQ of nucleic acid cell ID's indicating connectivity, "ID-C", as well as FISSEQ of nucleic acid barcode-tagged antibodies targeted to specific synaptic proteins, revealing synapse properties[507].

Developmental lineage[693,591] can be determined via FISSEQ of nucleic acid cell ID's encoding cell lineage:"ID-D", e.g., DNA barcodes which are "updated" once per cell cycle[722,124].

Expression of genes is measured in a spatially-resolved fashion via FISSEQ or fluorescent in-situ hybridization[118,96] of mRNA and/or of nucleic acid barcoded antibodies targeted against cellular proteins: "ID-E".

Implementing such a strategy would entail performing behavioral experiments on a single animal, with measurement of activity data occurring in real time. Then, the brain tissue would be fixed and thin-sectioned[463,462,117], perhaps using methods similar to those of Array Tomography[462]. The tissue sections would be subjected to highly multiplexed FISSEQ and immuno-staining cycles in a high-speed, high-resolution optical microscope.

6.3.2 Advantages

Natural multiplexing of immuno-labels and transcripts Attaching each protein-probing antibody to a unique nucleic acid barcode allows multiplex in-situ readout of synaptic and cellular proteins (exponentially parallelized compared to the typical 4-8 fluorescent colors per staining cycle).

Furthermore, in-situ sequencing of mRNA is inherently multiplexed. It will likely be possible with FISSEQ to achieve orders of magnitude higher multiplexing compared with recent gene expression

atlases (8 hybridization probes per brain in 25 μm sections)[397], while performing these analyses on single brains rather than populations of brains.

Error-correction By combining many types of measurements on a single piece of tissue, there is the possibility for error-correction: for example, mRNA expression levels could cross-validate cell type inferences made on the basis of synaptic protein abundances and distance-dependent connectivity patterns.

Furthermore, an array of molecular barcoding techniques could cross-validate or even substitute for in-situ sequencing, e.g., multiplexed in-situ probe hybridization[118,96**].

Combining structural and dynamic measurements During thin sectioning, electrodes or other recording devices[434] could potentially remain inside the tissue, with the microtome simply slicing through them – although damage to the knife would be a serious concern, perhaps necessitating soft, thin electrodes. The positions of the electrodes or other recording devices could be known post-facto from microscopy or pre-facto from high-resolution CT scans. This would allow molecular composition and connectivity to be ascertained for cells of known activity history and representation/coding properties. Optical imaging of neural activity would integrate even more readily with fixed-tissue optical microscopy for FISSEQ. Much more speculatively, molecular recordings of time-dependent signals[735,227] could be read out directly though FISSEQ or other forms of optical microscopy[678].

**Fluorescent in-situ hybridization approaches have demonstrated experimentally a 32-fold simultaneous multiplexing capacity using Binomial$(7, 3) = 35$ STORM activator/emitter photo-switchable pairs[416]. This approach could theoretically scale to at least 792 effective colors using available emitters, or to tens of thousands of effective colors if an infrared (IR) fluorophore was added to the color palette or other methods were used to distinguish dye pairs[655].

6.3.3 Limitations and extensions

Measuring morphology is important, since mechanisms such as ephaptic coupling[25], BDNF signaling[289], nitric oxide release[142] and many others can functionally link nearby neurons in a distance-dependent manner. Also, the positions of inputs within the dendritic tree govern their electrical integration[80,174]. Therefore, knowledge of the precise spatial appositions of neuronal processes seems relevant for understanding elementary neuron-neuron interactions. Variants of FISSEQ-BOINC, employing FISSEQ barcodes distributed *throughout* all cellular compartments, could reveal at least the gross morphology of every cell, much as is done in current BrainBow techniques[410,321,95]. Certainly, a genetically targeted subset of cell shapes could be imaged in this way.

Neuromodulators (e.g., neuropeptides and biogenic amines) can strongly modify the behavior of neural circuits, effectively forming "circuits within circuits" that are activated or inactivated by various modulators[44,45]. Because many neuromodulatory receptors[129] and release sites[537] are extrasynaptic[44,670], mapping the neuromodulatory circuitry will require more than just *synaptically-localized* immuno-staining. While this goes beyond the pure synaptic FISSEQ-BOINC approach described above, this could also be done using optical imaging and multiplexed antibody staining in the same setup. Alternatively, correlations between gene expression patterns and neuromodulatory responses could be measured independently, and then used to *infer* single-cell neuromodulatory properties from FISSEQ transcriptomics data.

We have not discussed how to measure the *dynamics* of connectomes, or of the associated molecular annotations. This will require additional new concepts, perhaps variants of existing molecular recording ideas[735,227,434], but tailored to particular (e.g., slower) timescales and processes of interest (e.g., transcription). Integrating activity data into Rosetta measurements raises highly non-trivial technology problems if it is to be done at scale[434].

6.4 Discussion

FISSEQ-BOINC is a hypothetical connectomics strategy which uses Fluorescent In-Situ Sequencing (FISSEQ) to directly read the sequences of co-localized RNA barcodes at the synaptic cleft. Once the basic molecular mechanisms are established, preliminary estimates indicate that a FISSEQ-BOINC analysis of an entire mouse brain could cost $10M-$20M for a three-year project, primarily in the form of microscopy equipment[433]. Improvements to the speed of 50–100 nm 4-color super-resolution fluorescence microscopy in fixed-tissue could reduce this cost further.

FISSEQ-BOINC is only one example of a plausible light microscopic strategy for high-speed, molecularly annotated connectomics. Unforeseen limitations of this plan could be revealed experimentally and alternative designs may prove superior. Nevertheless, the FISSEQ-BOINC strategy illustrates the existence of a flexible emerging design space. Ultimately, such an approach could simultaneously provide spatial localization of neuronal somas, determination of the neuron-neuron connectivity matrix, and cellular-resolution molecular annotations indicative of cell types, synapse properties, and developmental lineages. Furthermore, molecularly annotated connectomics approaches could synergize with strategies – such as the Human Brain Project[443,332] – that aim to build large-scale data-driven simulations via integration of diverse measurements and data-sets.

Several recent and ongoing developments converge to enable the possibility of FISSEQ-BOINC or similar strategies. The problem of tracing thin axons over large distances though vast image stacks is, in principle, obviated by the use of digitally-encoded biopolymers which can be *physically* transported along the axon by endogenous cellular mechanisms. This combinatorial sequence space can be accessed by using N cycles of fluorescence-coupled biochemistry to read out 4^N effective "colors". Advances in light microscopy beyond the diffraction limit – which could be as simple as $\sim$ 100 nm physical or optical sectioning – allow spatial resolution of many of the key objects of interest within any single fluorescent image, but further improvements in the *effective* spatial resolution can be ob-

tained by stratifying otherwise unresolvable objects into *separate* image frames using flexible in-situ DNA manipulation techniques.

FISSEQ-BOINC is currently at the level of a theoretical proposal. The implementation of FISSEQ-BOINC or related strategies will require the solution of a number of experimental challenges in in-situ biochemistry, imaging and automation. None of these appears to be insurmountable, however, and ongoing advances in fields such as high-speed super-resolution microscopy and automated tissue sectioning could remove some of the existing technical obstacles. We can thus envision at least one path, which may be one among many viable alternatives, towards whole-brain-scale, molecularly annotated connectomics.

6.5 Supplementary Information

6.5.1 Implementing barcode-trafficking to the synapse

While each of the below approaches will likely lead to an enhancement of synapse-localized barcodes, compared to passive diffusion, none is likely to yield the stringent synapse-specificity required for FISSEQ-BOINC: some fraction of barcode RNA will remain localized *outside* the synapse. Thus, one of these approaches will need to be combined with a secondary spatial restriction such as location-restricted FISSEQ, as outlined in Section 6.5.3.

Barcode targeting via protein fusions A cell-barcode in the genome could be transcribed into RNA molecules bearing either the MS2-binding RNA aptamer sequence or the PP7-binding RNA aptamer sequence (via direct genetic fusion or RNA-RNA interaction[149]). The cytoplasmic domain of the pre-synaptic protein neurexin could be fused to MS2 protein, and the cytoplasmic domain of the post-synaptic protein neuroligin could be fused to PP7. These protein-RNA interactions are quite strong, e.g., with a 3 nM affinity constant for the MS2 aptamer/MS2 protein interaction[615]. Alter-

natively, RNA barcodes could perhaps be fused covalently to the targeting proteins via cap-snatching protein mutants from viruses[212] (a form of in-vivo mRNA display) or engineered ribozymes[50]. The barcode RNAs could thereby be localized to the pre-synaptic and post-synaptic compartments.

The difficulty for this approach lies in the molecular diversity of synapses. Taking the neurexin/neuroligin example, there are four neuroligin genes in the mouse. The different subtypes of neuroligin can be found at different subsets of synapses, with neuroligin 1 at excitatory synapses and neuroligin 2 at inhibitory synapses. Neuroligin 3 is found at both excitatory and inhibitory synapses, but likely not at every synapse in the mouse brain. The C-terminal tails of the various neurexins/neuroligins are likely sufficient to direct targeting of the appropriate fusion proteins, although the cell-type context dependence of this targeting would need to be tested.

Thus, this approach may require not just two MS2/PP7-tagged synaptic proteins such as neurexin and neuroligin (i.e., one pre-synaptic and one post-synaptic), but rather a small set of MS2/PP7-tagged pre-synaptic proteins and small set of MS2/PP7-tagged post-synaptic proteins, to cover the molecular diversity of all synapses. There are likely other groups of (e.g., non-membrane) proteins which *collectively* could be used to target barcodes to *all* synapses: candidates include PSD95, gephryin, SHANK3, Synapsin and others.

In this scheme, the cell barcode itself need only bear the MS2 or PP7 aptamer sequence; a transgenic mouse could be created (e.g., with CRISPR) that fuses the MS2 or PP7 proteins to multiple endogenous pre-synaptic or post-synaptic proteins.

Barcode targeting via FINGRs Another targeting strategy would utilize fibronectin intrabodies generated with mRNA display (FINGRs)[251]. These are a form of genetically-encoded "protein aptamer" against a target protein of interest, whose expression level is additionally tuned to be at or below the level of the target, leading to highly specific labeling. FINGRs have already been generated against Gephyrin and PSD95[251].

Barcode targeting via endogenous dendritic or axonal mRNA localization signals Sequence signals in the 3'-UTR of mRNAs direct their localization to neuronal processes, e.g., the dendrites, via the formation of ribo-nucleoprotein "granules" which are transported by cytoskeletal motor proteins to their appropriate sub-cellular destinations[686]. Further sequence signals in the 5'-UTR appear to be sufficient to direct localization to the synapse[458], in some scenarios, although the full molecular underpinnings of subcellular RNA localization are not well known. Synapse associated poly-ribosome complexes, which perform spatially-localized protein translation at synapses, appear to be tightly localized to the synapse, and in particular to the base of the dendritic spine[631].

In principle, the appropriate RNA localization tags could be appended to cell-barcode RNAs to direct their localization to the pre-synaptic or post-synaptic densities. If multiple distinct localization tags must be appended, in a mutually exclusive fashion, to a single stochastically-generated RNA barcode, RNA trans-splicing or transposon traps could be used, as discussed in Section 6.5.2. Unfortunately, very few RNAs appear to localize exclusively to the synapse itself[97] let alone to the PSDs, so this will necessitate combination with the methods of Section 6.5.3 or similar.

6.5.2 Implementing molecular stratification at the synapse

Implementing molecular stratification via alternative RNA splicing Individual cells can *simultaneously* express at least 14-50 RNA splice variants of the same gene[492]. For deterministic molecular stratification to distinguish pre-synaptic from post-synaptic barcodes, two mutually-exclusive exons could be placed downstream of the barcode RNA: for example, one exon could contain the MS2 aptamer and reverse transcription priming site 1, while the other exon could contain the PP7 aptamer and reverse transcription priming site 2. Then, the same (e.g., genomically-encoded) DNA barcode sequence would give rise to two distinct RNA sequences, one targeted to the pre-synaptic compartment and specific to the first primer, and the other targeted to the post-synaptic compartment and specific to the second primer (using different sequencing adaptors might be prefer-

able to different reverse-transcriptase primer binding sites, so that rolony preparation could occur in a single step).

In another implementation of the same idea, the cell could express multiple alternative RNAs which could be trans-spliced (rather than cis-spliced) onto a given barcode RNA. This has the advantage that alternative exons do not need to be engineered into a single gene[684]. The efficiency of trans-splicing would likely be a limiting factor here, especially since un-spliced targeting RNAs could saturate the available synaptic proteins.

Implementing deterministic molecular stratification via site-directed gene duplication Alternatively, gene duplication events could be targeted to a predetermined genomic location, e.g., via a "transposon trap"[402]. A barcode would first be generated within the retrotransposon sequence at a defined "start-site" location in the genome. Elsewhere in the genome would be placed two "landing sites" of the form: Promoter - Landing Site - PreTag/PostTag, where PreTag and PostTag are targeting sequences for pre-synaptic or post-synaptic localization. The retrotransposon can then be induced to "copy-and-paste" the barcode to these predefined landing sites. The landing sites would be known sequences where that transposon has a high probability of landing. Transposon-based duplication might have the advantage of being less dependent on cell-type-specific regulation as compared with alternative splicing.

Implementing molecular stratification via overlapping genes (plus vs. minus strands) Alternatively, to implement deterministic two-fold molecular stratification, the same DNA encoded cell barcode could be transcribed from one promoter in the forward direction – leading to one set of primer binding sites and localization tags – and from another promoter in the reverse direction, appending the second set of primer binding sites and localization tags. For a sufficiently diverse barcode space, the reverse complement of a given barcode in the pool would not itself be present in the pool,

meaning that a cell could be identified *either* by its forward or reverse-complemented barcodes. It might be necessary to prevent spurious hybridization of the forward and reverse-complemented barcode RNAs (leading to spurious generation of RNA barcode dimers as well as PKR-activating long dsRNAs[738]), but it should be noted that many opposite-strand overlapping genes occur naturally in the human and mouse genomes[570].

6.5.3 Restriction of FISSEQ biochemistry to the synapse

Additional synapse specificity of the FISSEQ signal could be achieved by restricting the sequencing chemistry to the pre-synaptic and post-synaptic densities using a form of protein tagging. This could be achieved by conjugating the various enzymes used in the FISSEQ rolony preparation to antibodies against synaptic proteins. Such enzyme-antibody conjugates are not unreasonable given the success of previous enzyme antibody conjugates such as horseradish peroxidase, urease, and alkaline phosphatase. Moreover, by multiple conjugating enzymes in successive steps of the FISSEQ process to antibodies targeting different synaptic proteins found at the same synapse (e.g. MMuLV RT—anti-PSD95, CircLigase—anti-NR1, Phi29—anti-NLGN3), spurious reactions at non-synaptic sites could be progressively reduced. Enzyme-antibody conjugates could be applied at a non-permissive temperature (or in the absence of substrate), unbound copies washed away, and then switched to a permissive temperature for the reaction.

Alternatively, a genetically-encoded non-specific biotin ligase[562], fused to a synaptic protein, could be used to biotinylate the proteins at the synapse, in a strategy similar to that of[550]. One of the FISSEQ enzymes could then be linked to streptavidin. After enzyme addition and a wash step to remove unbound enzyme, enzyme activity would be restricted to the synapse, such that FISSEQ signals would only originate from the synapse itself.

Note that protein localization at the synapse, as is exploited in this strategy, can be highly precise, perhaps due in part to synapse-localized translation in some cases[631,244].

6.5.4 Prospects for informatic deconvolution

In the case where two DNA molecules are sequenced within a single optical resolution voxel (e.g., a diffraction-limited spot), the information content of each base sequenced is 3.25 bits[††] (whereas 4 bits would be recovered if it could be known which amplicon generated which signal). *Informatic deconvolution* is the process of providing additional information in order to make up for the missing 0.75 bits and generate a full sequence pair. This additional information can come from two sources: priori knowledge of all sequences in the pool, or additional "programmatic sequencing" reactions. It would also be necessary to append additional sequence tags to the barcodes, indicating which barcodes are pre-synaptic and which are post-synaptic. Otherwise, only an unordered pair of sequences is attributed to each synapse.

Known barcode pool Consider first the problem of adding information from the known barcode pool. Let n be the number of neurons (unique, known barcodes), s be the number of synapses observed and N be the barcode length. In a given resolution voxel (e.g., synapse) containing both pre-synaptic and post-synaptic barcodes, the observation consists of a list of unordered pairs corresponding to the labels at each base, such as "(A and T) or (T and A)".

Denote the observation as x. There are $< 2^N$ sequence pairs consistent with x, given no prior knowledge: the scaling will be $(\frac{1}{4} \times 1 + \frac{3}{4} \times 2)^N = 1.75^N$ on average. These are embedded in a space of 4^{2N} possible sequence pairs independent of the observation. We know that at least one pair of barcodes, each chosen from the set of size n of known barcodes, is consistent with x. Perfect deconvolution is possible if and only if there is no other such pair which is also consistent with x.

For random sequences, the probability that any other pair of known barcodes is also, by chance,

[††]Four of 16 possibilities (AA, TT, CC or GG) each convey 4 bits of information since the bases of both strands are disambiguated, whereas the remaining 12 possibilities convey only $4 - 1 = 3$ bits of information since the bit specifying which base goes with which strand is left ambiguous. Thus the Shannon entropy is on average $\frac{4}{16} \cdot 4 + \frac{12}{16} \cdot 3 = 3.25$ bits per base sequenced.

consistent with x is

$$< \frac{n^2 \cdot 2^N}{4^{2N}} = n^2 \cdot 2^{-3N}$$

Since there are s synapses in the brain, the expected number of ambiguous synapses is then $< s \cdot n^2 \cdot 2^{-3N}$.

For a mouse brain with $s < 10^{12}$ and $n = 10^8$, the expected number of ambiguous synapses via informatic deconvolution of pre-synaptic and post-synaptic barcodes is at most $S_{\text{ambiguous}} = 10^{28} \cdot 2^{-3N}$. For $N = 30$, $S_{\text{ambiguous}} = 8$ whereas $S_{\text{ambiguous}} = 0.0002$ for $N = 35$. Therefore, 30-35 base barcodes could potentially lead to nearly ambiguity-free connectomes via informatic deconvolution at the synapses.

Supplementary Figure 6.3 shows a simulation of these statistics for small N and comparison with the above simple model.

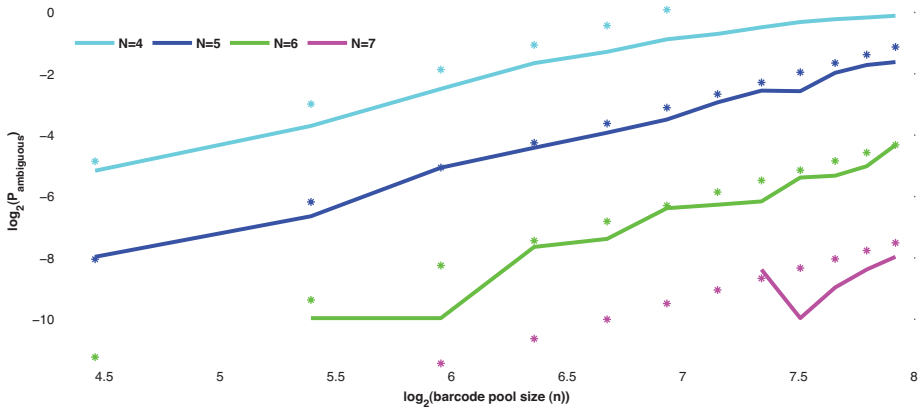

Figure 6.3: Scaling properties of informatic deconvolution from a known barcode pool. Simulated barcode pools were generated randomly from an equal mixture of A, T, C and G (with a check to ensure uniqueness within the pool) and the probability of ambiguous informatic deconvolution was evaluated as a function of the barcode length N and barcode pool size n. Solid lines: simulations. Dotted lines: the model $\log_2(P_{\text{ambiguous}}) = 2 \times \log_2(n) + (\log_2(1.75) - 4) \times N - 1$.

Programmatic sequencing Additional *multi-base* sequencing reactions can also provide the missing 0.75 bits of information. These can be implemented using a sequencing by ligation strategy,

which selects for correct hybridization of a multi-base ligation probe. Ligation efficiency is decreased by orders of magnitude by the presence of a single nucleotide mismatch within a symmetrical 12-base footprint, six bases on each side of the single-strand break[535].

As an example, through the appropriate choice of ligation probe-sets, a fluorescent signal could be indicative that bases 1 and 2 of the read are the *same* base (reminiscent of a logical AND gate). If we had previously observed A and T signals at base 1, and A and G signals at base 2, this additional information would unambiguously imply that the two barcodes begin with the sequences "AA" and "TG" (the alternative possibility "AG" and "TA" is ruled out because the extra multi-base read has indicated that the first two bases are identical in at least one of the molecules). Such "parity" sequencing reactions must be programmed, either through the design of the template molecules, or through the enzyme and sequencing reagents interrogating the template molecules. This scheme would increase the number of required biochemical cycles.

USING INFORMATIC DECONVOLUTION FOR FISSEQ ERROR-CORRECTION FISSEQ inside the cell's nucleus can "average" over many rolonies corresponding to the same cell-barcode, allowing unambiguous knowledge of the *pool* of all cell-barcodes (not to mention their corresponding soma positions) via nuclear FISSEQ. This knowledge could be used – in a manner analogous to informatic deconvolution – to disambiguate error-prone sequencing reads from the synapses, which might derive from only 1-2 rolonies. This could be valuable, for example, for "factoring out" the error rate associated with the reverse transcriptase step in RNA FISSEQ. Note that, unlike in traditional bulk sequencing library preparation, FISSEQ does not involve sequential, bottlenecked amplification steps that can, e.g., "lock in" polymerase errors generated during the first few cycles of PCR; indeed, in rolling-circle amplification, only the original template molecule itself is copied.

6.5.5 Hybrid strategies

Hybrid strategies could combine favorable aspects of BOINC and FISSEQ-BOINC. One possibility is as follows: 1) first localize each neuron and identify its corresponding barcode via FISSEQ of the nuclei, and then 2) subsequently subject the entire brain, post-FISSEQ, to bulk sequencing to determine the barcode *pairs* via BOINC[734,532,433]. In this scenario, only (multiple redundant copies of) a single barcode – the self-barcode of a particular cell – is in situ sequenced in each nucleus, greatly reducing the optical resolution requirement and hence allowing a significant speedup.

Cost estimate: To image only the nuclei, which are separated by $(1\,\mathrm{mm}^3/100000)^{1/3} \approx 20\,\mu\mathrm{m}$ on average, a wide-field scan could first be applied to locate the nuclei. Then, using random-access confocal scanning in 3D, at 10 ms dwell time per pre-identified nucleus (a somewhat arbitrary estimate), the per-cycle imaging time would be $10\,\mathrm{ms} \times \varrho \times 420\,\mathrm{mm}^3$ where $\varrho = 100\,000/\mathrm{mm}^3$ is the approximate density of neuronal nuclei. Thirty cycles of FISSEQ on all mouse brain neuronal nuclei would then take only five months on a single machine, i.e., for a cost in the range of $200k. The tissue could then be subjected to bulk sequencing of barcode *pairs* corresponding to synaptically connected cells, at the cost associated with BOINC, i.e., potentially <$1M[433]. The hybrid process could thus achieve a 1-year project cost in the $1M range for a whole mouse brain barcode-based connectome with precisely known soma position for each barcoded cell.

Rather than believe that Watson and Crick made the DNA structure, I would rather stress that the structure made Watson and Crick.

Francis Crick

7

DNA as an Informational Substrate

Much of this thesis has focused on the use of DNA for the storage of *arbitrary* information, as opposed to just *genetic* information – for example, we have studied the use of DNA as a connectomic barcode[734], as proposed and experimentally pursued by Zador et al, or as a local storage medium for time traces of neuronal activity[373], as suggested by Kording et al and pursued in our own recent work. Here we expand on this notion, demonstrating or proposing several other applications of DNA as a

nanoscale informational substrate.:

- As a broadly applicable tool, we harnessed a previous result[496] on the mechanism rolling circle ssDNA production as a means for production of *arbitrary sequence* ssDNA inside the E. coli bacterium. This has potential applications to genome engineering, in-vivo structural DNA nanotechnology, and other areas.

- We proposed a molecular recording device for time-series of biological sensor readings which occur on a timescale of minutes to hours (e.g., characteristic of many changes in gene expression), rather than the milliseconds to seconds regime for which the polymerase-based tickertapes studied in Chapter 3 and Chapter 4 were designed. The proposed systems harness the natural process of CRISPR mediated immunity in bacteria[430], which constructs a linear array of DNA sequences harvested from pathogenic invaders. Such slow-timescale molecular recorders may be more practical (e.g., non-toxic to the host cell) in the near term, especially as they rely on the "transplantation" and judicious combination of existing, largely unmodified, molecular machinery rather than on the engineering of entirely novel molecular mechanisms.

- The sequence-specific hybridization of complementary single-stranded DNA (ssDNA) strands has led to an explosion of research into *structural DNA nanotechnology*, wherein many ssDNA strands of user-programmed sequence self-assemble in solution to form a user-defined nanoscale object or machine[581,525]. We consider both an application of this methodology to constructing one-dimensional nano-arrays, and a proposed extension of it – a series of experiments and design exercises, aimed at uncovering principles for the integration of bottom-up nanotechnology based on self-assembly with top-down nanotechnology based on photolithography. This has seeded a research program based on harnessing nanoscale combinatorial molecular recognition coupled with DNA synthesis, sequencing, microscopy and photolithography to synergize top-down and bottom-up approaches, sidestepping the limits of each.

7.1 In-vivo arbitrary sequence ssDNA production

We (joint with Kevin Esvelt) have demonstrated in-vivo arbitrary-sequence ssDNA production. In rolling-circle replication, the plus-strand origin of a circular plasmid or virus is nicked by the viral replicase (gII protein) and extended by host DNA polymerase, displacing the existing strand[542]. After replicating the entire genome, the replicase again nicks the DNA at the origin and re-circularizes the displaced strand into a circular ssDNA. Rolling-circle origins from several phage, virus and plasmid species can be separated[496,161] into "start" and "stop" signals encoding ssDNA synthesis and termination, respectively Figure 7.1. By flanking any arbitrary (e.g., genome-integrated) dsDNA sequence with these signals, it should be possible to generate circular ssDNA of that sequence within the cell Figure 7.1.

We first verified that gII protein could drive replication of an f1-origin-containing plasmid which lacked any other mode of replication; even in the absence of the f1 minus-strand origin, exogenously supplied gII drove replication of a plasmid containing the f1 plus-strand origin as its sole origin of replication (presumably due to spontaneous priming of minus-strand synthesis by endogenous RNAs). Thus, gII is sufficient for replication via ssDNA production in the context of the E. coli host cell; the full machinery of a helper phage, as was used in previous work in in-vivo ssDNA[405], is not necessary.

Using a pUC plasmid (UK-civMAGE-3) bearing the f1-origin signal, and a separate SC101 plasmid (ST-gII-m35) driving expression of f1 gpII, we verified ssDNA production using a Cy5 labeled fluorescent probe oligo in an agarose gel (containing Mg^{2+} to aid in probe hybridization) Figure 7.5B. Probe hybridization was abolished in the absence of gII protein or using a nonfunctional mutant gII protein driven from the same plasmid. Thus, gII can drive ssDNA production from a plasmid which also replicates via pUC.

Interestingly, we found Figure 7.2, that expression of gII from a construct with weaker RBS strength gave more ssDNA production (and faster f1-based full-plasmid replication) than expression of gII

from a construct with higher RBS strength.

With these basic parameters established, next steps could include attempting to drive ssDNA production from a (plasmid-based or genomically-integrated) split origin-terminator setup, rather than a single-origin plasmid.

We foresee at least two potential applications for arbitrary-sequence in-vivo ssDNA production, as shown in Figure 7.4A: multiplex genome engineering and in-vivo nano-assembly. In particular, in-vivo arbitrary sequence ssDNA production could lead to a strategy, shown in Figure 7.5 for achieving continuous multiplex automated genome engineering (cMAGE) without complex machinery or researcher intervention. Whereas traditional MAGE[687] relies on electroporation to deliver oligonucleotides to the cell, cMAGE produces all ssDNA continuously from a single synthetic plasmid, by copying one strand via the rolling circle replication machinery of filamentous phages. In principle, our strategy avoids problems associated with transformation efficiency, strand concentration, and cell death caused by electroporation, as well as eliminating the need for complex machinery or researcher intervention, thus potentially providing a significant workflow improvement with respect to traditional MAGE.

In particular, we proposed that the resulting circular ssDNA could be cut into defined linear oligonucleotides by a Type II CRISPR system[430] and incorporated into the replicating genome by binding to the lagging strand during genome replication at multiple target sites within the cell, as in traditional MAGE[687]. Consequently, only one plasmid would need to be delivered into the cell to generate multiple copies of many distinct oligonucleotides. Furthermore, because Type II CRISPR systems function robustly in many cell types and rolling circle replication via an ssDNA intermediate is a general method occurring in all kingdoms of life[192], cMAGE could then be applied to any cell type into which a single dsDNA plasmid can be delivered, dramatically expanding the *range of cell types* amenable to multiplex genome engineering. While we have not yet had success with this CRISPR-based ssDNA cutting strategy in-vivo, we have initiated research into other mechanisms of in-vivo sequence-specific ssDNA

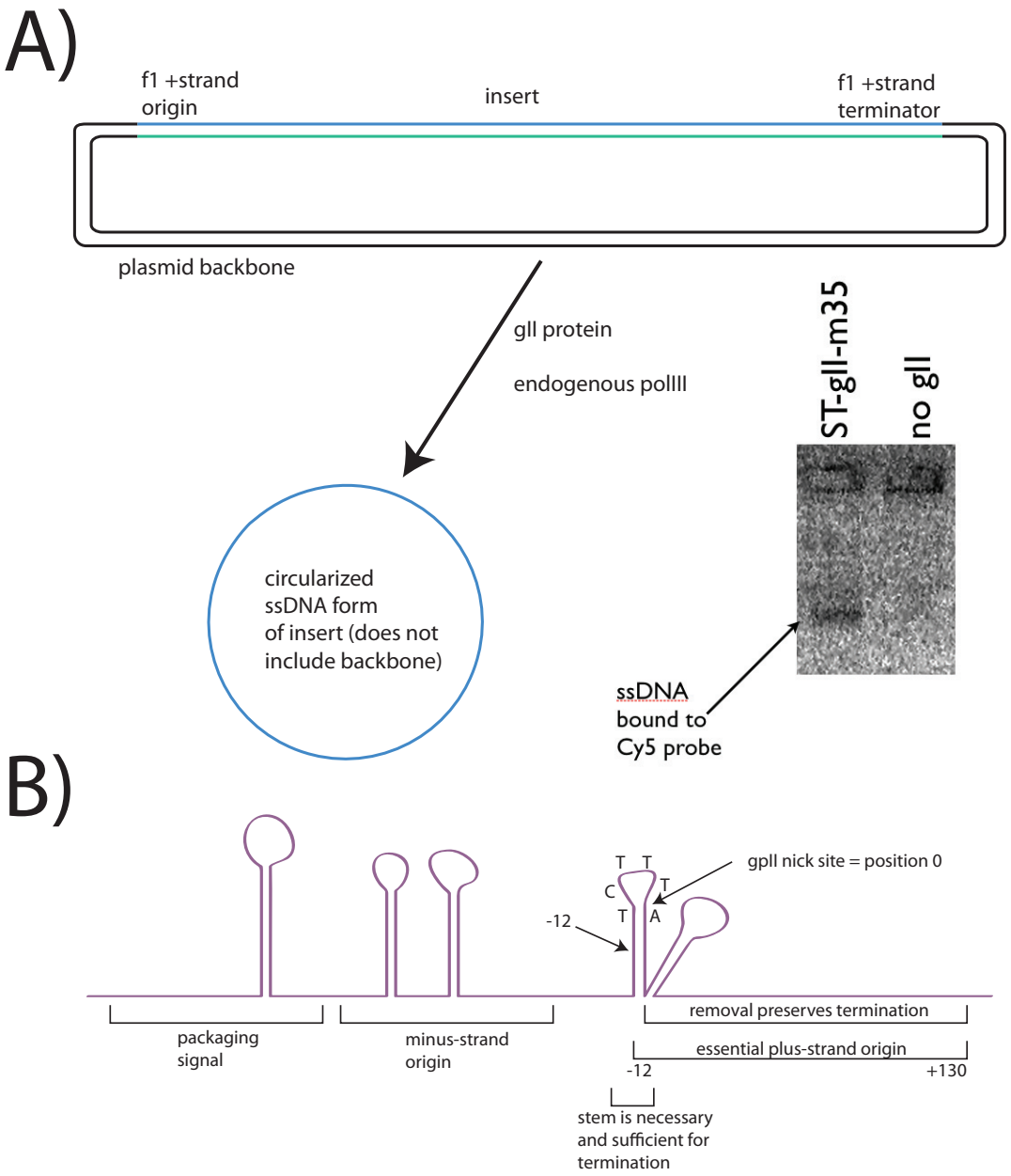

Figure 7.1: In-vivo arbitrary-sequence ssDNA production. A) Strategy for producing arbitrary-sequence circular ssDNA from a dsDNA parent plasmid. The inset shows a probe-labeled agarose gel demonstrating ssDNA production (using a single origin rather than a split origin-terminator system) in the presence of gII protein but not in its absence. B) Structural and sequence motifs in the filamentous phage origin of replication, which are used to construct start and stop signals for ssDNA production.

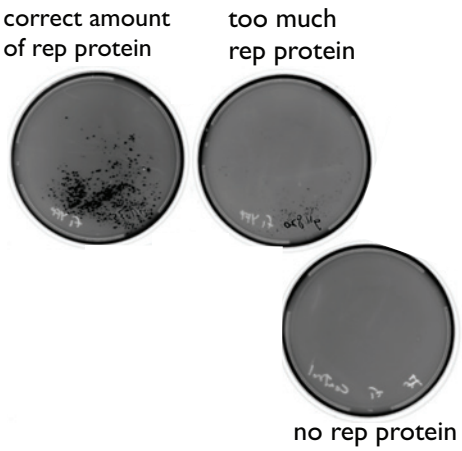

Figure 7.2: Antibiotic selection was used to measure replication from an f1 origin – which occurs via a single stranded intermediate – in the presence of varying levels of gII protein, supplied from a separate plasmid. Production of GII from a comparatively low-strength RBS and medium-copy expression plasmid led to optimal ssDNA production. Only under these "optimized" expression conditions did we measure significant and robust ssDNA production through the hybridization probe assay.

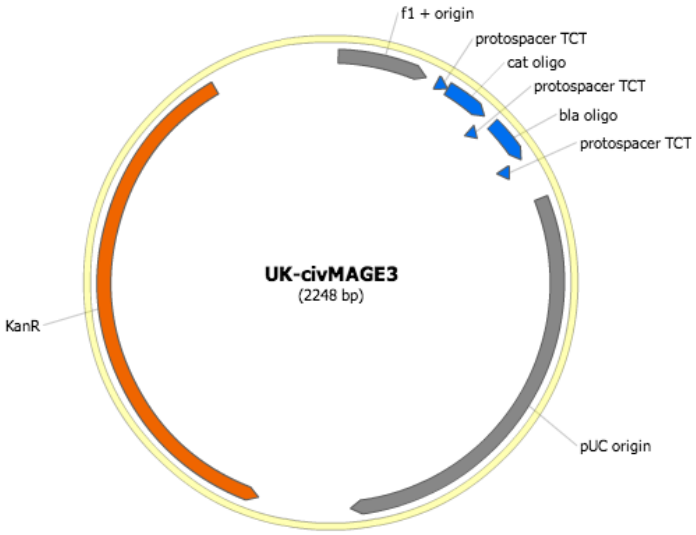

Figure 7.3: Layout of the UK-civMAGE-3 plasmid used for testing in-vivo ssDNA production driven by gII protein.

Applications:

1) chop up the DNA and use it for highly efficient genome editing (continuous MAGE)

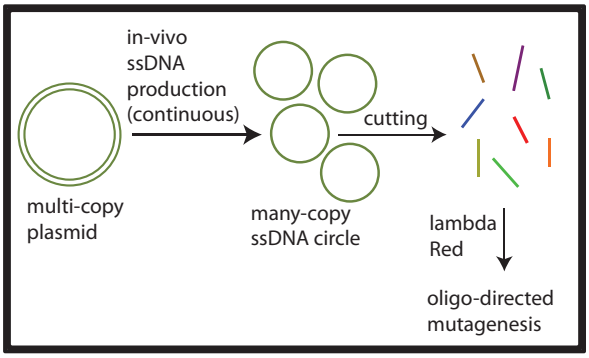

2) fold nanostructures in-vivo to arrange proteins into sub-cellular devices

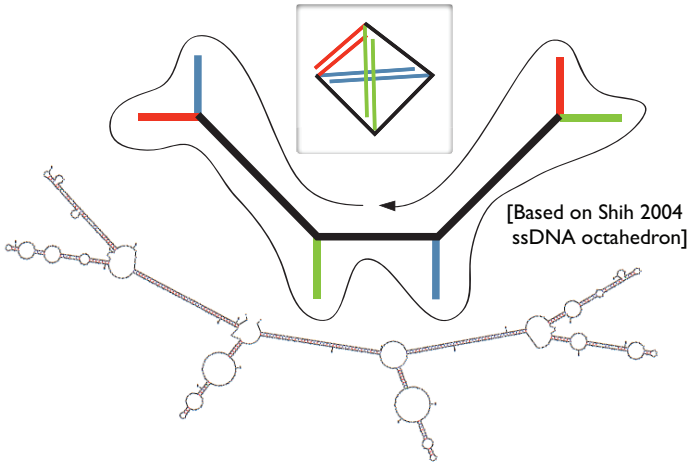

Figure 7.4: Potential applications of in-vivo arbitrary-sequence ssDNA production.

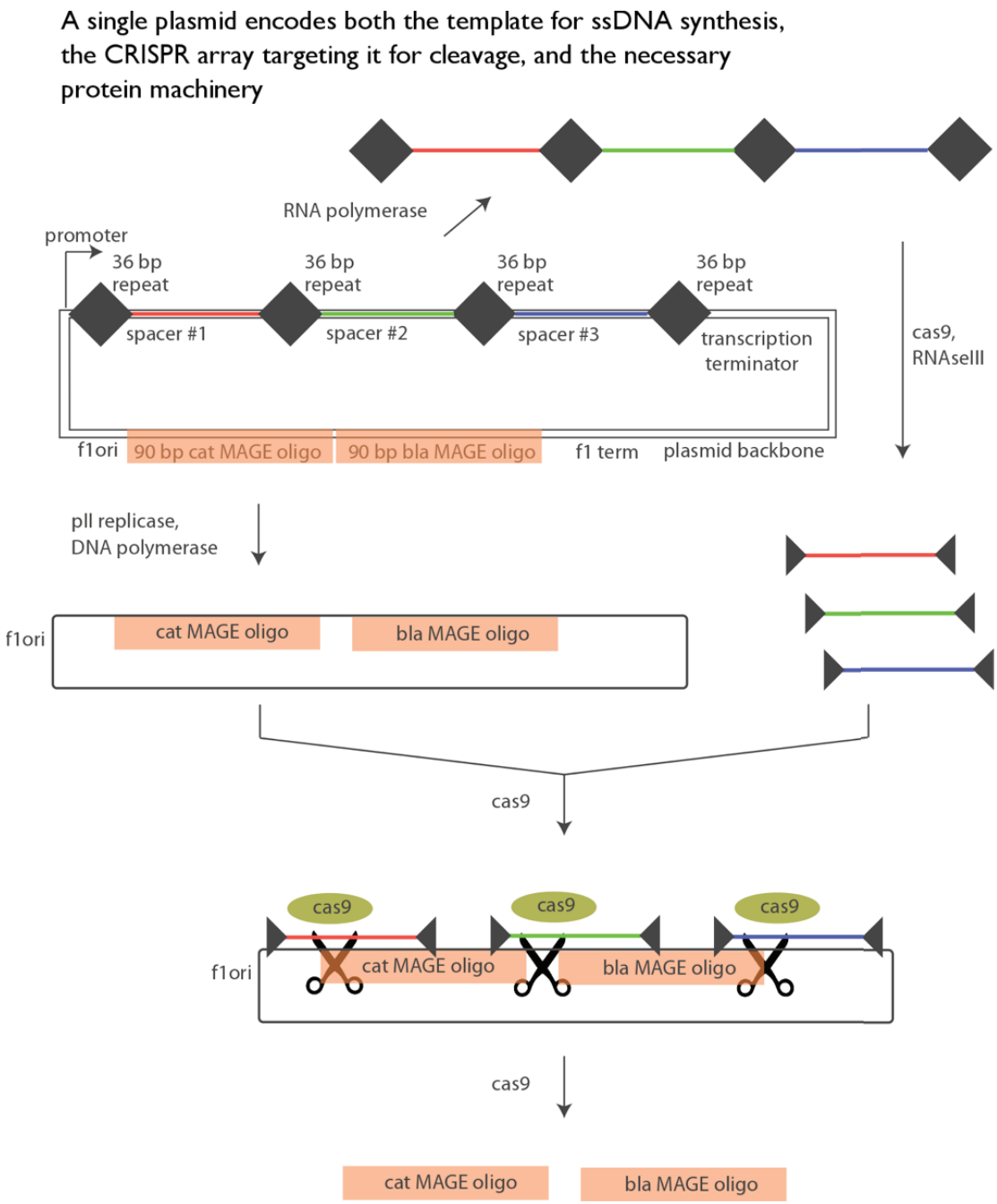

Figure 7.5: Design scheme for continuous multiplex genome engineering, showing a proposed CRISPR-based ssDNA cutting mechanism. We have since found that this cutting mechanism does not appear to work as intended, and alternatives are being pursued.

cutting. One mechanism under consideration is the use of holiday junction resolvase enzymes[72] to cut immobile, designed junction structures that fold in the ssDNA form of the plus strand, but which are not present in the dsDNA form.

Arbitrary sequence in-vivo ssDNA production could also find application to in-vivo nano-fabrication, perhaps using designs inspired by William Shih's 2004 single-stranded octahedron[603]. We have designed variants of this system which would strictly use a single ssDNA (whereas Shih's original paper used 5 additional short synthetic strands), by replacing DX crossover regions with simple duplexes, as shown in Figure 7.4B.

7.2 Slow timescale tickertapes

Clustered regularly interspaced short palindromic repeats (CRISPR) mediated immunity in bacteria consists of an immunization stage, in which invading viral nucleic acids are incorporated into a genomic locus as roughly 30 nucleotide long "spacers", followed by an immunity stage, in which RNAs expressed from the spacer DNAs are used to guide the cleavage of subsequent instances of the invader. The spacers are arranged in a linear array, separated by repeat sequences, and such that nearly all – though perhaps not strictly all – new spacers are incorporated at the far end of the array, closest to the so-called "leader" sequence[727]. With Kevin Esvelt, Alex Chavez and Jonathan Gootenberg, we have designed a system for molecular recording of sensor time-series in which the sensor biases the relative rate of incorporation of two competing spacer sequences.

This scheme relies on two key insights: 1) the availability orthogonal CRISPR systems to avoid self-targeting and crosstalk[188] and 2) the ability to generate a dsDNA sequence in-vivo using a genomically encoded template, such that the dsDNA sequence generated is not itself present in the genome – this prevents the Cas9-based cleavage mechanism from cutting the host cell's genome. This latter capability relies on the in-vivo ssDNA production mechanism discussed above, specifically as applied

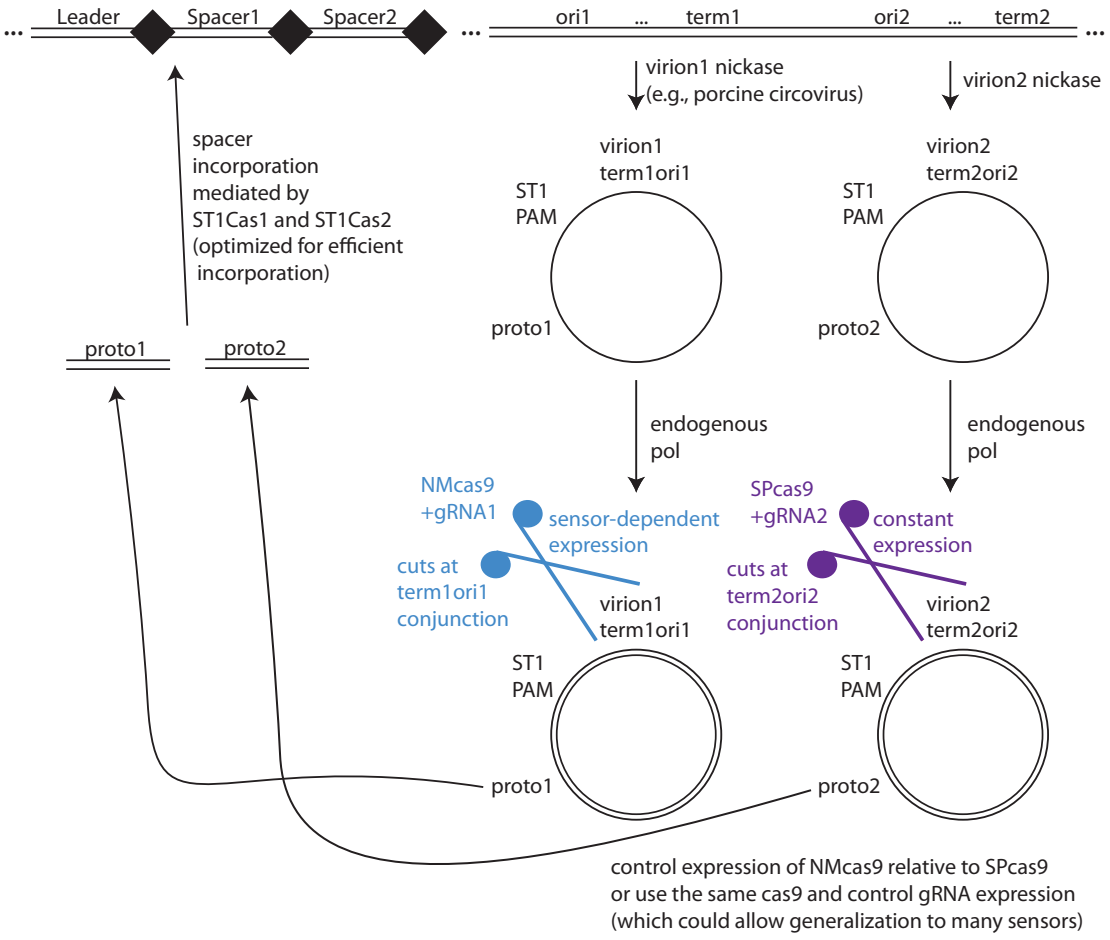

Figure 7.6: Design sketch for an intracellular molecular recording device operating on slow timescales, in which a time series of sensor values is recorded as a string of CRISPR spacer sequences incorporated into a genomic locus.

to genome-integrated origin-terminator constructs, in which the direct conjunction of the terminator and origin sequence is present in the synthesized circular DNA, but not in the genomic template. This mechanism for expression of DNA circles from a genomic template is similar to the mechanism of induction used by integrating ("temperate") filamentous phages[542], such as CTXϕ and its satellite phages. In the present scenario, it would need to be adapted to mammalian chromosomes and mammalian rolling circle viruses such as the porcine circovirus[192]. Partial homology between origin and terminator sequences might also need to be mutated away to completely prevent cutting of the genome-embedded sequences.

It would also likely be necessary to optimize the absolute and relative expression of Cas1/Cas2, and perhaps further optimize the system, via directed evolution of these proteins, in order to ensure sufficiently high spacer acquisition rates to achieve time-resolved recording on timescales of practical interest.

7.3 Autonomously stretching and directly visualizing a single DNA double helix: a route to versatile 1D nano-arrays?

Using structural DNA nanotechnology[525], we (joint with Mingjie Dai and Ralf Jungmann) have designed and experimentally validated a system to stretch out a single DNA double-helix or ssDNA strand of arbitrary user-programmable sequence within a defined "frame" structure. This could be used to display the strand for high-resolution microscopy studies (e.g., electron microscopy or atomic force microscopy), or to harness it as a completely addressable scaffold – down to the 0.34 nm linear precision of the DNA base pair – for arranging nanoscale components along a 1D array.

The DNA double helix represents a versatile substrate for constructing one-dimensional nanostructures: arbitrary DNA sequence motifs can be arranged in any order along its length, allowing sequence-specific DNA binding moieties to be placed in close proximity. To capture the potential

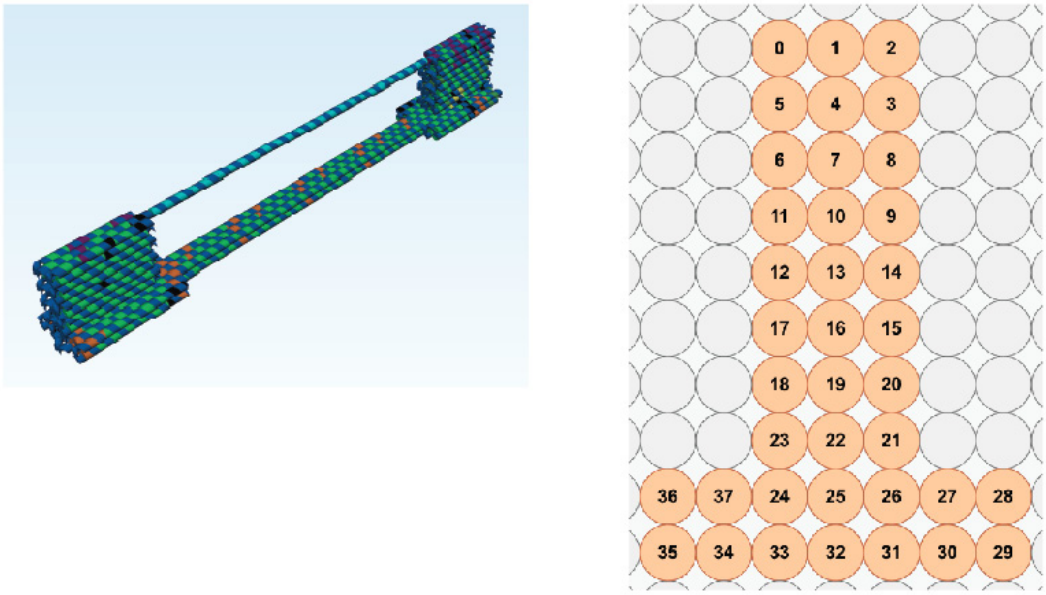

Figure 7.7: Design of the DNA tightrope in caDNAno2. The three-dimensional view and square-lattice [341] cross-section of the scaffolded DNA origami nanostructure are shown. Each cylinder or circle represents a single DNA double helix, linked with its neighbors by single-stranded crossovers, in a pattern reminiscent of basket weaving.

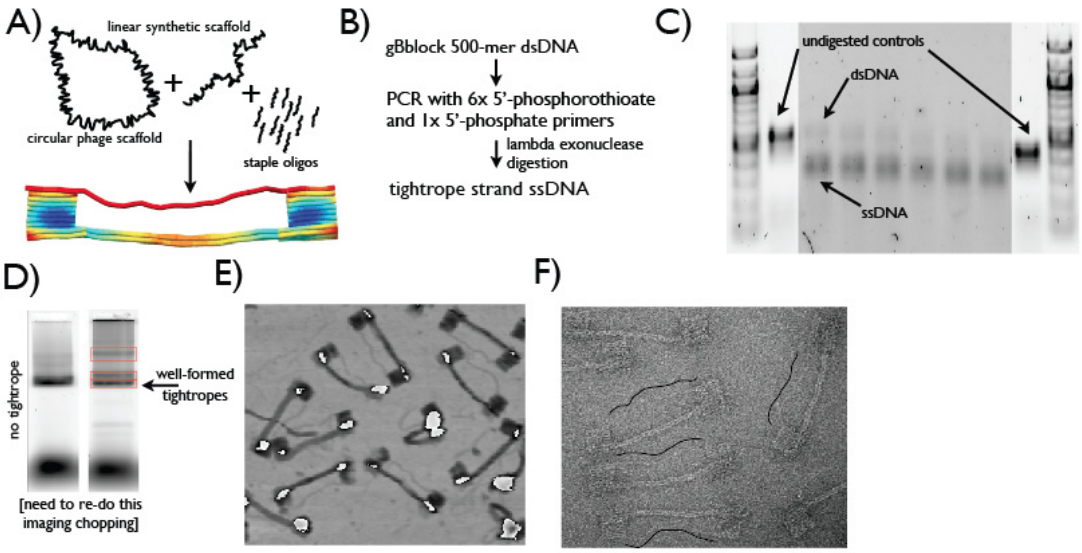

Figure 7.8: Construction and imaging of the DNA tightrope. A) The structure is assembled by combining circular m13mp18 phage ssDNA with DNA origami staple oligonucleotides and with a user-designed linear ssDNA strand generated from a synthetic dsDNA by exonuclease digestion. 3D model produced by CanDo[347]. B) Scheme for amplification and exonuclease digestion of the linear strand. C) Agarose gel illustrating the near-complete conversion of dsDNA to ssDNA by exonuclease digestion, for various lengths of starting dsDNA. D) Agarose gel confirming folding of the scaffolded DNA origami structure. E) AFM image showing visible tightropes. F) Negative stain TEM image showing visible DNA tightropes; black lines are drawn in, offset from the DNA tightropes, to highlight the paths of the DNA tightropes.

of the DNA helix for nanotechnology, it would be useful to constrain DNA to adopt a straightened linear conformation, rather than a random coil. While we have elsewhere assisted in demonstrating a DNA elongation and deposition method that relies on macroscale instrumentation[516], here we develop a simple and customizable DNA origami platform that stretches an arbitrary double-stranded DNA segment like a tightrope across two rigid pillars with a defined pillar-to-pillar spacing. In addition to straightening the DNA, the platform is easy to identify by imaging and can be functionalized with organic or inorganic groups at many addressable sites. The tightrope can be placed in tension by modulating its length relative to that of the supporting structure. This system should facilitate the rapid prototyping of one-dimensional nano-systems.

The support for the track was designed using caDNAno[167] and is assembled using standard 3D

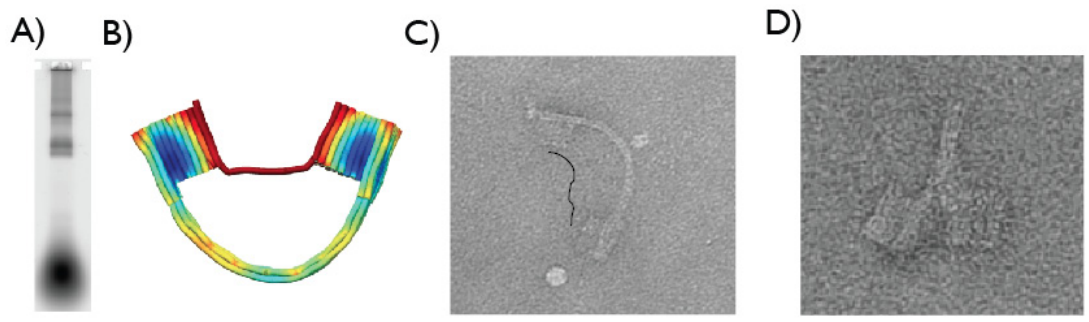

Figure 7.9: Effects of shortening the tightrope. A) Agarose gel showing successful folding of tightrope structures with shortened linear gBlock strands. B) CanDo [347] analysis showing the expected bent structure backbone resulting from mechanical strain. C) TEM image confirming the bent configuration; the tightrope is visible and an offset black line is drawn in to highlight its position. D) Another configuration observed in TEM, probably representing mechanical buckling of the structure backbone under strain.

scaffolded DNA origami techniques[166,108], whereby the m13mp18 genome is folded via 175 short staple strands. The tightrope strand begins as a 300 to 500-mer dsDNA "gBlock" available commercially from Integrated DNA Technologies. This gene block is then amplified by PCR with a phosphorothioate forward primer and a phosphate reverse primer, and the amplicons are subsequently exposed to lambda-exonuclease. The phosphate-primed strands are digested by the exonuclease, while the phophorothioate-modified strands remain intact, and can then be integrated with the support to form the ssDNA tightrope.

7.4 NM2CM: STRATEGIES FOR INTEGRATING TOP-DOWN AND BOTTOM-UP NANOTECHNOLOGY, TO CONSTRUCT FULLY PROGRAMMABLE BIO-CHIPS

No integrated architecture has yet been proposed which fully specifies the steps necessary to produce structures with a) overall sizes on the scale of today's computer chips (centimeters), b) addressable features on the 10 nm scale, and c) the ability to attach a wide range of discrete components at customizable locations. We have performed initial theoretical and experimental investigations into a scheme for nanometer-to-centimeter fabrication integration via top-down organization of DNA nanorods using

DNA hybridization interactions. In particular, George Church and I – leveraging previous work by the Church lab and collaborators on lithographic fabrication of periodic, chemically uniform nano-arrays for sequencing applications, as well as of aperiodic DNA microarrays – defined a deterministic strategy for ordering molecular components across millimeter or centimeter length scales while (we expect) maintaining few-nanometer precision in the placement of individual components. We proposed a solution that combines two levels of photo-lithography with DNA nano-structure patterning.

7.4.1 de Bruijn rod bridging

Although conventional lithographic techniques can produce patterns at high spatial resolution, they provide no means to specifically interface these patterns with diverse molecular-scale components. In contrast, the self-assembly of information-bearing bio-polymers exploits the specificity of molecular recognition to generate combinatorial numbers of specific binding interactions. Here we outline – based on a proposal by George George, which was created in response to discussions with the author and others – a method which specifies the construction of an array of uniquely addressable bio-molecular lattice points (UALPs) on a surface, with spacing on the order of 500 nm. Such an array could be used to provide docking and interconnection sites for inorganic components templated on DNA nanostructures. Such an array could also serve as a surface-based seed layer for growth into the third dimension via templated self-assembly of subsequent layers. Several capabilities in nanotechnology can be leveraged to create fully addressable nano-arrays.

1) Construction of periodic spot arrays: Interference photo-lithography[308] allows rapid and low-cost fabrication of periodic patterns over large areas. The resulting chips may consist of an array of positively charged amino-silane spots on silicon or glass surfaces. Changing the pitch is merely a matter of changing the incidence angle. As a rule of thumb, it is easy to obtain a 3× ratio between pitch and spot diameter but difficult to obtain a 10× ratio: thus 300 nm spot diameter at 1000 nm pitch is feasible, as is 100–150 nm spot diameter at 400 nm pitch, but 200 nm spot diameter at 2000 nm pitch

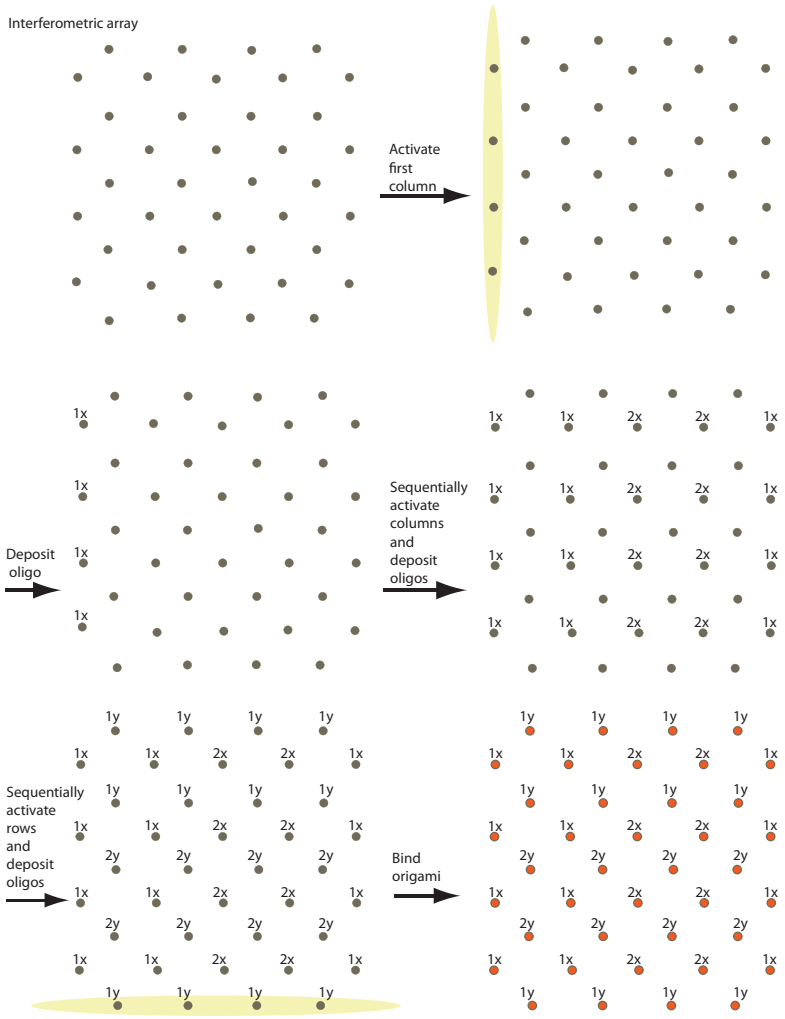

Figure 7.10: Construction of DNA spots in a de Bruijn pattern. A diffraction-limited UV line focus, produced by a cylindrical lens, is scanned through a series of discrete positions, aligned to a nano-grid fabricated using interference lithography. The line foci sequentially activate lines of nano-grid spots along the x or y axes via nitro-benzyl chemistry, followed by deposition of the corresponding oligo type. Each axis corresponds to a De Bruijn sequence of the different spot types, with sub-sequence length $s = 2$. Thus, each pair of consecutive DNA spots along an axis uniquely identifies the location along the axis. The alphabet size n is the number of DNA spot types along each axis. Shown here is the De Bruin sequence with $n = 2$ and $s = 2 : 1122(1)$. Note that, for a pattern with 10^8 UALPs, $n = 100$ and $2 * 10^4$ separate oligo deposition steps are required. Assuming that one activation and deposition step occurs every 5 seconds, the entire process (up to rod deposition) takes one day. For comparison, if each spot had to be individually activated and deposited at 5 seconds per step to ensure unique addressability in 2D, the process would take 5 seconds $* 10^8 = 15$ years. The use of a de Bruijn spot pattern and cylindrical lens allows us to circumvent this problem, as would the use of DMD-driven parallel oligo synthesis or deposition.

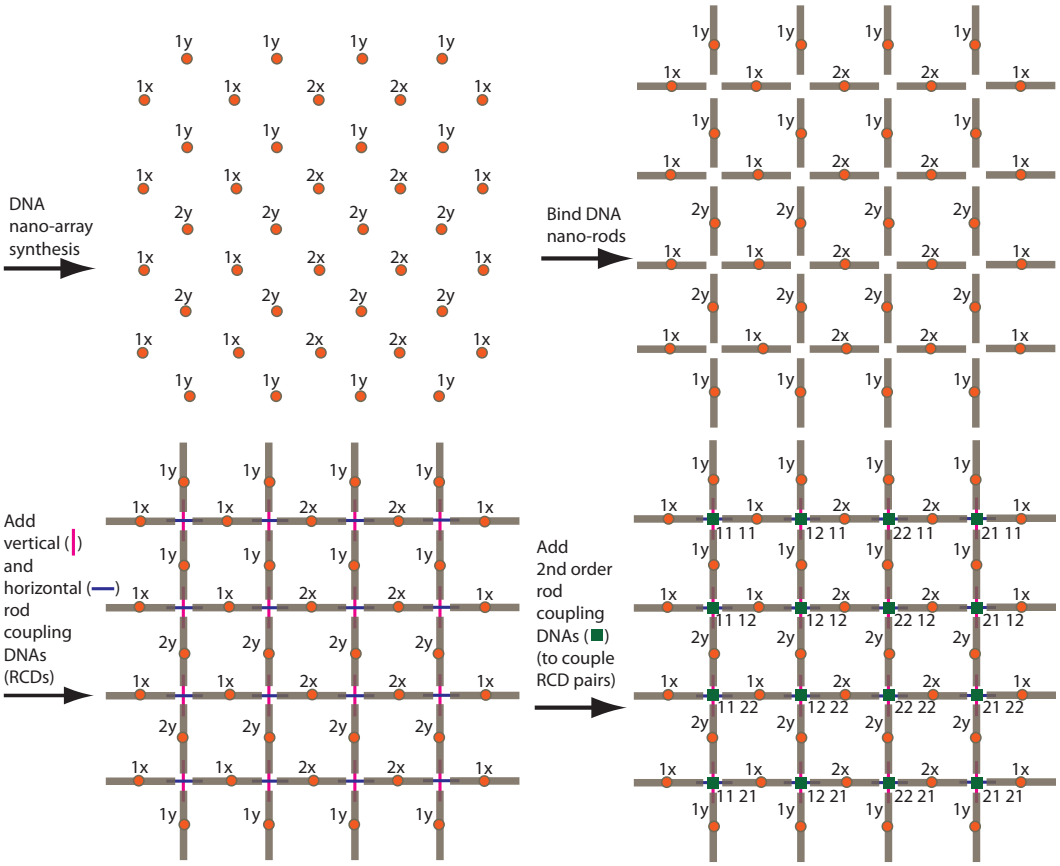

Figure 7.11: Conversion of the de Bruijn DNA origami pattern to a set of uniquely addressable bio-molecular lattice points (UALPs). Rigid DNA nanostructure rods bind to individual spots on the surface via binding sites on the DNA origami adaptors (orange). Contact points between rods bound to adjacent spots define unique x or y coordinates. Cooperative hybridization to markers (rod coupling DNAs) indexing these x and y coordinates allows unique addressing of 2D positions. Rods have directionality to define ordered pairs. i_x and i_y rod types are distinct to prevent mixing of the two coordinates. The total number of UALPs along an axis is n^2, where n is the number of distinct spot types per axis. The total number of UALPs in 2D is n^4. In the example shown: there are $n = 2$ distinct spot types, $n^2 = 4$ unique positions along each axis, and $n^4 = 16$ UALPs in 2D.

may not be feasible.

2) Decoration of periodic spot arrays with DNA nano-structures at one-to-one occupancy: Rolling circle nano-balls (rolonies, see Figure 7.12) have been shown to bind size-matched positively charged surface spots fabricated by methods such as interference lithography[170]. Rolonies sterically and electrostatically exclude one another on size-matched spots. Therefore the rolony concentration in solution can be held well above that needed to achieve a Poisson average spot occupancy of one, driving the system to stoichiometric spot occupancy. Rolonies have customizable size via the duration of the RCA reaction and each rolony may possess a unique 5' end with a hybridization-addressable sequence, e.g., defined by an overhang on the RCA primer.

Similarly, DNA origami bind to size and shape matched e-beam lithographic spots with one to one occupancy[345], and this property should extend to size-matched spots fabricated by interference photolithography or other low-cost methods for creating periodic arrays of nano-sized spots. Lambda-inside-m13 phage scaffolds have also been used to make lambda-sized origami. Furthermore, single-stranded tile (SST) structure fusion may be a viable approach to make larger SST structures[695,723]. All these facts suggest that 200 nm × 200 nm rectangles or circles should be achievable and possibly larger.

Nano-structures would be greatly superior to rolonies due to their precision and addressability. Note that in practice, attaching rolonies to DNA origami in a well-controlled fashion has seemed non-trivial due to non-specific aggregation.

3) Rigid DNA rods on the 1 um scale: 6-helix-bundle DNA origami rods span 450 nm per monomer and 900 nm per dimer, while the largest fully addressable 12-helix-bundle single-stranded tile rods currently span 1 um.

4) Custom aperiodic oligonucleotide arrays with micron-scale feature sizes: these can be readily generated using light-driven chemistry[112,613], thus placing distinct user-defined DNA sequences at defined locations on a surface. Digital micro-mirror devices (DMDs) and spatial light modulators (SLMs) can be used to activate chemical steps in parallel, or alternatively, 2D or 3D spot-scanning or line-scanning

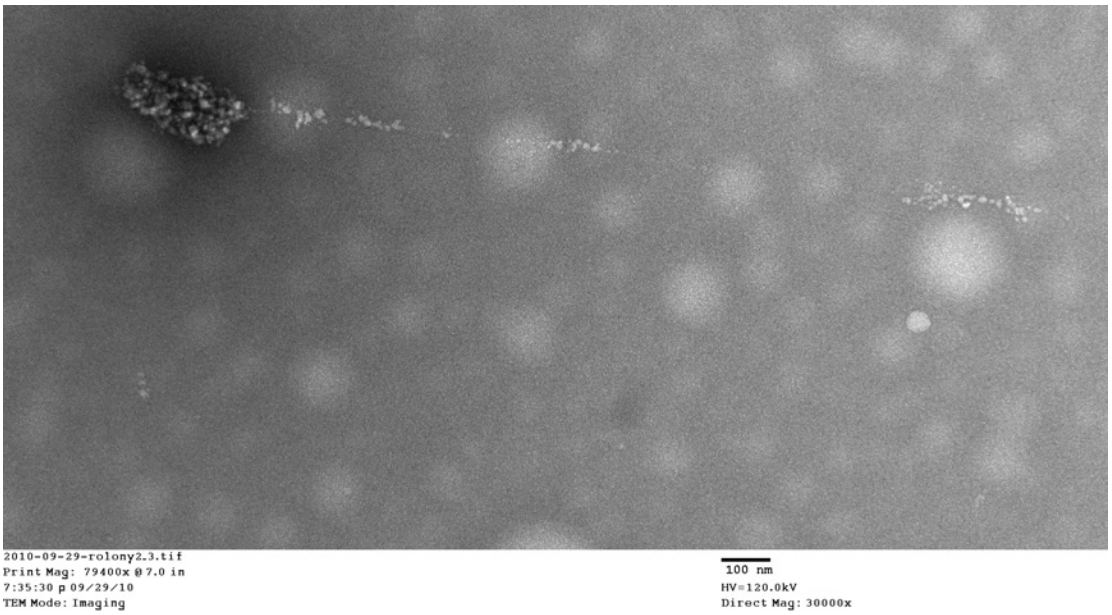

Figure 7.12: Negative stain TEM image of a single rolony on a glow-discharged carbon grid-suspended film.

optics can be used in a serial process. Any of these technologies can in principle generate diffraction-limited feature sizes on the order of 300 nm for UV light. In practice, oligonucleotide arrays have been limited to feature sizes of approximately 2 um, due to light scattering by the liquid medium in the synthesis flow cell. The feature size limit imposed by light scattering depends on the tolerance of the system with respect to optical crosstalk between spots: probably the micro-array manufacturers are being quite conservative about avoiding crosstalk at the expense of larger feature sizes. In the nm2cm application, we may be able to go well below 2 um features with the same optical setup if tolerances are high compared to those for oligonucleotide array synthesis. Furthermore, scattering can be suppressed by several methods, including drying the flow cell between chemical steps and using a dipping lens to limit the optical path length through the fluid. In principle there is no fundamental difference in theoretically attainable resolution between standard lithography and light-directed DNA synthesis/deposition.

Furthermore, the required resolutions of the optical systems involved depend on the parameters

of the components used in later stages of the fabrication process (see below). In the rod-bridging strategy described below, if interference lithography could pattern 200 nm spots at 2 um pitch, and if a 2 um origami rod was available, then DMD optics at the conservative tolerances used by micro-array manufacturers would already suffice for aperiodic light patterning, since DMD-directed DNA synthesis can already achieve $\sim$2 μm pitch in the micro-array field. Alternatively, construction of a periodic array with 200-300 nm spot size at 1 um pitch via interference lithography, followed by DMD-directed oligo synthesis at 1 um pitch would be sufficient, since 1 um rigid origami or SST rods are already available, as are 2D origami or SST assemblies with $\sim$ 200 nm diameter. In the below, we focus on a line-scanning scenario for illustration, assuming that light scattering can be minimized or tolerated, given the dimensions of the other components involved.

Combining capabilities 1 through 4 leads in principle to a strategy for construction of a uniquely addressable lattice in 2D. This strategy is shown in Figure 7.10 and Figure 7.11.

A. Use interference lithography to create a face-centered square lattice with uniform chemistry (i.e., no oligos yet).

B. Use nitrobenzyl photo-chemistry [247] to make these generic dots photo-activatable ("caged").

C. Use spatially patterned light, aligned to the underlying lattice generated in steps A and B, to selectively deposit or synthesize oligos within the interference lithographic spots. With sufficiently high-resolution digital micro-mirror device (DMD) or spatial light modulator (SLM) patterning, this in principle could result in a different oligonucleotide sequence being attached within each spot. Here, however, only $2n$ distinct oligonucleotide sequences ($1x$, ..., nx, $1y$, ..., ny) will be synthesized. Figure 7.10 shows an example where $n = 2$. Because the oligonucleotide sequences are to be arranged in non-crossing lines, it is possible to use focused lines of activation light from a cylindrical lens instead of DMD patterning, although DMD patterning would also be an excellent option. The line width could in theory be diffraction limited at $\frac{}{2*\mathrm{NA}} = 360$ nm for 360 nm UV light with NA $= 1/2$. In practice, the effects of light scattering must be taken into account to determine the effective line width

that is achievable (or the effective spot size, for DMD patterning).

D. Build $2n$ different DNA nanostructure exclusionary objects (DEOs: orange disks in the figure), which bind to the corresponding DNA $2n$ spot types synthesized in step C. These are DNA origami, or other nano-structures, which can expose defined DNA adaptor sequences and which size-exclude one another on the spots from step C. Note that for a pattern with N UALPs, only $2 * n = 2 * N^{1/4}$ distinct DEOs must be synthesized.

E. Bind $2n$ types of rods to the corresponding adaptor sequences on the origami from step D, and at least $2 * n^2$ pairwise rod-coupling DNAs (RCDs: oligos or DNA nano-structures), which bind selectively to oriented rod-pairs via attachment sites on the ends of the rods. The rods will have a preferred orientation defining left-right, front-back and up-down axes for each rod. Each of the 4-way rod junctions will have two RCDs corresponding to the x and y axes. This results in a unique address for each of n^4 junctions, defined by the identity of the pair of RCDs at that site. Thus, each four-way rod junction comprises a UALP. The junction address can be queried by cooperative binding to its two RCDs, e.g., using cooperative hybridization probes. The cooperative hybridization probe can then be thought of as a *second-order RCD* specific to a given UALP. Note that for $n = 100$ spot types per axis, $2 * 100^2$ first-order RCDs must be synthesized. This can be achieved by amplification of oligo library synthesis (OLS) pools[375], which now routinely contain $5*10^4$ distinct user-specified sequences. In contrast, direct synthesis of $n^4 = 10^8$ second-order RCDs is a technical challenge. If not all UALPs must be uniquely addressed, redundancy can be encoded into the the first-order RCDs, allowing a much smaller number of second-order RCDs to be used. Alternatively, clever library synthesis methods may be employed, e.g., using sequential ligations, to produce $O(10^8)$ defined second-order RCDs.

F. Each axis (x and y) coordinate is set by adjacent DEO pairs. These can be thought of as a de Bruijn sequence with alphabet size n, subsequence length $s = 2$, full sequence length $n^s = n^2$. In general, this process leads to a grid of n^4 UALPs. *For* $n = 100$ *and grid spacing of 1 um, we have* $100^4 = 10^8$ *UALPs in a total grid size of 1* cm^2.

Findings from the nm2cm design exercise

Because of the inherent constraints on interference lithography (3× pitch to spot size ratio is easy while 10× is hard), if rigid 2 μm rods were used (for ease of a subsequent non-periodic photo-patterning step using a digital micro-mirror device or spatial light modulator), you would probably want 500 nm × 500 nm origami or SST spot-covering structures. This is still somewhat beyond the limits of DNA origami and SST technology, however. If a 1 μm pitch was used, then probably a 200-300 nm spot diameter would be sufficient, but the non-periodic light patterning would be somewhat more difficult.

7.4.2 Aperiodic polymer nucleation: a strand-efficient strategy for self-assembling long, rigid, fully-addressable nano-rods

We took initial steps to develop new ways to form rigid, multi-micron-long, fully-addressable nano-rods, as are required in the above deterministic nm2cm scheme.

Lambda origami

The phage lambda genome length is 48,490 bp, so a lamdba 6-helix origami bundle (6hb[165]) would have length (48,490)×(0.34 nm)/6 = 2747.76 nm. A dimer of lambda 6hbs would surpass 5 um length, which matches the "feature size" on an Affymetrix Human Tiling 1.0R Array Set. Similarly, a disk-shaped lambda origami would have > 200 nm diameter, matching the available interference lithography spot size. One technical issue is the the presence of single-stranded nicks in the commercially available lambda DNA, preventing its direct use as an origami scaffold. Various groups are pursuing in-house phage production or enzymatic repair of the commercial lambda DNA, in order to solve these problems. On the other hand, it is still unclear whether 3D folding of such a long scaffold will occur reliably. We therefore chose to take a different approach to constructing long nanorods, which we describe in the next subsection.

The "molecular ruler" idea

Current synthetic approaches to self-assembly have centered on two paradigms: the creation of periodic crystalline structures from small numbers of symmetrical building blocks, and the use of large numbers of unique, asymmetric building-blocks to fully define a complex self-assembled object[723,695,156]. Robert Barish, Dave Zhang and I demonstrated proof of principle for a hybrid approach: the nucleated growth of periodic crystals on aperiodic polymer templates. An aperiodic single-stranded DNA template serves as the nucleus for growth of periodic but finite DNA crystals, and the template is stretched and rigidified during the crystal growth process. The polymer template thus serves as a "molecular ruler"[449] that constrains an otherwise unbounded crystal growth process. Further elaboration of the molecular ruler principle in synthetic self-assembly may lead to efficient methods for construction of complex multi-scale architectures. Key questions for experimental investigation include:

1) Can an aperiodic scaffold with secondary structure serve as nucleus?

2) Can a floppy scaffold be ratcheted into a well-defined, finite shape?

3) Does growth of the crystal remain finite?

4) Can this be done in a system with strong binding interactions, such as the SST system?

5) Isothermal vs. annealed: will floppy scaffolds lead to slow isothermal growth kinetics?

Results on aperiodic polymer nucleation

To test nucleation of periodic lattices on an aperiodic template, we (joint with Dave Zhang) first adapted a single-stranded tile (SST) ribbon system[723]. By choosing each row of repeated tiles to be a unique species, this system was previously used[723] to construct ribbons of well-defined widths that are periodic along their lengths ("unique row ribbons"). We generated a set of 160 SST adaptor tiles which bind to an 1.15 um long stretch of the circular m13mp18 ssDNA template. These adaptor tiles

connect to the first layer of a unique-row SST ribbon and nucleate the assembly of the ribbon. Figure 7.13A shows the conceptual scheme.

For controlled growth on the scaffold, it is essential that the nucleating structure, consisting of the scaffold annealed to the adaptor tile layer, forms before the temperature of spontaneous self-nucleation of the SST ribbon. To ensure that the unique-row SST ribbon nucleates at a temperature lower than the melting temperature of adaptor-scaffold contacts, we designed the unique-row SST ribbon system such that each 10 or 11 nucleotide binding domain possesses only one C or G base and otherwise consists of A and T nucleotides. Under these conditions, spontaneous nucleus formation is expected to occur at roughly 25-35C (for 1.6 uM each lattice strand), while nucleated lattice growth (strength 2) occurs at 50-55C (1.6 uM each lattice strand) binding of adaptors to scaffold occurs at 60C (10 nM scaffold, 10 nM each adaptor). This consideration is important because the scaffold contains secondary structure as well as regions of varying GC content; therefore the adaptor-scaffold contacts may have limited thermodynamic stability.

The unique-row SST lattice can be designed to have any number of layers. We tested the use of one-pot thermal annealing to form successively larger lattices from zero to thirteen helical rows above the adaptor layer. The scaffold was combined with the lattice tiles in a ratio of 1:160, corresponding to the 160-tile designed length of the ribbon, and with a 10x excess of the 160 individual adaptor tiles, and annealed from 90C to room temperature. Figure 7.13B shows the result of applying this procedure to successively greater numbers of lattice rows. Rows 1-3 add successfully to the nucleating structure. Figure 7.13D shows a typical AFM image of a gel extraction from the band corresponding to addition of layer 3. Note the scaffold strand is rigidified by the growth of the crystal. The kinks in the structure likely correspond to lattice defects where crystal growth was hindered. Beginning with layer 4, most of the ribbon structures appear to aggregate.

We analyzed the mechanism of aggregation and found that it could be suppressed at high temperature. Adding super-stoichiometric quantities of the lattice strands relative to the scaffold did not

abolish aggregation, nor did the use of PAGE purified lattice strands. Adding large excess of lattice strands led to spontaneous self-nucleation of unique-row SST lattices; this spurious nucleation could be suppressed by adding complements of the individual binding domains for the top halves of each lattice tile (we referred to this as the "sticky block" strategy). It was also possible to nucleate 3-layer SST lattices by isothermal layer-by-layer growth on pre-annealed scaffold/adaptor complexes. A cycle time of 30 minutes was sufficient to bring the reaction to a level of completion similar to that achieved with thermal annealing (Figure 7.13C).

We (joint with Robert Barish) next explored the assembly of lattices from rigid double-crossover (DX) tiles. A 6-layer-wide unique-row DX ribbon was nucleated on BsrbI-linearized m13mp18 ss-DNA scaffold. A rectangular DNA origami structure was folded from the remainder of the scaffold strand in order to aid in visualization of scaffold-nucleated ribbons. Figure 7.14A shows a schematic of the design. Figure 7.14B shows the detailed strand layout of the scaffold-adaptor complex and nucleated lattice. The design is inspired by[561] in which algorithmic DX lattices implementing XOR logic were nucleated on a periodic scaffold. Our design differs from[561] in that we nucleate on a *fully addressable aperioidic scaffold with high secondary structure and well-defined length*; also, we nucleate *finite structures rather than infinite crystals*.

Thus it was unknown whether nucleation of DX tiles could occur in this context and lead to crystal formation. Figure 7.14C shows typical AFM images obtained after ligation of crystals formed with an excess of lattice tiles relative to the seed strand. The origami structures formed on the seed (green circles) are clearly associated with long ribbons, indicating that the ribbon structures are nucleated on the m13 scaffold strand. Figure 7.14D shows an assembly formed at a sub-stoichiometric excess of the lattice strands. Here the straight edge corresponding to the scaffold nucleus is easily distinguished from the opposite jagged edge, suggesting that crystal growth proceeds bottom-up from the nucleus and that it occurs asynchronously across the nucleus.

We also nucleated the growth of infinite-width lattices on the m13 scaffold, as shown in Figure 7.14E.

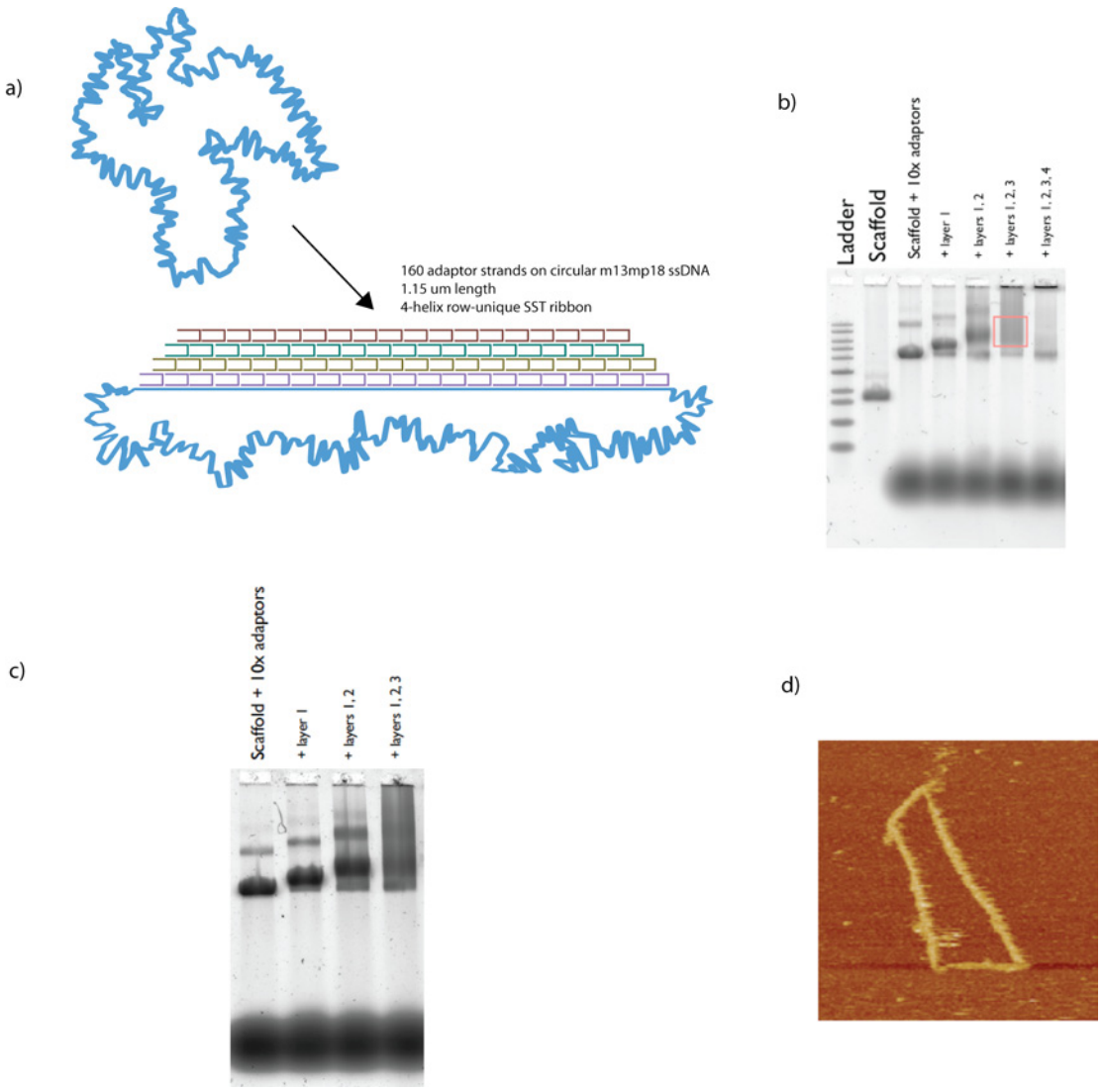

Figure 7.13: Nucleation of single-stranded tile ribbons on circular m13mp18. A) Design schema for rigidifying an aperiodic, floppy template sequence by using an aperiodic adapter tile layer to template growth of row-unique periodic single-stranded-tile crystals. B) Agarose gel on thermal annealing products showing structure aggregation, particularly after addition of layer 3. C) Isothermal growth experiment showing similar results to the annealing scenario. D) AFM image of a structure gel-extracted from the red box in B.

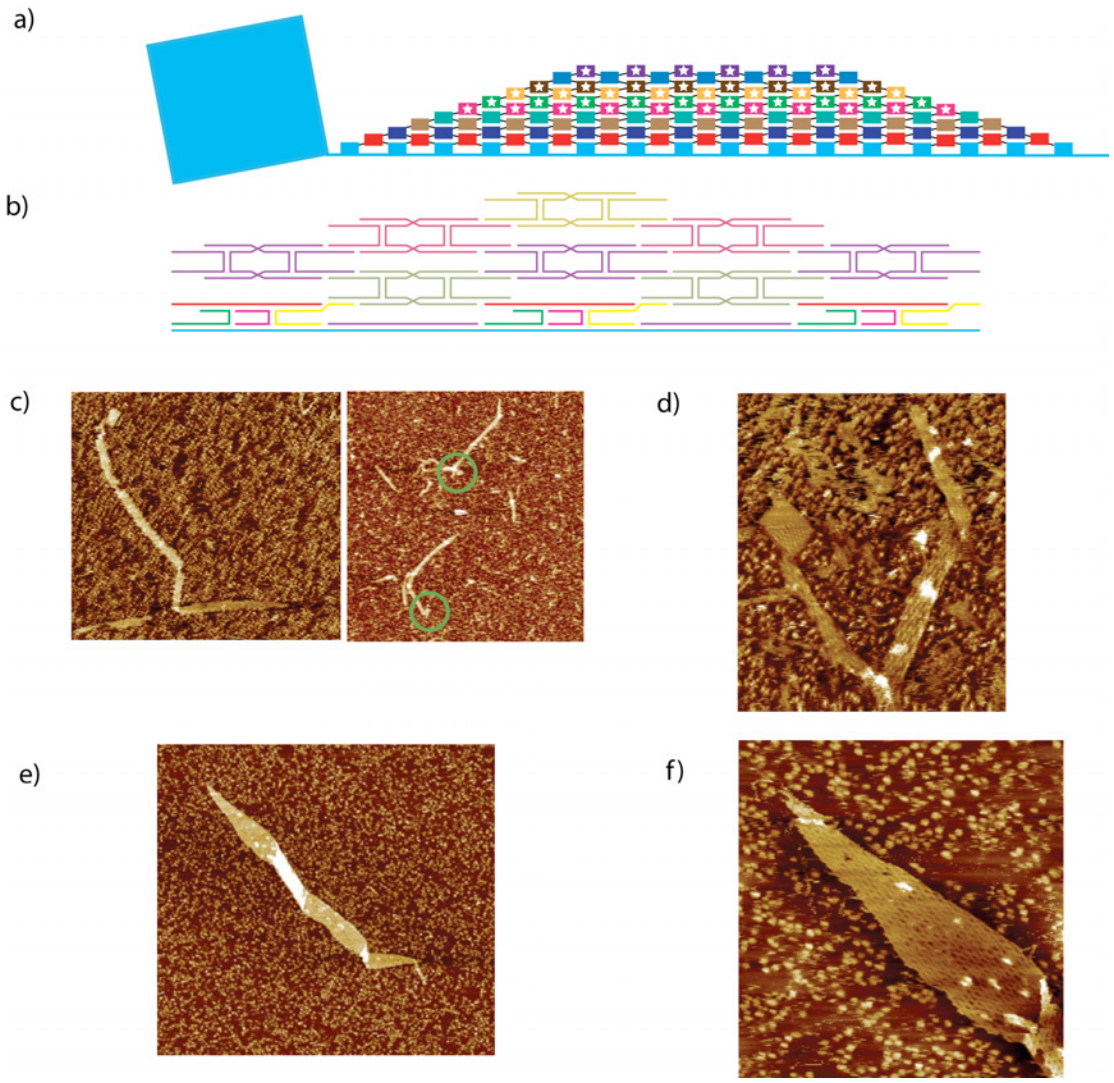

Figure 7.14: Nucleation of double-crossover lattices on linearized m13mp18. A) Design schema. B) Structure of the DX crossover lattice. C) AFM images of DX lattice formation on linearized m13mp18 ssDNA scaffold. A rectangular DNA origami folded from part of the scaffold serves as a marker for the presence of the scaffold. D) Zoom-in on a structure from the same experiment as in C. E) Nucleated the growth of infinite-width lattices on the m13 scaffold, without a designed origami marker on the scaffold. F) Zoom-in on the structure from E.

Again, the straight edge corresponding to the scaffold strand is distinguished from the jagged edge where crystal growth terminated asynchronously. Unlike self-nucleated DAO-E lattices, these scaffold-nucleated lattices have a characteristic right-handed super-twist resulting from constrained contacts with the scaffold. Figure 7.14F shows a high-resolution image where individual DX tiles and their contacts with the scaffold are visible.

8

Addendum: Hardware for Personal Phenotyping

We (joint with Charles Fracchia) have designed and experimentally prototyped the earliest incarnation of Bio-Glasses, a wearable system for continuous physiological monitoring. Based on open-source Fab Lab tools[222], we have developed early prototypes of a glasses-

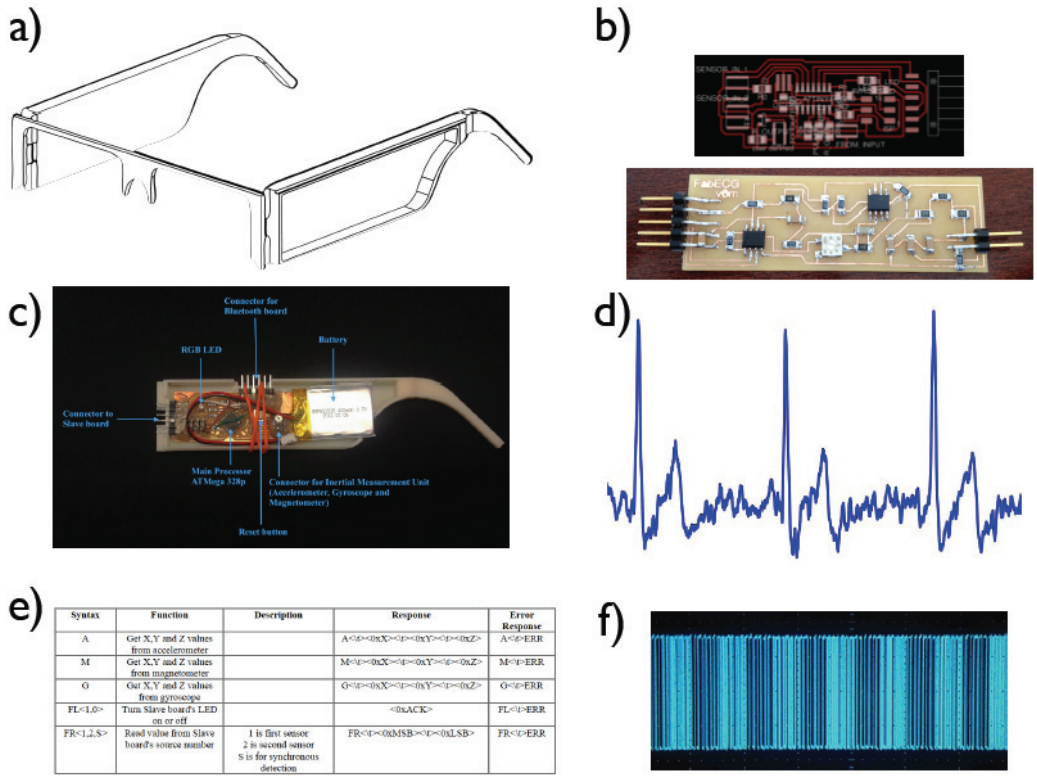

Syntax	Function	Description	Response	Error Response
A	Get X,Y and Z values from accelerometer		A<\t><0xX><\t><0xY><\t><0xZ>	A<\t>ERR
M	Get X,Y and Z values from magnetometer		M<\t><0xX><\t><0xY><\t><0xZ>	M<\t>ERR
G	Get X,Y and Z values from gyroscope		G<\t><0xX><\t><0xY><\t><0xZ>	G<\t>ERR
FL<1,0>	Turn Slave board's LED on or off		<0xACK>	FL<\t>ERR
FR<1,2,S>	Read value from Slave board's source number	1 is first sensor 2 is second sensor S is for synchronous detection	FR<\t><0xMSB><\t><0xLSB>	FR<\t>ERR

Figure 8.1: Early prototype hardware for glasses-mounted physiology. a) CAD of initial prototype for 3D printed glasses frames. b) Electronics for bio-sensing. c) Integration of electronics with 3D printed frames. d) EKG measured using custom-built electronics – based on [484] – using fabric electrodes: the same electronics is applicable to EMG and EEG. e) RS232 interface for communication between digital sub-systems in a multi-sensor glasses prototype. f) FSK modulated audio can be used to log data to an Android phone.

mounted sensor platform which integrates two analog sensors (e.g., electroencephalography and galvanic skin response), one synchronous detection sensor (e.g., IR reflection to measure pulse), as well as an accelerometer and gyro to measure head movements. The system communicates with a host using Bluetooth. In a more recent iteration, the lightweight electronics are cast in a silicone shell which enables them to be mounted on any glasses stem.

We are also developing open and easy-to-use protocols for transmitting time-stamped data from such sensors. By developing and open and interoperable ecosystem of sensors and interconnects, we

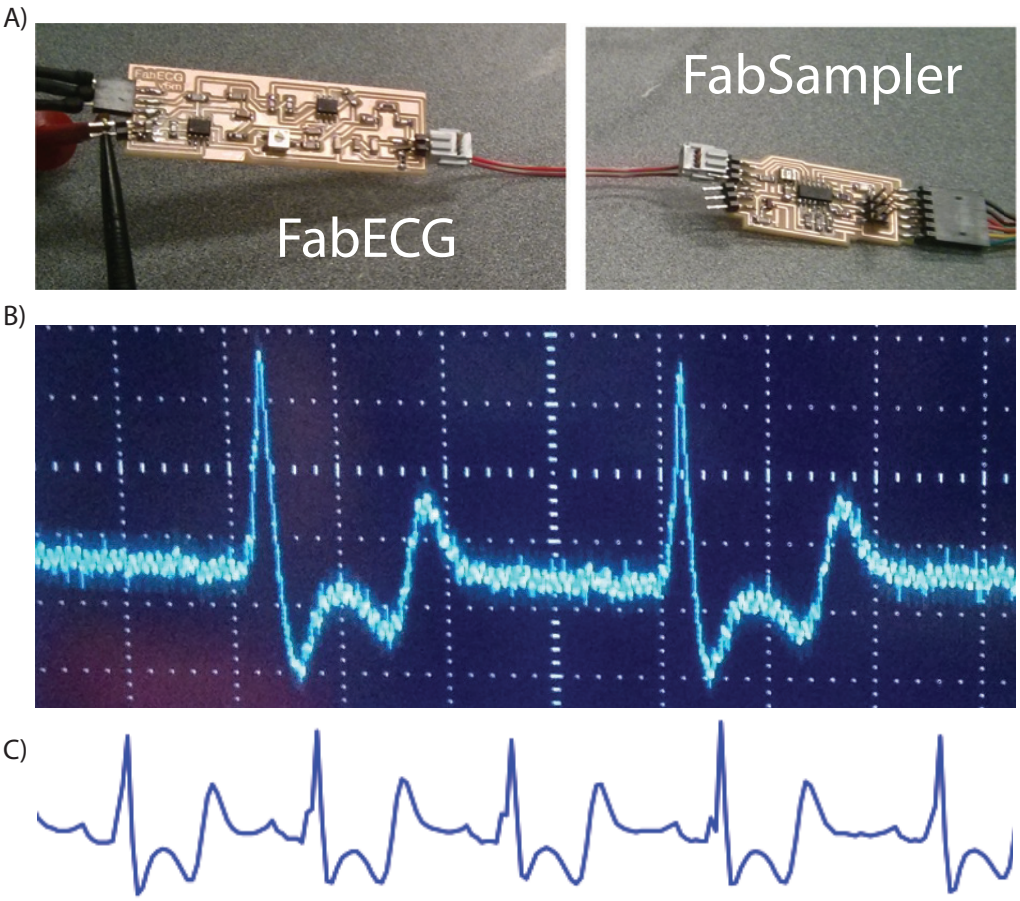

Figure 8.2: Benchmarking the FabECG with medical-grade electrodes on the chest. a) Setup for data acquisition using the FabSampler electronics. b) Data acquisition using an oscilloscope. c) Data acquisition using FabSampler and Python on a laptop.

hope ultimately to enable the integration of rich real-time physiological data – personal phenotyping – into projects like the the Personal Genome Project[41].

References

[1] (1989). Human physiology.

[2] (2006). C95.1-2005. ieee standard for safety levels with respect to human exposure to radio frequency electromagnetic fields, 3 khz to 300 ghz.

[3] (2007). *Equipment classification and requirements*. International Electrotechnical Commission, 2 edition.

[4] (2008). Guidance for industry and fda staff: Information for manufacturers seeking marketing clearance of diagnostic ultrasound systems and transducers.

[5] (2008). Piezoelectric and acoustic materials for transducer applications.

[6] (2010). Diagnostic ultrasound.

[7] (2013). *Monza 5 Tag Chip datasheet*. Impinj, Inc., Seattle, WA, USA.

[8] (2013). *P series linear photodiode array imager datasheet*. Reticon, Inc., Sunnyvale, CA, USA.

[9] (2013). *UHF / Microwave RFID Transponder ASIC IPMS_MWST1*. Fraunhofer Institute for Photonic Microsystems.

[10] Abrahamsson, S., Chen, J., Hajj, B., Stallinga, S., Katsov, A. Y., Wisniewski, J., Mizuguchi, G., Soule, P., Mueller, F., Darzacq, C. D., et al. (2012). Fast multicolor 3d imaging using aberration-corrected multifocus microscopy. *Nature methods*, 10(1), 60–63.

[11] Ackman, J. B., Burbridge, T. J., & Crair, M. C. (2012). Retinal waves coordinate patterned activity throughout the developing visual system. *Nature*, 490(7419), 219–225.

[12] Acosta, V., Bauch, E., Ledbetter, M., Santori, C., Fu, K.-M., Barclay, P., Beausoleil, R., Linget, H., Roch, J., Treussart, F., et al. (2009). Diamonds with a high density of nitrogen-vacancy centers for magnetometry applications. *Physical Review B*, 80(11), 115202.

[13] Acosta, V. M. (2011). *PhD Thesis (Physics, UC Berkeley): Optical Magnetometry with Nitrogen-Vacancy Centers in Diamond*.

[14] Acosta, V. M., Jarmola, A., Zipp, L. J., Ledbetter, M., Bauch, E., & Budker, D. (2011). Broadband magnetometry by infrared-absorption detection of diamond nv centers and associated temperature dependence. In *Proc. of SPIE Vol*, volume 7948 (pp. 79480W–1).

[15] Adar, S. & Livneh, Z. (2006). Translesion dna synthesis across non-dna segments in cultured human cells. *dna repair*, 5(4), 479–490.

[16] Ahrens, M. B., Li, J. M., Orger, M. B., Robson, D. N., Schier, A. F., Engert, F., & Portugues, R. (2012). Brain-wide neuronal dynamics during motor adaptation in zebrafish. *Nature*, 485(7399), 471–477.

[17] Ahrens, M. B., Orger, M. B., Robson, D. N., Li, J. M., & Keller, P. J. (2013). Whole-brain functional imaging at cellular resolution using light-sheet microscopy. *Nature Methods*, 10, 413–420.

[18] Aitken, C. E., Marshall, R. A., & Puglisi, J. D. (2008). An oxygen scavenging system for improvement of dye stability in single-molecule fluorescence experiments. *Biophysical journal*, 94(5), 1826–1835.

[19] Akemann, W., Sasaki, M., Mutoh, H., Imamura, T., Honkura, N., & Knöpfel, T. (2013). Two-photon voltage imaging using a genetically encoded voltage indicator. *Scientific reports*, 3.

[20] Alivisatos, A. P., Andrews, A. M., Boyden, E. S., Chun, M., Church, G. M., Deisseroth, K., Donoghue, J. P., Fraser, S. E., Lippincott-Schwartz, J., Looger, L. L., Masmanidis, S., McEuen, P. L., Nurmikko, A. V., Park, H., Peterka, D. S., Reid, C., Roukes, M. L., Scherer, A., Schnitzer, M., Sejnowski, T. J., Shepard, K. L., Tsao, D., Turrigiano, G., & Weiss, P. S. (2013). Nanotools for neuroscience and brain activity mapping. *ACS Nano*, 7(3), 1850–1866.

[21] Alivisatos, A. P., Chun, M., Church, G. M., Greenspan, R. J., Roukes, M. L., & Yuste, R. (2012). The brain activity map project and the challenge of functional connectomics. *Neuron*, 74(6), 970–974.

[22] Allen, J. S., Damasio, H., & Grabowski, T. J. (2002). Normal neuroanatomical variation in the human brain: an MRI-volumetric study. *American Journal of Physical Anthropology*, 118(4), 341–358.

[23] Anastassiou, C. A., Buzsaki, C., & Koch, C. (2013). Biophysics of extracellular spikes. *Principles of Neural Coding*, (pp.15).

[24] Anastassiou, C. A., Montgomery, S. M., Barahona, M., Buzsáki, G., & Koch, C. (2010). The effect of spatially inhomogeneous extracellular electric fields on neurons. *The Journal of neuroscience*, 30(5), 1925–1936.

[25] Anastassiou, C. A., Perin, R., Markram, H., & Koch, C. (2011). Ephaptic coupling of cortical neurons. *Nature neuroscience*, 14(2), 217–223.

[26] Anderson, J. R. (1996). Act: A simple theory of complex cognition. *American Psychologist*, 51(4), 355.

[27] Anderson, J. R., Bothell, D., Byrne, M. D., Douglass, S., Lebiere, C., & Qin, Y. (2004). An integrated theory of the mind. *Psychological review*, 111(4), 1036.

[28] Anselmi, F., Leibo, J. Z., Rosasco, L., Mutch, J., Tacchetti, A., & Poggio, T. (2013). Unsupervised learning of invariant representations in hierarchical architectures. *arXiv preprint arXiv:1311.4158*.

[29] Aoto, J., Martinelli, D. C., Malenka, R. C., Tabuchi, K., & Südhof, T. C. (2013). Presynaptic neurexin-3 alternative splicing< i> trans</i>-synaptically controls postsynaptic ampa receptor trafficking. *Cell*, 154(1), 75–88.

[30] Ardid, S. & Wang, X.-J. (2013). A tweaking principle for executive control: Neuronal circuit mechanism for rule-based task switching and conflict resolution. *The Journal of Neuroscience*, 33(50), 19504–19517.

[31] Arnold, D. B. (2007). Polarized targeting of ion channels in neurons. *Pflügers Archiv-European Journal of Physiology*, 453(6), 763–769.

[32] Atanasijevic, T., Shusteff, M., Fam, P., & Jasanoff, A. (2006). Calcium-sensitive MRI contrast agents based on super paramagnetic iron oxide nanoparticles and calmodulin. *Proceedings of the National Academy of Sciences of the United States of America*, 103(40), 14707–14712.

[33] Avital, G., Hashimshony, T., & Yanai, I. (2014). Seeing is believing: new methods for in situ single-cell transcriptomics. *Genome Biology*, 15(3), 110.

[34] Azevedo, F. A. C., Carvalho, L. R. B., Grinberg, L. T., Marcelo Farfel, J., Ferretti, R. E. L., Leite, R. E. P., Jacob Filho, W., Lent, R., & Herculano-Houzel, S. (2009). Equal numbers of neuronal and nonneuronal cells make the human brain an isometrically scaled-up primate brain. *Journal of Comparative Neurology*, 513(5), 532–541.

[35] Babadi, B. & Abbott, L. F. (2013). Pairwise analysis can account for network structures arising from spike-timing dependent plasticity. *PLoS Comput Biol*, 9(2), e1002906.

[36] Bae, B.-I., Tietjen, I., Atabay, K. D., Evrony, G. D., Johnson, M. B., Asare, E., Wang, P. P., Murayama, A. Y., Im, K., Lisgo, S. N., et al. (2014). Evolutionarily dynamic alternative splicing of gpr56 regulates regional cerebral cortical patterning. *Science*, 343(6172), 764–768.

[37] Bai, X.-c., Martin, T. G., Scheres, S. H., & Dietz, H. (2012). Cryo-em structure of a 3d dna-origami object. *Proceedings of the National Academy of Sciences*, 109(49), 20012–20017.

[38] Baillie, J. K., Barnett, M. W., Upton, K. R., Gerhardt, D. J., Richmond, T. A., De Sapio, F., Brennan, P. M., Rizzu, P., Smith, S., Fell, M., et al. (2011). Somatic retrotransposition alters the genetic landscape of the human brain. *Nature*, 479(7374), 534–537.

[39] Bakkum, D. J., Frey, U., Radivojevic, M., Russell, T. L., Müller, J., Fiscella, M., Takahashi, H., & Hierlemann, A. (2013). Tracking axonal action potential propagation on a high-density microelectrode array across hundreds of sites. *Nature communications*, 4.

[40] Bakopoulos, P., Karanasiou, I. S., Pleros, N., Zakynthinos, P., Uzunoglu, N., & Avramopoulos, H. (2009). A tunable continuous wave (CW) and short-pulse optical source for THz brain imaging applications. *Measurement Science and Technology*, 20, e104001.

[41] Ball, M. P., Thakuria, J. V., Zaranek, A. W., Clegg, T., Rosenbaum, A. M., Wu, X., Angrist, M., Bhak, J., Bobe, J., Callow, M. J., et al. (2012). A public resource facilitating clinical use of genomes. *Proceedings of the National Academy of Sciences*, 109(30), 11920–11927.

[42] Bandettini, P. A. (2009). Functional mri limitations and aspirations. In *Neural Correlates of Thinking* (pp. 15–38). Springer.

[43] Bansal, A. K., Truccolo, W., Vargas-Irwin, C. E., & Donoghue, J. P. (2012). Decoding 3-d reach and grasp from hybrid signals in motor and premotor cortices: spikes, multiunit activity and local field potentials. *Journal of Neurophysiology*, 107(3), 1337–55.

[44] Bargmann, C. I. (2012). Beyond the connectome: How neuromodulators shape neural circuits. *Bioessays*, 34(6), 458–465.

[45] Bargmann, C. I. & Marder, E. (2013). From the connectome to brain function. *Nature Methods*, 10(6), 483–490.

[46] Barnes, W. M. (1992). The fidelity of< i> taq</i> polymerase catalyzing pcr is improved by an n-terminal deletion. *Gene*, 112(1), 29–35.

[47] Barnett, L., Platisa, J., Popovic, M., Pieribone, V. A., & Hughes, T. (2012). A fluorescent, genetically-encoded voltage probe capable of resolving action potentials. *PLoS ONE*, 7(9), e43454.

[48] Barth, A. L. & Poulet, J. F. (2012). Experimental evidence for sparse firing in the neocortex. *Trends in Neurosciences*, 35(6), 345 – 355.

[49] Basarir, O., Bramhavar, S., Basilio-Sanchez, G., Morse, T., & Ekinci, K. L. (2010). Sensitive micromechanical displacement detection by scattering evanescent optical waves. *Optics letters*, 35(11), 1792–1794.

[50] Baskerville, S. & Bartel, D. P. (2002). A ribozyme that ligates rna to protein. *Proceedings of the National Academy of Sciences*, 99(14), 9154–9159.

[51] Beard, W. A., Shock, D. D., Berg, B. J. V., & Wilson, S. H. (2002). Efficiency of correct nucleotide insertion governs dna polymerase fidelity. *Journal of Biological Chemistry*, 277(49), 47393–47398.

[52] Bebenek, K. & Kunkel, T. A. (1995). Analyzing fidelity of dna polymerases. *Methods in enzymology*, 262, 217–232.

[53] Becker, C., Ali, K., Knott, G., & Fua, P. (2012). Learning context cues for synapse segmentation in em volumes. In *Medical Image Computing and Computer-Assisted Intervention–MICCAI 2012* (pp. 585–592). Springer.

[54] Bédard, C., Kröger, H., & Destexhe, A. (2004). Modeling extracellular field potentials and the frequency-filtering properties of extracellular space. *Biophysical journal*, 86(3), 1829–1842.

[55] Belgard, T. G. & Geschwind, D. H. (2012). Retooling spare parts: gene duplication and cognition. *Nature neuroscience*, 16(1), 6–8.

[56] Bennett, C. H. (1973). Logical reversibility of computation. *IBM Journal of Research and Development*, 17(6), 525–532.

[57] Berkovits, R. (1991). Sensitivity of the multiple-scattering speckle pattern to the motion of a single scatterer. *Physical Review B*, 43(10), 8638–8640.

[58] Bernstein, J. G., Garrity, P. A., & Boyden, E. S. (2012). Optogenetics and thermogenetics: technologies for controlling the activity of targeted cells within intact neural circuits. *Current Opinion in Neurobiology*, 22(1), 61 – 71.

[59] Bertolotti, J., van Putten, E. G., Blum, C., Lagendijk, A., Vos, W. L., & Mosk, A. P. (2012). Non-invasive imaging through opaque scattering layers. *Nature*, 491(7423), 232–234.

[60] Bett, A. W., Dimroth, F., Löckenhoff, R., Oliva, E., & Schubert, J. (2008). III-V solar cells under monochromatic illumination. In *Photovoltaic Specialists Conference, 2008* (pp. 1–5).

[61] Bhand, M., Mudur, R., Suresh, B., Saxe, A., & Ng, A. (2011). Unsupervised learning models of primary cortical receptive fields and receptive field plasticity. In *Advances in neural information processing systems* (pp. 1971–1979).

[62] Biederman, W., Yaeger, D. J., Narevsky, N., Koralek, A. C., Carmena, J. M., Alon, E., & Rabaey, J. M. (2013). A fully-integrated, miniaturized (0.125 mm^2) 10.5 μW wireless neural sensor. *IEEE Journal of Solid-State Circuits*, 48(4), 960–970.

[63] Blanchard, R., Boriskina, S. V., Genevet, P., Kats, M. A., Tetienne, J.-P., Yu, N., Scully, M. O., Dal Negro, L., & Capasso, F. (2011). Multi-wavelength mid-infrared plasmonic antennas with single nanoscale focal point. *Optics Express*, 19(22), 22113–22124.

[64] Bleckert, A., Parker, E. D., Kang, Y., Pancaroglu, R., Soto, F., Lewis, R., Craig, A. M., & Wong, R. O. (2013). Spatial relationships between gabaergic and glutamatergic synapses on the dendrites of distinct types of mouse retinal ganglion cells across development. *PloS one*, 8(7), e69612.

[65] Blinder, P., Shih, A. Y., Rafie, C., & Kleinfeld, D. (2010). Topological basis for the robust distribution of blood to rodent neocortex. *Proceedings of the National Academy of Sciences*, 107(28), 12670–12675.

[66] Blinder, P., Tsai, P. S., Kaufhold, J. P., Knutsen, P. M., Suhl, H., & Kleinfeld, D. (2013a). The cortical angiome: an interconnected vascular network with noncolumnar patterns of blood flow. *Nature Neuroscience*.

[67] Blinder, P., Tsai, P. S., Kaufhold, J. P., Knutsen, P. M., Suhl, H., & Kleinfeld, D. (2013b). The cortical angiome: an interconnected vascular network with noncolumnar patterns of blood flow. *Nature neuroscience*.

[68] Bock, D. D., Lee, W.-C. A., Kerlin, A. M., Andermann, M. L., Hood, G., Wetzel, A. W., Yurgenson, S., Soucy, E. R., Kim, H. S., & Reid, R. C. (2011). Network anatomy and in vivo physiology of visual cortical neurons. *Nature*, 471(7337), 177–182.

[69] Bodurka, J. & Bandettini, P. A. (2002). Toward direct mapping of neuronal activity: Mri detection of ultraweak, transient magnetic field changes. *Magnetic Resonance in Medicine*, 47(6), 1052–1058.

[70] Boeckers, T. M., Liedtke, T., Spilker, C., Dresbach, T., Bockmann, J., Kreutz, M. R., & Gundelfinger, E. D. (2005). C-terminal synaptic targeting elements for postsynaptic density proteins prosap1/shank2 and prosap2/shank3. *Journal of neurochemistry*, 92(3), 519–524.

[71] Bohland, J. W., Wu, C., Barbas, H., Bokil, H., Bota, M., Breiter, H. C., Cline, H. T., Doyle, J. C., Freed, P. J., Greenspan, R. J., et al. (2009). A proposal for a coordinated effort for the determination of brainwide neuroanatomical connectivity in model organisms at a mesoscopic scale. *PLoS computational biology*, 5(3), e1000334.

[72] Bolt, E. L. & Lloyd, R. G. (2002). Substrate specificity of rusa resolvase reveals the dna structures targeted by ruvab and recg in vivo. *Molecular cell*, 10(1), 187–198.

[73] Bonnet, J., Yin, P., Ortiz, M. E., Subsoontorn, P., & Endy, D. (2013). Amplifying genetic logic gates. *Science*, 340(6132), 599–603.

[74] Born, G., Breuer, D., Wang, S., Rohlmann, A., Coulon, P., Vakili, P., Reissner, C., Kiefer, F., Heine, M., Pape, H.-C., et al. (2014). Modulation of synaptic function through the α-neurexin–specific ligand neurexophilin-1. *Proceedings of the National Academy of Sciences*, 111(13), E1274–E1283.

[75] Boudsocq, F., Iwai, S., Hanaoka, F., & Woodgate, R. (2001). Sulfolobus solfataricus p2 dna polymerase iv (dpo4): an archaeal dinb-like dna polymerase with lesion-bypass properties akin to eukaryotic polη. *Nucleic Acids Research*, 29(22), 4607–4616.

[76] Boughorbel, F., Kooijman, C., Lich, B., & Bosch, E. (2012). Sem imaging method. US Patent 8,232,523.

[77] Bozinovic, N., Yue, Y., Ren, Y., Tur, M., Kristensen, P., Huang, H., Willner, A. E., & Ramachandran, S. (2013). Terabit-scale orbital angular momentum mode division multiplexing in fibers. *Science*, 340(6140), 1545–1548.

[78] Braitenberg, V. & Schüz, A. (1991). *Anatomy of the cortex: Statistics and geometry*. Springer-Verlag Publishing.

[79] Braman, J. (2004). *In vitro mutagenesis protocols*, volume 182. Springer.

[80] Branco, T., Clark, B. A., & Häusser, M. (2010). Dendritic discrimination of temporal input sequences in cortical neurons. *Science*, 329(5999), 1671–1675.

[81] Briggman, K. L. & Bock, D. D. (2012). Volume electron microscopy for neuronal circuit reconstruction. *Current opinion in neurobiology*, 22(1), 154–161.

[82] Briggman, K. L., Helmstaedter, M., & Denk, W. (2011). Wiring specificity in the direction-selectivity circuit of the retina. *Nature*, 471(7337), 183–188.

[83] Brodmann, K. (1909). *Vergleichende Lokalisationslehre der Grosshirnrinde in ihren Prinzipien dargestellt auf Grund des Zellenbaues*. Barth.

[84] Broxton, M., Grosenick, L., Yang, S., Cohen, N., Andalman, A., Deisseroth, K., & Levoy, M. (2013). Wave optics theory and 3-d deconvolution for the light field microscope.

[85] Broyde, S., Wang, L., Rechkoblit, O., Geacintov, N. E., & Patel, D. J. (2008). Lesion processing: high-fidelity versus lesion-bypass dna polymerases. *Trends in biochemical sciences*, 33(5), 209–219.

[86] Buchanan, M. (2013). Brain teaser. *Nature Physics*, 9(9), 525–525.

[87] Buonomano, D. V. & Maass, W. (2009). State-dependent computations: spatiotemporal processing in cortical networks. *Nature Reviews Neuroscience*, 10(2), 113–125.

[88] Bush, S. F. (2011). Toward in vivo nanoscale communication networks: utilizing an active network architecture. *Front. Comput. Sci China*, 5(3), 316–326.

[89] Busse, B. & Smith, S. (2013). Automated analysis of a diverse synapse population. *PLoS computational biology*, 9(3), e1002976.

[90] Bustamante, C., Cheng, W., & Mejia, Y. X. (2011). Revisiting the central dogma one molecule at a time. *Cell*, 144(4), 480–497.

[91] Buzsáki, G. (2004). Large-scale recording of neuronal ensembles. *Nature neuroscience*, 7(5), 446–451.

[92] Buzsáki, G. (2010). Neural syntax: cell assemblies, synapsembles, and readers. *Neuron*, 68(3), 362–385.

[93] Buzsáki, G., Anastassiou, C. A., & Koch, C. (2012). The origin of extracellular fields and currents—eeg, ecog, lfp and spikes. *Nature Reviews Neuroscience*, 13(6), 407–420.

[94] Buzsáki, G. (2004). Large-scale recording of neuronal ensembles. *Nature Neuroscience*, 7.

[95] Cai, D., Cohen, K. B., Luo, T., Lichtman, J. W., & Sanes, J. R. (2013). Improved tools for the brainbow toolbox. *Nature Methods*, 10(6), 540–547.

[96] Cai, L. (2013). Turning single cells into microarrays by super-resolution barcoding. *Briefings in functional genomics*, 12(2), 75–80.

[97] Cajigas, I. J., Tushev, G., Will, T. J., Fuerst, N., Schuman, E. M., et al. (2012). The local transcriptome in the synaptic neuropil revealed by deep sequencing and high-resolution imaging. *Neuron*, 74(3), 453–466.

[98] Callaway, E. M. & Borrell, V. (2011). Developmental sculpting of dendritic morphology of layer 4 neurons in visual cortex: influence of retinal input. *The Journal of Neuroscience*, 31(20), 7456–7470.

[99] Campbell, A. K. & Herring, P. J. (1987). A novel red fluorescent protein from the deep sea luminous fish *Malacosteus niger*. *Comparative Biochemistry and Physiology Part B*, 86B(2), 411–417.

[100] Camuñas Mesa, L. A. & Quian Quiroga, R. (2013). A detailed and fast model of extracellular recordings. *Neural Computation*, 25(5), 1191–1212.

[101] Cannon, G. J. & Swanson, J. A. (1992). The macrophage capacity for phagocytosis. *Journal of Cell Science*, 101, 907–913.

[102] Cao, G., Platisa, J., Pieribone, V. A., Raccuglia, D., Kunst, M., & Nitabach, M. N. (2013). Genetically targeted optical electrophysiology in intact neural circuits. *Cell*.

[103] Carandini, M. (2012). From circuits to behavior: a bridge too far? *Nature neuroscience*, 15(4), 507–509.

[104] Carandini, M. & Heeger, D. J. (2011). Normalization as a canonical neural computation. *Nature Reviews Neuroscience*, 13(1), 51–62.

[105] Carmena, J. M., Lebedev, M. A., Crist, R. E., O'Doherty, J. E., Santucci, D. M., Dimitrov, D. F., Patil, P. G., Henriquez, C. S., & Nicolelis, M. A. L. (2003). Learning to control a brain-machine interface for reaching and grasping by primates. *PLoS Biol*, 1(2), e42.

[Carp et al.] Carp, S. A., Roche-Labarbe, N., Franceschini, M.-A., Srinivasan, V. J., Sakadžić, S., & Boas, D. A. Due to intravascular multiple sequential scattering, diffuse correlation spectroscopy of tissue primarily measures relative red blood cell motion within vessels. *Biomedical Optics Express*, 2(7), 2047–2054.

[106] Carr, P. A. & Church, G. M. (2009). Genome engineering. *Nature biotechnology*, 27(12), 1151–1162.

[107] Castillo, M., Acevedo, P., & Moreno, E. (2003). KLM model for lossy piezoelectric transducers. *Ultrasonics*, 41(8), 671–679.

[108] Castro, C. E., Kilchherr, F., Kim, D.-N., Shiao, E. L., Wauer, T., Wortmann, P., Bathe, M., & Dietz, H. (2011). A primer to scaffolded dna origami. *Nature methods*, 8(3), 221–229.

[109] Chadderton, P., Margrie, T. W., & Häusser, M. (2004). Integration of quanta in cerebellar granule cells during sensory processing. *Nature*, 428(6985), 856–860.

[110] Chaigne, T., Katz, O., Boccara, A. C., Fink, M., Bossy, E., & Gigan, S. (2013). Controlling light in scattering media noninvasively using the photo-acoustic transmission-matrix.

[111] Charvet, C. J., Cahalane, D. J., & Finlay, B. L. (2013). Systematic, cross-cortex variation in neuron numbers in rodents and primates. *Cerebral Cortex*, (pp. bht214).

[112] Chen, S., Phillips, M. F., Cerrina, F., & Smith, L. M. (2009). Controlling oligonucleotide surface density in light-directed dna array fabrication. *Langmuir*, 25(11), 6570–6575.

[113] Chen, X., Vinade, L., Leapman, R. D., Petersen, J. D., Nakagawa, T., Phillips, T. M., Sheng, M., & Reese, T. S. (2005). Mass of the postsynaptic density and enumeration of three key molecules. *Proceedings of the National Academy of Sciences of the United States of America*, 102(32), 11551–11556.

[114] Cheng, A., Gonçalves, J. T., Golshani, P., Arisaka, K., & Portera-Cailliau, C. (2011). Simultaneous two-photon calcium imaging at different depths with spatiotemporal multiplexing. *Nature methods*, 8(2), 139–142.

[115] Chmyrov, A., Keller, J., Grotjohann, T., Ratz, M., d'Este, E., Jakobs, S., Eggeling, C., & Hell, S. W. (2013). Nanoscopy with more than 100,000 doughnuts. *Nature methods*, 10(8), 737–740.

[116] Cho, N., Song, S.-J., Kim, S., Kim, S., & Yoo, H.-J. (2005). A 5.1-μw UHF RFID tag chip integrated with sensors for wireless environmental monitoring. In *Solid-State Circuits Conference, 2005* (pp. 279–282).

[117] Choe, Y., Mayerich, D., Kwon, J., Miller, D. E., Chung, J. R., Sung, C., Keyser, J., & Abbott, L. C. (2011). Knife-edge scanning microscopy for connectomics research. In *Neural Networks (IJCNN), The 2011 International Joint Conference on* (pp. 2258–2265).: IEEE.

[118] Choi, H. M., Chang, J. Y., Trinh, L. A., Padilla, J. E., Fraser, S. E., & Pierce, N. A. (2010). Programmable in situ amplification for multiplexed imaging of mrna expression. *Nature biotechnology*, 28(11), 1208–1212.

[119] Chung, J. R., Sung, C., Mayerich, D., Kwon, J., Miller, D. E., Huffman, T., Keyser, J., Abbott, L. C., & Choe, Y. (2011). Multiscale exploration of mouse brain microstructures using the knife-edge scanning microscope brain atlas. *Frontiers in neuroinformatics*, 5.

[120] Chung, K., Wallace, J., Kim, S.-Y., Kalyanasundaram, S., Andalman, A. S., Davidson, T. J., Mirzabekov, J. J., Zalocusky, K. A., Mattis, J., Denisin, A. K., et al. (2013). Structural and molecular interrogation of intact biological systems. *Nature*, 497(7449), 332–337.

[121] Church, G. (2004). dntp derivatives for single molecule' and polony fluorescent in situ sequencing (fisseq).

[122] Church, G. M., Marblestone, A. H., & Kalhor, R. (2014). *The Future of the Brain: Essays From The World's Leading Neuroscientists*, chapter Rosetta Brain. Princeton University Press.

[123] Church, G. M. & Shendure, J. (2003). Nucleic acid memory device. US Patent App. 10/427,745.

[124] Church, G. M. & Shendure, J. (2007). Nucleic acid memory device. US Patent App. 11/766,222.

[125] Churchland, M. M., Cunningham, J. P., Kaufman, M. T., Foster, J. D., Nuyujukian, P., Ryu, S. I., & Shenoy, K. V. (2012). Neural population dynamics during reaching. *Nature*.

[126] Cinti, C., Taranta, M., Naldi, I., & Grimaldi, S. (2011). Newly engineered magnetic erythrocytes for sustained and targeted delivery of anti-cancer therapeutic compounds. *PLoS ONE*, 6(2), e17132.

[127] Collins, C. M., Liu, W., Wang, J., Gruetter, R., Vaughan, J. T., Ugurbil, K., & Smith, M. B. (2004). Temperature and SAR calculations for a human head within volume and surface coils at 64 and 300 MHz. *Journal of Magnetic Resonance Imaging*, 19(5), 650–656.

[128] Conkey, D. B., Caravaca-Aguirre, A. M., & Piestun, R. (2012). High-speed scattering medium characterization with application to focusing light through turbid media. *Optics Express*, 20(2), 1733–1740.

[129] Connelly, W. M., Errington, A. C., Di Giovanni, G., & Crunelli, V. (2013). Metabotropic regulation of extrasynaptic gabaa receptors. *Frontiers in Neural Circuits*, 7, 171.

[130] Cook, M., Jug, F., & Krautz, C. (2011). Neuronal projections can be sharpened by a biologically plausible learning mechanism. In *Artificial Neural Networks and Machine Learning–ICANN 2011* (pp. 101–108). Springer.

[131] Corneil, D. S., Neftci, E., Indiveri, G., & Pfeiffer, M. (2014). Learning, inference, and replay of hidden state sequences in recurrent spiking neural networks. In *COSYNE 2014*, number EPFL-POSTER-197325.

[132] Corrêa, S. A., Müller, J., Collingridge, G. L., & Marrion, N. V. (2009). Rapid endocytosis provides restricted somatic expression of a k+ channel in central neurons. *Journal of cell science*, 122(22), 4186–4194.

[133] Costa, R. M., Cohen, D., & Nicolelis, M. A. (2004). Differential corticostriatal plasticity during fast and slow motor skill learning in mice. *Current Biology*, 14(13), 1124–1134.

[134] Cover, T. M. & Thomas, J. A. (2006). *Elements of Information Theory*. Wiley Series in Telecommunications and Signal Processing. Wiley-Interscience, 2 edition.

[135] Creutzfeldt, O. D. (1977). Generality of the functional structure of the neocortex. *Naturwissenschaften*, 64(10), 507–517.

[136] Cybulski, T. R., Glaser, J. I., Marblestone, A. H., Zamft, B. M., Boyden, E. S., Church, G. M., & Kording, K. P. (2014). Spatial information in large-scale neural recordings. *arXiv preprint arXiv:1402.3375*.

[137] Dahan, M., Laurence, T., Pinaud, F., Chemla, D. S., Alivisatos, A. P., Sauer, M., & Weiss, S. (2001). Time-gated biological imaging by use of colloidal quantum dots. *Opt. Lett.*, 26(11), 825–827.

[138] Damasio, A. R. (1989). Time-locked multiregional retroactivation: A systems-level proposal for the neural substrates of recall and recognition. *Cognition*, 33(1), 25–62.

[139] Dani, A., Huang, B., Bergan, J., Dulac, C., & Zhuang, X. (2010). Superresolution imaging of chemical synapses in the brain. *Neuron*, 68(5), 843–856.

[140] Danielson, B. L. & Whittenberg, C. (1987). Guided-wave reflectometry with micrometer resolution. *Applied Optics*, 26(14), 2836–2842.

[141] David, O., Maess, B., Eckstein, K., & Friederici, A. D. (2011). Dynamic causal modeling of subcortical connectivity of language. *The Journal of Neuroscience*, 31(7), 2712–2717.

[142] Dawson, T. & Snyder, S. H. (1994). Gases as biological messengers: nitric oxide and carbon monoxide in the brain. *The Journal of neuroscience*, 14(9), 5147–5159.

[143] De la Rossa, A., Bellone, C., Golding, B., Vitali, I., Moss, J., Toni, N., Lüscher, C., & Jabaudon, D. (2013). In vivo reprogramming of circuit connectivity in postmitotic neocortical neurons. *Nature neuroscience*, 16(2), 193–200.

[144] Dean, T., Ahanonu, B., Chowdhury, M., Datta, A., Esteva, A., Eth, D., Redmon, N., Rumyantsev, O., & Tarter, Y. (2013). On the technology prospects and investment opportunities for scalable neuroscience.

[145] Dean, T. L., Corrado, G., & Shlens, J. (2012). Three controversial hypotheses concerning computation in the primate cortex. In *AAAI*.

[146] DeFelipe, J. (2010). The evolution of the brain, the human nature of cortical circuits, and intellectual creativity. *Frontiers in neuroanatomy*, 5, 29–29.

[147] Deichmann, R., Adolf, H., Nöth, U., Morrissey, S. P., Schwarzbauer, C., & Haase, A. (1995). Fast T_2-mapping with SNAPSHOT FLASH imaging. *Magnetic Resonance Imaging*, 13(4), 633–639.

[148] Deisseroth, K. (2012). Optogenetics and psychiatry: applications, challenges, and opportunities. *Biological psychiatry*, 12, 71.

[149] Delebecque, C. J., Lindner, A. B., Silver, P. A., & Aldaye, F. A. (2011). Organization of intracellular reactions with rationally designed rna assemblies. *Science*, 333(6041), 470–474.

[150] Denk, W., Briggman, K. L., & Helmstaedter, M. (2012). Structural neurobiology: missing link to a mechanistic understanding of neural computation. *Nature Reviews Neuroscience*, 13(5), 351–358.

[151] Denk, W. & Horstmann, H. (2004). Serial block-face scanning electron microscopy to reconstruct three-dimensional tissue nanostructure. *PLoS biology*, 2(11), e329.

[152] Derbyshire, V., Freemont, P. S., Sanderson, M. R., Beese, L., Friedman, J. M., Joyce, C. M., & Steitz, T. A. (1988). Genetic and crystallographic studies of the 3', 5'-exonucleolytic site of dna polymerase i. *Science*, 240(4849), 199–201.

[153] Derode, A., Tourin, A., de Rosny, J., Tanter, M., Yon, S., & Fink, M. (2003). Taking advantage of multiple scattering to communicate with time-reversal antennas. *Physical Review Letters*, 90(1), e014301.

[154] DeWolf, T. & Eliasmith, C. (2011). The neural optimal control hierarchy for motor control. *Journal of Neural Engineering*, 8(6), 065009.

[155] Diebold, E. D., Buckley, B. W., Gossett, D. R., & Jalali, B. (2013). Digitally-synthesized beat frequency multiplexing for sub-millisecond fluorescence microscopy. In *Novel Techniques in Microscopy*: Optical Society of America.

[156] Dietz, H., Douglas, S. M., & Shih, W. M. (2009). Folding dna into twisted and curved nanoscale shapes. *Science*, 325(5941), 725–730.

[157] Dobbing, J. & Sands, J. (1973). Quantitative growth and development of human brain. *Archives of Disease in Childhood*, 48(10), 757–767.

[158] Dolde, F., Fedder, H., Doherty, M., Nöbauer, T., Rempp, F., Balasubramanian, G., Wolf, T., Reinhard, F., Hollenberg, L., Jelezko, F., et al. (2011a). Electric-field sensing using single diamond spins. *Nature Physics*, 7(6), 459–463.

[159] Dolde, F., Fedder, H., Doherty, M. W., Nöbauer, T., Rempp, F., Balasubramanian, G., Wolf, T., Reinhard, F., Hollenberg, L. C. L., Jelezko, F., & Warchtrup, J. (2011b). Electric-field sensing using single diamond spins. *Nature Physics*, 7, 459–463.

[160] Dorjsuren, D., Wilson, D. M., Beard, W. A., McDonald, J. P., Austin, C. P., Woodgate, R., Wilson, S. H., & Simeonov, A. (2009). A real-time fluorescence method for enzymatic characterization of specialized human dna polymerases. *Nucleic acids research*, 37(19), e128–e128.

[161] Dotto, G. P., Horiuchi, K., & Zinder, N. D. (1984). The functional origin of bacteriophage f1 dna replication: Its signals and domains. *Journal of molecular biology*, 172(4), 507–521.

[162] Douglas, R. J. & Martin, K. A. (2004). Neuronal circuits of the neocortex. *Annu. Rev. Neurosci.*, 27, 419–451.

[163] Douglas, R. J. & Martin, K. A. (2007). Mapping the matrix: the ways of neocortex. *Neuron*, 56(2), 226–238.

[164] Douglas, R. J., Martin, K. A., & Whitteridge, D. (1989). A canonical microcircuit for neocortex. *Neural computation*, 1(4), 480–488.

[165] Douglas, S. M., Chou, J. J., & Shih, W. M. (2007). Dna-nanotube-induced alignment of membrane proteins for nmr structure determination. *Proceedings of the National Academy of Sciences*, 104(16), 6644–6648.

[166] Douglas, S. M., Dietz, H., Liedl, T., Högberg, B., Graf, F., & Shih, W. M. (2009a). Self-assembly of dna into nanoscale three-dimensional shapes. *Nature*, 459(7245), 414–418.

[167] Douglas, S. M., Marblestone, A. H., Teerapittayanon, S., Vazquez, A., Church, G. M., & Shih, W. M. (2009b). Rapid prototyping of 3d dna-origami shapes with cadnano. *Nucleic acids research*, 37(15), 5001–5006.

[168] Dowski, E. R., Cathey, W. T., et al. (1995). Extended depth of field through wave-front coding. *Applied Optics*, 34(11), 1859–1866.

[169] Drexler, K. E. (2013). *Radical abundance: How a revolution in nanotechnology will change civilization*. PublicAffairs.

[170] Drmanac, R., Sparks, A. B., Callow, M. J., Halpern, A. L., Burns, N. L., Kermani, B. G., Carnevali, P., Nazarenko, I., Nilsen, G. B., Yeung, G., et al. (2010). Human genome sequencing using unchained base reads on self-assembling dna nanoarrays. *Science*, 327(5961), 78–81.

[171] Drobizhev, M., Makarov, N. S., Tillo, S. E., Hughes, T. E., & Rebane, A. (2011). Two-photon absorption properties of fluorescent proteins. *Nature methods*, 8(5), 393–399.

[172] Du, J., Blanche, T. J., Harrison, R. R., Lester, H. A., & Masmanidis, S. C. (2011). Multiplexed, high density electrophysiology with nanofabricated neural probes. *PLoS ONE*, 6(10), e26204.

[173] Ducros, M., Houssen, Y. G., Bradley, J., de Sars, V., & Charpak, S. (2013). Encoded multisite two-photon microscopy. *Proceedings of the National Academy of Sciences*, 110(32), 13138–13143.

[174] Dudman, J. T., Tsay, D., & Siegelbaum, S. A. (2007). A role for synaptic inputs at distal dendrites: instructive signals for hippocampal long-term plasticity. *Neuron*, 56(5), 866–879.

[175] Dulcis, D., Jamshidi, P., Leutgeb, S., & Spitzer, N. C. (2013). Neurotransmitter switching in the adult brain regulates behavior. *science*, 340(6131), 449–453.

[176] Dyson, F. (2009). Radiotelepathy, the direct communication of feelings and thought from brain to brain. In J. Brockman (Ed.), *What Will Change Everything?* Edge.org.

[177] Egner, A., Jakobs, S., & Hell, S. W. (2002). Fast 100-nm resolution three-dimensional microscope reveals structural plasticity of mitochondria in live yeast. *Proceedings of the National Academy of Sciences*, 99(6), 3370–3375.

[178] El-Deiry, W. S., Downey, K. M., & So, A. G. (1984). Molecular mechanisms of manganese mutagenesis. *Proceedings of the National Academy of Sciences*, 81(23), 7378–7382.

[179] El-Husseini, A. E.-D., Craven, S. E., Brock, S. C., & Bredt, D. S. (2001). Polarized targeting of peripheral membrane proteins in neurons. *Journal of Biological Chemistry*, 276(48), 44984–44992.

[180] Eliasmith, C. (2013). *How to build a brain: A neural architecture for biological cognition*. Oxford University Press.

[181] Eliasmith, C. & Anderson, C. C. H. (2004). *Neural engineering: Computation, representation, and dynamics in neurobiological systems*. MIT Press.

[182] Eliasmith, C., Stewart, T. C., Choo, X., Bekolay, T., DeWolf, T., Tang, C., & Rasmussen, D. (2012). A large-scale model of the functioning brain. *science*, 338(6111), 1202–1205.

[183] Elowitz, M. B. & Leibler, S. (2000). A synthetic oscillatory network of transcriptional regulators. *Nature*, (6767), 335–338.

[184] Elston, G. N. (2002). Cortical heterogeneity: implications for visual processing and polysensory integration. *Journal of neurocytology*, 31(3-5), 317–335.

[185] Elston, G. N. (2003). Cortex, cognition and the cell: new insights into the pyramidal neuron and prefrontal function. *Cerebral Cortex*, 13(11), 1124–1138.

[186] Engelhardt, B. (2006). Molecular mechanisms involved in t cell migration across the blood-brain barrier. *Journal of Neural Transmission*, 113(4), 477–485.

[187] Engert, F. & Bonhoeffer, T. (1999). Dendritic spine changes associated with hippocampal long-term synaptic plasticity. *Nature*, 399(6731), 66–70.

[188] Esvelt, K. M., Mali, P., Braff, J. L., Moosburner, M., Yaung, S. J., & Church, G. M. (2013). Orthogonal cas9 proteins for rna-guided gene regulation and editing. *Nature methods*, 10(11), 1116–1121.

[189] Evrony, G. D., Cai, X., Lee, E., Hills, L. B., Elhosary, P. C., Lehmann, H. S., Parker, J., Atabay, K. D., Gilmore, E. C., Poduri, A., et al. (2012). Single-neuron sequencing analysis of l1 retrotransposition and somatic mutation in the human brain. *Cell*, 151(3), 483–496.

[190] Fang-Yen, C., Chu, M. C., Seung, H. S., Dasari, R. R., & Feld, M. S. (2004). Noncontact measurement of nerve displacement during action potential with a dual-beam low-coherence interferometer. *Optics letters*, 29(17), 2028–2030.

[191] Fatouros, P. P. & Marmarou, A. (1999). Use of magnetic resonance imaging for in vivo measurements of water content in human brain: method and normal values. *Journal of Neurosurgery*, 90(1), 109–115.

[192] Faurez, F., Dory, D., Grasland, B., Jestin, A., et al. (2009). Replication of porcine circoviruses. *Virol J*, 6, 60.

[193] Fee, M. S., Mitra, P. P., & Kleinfeld, D. (1996). Variability of extracellular spike waveforms of cortical neurons. *Journal of neurophysiology*, 76(6), 3823–3833.

[194] Feinberg, E. H., VanHoven, M. K., Bendesky, A., Wang, G., Fetter, R. D., Shen, K., & Bargmann, C. I. (2008). Gfp reconstitution across synaptic partners (grasp) defines cell contacts and synapses in living nervous systems. *Neuron*, 57(3), 353–363.

[195] Feldmeyer, D., Egger, V., Lübke, J., & Sakmann, B. (1999). Reliable synaptic connections between pairs of excitatory layer 4 neurones within a single 'barrel'of developing rat somatosensory cortex. *The Journal of Physiology*, 521(1), 169–190.

[196] Fiebig, M. (2005). Revival of the magnetoelectric effect. *Journal of Physics D: Applied Physics*, 38(8), R123.

[197] Fiete, I. R., Senn, W., Wang, C. Z., & Hahnloser, R. H. (2010). Spike-time-dependent plasticity and heterosynaptic competition organize networks to produce long scale-free sequences of neural activity. *Neuron*, 65(4), 563–576.

[198] Filonov, G. S., Krumholz, A., Xia, J., Yao, J., Wang, L. V., & Verkhusha, V. V. (2012). Deep-tissue photoacoustic tomography of a genetically encoded near-infrared fluorescent probe. *Angewandte Chemie*, 51(6), 1448–1451.

[199] Filonov, G. S., Platkevich, K. D., Ting, L.-M., Zhang, J., Kim, K., & Verkhusha, V. V. (2011). Bright and stable near-infrared fluorescent protein for *in vivo* imaging. *Nature Biotechnology*, 29(8), 757–761.

[200] Fino, E. & Yuste, R. (2011). Dense inhibitory connectivity in neocortex. *Neuron*, 69(6), 1188–1203.

[201] Fishell, G. & Heintz, N. (2013). The neuron identity problem: Form meets function. *Neuron*, 80(3), 602–612.

[202] Fitzsimonds, R. M., Song, H.-j., & Poo, M.-m. (1997). Propagation of activity-dependent synaptic depression in simple neural networks. *Nature*, 388(6641), 439–448.

[203] Flusberg, B. A., Cocker, E. D., Piyawattanametha, W., Jung, J. C., Cheung, E. L. M., & Schnitzer, M. J. (2005). Fiber-optic fluorescence imaging. *Nature Methods*, 2(12), 941–950.

[204] Fontaine, J. J., Diels, J.-C., Wang, C.-Y., & Sallaba, H. (1981). Subpicosecond-time-domain reflectometry. *Optics Letters*, 6(9), 405–407.

[205] for Brain Science, A. I. (2012). Allen mouse brain connectivity atlas.

[206] Foster, F. S., Pavlin, C. J., Harasiewicz, K. A., Christopher, D. A., & Turnbull, D. H. (2000). Advances in ultrasound biomicroscopy. *Ultrasound in Medicine & Biology*, 26(1), 1–27.

[207] Frank, E. G. & Woodgate, R. (2007). Increased catalytic activity and altered fidelity of human DNA polymerase iota in the presence of manganese. *The Journal of Biological Chemistry*, 282(34), 24689–24696.

[208] Freitas Jr., R. A. (1999). *Nanomedicine, Volume I: Basic Capabilities*. Landes Bioscience.

[209] Friedland, A. E., Lu, T. K., Wang, X., Shi, D., Church, G. M., & Collins, J. J. (2009). Synthetic gene networks that count. *Science*, 324(5931), 1199–1202.

[210] Frost, D. O. (1982). Anomalous visual connections to somatosensory and auditory systems following brain lesions in early life. *Developmental Brain Research*, 3(4), 627–635.

[211] Frost, D. O. & Metin, C. (1985). Induction of functional retinal projections to the somatosensory system.

[212] Fujimura, T. & Esteban, R. (2011). Cap-snatching mechanism in yeast la double-stranded rna virus. *Proceedings of the National Academy of Sciences*, 108(43), 17667–17671.

[213] Gabriel, S., Lau, R., & Gabriel, C. (1996). The dielectric properties of biological tissues: Iii. parametric models for the dielectric spectrum of tissues. *Phys. Med. Biol*, 41(11).

[214] Galarreta, M. & Hestrin, S. (2001). Electrical synapses between gaba-releasing interneurons. *Nature Reviews Neuroscience*, 2(6), 425–433.

[215] Gao, L., Shao, L., Higgins, C. D., Poulton, J. S., Peifer, M., Davidson, M. W., Wu, X., Goldstein, B., & Betzig, E. (2012). Noninvasive imaging beyond the diffraction limit of 3d dynamics in thickly fluorescent specimens. *Cell*, 151(6), 1370–1385.

[216] Gauci, J. & Stanley, K. O. (2010). Autonomous evolution of topographic regularities in artificial neural networks. *Neural computation*, 22(7), 1860–1898.

[217] Ge, D., Le Carpentier, E., Idier, J., & Farina, D. (2011). Spike sorting by stochastic simulation. *IEEE transactions on neural systems and rehabilitation engineering : a publication of the IEEE Engineering in Medicine and Biology Society*, 19(3), 249–259.

[218] George, D. & Hawkins, J. (2009). Towards a mathematical theory of cortical micro-circuits. *PLoS computational biology*, 5(10), e1000532.

[219] Gerhard, F., Kispersky, T., Gutierrez, G. J., Marder, E., Kramer, M., & Eden, U. (2013). Successful reconstruction of a physiological circuit with known connectivity from spiking activity alone. *PLoS computational biology*, 9(7), e1003138.

[220] Gerlach, C., Rohr, J. C., Perié, L., van Rooij, N., van Heijst, J. W., Velds, A., Urbanus, J., Naik, S. H., Jacobs, H., Beltman, J. B., et al. (2013). Heterogeneous differentiation patterns of individual cd8+ t cells. *Science*, 340(6132), 635–639.

[221] Gershenfeld, N. (2000). *The physics of information technology*. Cambridge University Press.

[222] Gershenfeld, N. (2012). How to make almost anything: The digital fabrication revolution. *Foreign Aff.*, 91, 58.

[223] Geschwind, D. H. & Rakic, P. (2013). Cortical evolution: judge the brain by its cover. *Neuron*, 80(3), 633–647.

[224] Gire, D. H., Restrepo, D., Sejnowski, T. J., Greer, C., De Carlos, J. A., & Lopez-Mascaraque, L. (2013). Temporal processing in the olfactory system: Can we see a smell? *Neuron*, 78(3), 416 – 432.

[225] Gittis, A. H., Moghadam, S. H., & du Lac, S. (2010). Mechanisms of sustained high firing rates in two classes of vestibular nucleus neurons: Differential contributions of resurgent Na, Kv3, and BK currents. *Journal of Neurophysiology*, 104(3), 1625–1634.

[226] Giuly, R. J., Kim, K.-Y., & Ellisman, M. H. (2013). Dp2: Distributed 3d image segmentation using micro-labor workforce. *Bioinformatics*, 29(10), 1359–1360.

[227] Glaser, J. I., Zamft, B. M., Marblestone, A. H., Moffitt, J. R., Tyo, K., Boyden, E. S., Church, G. M., & Kording, K. P. (2013). Statistical analysis of molecular signal recording. *PLoS Computational Biology*.

[228] Glenn, D., Zhang, H., Kasthuri, N., Schalek, R., Lo, P., Trifonov, A., Park, H., Lichtman, J., & Walsworth, R. (2012). Correlative light and electron microscopy using cathodoluminescence from nanoparticles with distinguishable colours. *Scientific reports*, 2.

[229] Glover, P. & Mansfield, Sir P. (2002). Limits to magnetic resonance microscopy. *Reports on Progress in Physics*, 65(10).

[230] Goard, M. & Dan, Y. (2009). Basal forebrain activation enhances cortical coding of natural scenes. *Nature neuroscience*, 12(11), 1444–1449.

[231] Goda, K., Ayazi, A., Gossett, D. R., Sadasivam, J., Lonappan, C. K., Sollier, E., Fard, A. M., Hur, S. C., Adam, J., Murray, C., et al. (2012). High-throughput single-microparticle imaging flow analyzer. *Proceedings of the National Academy of Sciences*, 109(29), 11630–11635.

[232] Goda, K. & Jalali, B. (2013). Dispersive fourier transformation for fast continuous single-shot measurements. *Nature Photonics*, 7(2), 102–112.

[233] Goda, K., Solli, D. R., Tsia, K. K., & Jalali, B. (2009a). Theory of amplified dispersive fourier transformation. *Physical Review A*, 80(4), 043821.

[234] Goda, K., Tsia, K., & Jalali, B. (2009b). Serial time-encoded amplified imaging for real-time observation of fast dynamic phenomena. *Nature*, 458(7242), 1145–1149.

[235] Goda, K., Tsia, K. K., & Jalali, B. (2008). Amplified dispersive fourier-transform imaging for ultrafast displacement sensing and barcode reading. *Applied Physics Letters*, 93(13), 131109–131109.

[236] Godlove, D. C., Maier, A., Woodman, G. F., & Schall, J. D. (2014). Microcircuitry of agranular frontal cortex: Testing the generality of the canonical cortical microcircuit. *The Journal of Neuroscience*, 34(15), 5355–5369.

[237] Goeppert-Mayer, M. (1931). Elementary processes with two quantum transitions. *Annalen der Physik*, 18(7-8).

[238] Gold, C., Henze, D. A., & Koch, C. (2007). Using extracellular action potential recordings to constrain compartmental models. *Journal of Computational Neuroscience*, 23, 39–58.

[239] Golden, J. A., Fields-Berry, S. C., & Cepko, C. L. (1995). Construction and characterization of a highly complex retroviral library for lineage analysis. *Proceedings of the National Academy of Sciences*, 92(12), 5704–5708.

[240] Gole, J., Gore, A., Richards, A., Chiu, Y.-J., Fung, H.-L., Bushman, D., Chiang, H.-I., Chun, J., Lo, Y.-H., & Zhang, K. (2013). Massively parallel polymerase cloning and genome sequencing of single cells using nanoliter microwells. *Nature biotechnology*, 31(12), 1126–1132.

[241] Gómez-Martínez, R., Vázquez, P., Duch, M., Muriano, A., Pinacho, D., Sanvicens, N., Sánchez-Baeza, F., Boya, P., de la Rosa, E. J., Esteve, J., Suárez, T., & Plaza, J. A. (2010). Intracellular silicon chips in living cells. *Small*, 6(4), 499–502.

[242] Gong, H., Zeng, S., Yan, C., Lv, X., Yang, Z., Xu, T., Feng, Z., Ding, W., Qi, X., Li, A., et al. (2013a). Continuously tracing brain-wide long-distance axonal projections in mice at a one-micron voxel resolution. *Neuroimage*.

[243] Gong, Y., Li, J. Z., & Schnitzer, M. J. (2013b). Enhanced archaerhodopsin fluorescent protein voltage indicators. *PLOS ONE*, 8(6), e66959.

[244] Graber, T. E., Hébert-Seropian, S., Khoutorsky, A., David, A., Yewdell, J. W., Lacaille, J.-C., & Sossin, W. S. (2013). Reactivation of stalled polyribosomes in synaptic plasticity. *Proceedings of the National Academy of Sciences*, 110(40), 16205–16210.

[245] Granger, R. (2006). Engines of the brain: The computational instruction set of human cognition. *AI Magazine*, 27(2), 15.

[246] Gray, C. M., Maldonado, P. E., Wilson, M., & McNaughton, B. (1995). Tetrodes markedly improve the reliability and yield of multiple single-unit isolation from multi-unit recordings in cat striate cortex. *Journal of Neuroscience Methods*, 63(1–2), 43–54.

[247] Greenberg, M. M. & Gilmore, J. L. (1994). Cleavage of oligonucleotides from solid-phase supports using o-nitrobenzyl photochemistry. *The Journal of Organic Chemistry*, 59(4), 746–753.

[248] Greig, L. C., Woodworth, M. B., Galazo, M. J., Padmanabhan, H., & Macklis, J. D. (2013). Molecular logic of neocortical projection neuron specification, development and diversity. *Nature Reviews Neuroscience*, 14(11), 755–769.

[249] Grillner, S. (2006). Biological pattern generation: the cellular and computational logic of networks in motion. *Neuron*, 52(5), 751–766.

[250] Grillner, S., Markram, H., De Schutter, E., Silberberg, G., & LeBeau, F. E. (2005). Microcircuits in action–from cpgs to neocortex. *Trends in neurosciences*, 28(10), 525–533.

[251] Gross, G. G., Junge, J. A., Mora, R. J., Kwon, H.-B., Olson, C. A., Takahashi, T. T., Liman, E. R., Ellis-Davies, G. C., McGee, A. W., Sabatini, B. L., et al. (2013). Recombinant probes for visualizing endogenous synaptic proteins in living neurons. *Neuron*, 78(6), 971–985.

[252] Guan, B.-O., Li, J., Jin, L., & Ran, Y. (2013). Fiber bragg gratings in optical microfibers. *Optical Fiber Technology*.

[253] Gustafsson, M., Agard, D., Sedat, J., et al. (1999). I5m: 3d widefield light microscopy with better than 100nm axial resolution. *Journal of microscopy*, 195(1), 10–16.

[254] Gustafsson, M. G. (2005). Nonlinear structured-illumination microscopy: wide-field fluorescence imaging with theoretically unlimited resolution. *Proceedings of the National Academy of Sciences of the United States of America*, 102(37), 13081–13086.

[255] Gustafsson, M. G., Shao, L., Carlton, P. M., Wang, C., Golubovskaya, I. N., Cande, W. Z., Agard, D. A., & Sedat, J. W. (2008). Three-dimensional resolution doubling in wide-field fluorescence microscopy by structured illumination. *Biophysical Journal*, 94(12), 4957–4970.

[256] Gyohda, A. & Komano, T. (2000). Purification and characterization of the r64 shufflon-specific recombinase. *Journal of bacteriology*, 182(10), 2787–2792.

[257] Haase, A., Frahm, J., Matthaei, D., Hänicke, W., & Merboldt, K.-D. (1986). FLASH imaging. *Journal of Magnetic Resonance*, 67(2), 258–266.

[258] Hall, L., Beart, G., Thomas, E., Simpson, D., McGuinness, L., Cole, J., Manton, J., Scholten, R., Jelezko, F., Wrachtrup, J., et al. (2012). High spatial and temporal resolution wide-field imaging of neuron activity using quantum nv-diamond. *Scientific reports*, 2.

[259] Halpern-Manners, N. W., Bajaj, V. S., Teisseyre, T. Z., & Pines, A. (2010). Magnetic resonance imaging of oscillating electrical currents. *Proceedings of the National Academy of Sciences*, 107(19), 8519–8524.

[260] Harats, M. G., Schwarz, I., Zimran, A., Banin, U., Chen, G., & Rapaport, R. (2011). Enhancement of two photon processes in quantum dots embedded in subwavelength metallic gratings. *Opt. Express*, 19(2), 1617–1625.

[261] Harris, J. J., Jolivet, R., & Attwell, D. (2012). Synaptic energy use and supply. *Neuron*, 75(5), 762–777.

[262] Harvey, C. D., Coen, P., & Tank, D. W. (2012). Choice-specific sequences in parietal cortex during a virtual-navigation decision task. *Nature*, 484(7392), 62–68.

[263] Hasselmo, M. E. & Wyble, B. P. (1997). Free recall and recognition in a network model of the hippocampus: simulating effects of scopolamine on human memory function. *Behavioural brain research*, 89(1), 1–34.

[264] Hattori, D., Demir, E., Kim, H. W., Viragh, E., Zipursky, S. L., & Dickson, B. J. (2007). Dscam diversity is essential for neuronal wiring and self-recognition. *Nature*, 449(7159), 223–227.

[265] Hauser, M. D., Chomsky, N., & Fitch, W. T. (2002). The faculty of language: What is it, who has it, and how did it evolve? *science*, 298(5598), 1569–1579.

[266] Hawrylycz, M. J., Lein, S., Guillozet-Bongaarts, A. L., Shen, E. H., Ng, L., Miller, J. A., van de Lagemaat, L. N., Smith, K. A., Ebbert, A., Riley, Z. L., et al. (2012). An anatomically comprehensive atlas of the adult human brain transcriptome. *Nature*, 489(7416), 391–399.

[267] Hayworth, K., Kasthuri, N., Schalek, R., & Lichtman, J. (2006). Automating the collection of ultrathin serial sections for large volume tem reconstructions. *Microsc Microanal*, 12(Suppl 2), 86–87.

[268] Hayworth, K. J. (2011). Lossless thick sectioning of plastic-embedded brain tissue to enable parallelizing of sbfsem and fibsem imaging. In *High resolution circuit reconstruction conference*.

[269] Hayworth, K. J. (2012). Electron imaging technology for whole brain neural circuit mapping. *International Journal of Machine Consciousness*, 04(01), 87–108.

[270] Hayworth, K. J. et al. (2011). Dynamically partitionable autoassociative networks as a solution to the neural binding problem. *Frontiers in computational neuroscience*, 6, 73–73.

[271] Hayworth, K. J. & Hayworth, A. A. (2013). Methods, apparatus and systems for production, collection, handling, and imaging of tissue sections. US Patent 20,130,216,451.

[272] Hebb, D. O. (2002). *The organization of behavior: A neuropsychological theory*. Psychology Press.

[273] Helmstaedter, M. (2013). Cellular-resolution connectomics: challenges of dense neural circuit reconstruction. *Nature methods*, 10(6), 501–507.

[274] Helmstaedter, M., Briggman, K. L., & Denk, W. (2011). High-accuracy neurite reconstruction for high-throughput neuroanatomy. *Nature neuroscience*, 14(8), 1081–1088.

[275] Helmstaedter, M., Briggman, K. L., Turaga, S. C., Jain, V., Seung, H. S., & Denk, W. (2013). Connectomic reconstruction of the inner plexiform layer in the mouse retina. *Nature*, 500(7461), 168–174.

[276] Henrique von Gersdorff, J. G. G. et al. (2002). Short-term plasticity at the calyx of held. *Nature Reviews Neuroscience*, 3(1), 53–64.

[277] Henze, D. A., Borhegyi, Z., Csicsvari, J., Mamiya, A., Harris, K. D., & Buzsáki, G. (2000). Intracellular features predicted by extracellular recordings in the hippocampus in vivo. *Journal of Neurophysiology*, 84(1), 390–400.

[278] Herculano-Houzel, S. (2010). Coordinated scaling of cortical and cerebellar numbers of neurons. *Frontiers in neuroanatomy*, 4.

[279] Herculano-Houzel, S. (2011). Scaling of brain metabolism with a fixed energy budget per neuron: implications for neuronal activity, plasticity, and evolution. *PLoS ONE*, 6, e17514.

[280] Higley, M. J. & Sabatini, B. L. (2008). Calcium signaling in dendrites and spines: practical and functional considerations. *Neuron*, 59(6), 902–913.

[281] Hikawa, N., Horie, H., Kawakami, T., Okuda, K., & Takenaka, T. (1989). Introduction of macromolecules into primary cultured neuronal cells by fusion with erythrocyte ghosts. *Brain Research*, 481(1), 162 – 164.

[282] Hill, S. L., Wang, Y., Riachi, I., Schürmann, F., & Markram, H. (2012). Statistical connectivity provides a sufficient foundation for specific functional connectivity in neocortical neural microcircuits. *Proceedings of the National Academy of Sciences*, 109(42), E2885–E2894.

[283] Hillman, E. M. (2007). Optical brain imaging in vivo: techniques and applications from animal to man. *Journal of biomedical optics*, 12(5), 051402–051402.

[284] Ho, J., Kim, S., & Poon, A. (2013). Midfield wireless powering for implantable systems. *Proceedings of the IEEE*, 101(6), 1369–1378.

[285] Hoerzer, G. M., Legenstein, R., & Maass, W. (2012). Emergence of complex computational structures from chaotic neural networks through reward-modulated hebbian learning. *Cerebral Cortex*.

[286] Holt, G. R. (1997). *A critical reexamination of some assumptions and implications of cable theory in neurobiology*. PhD thesis, California Institute of Technology.

[287] Holthoff, K. & Witte, O. W. (1996). Intrinsic optical signals in rat neocortical slices measured with near-infrared dark-field microscopy reveal changes in extracellular space. *The Journal of neuroscience*, 16(8), 2740–2749.

[288] Hopt, A. & Neher, E. (2001). Highly nonlinear photodamage in two-photon fluorescence microscopy. *Biophysical Journal*, 80(4), 2029–2036.

[289] Horch, H. W. & Katz, L. C. (2002). Bdnf release from single cells elicits local dendritic growth in nearby neurons. *Nature neuroscience*, 5(11), 1177–1184.

[290] Horowitz, V. R., Alemán, B. J., Christle, D. J., Cleland, A. N., & Awschalom, D. D. (2012). Electron spin resonance of nitrogen-vacancy centers in optically trapped nanodiamonds. *Proceedings of the National Academy of Sciences of the United States of America*, 109(34), 13493–13497.

[291] Horton, J. C. & Adams, D. L. (2005). The cortical column: a structure without a function. *Philosophical Transactions of the Royal Society B: Biological Sciences*, 360(1456), 837–862.

[292] Horton, N. G., Wang, K., Kobat, D., Clark, C. G., Wise, F. W., Schaffer, C. B., & Xu, C. (2013). *In vivo* three-photon microscopy of subcortical structures within an intact mouse brain. *Nature Photonics*, 7, 205–209.

[293] Hoshi, Y. (2003). Functional near-infrared optical imaging: Utility and limitations in human brain mapping. *Psychophysiology*, 40(4), 511–520.

[294] Howarth, C., Gleeson, P., & Attwell, D. (2012). Updated energy budgets for neural computation in the neocortex and cerebellum. *Journal of Cerebral Blood Flow & Metabolism*, 32(7), 1222–1232.

[295] Hromádka, T., DeWeese, M. R., & Zador, A. M. (2008). Sparse representation of sounds in the unanesthetized auditory cortex. *PLoS biology*, 6(1), e16.

[296] Hsieh, V. & Jasanoff, A. (2012). Bioengineered probes for molecular magnetic resonance imaging in the nervous system. *ACS Chemical Neuroscience*, 3(8), 593–602.

[297] Huang, G., Jiang, H., Matthews, K., & Wilford, P. (2013). Lensless imaging by compressive sensing. In *International Conference on Image Processing*.

[298] Huber, D., Gutnisky, D., Peron, S., O'Connor, D., Wiegert, J., Tian, L., Oertner, T., Looger, L., & Svoboda, K. (2012). Multiple dynamic representations in the motor cortex during sensorimotor learning. *Nature*, 484(7395), 473–478.

[299] Hulpiau, P. & Van Roy, F. (2009). Molecular evolution of the cadherin superfamily. *The international journal of biochemistry & cell biology*, 41(2), 349–369.

[300] Huppert, T. J., Franceschini, M. A., & Boas, D. A. (2009). 14 noninvasive imaging of cerebral activation with diffuse optical tomography.

[301] Hynynen, K., McDannold, N., Sheikov, N. A., Jolesz, F. A., & Vykhodtseva, N. (2005). Local and reversible blood–brain barrier disruption by noninvasive focused ultrasound at frequencies suitable for trans-skull sonications. *Neuroimage*, 24(1), 12–20.

[302] Iijima, T., Wu, K., Witte, H., Hanno-Iijima, Y., Glatter, T., Richard, S., & Scheiffele, P. (2011). Sam68 regulates neuronal activity-dependent alternative splicing of neurexin-1. *Cell*, 147(7), 1601–1614.

[303] Iliff, J. J., Wang, M., Liao, Y., Plogg, B. A., Peng, W., Gundersen, G. A., Benveniste, H., Vates, G. E., Deane, R., Goldman, S. A., et al. (2012). A paravascular pathway facilitates csf flow through the brain parenchyma and the clearance of interstitial solutes, including amyloid beta. *Sci Transl Med*, 4(147), 147ra111.

[304] Ingolia, N. T., Ghaemmaghami, S., Newman, J. R., & Weissman, J. S. (2009). Genome-wide analysis in vivo of translation with nucleotide resolution using ribosome profiling. *science*, 324(5924), 218–223.

[305] Ionescu, A. M. & Riel, H. (2011). Tunnel field-effect transistors as energy-efficient electronic switches. *Nature*, 479, 329–337.

[306] Irimia, A., Zang, H., Loukachevitch, L. V., Eoff, R. L., Guengerich, F. P., & Egli, M. (2006). Calcium is a cofactor of polymerization but inhibits pyrophosphorolysis by the sulfolobus solfataricus dna polymerase dpo4. *Biochemistry*, 45(19), 5949–5956.

[307] Isokawa, M. (2005). N-methyl-d-aspartic acid-induced and ca-dependent neuronal swelling and its retardation by brain-derived neurotrophic factor in the epileptic hippocampus. *Neuroscience*, 131(4), 801–812.

[308] Isoyan, A., WŘest, A., Wallace, J., Jiang, F., & Cerrina, F. (2008). 4x reduction extreme ultraviolet interferometric lithography. *Optics Express*, 16(12), 9106–9111.

[309] Issler, S. L. & Torardi, C. C. (1995). Solid state chemistry and luminescence of X-ray phosphors. *Journal of Alloys and Compounds*, 229(1), 54–65.

[310] Ivanov, K. P., Kalinina, M. K., & Levkovich, Y. I. (1981). Blood flow velocity in capillaries of brain and muscles and its physiological significance. *Microvascular Research*, 22(2), 143–155.

[311] Iwasa, K., Tasaki, I., & Gibbons, R. C. (1980). Swelling of nerve fibers associated with action potentials. *Science*, 210(4467), 338–339.

[312] Izhikevich, E. M. & Edelman, G. M. (2008). Large-scale model of mammalian thalamocortical systems. *Proceedings of the national academy of sciences*, 105(9), 3593–3598.

[313] Jackson, D. A., Pombo, A., & Iborra, F. (2000). The balance sheet for transcription. *The FASEB Journal*, 14(2), 242–254.

[314] Jacob, F. (1977). Evolution and tinkering. *Science*, 196(4295), 1161–1166.

[315] Jacobs, E. C., Bongarzone, E. R., Campagnoni, C. W., Kampf, K., & Campagnoni, A. T. (2003). Soma-restricted products of the myelin proteolipid gene are expressed primarily in neurons in the developing mouse nervous system. *Developmental neuroscience*, 25(2-4), 96–104.

[316] Jadhav, A. D., Aimo, I., Cohen, D., Ledochowitsch, P., & Maharbiz, M. M. (2012). Cyborg eyes. In *Micro Electro Mechanical Systems* (pp. 937–940).

[317] Jain, V., Murray, J. F., Roth, F., Turaga, S., Zhigulin, V., Briggman, K. L., Helmstaedter, M. N., Denk, W., & Seung, H. S. (2007). Supervised learning of image restoration with convolutional networks. In *Computer Vision, 2007. ICCV 2007. IEEE 11th International Conference on* (pp. 1–8).: IEEE.

[318] Jasanoff, A. (2007). Bloodless fmri. *Trends in neurosciences*, 30(11), 603–610.

[319] Jasanoff, A. (NIH Grant 1R01NS076462-01). Noninvasive imaging-based electrophysiology using microelectronic devices.

[320] Jasanoff, A. & Sun, P. Z. (2002). In vivo magnetic resonance microscopy of brain structure in unanesthetized flies. *Journal of Magnetic Resonance*, 158(1), 79–85.

[321] Jefferis, G. S. & Livet, J. (2012). Sparse and combinatorial neuron labelling. *Current opinion in neurobiology*, 22(1), 101–110.

[322] Jensen, W., Hofmann, U. G., & Yoshida, K. (2003). Assessment of subdural insertion force of single-tine microelectrodes in rat cerebral cortex. In *Engineering in Medicine and Biology Society*, volume 3 (pp. 2168–2171).

[323] Jin, X. & Costa, R. M. (2010). Start/stop signals emerge in nigrostriatal circuits during sequence learning. *Nature*, 466.

[324] Jonasz, M. (2007). Absorption coefficient of water: Data sources. *Topics in Particle and Dispersion Science*.

[325] Joseph, D. K., Huppert, T. J., Franceschini, M. A., & Boas, D. A. (2006). Diffuse optical tomography system to image brain activation with improved spatial resolution and validation with functional magnetic resonance imaging. *Applied optics*, 45(31), 8142–8151.

[326] Judkewitz, B., Wang, Y. M., Horstmeyer, R., Mathy, A., & Yang, C. (2013). Speckle-scale focusing in the diffusive regime with time reversal of variance-encoded light (trove). *Nature Photonics*.

[327] Jukovskaya, N., Tiret, P., Lecoq, J., & Charpak, S. (2011). What does local functional hyperemia tell about local neuronal activation? *The Journal of Neuroscience*, 31(5), 1579–1582.

[328] Kaas, J. H. (2012). Evolution of columns, modules, and domains in the neocortex of primates. *Proceedings of the National Academy of Sciences*, 109(Supplement 1), 10655–10660.

[329] Kadiu, I., Nowacek, A., McMillan, J., & Gendelman, H. E. (2011). Macrophage endocytic trafficking of antiretroviral nanoparticles. *Nanomedicine*, 6(6).

[330] Kalisman, N., Silberberg, G., & Markram, H. (2005). The neocortical microcircuit as a tabula rasa. *Proceedings of the National Academy of Sciences of the United States of America*, 102(3), 880–885.

[331] Kalmbach, A. S. & Waters, J. (2012). Brain surface temperature under a craniotomy. *Journal of Neurophysiology*, 108(11), 3138–3146.

[332] Kandel, E. R., Markram, H., Matthews, P. M., Yuste, R., & Koch, C. (2013). Neuroscience thinks big (and collaboratively). *Nature Reviews Neuroscience*, 14.

[333] Kang, J. W., Kim, P., Amadeo Alonzo, C., Park, H., & Yun, S. H. (2010). Two-photon microscopy by wavelength-swept pulses delivered through single-mode fiber. *Optics Letters*, 35(2), 181–183.

[334] Kappel, D., Nessler, B., & Maass, W. (2013). Stdp installs in winner-take-all circuits an online approximation to hidden markov model learning. *PLoS computational biology*, 10(3), e1003511.

[335] Karalis, A., Joannopoulos, J., & Soljačić, M. (2008). Efficient wireless non-radiative mid-range energy transfer. *Annals of Physics*, 323(1), 34 – 48.

[336] Karbowski, J. (2011). Scaling of brain metabolism and blood flow in relation to capillary and neural scaling. *PloS one*, 6(10), e26709.

[337] Katz, O., Small, E., Bromberg, Y., & Silberberg, Y. (2011). Focusing and compression of ultrashort pulses through scattering media. *Nature photonics*, 5(6), 372–377.

[338] Katz, O., Small, E., & Silberberg, Y. (2012). Looking around corners and through thin turbid layers in real time with scattered incoherent light. *Nature Photonics*.

[339] Kaynig, V., Vazquez-Reina, A., Knowles-Barley, S., Roberts, M., Jones, T. R., Kasthuri, N., Miller, E., Lichtman, J., & Pfister, H. (2013). Large-scale automatic reconstruction of neuronal processes from electron microscopy images. *arXiv preprint arXiv:1303.7186*.

[340] Ke, R., Mignardi, M., Pacureanu, A., Svedlund, J., Botling, J., Wählby, C., & Nilsson, M. (2013). In situ sequencing for rna analysis in preserved tissue and cells. *Nature methods*, 10(9), 857–860.

[341] Ke, Y., Douglas, S. M., Liu, M., Sharma, J., Cheng, A., Leung, A., Liu, Y., Shih, W. M., & Yan, H. (2009). Multilayer dna origami packed on a square lattice. *Journal of the American Chemical Society*, 131(43), 15903–15908.

[342] Keith, B. J., Jozwiakowski, S. K., & Connolly, B. A. (2012). A plasmid-based lacz-alpha gene assay for dna polymerase fidelity measurement. *Analytical biochemistry*.

[343] Kelman, Z. & O'Donnell, M. (1995). DNA polymerase III holoenzyme. *Annual Review of Biochemistry*, 64, 171–200.

[344] Keohavong, P. & Thilly, W. G. (1989). Fidelity of dna polymerases in dna amplification. *Proceedings of the National Academy of Sciences*, 86(23), 9253–9257.

[345] Kershner, R. J., Bozano, L. D., Micheel, C. M., Hung, A. M., Fornof, A. R., Cha, J. N., Rettner, C. T., Bersani, M., Frommer, J., Rothemund, P. W., et al. (2009). Placement and orientation

of individual dna shapes on lithographically patterned surfaces. *Nature Nanotechnology*, 4(9), 557–561.

[346] Khazen, G., Hill, S. L., Schürmann, F., & Markram, H. (2012). Combinatorial expression rules of ion channel genes in juvenile rat (rattus norvegicus) neocortical neurons. *PloS one*, 7(4).

[347] Kim, D.-N., Kilchherr, F., Dietz, H., & Bathe, M. (2012). Quantitative prediction of 3d solution shape and flexibility of nucleic acid nanostructures. *Nucleic acids research*, 40(7), 2862–2868.

[348] Kim, G., Kosterin, P., Obaid, A., & Salzberg, B. (2007). A mechanical spike accompanies the action potential in mammalian nerve terminals. *Biophysical journal*, 92(9), 3122–3129.

[349] Kim, J. (2010). *Next generation CAT system*. PhD thesis, Massachusetts Institute of Technology.

[350] Kim, J., Zhao, T., Petralia, R. S., Yu, Y., Peng, H., Myers, E., & Magee, J. C. (2011). mgrasp enables mapping mammalian synaptic connectivity with light microscopy. *Nature methods*, 9(1), 96–102.

[351] Kim, K. H., Buehler, C., & So, P. T. C. (1999). High-speed, two-photon scanning microscope. *Applied Optics*, 38(28), 6004–6009.

[352] Kinde, I., Wu, J., Papadopoulos, N., Kinzler, K. W., & Vogelstein, B. (2011). Detection and quantification of rare mutations with massively parallel sequencing. *Proceedings of the National Academy of Sciences*, 108(23), 9530–9535.

[353] Kirkby, L. A., Sack, G. S., Firl, A., & Feller, M. B. (2013). A role for correlated spontaneous activity in the assembly of neural circuits. *Neuron*, 80(5), 1129–1144.

[354] Kitagawa, Y., Hiraoka, Y., Honda, T., Ishikura, T., Nakamura, H., & Kimura, T. (2010). Low-field magnetoelectric effect at room temperature. *Nature Materials*, (10), 797–802.

[355] Kitaura, H., Tsujita, M., Huber, V. J., Kakita, A., Shibuki, K., Sakimura, K., Kwee, I. L., & Nakada, T. (2009). Activity-dependent glial swelling is impaired in aquaporin-4 knockout mice. *Neuroscience research*, 64(2), 208–212.

[356] Kleinfeld, D., Bharioke, A., Blinder, P., Bock, D. D., Briggman, K. L., Chklovskii, D. B., Denk, W., Helmstaedter, M., Kaufhold, J. P., Lee, W.-C. A., et al. (2011). Large-scale automated histology in the pursuit of connectomes. *The Journal of Neuroscience*, 31(45), 16125–16138.

[357] Knott, G., Rosset, S., & Cantoni, M. (2011). Focussed ion beam milling and scanning electron microscopy of brain tissue. *Journal of visualized experiments: JoVE*, (53).

[358] Kobat, D., Durst, M. E., Nishimura, N., Wong, A. W., Schaffer, C. B., & Xu, C. (2009). Deep tissue multiphoton microscopy using longer wavelength excitation. *Optics Express*, 17(16), 13354–13364.

[359] Kobat, D., Horton, N. G., & Xu, C. (2011). In vivo two-photon microscopy to 1.6-mm depth in mouse cortex. *Journal of Biomedical Optics*, 16(10), 106014–106014–4.

[360] Koch, C. (2004). *Biophysics of computation: information processing in single neurons*. Oxford university press.

[361] Koch, C. & Reid, R. C. (2012). Neuroscience: Observatories of the mind. *Nature*, 483(7390), 397–398.

[362] Koch, C. & Segev, I. (2000). The role of single neurons in information processing. *nature neuroscience*, 3, 1171–1177.

[363] Kodandaramaiah, S. B., Franzesi, G. T., Chow, B. Y., Boyden, E. S., & Forest, C. R. (2012). Automated whole-cell patch-clamp electrophysiology of neurons in vivo. *Nature Methods*, 9.

[364] Koehl, W. F., Buckley, B. B., Heremans, F. J., Calusine, G., & Awschalom, D. D. (2011). Room temperature coherent control of defect spin qubits in silicon carbide. *Nature*, 479(7371), 84–87.

[365] Komanduri, R. K., Oh, C., & Escuti, M. J. (2008). Reflective liquid crystal polarization gratings with high efficiency and small pitch. In *Photonic Devices+ Applications* (pp. 70500J–70500J).: International Society for Optics and Photonics.

[366] Komano, T. (1999). Shufflons: multiple inversion systems and integrons. *Annual review of genetics*, 33(1), 171–191.

[367] Konermann, S., Brigham, M. D., Trevino, A., Hsu, P. D., Heidenreich, M., Cong, L., Platt, R. J., Scott, D. A., Church, G. M., & Zhang, F. (2013). Optical control of mammalian endogenous transcription and epigenetic states. *Nature*.

[368] König, K., So, P., Mantulin, W., & Gratton, E. (1997). Cellular response to near-infrared femtosecond laser pulses in two-photon microscopes. *Optics letters*, 22(2), 135–136.

[369] Konopka, G., Friedrich, T., Davis-Turak, J., Winden, K., Oldham, M. C., Gao, F., Chen, L., Wang, G.-Z., Luo, R., Preuss, T. M., et al. (2012). Human-specific transcriptional networks in the brain. *Neuron*, 75(4), 601–617.

[370] Koomey, J. G., Berard, S., Sanchez, M., & Wong, H. (2011). Implications of historical trends in the electrical efficiency of computing. *IEEE Annals of the History of Computing*, 33(3), 46–54.

[371] Kopec, C. D., Real, E., Kessels, H. W., & Malinow, R. (2007). Glur1 links structural and functional plasticity at excitatory synapses. *The Journal of Neuroscience*, 27(50), 13706–13718.

[372] Koralek, A. C., Jin, X., Long II, J. D., Costa, R. M., & Carmena, J. M. (2012). Corticostriatal plasticity is necessary for learning intentional neuroprosthetic skills. *Nature*, 483.

[373] Kording, K. P. (2011). Of toasters and molecular ticker tapes. *PLoS Computational Biology*, 7(12), e1002291.

[374] Koretsky, A. P. (2012). Is there a path beyond BOLD? Molecular imaging of brain function. *NeuroImage*, 62(2), 1208–1215.

[375] Kosuri, S., Eroshenko, N., LeProust, E. M., Super, M., Way, J., Li, J. B., & Church, G. M. (2010). Scalable gene synthesis by selective amplification of dna pools from high-fidelity microchips. *Nature biotechnology*, 28(12), 1295–1299.

[376] Kou, J.-L., Ding, M., Feng, J., Lu, Y.-Q., Xu, F., & Brambilla, G. (2012). Microfiber-based bragg gratings for sensing applications: a review. *Sensors*, 12(7), 8861–8876.

[377] Kou, L., Labrie, D., & Chylek, P. (1993). Refractive indices of water and ice in the 0.65- to 2.5-μm spectral range. *Applied Optics*, 32(19), 3531–3540.

[378] Kouh, M. & Poggio, T. (2008). A canonical neural circuit for cortical nonlinear operations. *Neural computation*, 20(6), 1427–1451.

[379] Kralj, J. M., Douglass, A. D., Hochbaum, D. R., Maclaurin, D., & Cohen, A. E. (2012). Optical recording of action potentials in mammalian neurons using a microbial rhodopsin. *Nature Methods*, 9.

[380] Kreshuk, A., Straehle, C. N., Sommer, C., Koethe, U., Cantoni, M., Knott, G., & Hamprecht, F. A. (2011). Automated detection and segmentation of synaptic contacts in nearly isotropic serial electron microscopy images. *PloS one*, 6(10), e24899.

[381] Kriete, T., Noelle, D. C., Cohen, J. D., & O'Reilly, R. C. (2013). Indirection and symbol-like processing in the prefrontal cortex and basal ganglia. *Proceedings of the National Academy of Sciences*, 110(41), 16390–16395.

[382] Krimholtz, R. S., Leedom, D. A., & Matthaei, G. L. (1970). New equivalent circuits for elementary piezoelectric transducers. *Electronics Letters*, 6(13), 398–399.

[383] Krishna-K, K., Hertel, N., & Redies, C. (2011). Cadherin expression in the somatosensory cortex: evidence for a combinatorial molecular code at the single-cell level. *Neuroscience*, 175, 37–48.

[384] Kuchta, R. D., Benkovic, P., & Benkovic, S. J. (1988). Kinetic mechanism whereby dna polymerase i (klenow) replicates dna with high fidelity. *Biochemistry*, 27(18), 6716–6725.

[385] Kurzweil, R. (2012). *How to create a mind: The secret of human thought revealed*. Penguin.

[386] Lamy, F. & Fontaine, J. (1981). Transparent media characterization using sub-picosecond dye laser. In *European Hybrid Spectrometer Workshop on Holography and High-resolution Techniques*.

[387] Landauer, R. W. (1961). Irreversibility and heat generation in the computing process. *IBM Journal of Research and Development*, 5(3), 183–191.

[388] Larabell, C. A. & Le Gros, M. A. (2004). X-ray tomography generates 3-D reconstructions of the yeast, *Saccharomyces cerevisiae*, at 60-nm resolution. *Molecular Biology of the Cell*, 15(3), 957–962.

[389] Larson, D. R., Zipfel, W. R., Williams, R. M., Clark, S. W., Bruchez, M. P., Wise, F. W., & Webb, W. W. (2003). Water-soluble quantum dots for multiphoton fluorescence imaging in vivo. *Science*, 300(5624), 1434–1436.

[390] Lauxtermann, S., Israel, G., Seitz, P., Bloss, H., Ernst, J., Firla, H., & Gick, S. (2001). A megapixel high speed cmos imager with sustainable gigapixel/sec readout rate. In *at the 2001 IEEE Workshop on Charge-Coupled Devices and Advanced Image Sensors*.

[391] Lazebnik, M., Marks, D. L., Potgieter, K., Gillette, R., & Boppart, S. A. (2003). Functional optical coherence tomography for detecting neural activity through scattering changes. *Optics letters*, 28(14), 1218–1220.

[392] Lazzi, G. (2005). Thermal effects of bioimplants. *Engineering in Medicine and Biology Magazine, IEEE*, 24(5), 75–81.

[393] Le Bihan, D., Urayama, S.-i., Aso, T., Hanakawa, T., & Fukuyama, H. (2006). Direct and fast detection of neuronal activation in the human brain with diffusion mri. *Proceedings of the National Academy of Sciences*, 103(21), 8263–8268.

[394] Le Sage, D., Arai, K., Glenn, D., DeVience, S., Pham, L., Rahn-Lee, L., Lukin, M., Yacoby, A., Komeili, A., & Walsworth, R. (2013). Optical magnetic imaging of living cells. *Nature*, 496(7446), 486–489.

[395] Lecoq, J., Parpaleix, A., Roussakis, E., Ducros, M., Houssen, Y. G., Vinogradov, S. A., & Charpak, S. (2011). Simultaneous two-photon imaging of oxygen and blood flow in deep cerebral vessels. *Nature medicine*, 17(7), 893–898.

[396] Lee, J. H., Daugharthy, E. R., Scheiman, J., Kalhor, R., Yang, J. L., Ferrante, T. C., Terry, R., Jeanty, S. S., Li, C., Amamoto, R., et al. (2014). Highly multiplexed subcellular rna sequencing in situ. *Science*, 343(6177), 1360–1363.

[397] Lein, E. S., Hawrylycz, M. J., Ao, N., Ayres, M., Bensinger, A., Bernard, A., Boe, A. F., Boguski, M. S., Brockway, K. S., Byrnes, E. J., et al. (2006). Genome-wide atlas of gene expression in the adult mouse brain. *Nature*, 445(7124), 168–176.

[398] Lennie, P. (2003). The cost of cortical computation. *Current biology*, 13(6), 493–497.

[399] Levoy, M., Zhang, Z., & McDowall, I. (2009). Recording and controlling the 4d light field in a microscope using microlens arrays. *Journal of Microscopy*, 235(2), 144–162.

[400] Levskaya, A. (2011). The measure of mind.

[401] Li, A., Gong, H., Zhang, B., Wang, Q., Yan, C., Wu, J., Liu, Q., Zeng, S., & Luo, Q. (2010). Micro-optical sectioning tomography to obtain a high-resolution atlas of the mouse brain. *Science*, 330(6009), 1404–1408.

[402] Li, W., Prazak, L., Chatterjee, N., Grüninger, S., Krug, L., Theodorou, D., & Dubnau, J. (2013). Activation of transposable elements during aging and neuronal decline in drosophila. *Nature neuroscience*.

[403] Li, W.-h., Fraser, S. E., & Meade, T. J. (1999). A calcium-sensitive magnetic resonance imaging contrast agent. *Journal of the American Chemical Society*, 121(6), 1413–1414.

[404] Lieberman, P. (2002). On the nature and evolution of the neural bases of human language. *American Journal of Physical Anthropology*, 119(S35), 36–62.

[405] Lin, C., Rinker, S., Wang, X., Liu, Y., Seeman, N. C., & Yan, H. (2008). In vivo cloning of artificial dna nanostructures. *Proceedings of the National Academy of Sciences*, 105(46), 17626–17631.

[406] Lin, Y.-J. & Koretsky, A. P. (1997). Manganese ion enhances t1-weighted mri during brain activation: An approach to direct imaging of brain function. *Magnetic resonance in medicine*, 38(3), 378–388.

[407] Liu, D. S., Loh, K. H., Lam, S. S., White, K. A., & Ting, A. Y. (2013a). Imaging trans-cellular neurexin-neuroligin interactions by enzymatic probe ligation. *PloS one*, 8(2), e52823.

[408] Liu, T.-J. K., Marković, D., Stojanović, V., & Alon, E. (2012). The relay reborn. *IEEE Spectrum*, 49(4), 40–43.

[409] Liu, X., Cui, J., Sun, F., Song, X., Feng, F., Wang, J., Zhu, W., Lou, L., & Wang, G. (2013b). Fiber-integrated diamond-based magnetometer. *Applied Physics Letters*, 103(14), 143105–143105.

[410] Livet, J., Weissman, T. A., Kang, H., Draft, R. W., Lu, J., Bennis, R. A., Sanes, J. R., & Lichtman, J. W. (2007). Transgenic strategies for combinatorial expression of fluorescent proteins in the nervous system. *Nature*, 450, 56–62.

[411] Lizardi, P. M., Huang, X., Zhu, Z., Bray-Ward, P., Thomas, D. C., & Ward, D. C. (1998). Mutation detection and single-molecule counting using isothermal rolling-circle amplification. *Nature genetics*, 19(3), 225–232.

[412] Llinás, R. R., Walton, K. D., Nakao, M., Hunter, I., & Anquetil, P. A. (2005). Neuro-vascular central nervous recording/stimulating system. *Journal of Nanoparticle Research*, 7(2–3), 111–127.

[413] Loffredo, F. & Lee, R. T. (2008). Therapeutic vasculogenesis. *Circulation Research*, 103(2), 128–130.

[414] Logothetis, N. K. (2008). What we can do and what we cannot do with fmri. *Nature*, 453(7197), 869–878.

[415] Lu, R., Neff, N. F., Quake, S. R., & Weissman, I. L. (2011). Tracking single hematopoietic stem cells in vivo using high-throughput sequencing in conjunction with viral genetic barcoding. *Nature biotechnology*, 29(10), 928–933.

[416] Lubeck, E. & Cai, L. (2012). Single-cell systems biology by super-resolution imaging and combinatorial labeling. *Nature methods*, 9(7), 743–748.

[417] Luo, L., Callaway, E. M., & Svoboda, K. (2008). Genetic dissection of neural circuits. *Neuron*, 57(5), 634–660.

[418] Ma, W. J., Navalpakkam, V., Beck, J. M., Van Den Berg, R., & Pouget, A. (2011). Behavior and neural basis of near-optimal visual search. *Nature neuroscience*, 14(6), 783–790.

[419] Maass, W. (2000). On the computational power of winner-take-all. *Neural computation*, 12(11), 2519–2535.

[420] Maass, W. (2010). *Liquid state machines: motivation, theory, and applications*. London, UK: Imperial College Press.

[421] Machens, C. K. (2012). Building the human brain. *Science*, 338(6111), 1156–1157.

[422] MacKay, D. J. (2003). *Information theory, inference and learning algorithms*. Cambridge university press.

[423] Madejczyk, M. S. & Ballatori, N. (2012). The iron transporter ferroportin can also function as a manganese exporter. *Biochimica et Biophysica Acta (BBA)-Biomembranes*, 1818(3), 651–657.

[424] Madisen, L., Zwingman, T. A., Sunkin, S. M., Oh, S. W., Zariwala, H. A., Gu, H., Ng, L. L., Palmiter, R. D., Hawrylycz, M. J., Jones, A. R., et al. (2009). A robust and high-throughput cre reporting and characterization system for the whole mouse brain. *Nature neuroscience*, 13(1), 133–140.

[425] Mahalati, R. N., Gu, R. Y., & Kahn, J. M. (2013). Resolution limits for imaging through multi-mode fiber. *Optics Express*, 21(2), 1656–1668.

[426] Mahan, G. D., Engler, W. E., Tiemann, J. J., & Uzgiris, E. E. (1998). Ultrasonic tagging of light. *Proceedings of the National Academy of Sciences of the United States of America*, 95(24), 14015–14019.

[427] Mahjoubfar, A., Goda, K., Ayazi, A., Fard, A., Kim, S. H., & Jalali, B. (2011). High-speed nanometer-resolved imaging vibrometer and velocimeter. *Applied Physics Letters*, 98(10), 101107–101107.

[428] Mainen, Z. F. & Sejnowski, T. J. (1996). Influence of dendritic structure on firing pattern in model neocortical neurons. *Nature*, 382(6589), 363–366.

[429] Majewska, A. K., Newton, J. R., & Sur, M. (2006). Remodeling of synaptic structure in sensory cortical areas in vivo. *The Journal of neuroscience*, 26(11), 3021–3029.

[430] Mali, P., Esvelt, K. M., & Church, G. M. (2013). Cas9 as a versatile tool for engineering biology. *Nature methods*, 10(10), 957–963.

[431] Mandal, S. & Sarpeshkar, R. (2007). Low-power CMOS rectifier design for RFID applications. *IEEE Transactions on Circuits and Systems I*, 54(6), 1177–1188.

[432] Maravall, M., Mainen, Z., Sabatini, B., & Svoboda, K. (2000). Estimating intracellular calcium concentrations and buffering without wavelength ratioing. *Biophysical journal*, 78(5), 2655–2667.

[433] Marblestone, A. H., Daugharthy, E., Kalhor, R., Peikon, I., Kebschull, J., Shipman, S., Mishchenko, Y., Dalrymple, D. A., Zamft, B. M., Kording, K. P., Boyden, E. S., Zador, A. M., & Church, G. M. (2013a). Conneconomics: The economics of large-scale neural connectomics. *bioRxiv*.

[434] Marblestone, A. H., Zamft, B. M., Maguire, Y. G., Shapiro, M. G., Cybulski, T. R., Glaser, J. I., Amodei, D., Stranges, P. B., Kalhor, R., Dalrymple, D. A., Seo, D., Alon, E., Maharbiz, M. M., Carmena, J. M., Rabaey, J. M., Boyden, E. S., Church, G. M., & Kording, K. P. (2013b). Physical principles for scalable neural recording. *Frontiers in Computational Neuroscience*, 7, 137.

[435] Marcus, G. (2008). *The birth of the mind: How a tiny number of genes creates the complexities of human thought*. Basic Books.

[436] Marcus, G. (2009). How does the mind work? insights from biology. *Topics in cognitive science*, 1(1), 145–172.

[437] Marcus, G. F. (1998). Rethinking eliminative connectionism. *Cognitive psychology*, 37(3), 243–282.

[438] Marcus, G. F. (2003). *The algebraic mind: Integrating connectionism and cognitive science*. The MIT Press.

[439] Marcus, G. F. (2006). Cognitive architecture and descent with modification. *Cognition*, 101(2), 443–465.

[440] Marcus, G. F. & Davis, E. (2013). How robust are probabilistic models of higher-level cognition? *Psychological science*, 24(12), 2351–2360.

[441] Markov, N. T., Ercsey-Ravasz, M., Van Essen, D. C., Knoblauch, K., Toroczkai, Z., & Kennedy, H. (2013). Cortical high-density counterstream architectures. *Science*, 342(6158), 1238406.

[442] Markram, H. (2006). The blue brain project. *Nature Reviews Neuroscience*, 7(2), 153–160.

[443] Markram, H. (2012). The human brain project. *Scientific American*, 306(6), 50–55.

[444] Markram, H., Gerstner, W., & Sjöström, P. J. (2011). A history of spike-timing-dependent plasticity. *Frontiers in synaptic neuroscience*, 3.

[445] Markram, H., Lübke, J., Frotscher, M., Roth, A., & Sakmann, B. (1997). Physiology and anatomy of synaptic connections between thick tufted pyramidal neurones in the developing rat neocortex. *The Journal of physiology*, 500(Pt 2), 409.

[446] Marr, D. (1982). Vision: A computational investigation into the human representation and processing of visual information, henry holt and co. *Inc., New York, NY*, (pp.2).

[447] Marre, O., Amodei, D., Deshmukh, N., Sadeghi, K., Soo, F., Holy, T. E., & Berry, M. J. (2012). Mapping a complete neural population in the retina. *The Journal of Neuroscience*, 32(43), 14859–14873.

[448] Marshall, J. D. & Schnitzer, M. J. (2013). Optical strategies for sensing neuronal voltage using quantum dots and other semiconductor nanocrystals. *ACS Nano*, 7(5), 4601–4609.

[449] Marshall, W. F. (2004). Cellular length control systems. *Annu. Rev. Cell Dev. Biol.*, 20, 677–693.

[450] Martell, J. D., Deerinck, T. J., Sancak, Y., Poulos, T. L., Mootha, V. K., Sosinsky, G. E., Ellisman, M. H., & Ting, A. Y. (2012). Engineered ascorbate peroxidase as a genetically encoded reporter for electron microscopy. *Nature biotechnology*.

[451] Martin, J.-R. (2008). In vivo brain imaging: fluorescence or bioluminescence, which to choose? *Journal of Neurogenetics*, 22(3), 285–307.

[452] Martin, J.-R., Rogers, K. L., Chagneau, C., & Brûlet, P. (2007). In vivo bioluminescence imaging of ca2+ signalling in the brain of drosophila. *PLoS One*, 2(3), e275.

[453] Masters, B. R. (2006). *Confocal Microscopy and Multiphoton Excitation Microscopy*. Number PM161 in SPIE Press Monograph. SPIE Publications.

[454] Maze, J., Stanwix, P., Hodges, J., Hong, S., Taylor, J., Cappellaro, P., Jiang, L., Dutt, M. G., Togan, E., Zibrov, A., et al. (2008). Nanoscale magnetic sensing with an individual electronic spin in diamond. *Nature*, 455(7213), 644–647.

[455] McCabe, D. J., Tajalli, A., Austin, D. R., Bondareff, P., Walmsley, I. A., Gigan, S., & Chatel, B. (2011). Spatio-temporal focusing of an ultrafast pulse through a multiply scattering medium. *Nature Communications*, 2, 447.

[456] McElligott, J. & Melzack, R. (1967). Localized thermal changes evoked in the brain by visual and auditory stimulation. *Experimental neurology*, 17(3), 293–312.

[457] McKinney, E. H. (1966). Generalized birthday problem. *The American Mathematical Monthly*, 73(4), 385–387.

[458] Meer, E. J., Wang, D. O., Kim, S., Barr, I., Guo, F., & Martin, K. C. (2012). Identification of a cis-acting element that localizes mrna to synapses. *Proceedings of the National Academy of Sciences*, 109(12), 4639–4644.

[459] Merchán-Pérez, A., Rodríguez, J.-R., González, S., Robles, V., DeFelipe, J., Larrañaga, P., & Bielza, C. (2013). Three-dimensional spatial distribution of synapses in the neocortex: A dual-beam electron microscopy study. *Cerebral Cortex*.

[460] Merkle, R. C. (1989). *Large scale analysis of neural structures*. XEROX Corporation, Palo Alto Research Center.

[461] Meyer, H. S., Egger, R., Guest, J. M., Foerster, R., Reissl, S., & Oberlaender, M. (2013). Cellular organization of cortical barrel columns is whisker-specific. *Proceedings of the National Academy of Sciences*, (pp. 201312691).

[462] Micheva, K. D., O'Rourke, N., Busse, B., & Smith, S. J. (2010). Array tomography: high-resolution three-dimensional immunofluorescence. *Cold Spring Harbor Protocols*, 2010(11), pdb–top89.

[463] Micheva, K. D. & Smith, S. J. (2007). Array tomography: a new tool for imaging the molecular architecture and ultrastructure of neural circuits. *Neuron*, 55(1), 25–36.

[464] Mikula, S., Binding, J., & Denk, W. (2012). Staining and embedding the whole mouse brain for electron microscopy. *Nature methods*, 9(12), 1198–1201.

[465] Mishchenko, Y. (2009). Automation of 3d reconstruction of neural tissue from large volume of conventional serial section transmission electron micrographs. *Journal of neuroscience methods*, 176(2), 276–289.

[466] Mishchenko, Y. (2010). On optical detection of densely labeled synapses in neuropil and mapping connectivity with combinatorially multiplexed fluorescent synaptic markers. *PloS one*, 5(1), e8853.

[467] Mishchenko, Y. (2011). Reconstruction of complete connectivity matrix for connectomics by sampling neural connectivity with fluorescent synaptic markers. *Journal of neuroscience methods*, 196(2), 289–302.

[468] Mishchenko, Y., Hu, T., Spacek, J., Mendenhall, J., Harris, K. M., & Chklovskii, D. B. (2010). Ultrastructural analysis of hippocampal neuropil from the connectomics perspective. *Neuron*, 67(6), 1009–1020.

[469] Mishchenko, Y. & Paninski, L. (2012). A bayesian compressed-sensing approach for reconstructing neural connectivity from subsampled anatomical data. *Journal of computational neuroscience*, 33(2), 371–388.

[470] Mishchenko, Y., Vogelstein, J. T., & Paninski, L. (2011). A bayesian approach for inferring neuronal connectivity from calcium fluorescent imaging data. *The Annals of Applied Statistics*, 5(2B), 1229–1261.

[471] Mitra, R. D. & Church, G. M. (1999). In situ localized amplification and contact replication of many individual dna molecules. *Nucleic Acids Research*, 27(24), e34–e39.

[472] Miya, T., Terunuma, Y., Hosaka, T., & Miyashita, T. (1979). Ultimate low-loss single-mode fibre at 1.55 um. *Electronics Letters*, 15(4), 106–108.

[473] Miyakawa, H. & Aonishi, T. (2012). Apparent extracellular current density and extracellular space: basis for the current source density analysis in neural tissue. *arXiv preprint arXiv:1209.4722*.

[474] Mohr, P. J., Taylor, B. N., & Newell, D. B. (2010). CODATA recommended values of the fundamental physical constants: 2010. *Reviews of Modern Physics*, 84(4), 1527–1605.

[475] Molter, T. W., McQuaide, S. C., Suchorolski, M. T., Strovad, T. J., Burgess, L. W., Meldrum, D. R., & Lidstrom, M. E. (2009). A microwell array device capable of measuring single-cell oxygen consumption rates. *Sensors and Actuators B*, 135(2), 678–686.

[476] Monai, H., Inoue, M., Miyakawa, H., & Aonishi, T. (2012). Low-frequency dielectric dispersion of brain tissue due to electrically long neurites. *Physical Review E*, 86(6), 061911.

[477] Monai, H., Omori, T., Okada, M., Inoue, M., Miyakawa, H., & Aonishi, T. (2010). An analytic solution of the cable equation predicts frequency preference of a passive shunt-end cylindrical cable in response to extracellular oscillating electric fields. *Biophysical journal*, 98(4), 524–533.

[478] Moosmann, J., Ershov, A., Altapova, V., Baumbach, T., Prasad, M. S., LaBonne, C., Xiao, X., Kashed, J., & Hofmann, R. (2013). X-ray phase-contrast *in vivo* microtomography probes new aspects of *Xenopus* gastrulation. *Nature*, 497, 374–377.

[479] Morales, J., Alonso-Nanclares, L., Rodríguez, J.-R., DeFelipe, J., Rodríguez, Á., & Merchán-Pérez, Á. (2011). Espina: a tool for the automated segmentation and counting of synapses in large stacks of electron microscopy images. *Frontiers in neuroanatomy*, 5.

[480] Morgan, H., Hughes, M. P., & Green, N. G. (1999). Separation of submicron bioparticles by dielectrophoresis. *Biophysical journal*, 77(1), 516–525.

[481] Morgan, J. L. & Lichtman, J. W. (2013). Why not connectomics? *Nature methods*, 10(6), 494–500.

[482] Mountcastle, V. (1978). An organizing principle for cerebral function: The unit model and the distributed system.

[483] Moustakas, A. L., Baranger, H. U., Balents, L., Sengupta, A., & Simon, S. H. (2000). Communication through a diffusive medium. *Science*, 287(5451), 287–290.

[484] Moyes, C. & Jiang, M. (2012). Brain-computer interface.

[485] Mudry, E., Le Moal, E., Ferrand, P., Chaumet, P. C., & Sentenac, A. (2010). Isotropic diffraction-limited focusing using a single objective lens. *Physical review letters*, 105(20), 203903.

[486] Murray, T. A. & Levene, M. J. (2012). Singlet gradient index lens for deep in vivo multiphoton microscopy. *Journal of Biomedical Optics*, 17(2), 021106.

[487] Najafi, K. & Hetke, J. F. (1990). Strength characterization of silicon microprobes in neurophysiological tissues. *IEEE Transactions on Biomedical Engineering*, 37(5), 474–481.

[488] Naumann, E. A., Kampff, A. R., Prober, D. A., Schier, A. F., & Engert, F. (2010). Monitoring neural activity with bioluminescence during natural behavior. *Nature neuroscience*, 13(4), 513–520.

[489] Naumann, R., Anjum, F., Roth-Alpermann, C., & Brecht, M. (2012). Cytoarchitecture, areas, and neuron numbers of the etruscan shrew cortex. *Journal of Comparative Neurology*, 520(11), 2512–2530.

[490] Nelson, S. B. (2002). Cortical microcircuits-diverse or canonical? *Neuron*, 36(1), 19–27.

[491] Nessler, B., Pfeiffer, M., Buesing, L., & Maass, W. (2013). Bayesian computation emerges in generic cortical microcircuits through spike-timing-dependent plasticity. *PLoS computational biology*, 9(4), e1003037.

[492] Neves, G., Zucker, J., Daly, M., & Chess, A. (2004). Stochastic yet biased expression of multiple dscam splice variants by individual cells. *Nature genetics*, 36(3), 240–246.

[493] Nguyen, Q.-T., Schroeder, L. F., Mank, M., Muller, A., Taylor, P., Griesbeck, O., & Kleinfeld, D. (2009). An in vivo biosensor for neurotransmitter release and in situ receptor activity. *Nature neuroscience*, 13(1), 127–132.

[494] Nicolelis, M. A. L., Dimitrov, D., Carmena, J. M., Crist, R., Lehew, G., Kralik, J. D., & Wise, S. P. (2003). Chronic, multisite, multielectrode recordings in macaque monkeys. *Proceedings of the National Academy of Sciences*, 100(19), 11041–11046.

[495] Nixon, M., Katz, O., Small, E., Bromberg, Y., Friesem, A. A., Silberberg, Y., & Davidson, N. (2013). Real-time wavefront-shaping through scattering media by all optical feedback.

[496] Noirot-Gros, M.-F. & Ehrlich, S. D. (1996). Change of a catalytic reaction carried out by a dna replication protein. *Science*, 274(5288), 777–780.

[497] Nowlan, S. J. & Sejnowski, T. J. (1995). A selection model for motion processing in area mt of primates. *The Journal of Neuroscience*, 15(2), 1195–1214.

[498] Null, B., Liu, C. W., Hedehus, M., Conolly, S., & Davis, R. W. (2008). High-resolution, *in vivo* magnetic resonance imaging of *Drosophila* at 18.8 tesla. *PLoS ONE*, 3(7), e2817.

[499] Ochman, H. & Wilson, A. C. (1987). Evolution in bacteria: Evidence for a universal substitution rate in cellular genomes. *Journal of Molecular Evolution*, 26(1-2), 74–86.

[500] O'Connor, D. H., Peron, S. P., Huber, D., & Svoboda, K. (2010). Neural activity in barrel cortex underlying vibrissa-based object localization in mice. *Neuron*, 67(6), 1048–1061.

[501] Ogawa, S., Lee, T.-M., Nayak, A. S., & Glynn, P. (1990). Oxygenation-sensitive contrast in magnetic resonance image of rodent brain at high magnetic fields. *Magnetic resonance in medicine*, 14(1), 68–78.

[502] Oh, S., Fang-Yen, C., Choi, W., Yaqoob, Z., Fu, D., Park, Y., Dassari, R. R., & Feld, M. S. (2012). Label-free imaging of membrane potential using membrane electromotility. *Biophysical Journal*, 103(1), 11–18.

[503] Oh, S. W., Harris, J. A., Ng, L., Winslow, B., Cain, N., Mihalas, S., Wang, Q., Lau, C., Kuan, L., Henry, A. M., et al. (2014). A mesoscale connectome of the mouse brain. *Nature*.

[504] Ohmori, H., Friedberg, E. C., Fuchs, R. P., Goodman, M. F., Hanaoka, F., Hinkle, D., Kunkel, T. A., Lawrence, C. W., Livneh, Z., Nohmi, T., et al. (2001). The y-family of dna polymerases. *Molecular cell*, 8(1), 7–8.

[505] Ono, T. & Yano, Y. (1998). Key technologies for terabit/second wdm systems with high spectral efficiency of over 1 bit/s/hz. *Quantum Electronics, IEEE Journal of*, 34(11), 2080–2088.

[506] Oron, D., Tal, E., Silberberg, Y., et al. (2005). Scanningless depth-resolved microscopy. *Opt. Express*, 13(5), 1468–1476.

[507] O'Rourke, N. A., Weiler, N. C., Micheva, K. D., & Smith, S. J. (2012). Deep molecular diversity of mammalian synapses: why it matters and how to measure it. *Nature Reviews Neuroscience*, 13(6), 365–379.

[508] Osten, P. & Margrie, T. W. (2013). Mapping brain circuitry with a light microscope. *Nature methods*, 10(6), 515–523.

[509] Oyibo, H., Cao, G., Zhan, H., Koulakov, A., Enquist, L., Dubnau, J., & Zador, A. (2011). Probing the connectivity of neural circuits at single-neuron resolution using high-throughput dna sequencing.

[510] Ozeri, S. & Shmilovitz, D. (2010). Ultrasonic transcutaneous energy transfer for powering implanted devices. *Ultrasonics*, 50(6), 556–566.

[511] Packer, A. M., Roska, B., & Häusser, M. (2013). Targeting neurons and photons for optogenetics. *Nature neuroscience*, 16(7), 805–815.

[512] Papagiakoumou, E., Anselmi, F., Bègue, A., de Sars, V., Glückstad, J., Isacoff, E. Y., & Emiliani, V. (2010). Scanless two-photon excitation of channelrhodopsin-2. *Nature methods*, 7(10), 848–854.

[513] Papagiakoumou, E., Bègue, A., Leshem, B., Schwartz, O., Stell, B. M., Bradley, J., Oron, D., & Emiliani, V. (2013). Functional patterned multiphoton excitation deep inside scattering tissue. *Nature Photonics*.

[514] Pappu, R., Recht, B., Taylor, J., & Gershenfeld, N. (2002). Physical one-way functions. *Science*, 297(5589), 2026–2030.

[515] Parpaleix, A., Houssen, Y. G., & Charpak, S. (2013). Imaging local neuronal activity by monitoring po2 transients in capillaries. *Nature medicine*.

[516] Payne, A. C., Andregg, M., Kemmish, K., Hamalainen, M., Bowell, C., Bleloch, A., Klejwa, N., Lehrach, W., Schatz, K., Stark, H., et al. (2013). Molecular threading: Mechanical extraction, stretching and placement of dna molecules from a liquid-air interface. *PloS one*, 8(7), e69058.

[517] Pedreira, C., Martinez, J., Ison, M. J., & Quian Quiroga, R. (2012). How many neurons can we see with current spike sorting algorithms? *Journal of Neuroscience Methods*, 211(1), 58–65.

[518] Peikon, I., Gizatullina, D., & Zador, A. (2014). In vivo generation of dna sequence diversity for cellular barcoding. *bioRxiv*.

[519] Perin, R., Berger, T. K., & Markram, H. (2011). A synaptic organizing principle for cortical neuronal groups. *Proceedings of the National Academy of Sciences*, 108(13), 5419–5424.

[520] Perkel, J. M. (2013). This is your brain: Mapping the connectome. *Science*, 339(6117), 350–352.

[521] Petreanu, L., Mao, T., Sternson, S. M., & Svoboda, K. (2009). The subcellular organization of neocortical excitatory connections. *Nature*, 457(7233), 1142–1145.

[522] Petridou, N., Plenz, D., Silva, A. C., Loew, M., Bodurka, J., & Bandettini, P. A. (2006). Direct magnetic resonance detection of neuronal electrical activity. *Proceedings of the National Academy of Sciences*, 103(43), 16015–16020.

[523] Pi, H. J., Otmakhov, N., El Gaamouch, F., Lemelin, D., De Koninck, P., & Lisman, J. (2010). Camkii control of spine size and synaptic strength: role of phosphorylation states and nonenzymatic action. *Proceedings of the National Academy of Sciences*, 107(32), 14437–14442.

[524] Pillow, J. W., Shlens, J., Chichilnisky, E. J., & Simoncelli, E. P. (2013). A model-based spike sorting algorithm for removing correlation artifacts in multi-neuron recordings. *PLoS ONE*, 8(5), e62123.

[525] Pinheiro, A. V., Han, D., Shih, W. M., & Yan, H. (2011). Challenges and opportunities for structural dna nanotechnology. *Nature nanotechnology*, 6(12), 763–772.

[526] Plaza, S. M., Scheffer, L. K., & Chklovskii, D. B. (2014). Toward large-scale connectome reconstructions. *Current opinion in neurobiology*, 25, 201–210.

[527] Pnevmatikakis, E. A. & Paninski, L. (2013). Sparse nonnegative deconvolution for compressive calcium imaging: algorithms and phase transitions. *Advances in Neural Information Processing Systems (NIPS)*.

[528] Poeppel, D. (2012). The maps problem and the mapping problem: Two challenges for a cognitive neuroscience of speech and language. *Cognitive neuropsychology*, 29(1-2), 34–55.

[529] Poggio, T., Mutch, J., Leibo, J., Rosasco, L., & Tacchetti, A. (2012). The computational magic of the ventral stream: sketch of a theory (and why some deep architectures work).

[530] Polderman, K. H. (2004). Application of therapeutic hypothermia in the icu: opportunities and pitfalls of a promising treatment modality. part 1: Indications and evidence. *Intensive Care Medicine*, 30(4).

[531] Polikov, V. S., Tresco, P. A., & Reichert, W. M. (2005). Response of brain tissue to chronically implanted neural electrodes. *Journal of neuroscience methods*, 148(1), 1–18.

[532] Pollock, J. D., Wu, D.-Y., & Satterlee, J. S. (2014). Molecular neuroanatomy: a generation of progress. *Trends in neurosciences*.

[533] Popoff, S. M., Lerosey, G., Carminati, R., Fink, M., Boccara, A. C., & Gigan, S. (2010). Measuring the transmission matrix in optics. *Physical Review Letters*, 104(10), e100601.

[534] Prentice, J. S., Homann, J., Simmons, K. D., Tkacik, G., Balasubramanian, V., & Nelson, P. C. (2011). Fast, scalable, bayesian spike identification for multi-electrode arrays. *PLoS ONE*, 6(7), e19884.

[535] Pritchard, C. E. & Southern, E. M. (1997). Effects of base mismatches on joining of short oligodeoxynucleotides by dna ligases. *Nucleic acids research*, 25(17), 3403–3407.

[536] Priya, S., Ryu, J., Park, C.-S., Oliver, J., Choi, J.-J., & Park, D.-S. (2009). Piezoelectric and magnetoelectric thick films for fabricating power sources in wireless sensor nodes. *Sensors*, 9(8).

[537] Puopolo, M., Hochstetler, S. E., Gustincich, S., Wightman, R. M., & Raviola, E. (2001). Extrasynaptic release of dopamine in a retinal neuron: activity dependence and transmitter modulation. *Neuron*, 30(1), 211–225.

[538] Purves, D., Fitzpatrick, D., Katz, L., Lamantia, A., McNamara, J., Williams, S., & Augustine, G. (2001). *Neuroscience*. Sinauer Associates.

[539] Qamar, A. T., Cotton, R. J., George, R. G., Beck, J. M., Prezhdo, E., Laudano, A., Tolias, A. S., & Ma, W. J. (2013). Trial-to-trial, uncertainty-based adjustment of decision boundaries in visual categorization. *Proceedings of the National Academy of Sciences*, 110(50), 20332–20337.

[540] Quirin, S., Peterka, D. S., & Yuste, R. (2013). Instantaneous three-dimensional sensing using spatial light modulator illumination with extended depth of field imaging. *Optics express*, 21(13), 16007–16021.

[541] Rah, J.-C., Bas, E., Colonell, J., Mishchenko, Y., Karsh, B., Fetter, R. D., Myers, E. W., Chklovskii, D. B., Svoboda, K., Harris, T. D., et al. (2013). Thalamocortical input onto layer 5 pyramidal neurons measured using quantitative large-scale array tomography. *Frontiers in neural circuits*, 7.

[542] Rakonjac, J., Bennett, N. J., Spagnuolo, J., Gagic, D., & Russel, M. (2011). Filamentous bacteriophage: biology, phage display and nanotechnology applications. *Current issues in molecular biology*, 13(2), 51.

[543] Rapoport, B. I., Kedzierski, J. T., & Sarpeshkar, R. (2012). A glucose fuel cell for implantable brain-machine interfaces. *PLoS ONE*, 7(6), e38436.

[544] Rapoport, B. I., Wattanapanitch, W., Penagos Vargas, H. L., Musallam, S., Andersen, R. A., & Sarpeshkar, R. (2009). A biomimetic adaptive algorithm and low-power architecture for implantable neural decoders. In *Engineering in Medicine and Biology Society* (pp. 4214–4217).

[545] Raskar, R. & Tumblin, J. (2009). *Computational Photography: Mastering New Techniques for Lenses, Lighting, and Sensors*. AK Peters, Ltd.

[546] Reichardt, W., Poggio, T., & Hausen, K. (1983). Figure-ground discrimination by relative movement in the visual system of the fly. *Biological Cybernetics*, 46(1), 1–30.

[547] Reichert, W. M. (2010). *Indwelling neural implants: strategies for contending with the in vivo environment*. CRC Press.

[548] Reichert, W. M., He, W., & Bellamkonda, R. V. (2008). A molecular perspective on understanding and modulating the performance of chronic central nervous system (cns) recording electrodes.

[549] Reimann, M. W., Anastassiou, C. A., Perin, R., Hill, S. L., Markram, H., & Koch, C. (2013). A biophysically detailed model of neocortical local field potentials predicts the critical role of active membrane currents. *Neuron*, 79(2), 375–390.

[550] Rhee, H.-W., Zou, P., Udeshi, N. D., Martell, J. D., Mootha, V. K., Carr, S. A., & Ting, A. Y. (2013). Proteomic mapping of mitochondria in living cells via spatially restricted enzymatic tagging. *Science*, 339(6125), 1328–1331.

[551] Ribeiro, S., Gervasoni, D., Soares, E. S., Zhou, Y., Lin, S.-C., Pantoja, J., Lavine, M., & Nicolelis, M. A. L. (2004). Long-lasting novelty-induced neuronal reverberation during slow-wave sleep in multiple forebrain areas. *PLoS Biol*, 2(1), e24.

[552] Rider, T. H., Petrovick, M. S., Nargi, F. E., Harper, J. D., Schwoebel, E. D., Mathews, R. H., Blanchard, D. J., Bortolin, L. T., Young, A. M., Chen, J., et al. (2003). Ab cell-based sensor for rapid identification of pathogens. *Science*, 301(5630), 213–215.

[553] Riesenhuber, M. & Poggio, T. (1999). Hierarchical models of object recognition in cortex. *Nature neuroscience*, 2(11), 1019–1025.

[554] Risi, S. & Stanley, K. O. (2011). Enhancing es-hyperneat to evolve more complex regular neural networks. In *Proceedings of the 13th annual conference on Genetic and evolutionary computation* (pp. 1539–1546).: ACM.

[555] Rizk, M., Bossetti, C. A., Jochum, T. A., Callender, S. H., Nicolelis, M. A., Turner, D. A., & Wolf, P. D. (2009). A fully implantable 96-channel neural data acquisition system. *Journal of Neural Engineering*, 6(2), 6002.

[556] Roberts, M., Jeong, W.-K., Vázquez-Reina, A., Unger, M., Bischof, H., Lichtman, J., & Pfister, H. (2011). Neural process reconstruction from sparse user scribbles. In *Medical Image Computing and Computer-Assisted Intervention–MICCAI 2011* (pp. 621–628). Springer.

[557] Rodriguez, A., Whitson, J., & Granger, R. (2004). Derivation and analysis of basic computational operations of thalamocortical circuits. *Journal of cognitive neuroscience*, 16(5), 856–877.

[558] Roe, A. W., Pallas, S. L., Kwon, Y. H., & Sur, M. (1992). Visual projections routed to the auditory pathway in ferrets: receptive fields of visual neurons in primary auditory cortex. *The Journal of neuroscience*, 12(9), 3651–3664.

[559] Rooney, W. D., Johnson, G., Li, X., Cohen, E. R., Kim, S.-G., Ugurbil, K., & Springer, C. S. (2007). Magnetic field and tissue dependencies of human brain longitudinal ^1H_2O relaxation in vivo. *Magnetic Resonance in Medicine*, 57(2), 308–318.

[560] Roth, B. J. & Basser, P. J. (2009). Mechanical model of neural tissue displacement during lorentz effect imaging. *Magnetic Resonance in Medicine*, 61(1), 59–64.

[561] Rothemund, P. W., Papadakis, N., & Winfree, E. (2004). Algorithmic self-assembly of dna sierpinski triangles. *PLoS biology*, 2(12), e424.

[562] Roux, K. J., Kim, D. I., Raida, M., & Burke, B. (2012). A promiscuous biotin ligase fusion protein identifies proximal and interacting proteins in mammalian cells. *The Journal of cell biology*, 196(6), 801–810.

[563] Roxin, A., Brunel, N., Hansel, D., Mongillo, G., & van Vreeswijk, C. (2011). On the distribution of firing rates in networks of cortical neurons. *The Journal of Neuroscience*, 31(45), 16217–16226.

[564] Rueffler, C., Hermisson, J., & Wagner, G. P. (2012). Evolution of functional specialization and division of labor. *Proceedings of the National Academy of Sciences*, 109(6), E326–E335.

[565] Rusakov, D. A., Kullmann, D. M., & Stewart, M. G. (1999). Hippocampal synapses: do they talk to their neighbours? *Trends in neurosciences*, 22(9), 382–388.

[566] Sadek, A. S., Karabalin, R. B., Du, J., Roukes, M. L., Koch, C., & Masmanidis, S. C. (2010). Wiring nanoscale biosensors with piezoelectric nanomechanical resonators. *Nano letters*, 10(5), 1769–1773.

[567] Sahani, M. (1999). Latent variable models for neural data analysis.

[568] Sale, J. E., Lehmann, A. R., & Woodgate, R. (2012). Y-family dna polymerases and their role in tolerance of cellular dna damage. *Nature Reviews Molecular Cell Biology*, 13(3), 141–152.

[569] Sanjana, N. E., Levanon, E. Y., Hueske, E. A., Ambrose, J. M., & Li, J. B. (2012). Activity-dependent a-to-i rna editing in rat cortical neurons. *Genetics*, 192(1), 281–287.

[570] Sanna, C. R., Li, W.-H., & Zhang, L. (2008). Overlapping genes in the human and mouse genomes. *BMC genomics*, 9(1), 169.

[571] Sarpeshkar, R. (1998). Analog versus digital: Extrapolating from electronics to neurobiology. *Neural Computation*, 10(7), 1601–1638.

[572] Sarpeshkar, R. (2010). *Ultra Low Power Bioelectronics*. Cambridge University Press.

[573] Saunders, C. & Scully, P. (2005). Distributed plastic optical fibre measurement of ph using a photon counting otdr. In *Journal of Physics: Conference Series*, volume 15 (pp.61).: IOP Publishing.

[574] Scanziani, M. & Häusser, M. (2009). Electrophysiology in the age of light. *Nature*, 461(7266), 930–939.

[575] Schietinger, S., Barth, M., Aichele, T., & Benson, O. (2009). Plasmon-enhanced single photon emission from a nanoassembled metal- diamond hybrid structure at room temperature. *Nano letters*, 9(4), 1694–1698.

[576] Schmidt, R., Wurm, C. A., Jakobs, S., Engelhardt, J., Egner, A., & Hell, S. W. (2008). Spherical nanosized focal spot unravels the interior of cells. *Nature methods*, 5(6), 539–544.

[577] Schneidman, E., Berry, M. J., Segev, R., & Bialek, W. (2006). Weak pairwise correlations imply strongly correlated network states in a neural population. *Nature*, 440(7087), 1007–1012.

[578] Schrödel, T., Prevedel, R., Aumayr, K., Zimmer, M., & Vaziri, A. (2013). Brain-wide 3d imaging of neuronal activity in caenorhabditis elegans with sculpted light. *Nature Methods*.

[579] Schwan, H. & Cole, K. (1960). Bioelectricity: alternating current admittance of cells and tissues. *Medical physics*, 3, 52.

[580] Scott Provost, G., Kretz, P. L., Hamner, R. T., Matthews, C. D., Rogers, B. J., Lundberg, K. S., Dycaico, M. J., & Short, J. M. (1993). Transgenic systems for in vivo mutation analysis. *Mutation Research/Fundamental and Molecular Mechanisms of Mutagenesis*, 288(1), 133–149.

[581] Seeman, N. C. (2007). An overview of structural dna nanotechnology. *Molecular biotechnology*, 37(3), 246–257.

[582] Segev, R., Goodhouse, J., Puchalla, J., & Berry, II, M. J. (2004). Recording spikes from a large fraction of the ganglion cells in a retinal patch. *Nature Neuroscience*, 7(10), 1155–1162.

[583] Sela, G., Dana, H., & Shoham, S. (2013). Ultra-deep penetration of temporally-focused two-photon excitation. In *SPIE BiOS* (pp. 858824–858824).: International Society for Optics and Photonics.

[584] Seliger, H. H. & McElroy, W. D. (1960). Spectral emission and quantum yield of firefly bioluminescence. *Archives of Biochemistry and Biophysics*, 88(1), 136–141.

[585] Seo, D., Carmena, J. M., Rabaey, J. M., Alon, E., & Maharbiz, M. M. (2013). Neural dust: An ultrasonic, low power solution for chronic brain-machine interfaces. *ArXiv preprint*.

[586] Seung, S. (2012). *Connectome: How the brain's wiring makes us who we are*. Houghton Mifflin Harcourt.

[587] Seung, S. (2013). Eyewire.

[588] Shafi, M., Zhou, Y., Quintana, J., Chow, C., Fuster, J., & Bodner, M. (2007). Variability in neuronal activity in primate cortex during working memory tasks. *Neuroscience*, 146(3), 1082–1108.

[589] Shanahan, M. (2006). A cognitive architecture that combines internal simulation with a global workspace. *Consciousness and Cognition*, 15(2), 433–449.

[590] Shao, L., Isaac, B., Uzawa, S., Agard, D. A., Sedat, J. W., & Gustafsson, M. G. (2008). I5s: Wide-field light microscopy with 100-nm-scale resolution in three dimensions. *Biophysical journal*, 94(12), 4971–4983.

[591] Shapiro, E., Biezuner, T., & Linnarsson, S. (2013a). Single-cell sequencing-based technologies will revolutionize whole-organism science. *Nature Reviews Genetics*, 14(9), 618–630.

[592] Shapiro, M., Goodwill, P., Neogy, A., Schaffer, D., & Conolly, S. (In revision). Genetically encoded gas nanostructures as ultrasonic molecular reporters.

[593] Shapiro, M. G., Atanasijevic, T., Faas, H., Westmeyer, G. G., & Jasanoff, A. (2006). Dynamic imaging with MRI contrast agents: quantitative considerations. *Magnetic Resonance Imaging*, 24(4), 449–462.

[594] Shapiro, M. G., Homma, K., Villarreal, S., Richter, C.-P., & Bezanilla, F. (2012). Infrared light excites cells by changing their electrical capacitance. *Nature Communications*, 3(736).

[595] Shapiro, M. G., Priest, M. F., Siegel, P. H., & Bezanilla, F. (2013b). Temperature-mediated effects of millimeter wave stimulation on membrane protein function. *Biophysical Journal*, 104(2), 679a.

[596] Shapiro, M. G., Westmeyer, G. G., Romero, P. A., Szablowski, J. O., Küster, B., Shah, A., Otey, C. R., Langer, R., Arnold, F. H., & Jasanoff, A. (2010). Directed evolution of a magnetic resonance imaging contrast agent for noninvasive imaging of dopamine. *Nature Biotechnology*, 28(3), 264–270.

[597] Sharma, J., Angelucci, A., & Sur, M. (2000). Induction of visual orientation modules in auditory cortex. *Nature*, 404(6780), 841–847.

[598] Shcherbakova, D. M. & Verkhusha, V. V. (2013). Near-infrared fluorescent proteins for multicolor *in vivo* imaging. *Nature Methods*.

[599] Shcherbo, D., Murphy, C. S., Ermakova, G. V., Solovieva, E. A., Chepurnykh, T. V., Shcheglov, A. S., Verkhusha, V. V., Pletnev, V. Z., Hazelwood, K. L., Roche, P. M., Lukyanov, S., Zaraisky, A. G., Davidson, M. W., & Chudakov, D. M. (2009). Far-red fluorescent tags for protein imaging in living tissues. *Biochem J*, 418(3), 567–574.

[600] Shendure, J. & Ji, H. (2008). Next-generation dna sequencing. *Nature biotechnology*, 26(10), 1135–1145.

[601] Shepherd, G. M. & Svoboda, K. (2005). Laminar and columnar organization of ascending excitatory projections to layer 2/3 pyramidal neurons in rat barrel cortex. *The Journal of neuroscience*, 25(24), 5670–5679.

[602] Shih, A. Y., Blinder, P., Tsai, P. S., Friedman, B., Stanley, G., Lyden, P. D., & Kleinfeld, D. (2012). The smallest stroke: occlusion of one penetrating vessel leads to infarction and a cognitive deficit. *Nature neuroscience*, 16(1), 55–63.

[603] Shih, W. M., Quispe, J. D., & Joyce, G. F. (2004). A 1.7-kilobase single-stranded dna that folds into a nanoscale octahedron. *Nature*, 427(6975), 618–621.

[604] Shin, C. S., Avalos, C. E., Butler, M. C., Trease, D. R., Seltzer, S. J., Peter Mustonen, J., Kennedy, D. J., Acosta, V. M., Budker, D., Pines, A., et al. (2012). Room-temperature operation of a radiofrequency diamond magnetometer near the shot-noise limit. *Journal of Applied Physics*, 112(12), 124519–124519.

[605] Shiroguchi, K., Jia, T. Z., Sims, P. A., & Xie, X. S. (2012). Digital rna sequencing minimizes sequence-dependent bias and amplification noise with optimized single-molecule barcodes. *Proceedings of the National Academy of Sciences*, 109(4), 1347–1352.

[606] Shiu, D.-s., Foschini, G. J., Gans, M. J., & Kahn, J. M. (2000). Fading correlation and its effect on the capacity of multielement antenna systems. *IEEE Transactions on Communications*, 48(3), 502–513.

[607] Shoham, S., O'Connor, D. H., & Segev, R. (2006). How silent is the brain: is there a dark matter problem in neuroscience? *Journal of Comparative Physiology A*, 192(8), 777–784.

[608] Shu, X., Lev-Ram, V., Deerinck, T. J., Qi, Y., Ramko, E. B., Davidson, M. W., Jin, Y., Ellisman, M. H., & Tsien, R. Y. (2011). A genetically encoded tag for correlated light and electron microscopy of intact cells, tissues, and organisms. *PLoS biology*, 9(4), e1001041.

[609] Silver, I. A. & Erecińska, M. (1994). Extracellular glucose concentration in mammalian brain: continuous monitoring of changes during increased neuronal activity and upon limitation in oxygen supply in normo-, hypo-, and hyperglycemic animals. *The Journal of Neuroscience*, 14(8), 5068–5076.

[610] Simon, H. A. (1996). *The sciences of the artificial*. MIT press.

[611] Simpson, H. D. & Goodhill, G. J. (2011). A simple model can unify a broad range of phenomena in retinotectal map development. *Biological cybernetics*, 104(1-2), 9–29.

[612] Singh, R. & Eliasmith, C. (2006). Higher-dimensional neurons explain the tuning and dynamics of working memory cells. *The journal of neuroscience*, 26(14), 3667–3678.

[613] Singh-Gasson, S., Green, R. D., Yue, Y., Nelson, C., Blattner, F., Sussman, M. R., & Cerrina, F. (1999). Maskless fabrication of light-directed oligonucleotide microarrays using a digital micromirror array. *Nature biotechnology*, 17(10), 974–978.

[614] Sirotin, Y. B. & Das, A. (2009). Anticipatory haemodynamic signals in sensory cortex not predicted by local neuronal activity. *Nature*, 457(7228), 475–479.

[615] Slobodin, B. & Gerst, J. E. (2010). A novel mrna affinity purification technique for the identification of interacting proteins and transcripts in ribonucleoprotein complexes. *RNA*, 16(11), 2277–2290.

[616] Smetters, D., Majewska, A., & Yuste, R. (1999). Detecting action potentials in neuronal populations with calcium imaging. *METHODS: A Companion to Methods in Enzymology*, 18.

[617] Smith, K. D. & Zhu, L. (2010). Brain hypothermia induced by cold spinal fluid using a torso cooling pad: theoretical analyses. *Medical & biological engineering & computing*, 48(8), 783–791.

[618] Solari, S. V. H. & Stoner, R. (2011). Cognitive consilience: primate non-primary neuroanatomical circuits underlying cognition. *Frontiers in neuroanatomy*, 5.

[619] Song, S., Sjöström, P. J., Reigl, M., Nelson, S., & Chklovskii, D. B. (2005). Highly nonrandom features of synaptic connectivity in local cortical circuits. *PLoS biology*, 3(3), e68.

[620] Sorensen, S. A., Bernard, A., Menon, V., Royall, J. J., Glattfelder, K. J., Hirokawa, K., Mortrud, M., Miller, J. A., Zeng, H., Hohmann, J. G., et al. (2013). Correlated gene expression and target specificity demonstrate excitatory projection neuron diversity. *Cerebral Cortex*, (pp. bht243).

[621] Sotero, R. C. & Iturria-Medina, Y. (2011). From blood oxygenation level dependent (BOLD) signals to brain temperature maps. *Bulletin of Mathematical Biology*, 73(11), 2731–2747.

[622] Speakman, J. R. (2013). Measuring energy metabolism in the mouse—theoretical, practical, and analytical considerations. *Frontiers in Integrative Physiology*, 4(34).

[623] Spencer, Q. H., Peel, C. B., Swindlehurst, A. L., & Haardt, M. (2004). An introduction to the multi-user MIMO downlink. *IEEE Communications Magazine*, 42(10), 60–67.

[624] Spruston, N. (2001). Axonal gap junctions send ripples through the hippocampus. *Neuron*, 31(5), 669 – 671.

[625] Stanley, S. A., Gagner, J. E., Damanpour, S., Yoshida, M., Dordick, J. S., & Friedman, J. M. (2012). Radio-wave heating of iron oxide nanoparticles can regulate plasma glucose in mice. *Science*, 336(6081), 604–608.

[626] Stansberg, C., Ersland, K. M., van der Valk, P., & Steen, V. M. (2011). Gene expression in the rat brain: High similarity but unique differences between frontomedial-, temporal-and occipital cortex. *BMC neuroscience*, 12(1), 15.

[627] Stanwix, P. L., Pham, L. M., Maze, J. R., Le Sage, D., Yeung, T. K., Cappellaro, P., Hemmer, P. R., Yacoby, A., Lukin, M. D., & Walsworth, R. L. (2010). Coherence of nitrogen-vacancy electronic spin ensembles in diamond. *Physical Review B*, 82(20), 201201.

[628] Stehling, M. K., Turner, R., & Mansfield, P. (1991). *Science*, 254(5028), 43–50.

[629] Stepnoski, R., LaPorta, A., Raccuia-Behling, F., Blonder, G., Slusher, R., & Kleinfeld, D. (1991). Noninvasive detection of changes in membrane potential in cultured neurons by light scattering. *Proceedings of the National Academy of Sciences*, 88(21), 9382–9386.

[630] Stevenson, I. H. & Kording, K. P. (2011). How advances in neural recording affect data analysis. *Nature Neuroscience*, 14, 139–142.

[631] Steward, O. & Worley, P. (2001). Localization of mrnas at synaptic sites on dendrites. In *Cell Polarity and Subcellular RNA Localization* (pp. 1–26). Springer.

[632] Stewart, T. C., Bekolay, T., & Eliasmith, C. (2012). Learning to select actions with spiking neurons in the basal ganglia. *Frontiers in neuroscience*, 6.

[633] Stewart, T. C., Choo, X., & Eliasmith, C. (2010). Symbolic reasoning in spiking neurons: A model of the cortex/basal ganglia/thalamus loop. In *Proceedings of the 32nd annual conference of the cognitive science society* (pp. 1100–1105).

[634] Steyaert, M. S. J., Sansen, W. M. C., & Chang, Z.-Y. (1987). A micropower low-noise monolithic instrumentation amplifier for medical purposes. *IEEE Journal of Solid-State Circuits*, 22(6), 1163–1168.

[635] Stocco, A., Lebiere, C., O'Reilly, R. C., & Anderson, J. R. (2012). Distinct contributions of the caudate nucleus, rostral prefrontal cortex, and parietal cortex to the execution of instructed tasks. *Cognitive, Affective, & Behavioral Neuroscience*, 12(4), 611–628.

[636] Storace, D. A., Sung, U., Platisa, J., Cohen, L. B., & Pieribone, V. A. (2013). In Vivo Imaging of Odor-Evoked Responses in the Olfactory Bulb using Arclight, a Novel Fp Voltage Probe. *Biophysical Journal*, 104, 679.

[637] Stratford, K., Tarczy-Hornoch, K., Martin, K., Bannister, N., & Jack, J. (1996). Excitatory synaptic inputs to spiny stellate cells in cat visual cortex.

[638] Stratton, P., Cheung, A., Wiles, J., Kiyatkin, E., Sah, P., & Windels, F. (2012). Action potential waveform variability limits multi-unit separation in freely behaving rats. *PloS one*, 7(6), e38482.

[639] Striker, G., Subramaniam, V., Seidel, C. A. M., & Volkmer, A. (1999). Photochromicity and fluorescence lifetimes of green fluorescent protein. *The Journal of Physical Chemistry B*, 103(40), 8612–8617.

[640] Strong, S. P., Koberle, R., de Ruyter van Steveninck, R. R., & Bialek, W. (1998). Entropy and information in neural spike trains. *Physical Review Letters*, 80, 197–200.

[641] Studer, V., Bobin, J., Chahid, M., Mousavi, H. S., Candes, E., & Dahan, M. (2012). Compressive fluorescence microscopy for biological and hyperspectral imaging. *Proceedings of the National Academy of Sciences of the United States of America*, 109(26), E1679–E1687.

[642] Sukstanskii, A. & Yablonskiy, D. (2004). An analytical model of temperature regulation in human head. *Journal of thermal biology*, 29(7), 583–587.

[643] Sukstanskii, A. & Yablonskiy, D. (2007). Theoretical limits on brain cooling by external head cooling devices. *European journal of applied physiology*, 101(1), 41–49.

[644] Sukstanskii, A. L. & Yablonskiy, D. A. (2006). Theoretical model of temperature regulation in the brain during changes in functional activity. *Proceedings of the National Academy of Sciences*, 103(32), 12144–12149.

[645] Sumida, S., Okazaki, S., Asakura, S., Nakagawa, H., Murayama, H., & Hasegawa, T. (2005). Distributed hydrogen determination with fiber-optic sensor. *Sensors and Actuators B: Chemical*, 108(1), 508–514.

[646] Sun, B., Edgar, M. P., Bowman, R., Vittert, L. E., Welsh, S., Bowman, A., & Padgett, M. J. (2013a). 3D computational imaging with single-pixel detectors. *Science*, 340(6134), 844–847.

[647] Sun, X. R., Badura, A., Pacheco, D. A., Lynch, L. A., Schneider, E. R., Taylor, M. P., Hogue, I. B., Enquist, L. W., Murthy, M., & Wang, S. S.-H. (2013b). Fast gcamps for improved tracking of neuronal activity. *Nature communications*, 4.

[648] Sun, Y.-H. & Chang, K. (2002). A high-efficiency dual-frequency rectenna for 2.45- and 5.8-GHz wireless power transmission. *IEEE Transactions on Microwave Theory and Techniques*, 50(7), 1784–1789.

[649] Suner, S., Fellows, M. R., Vargas-Irwin, C., Nakata, G. K., & Donoghue, J. P. (2005). Reliability of signals from a chronically implanted, silicon-based electrode array in non-human primate primary motor cortex. *Neural Systems and Rehabilitation Engineering, IEEE Transactions on*, 13(4), 524–541.

[650] Taillefumier, T. & Magnasco, M. O. (2013). A phase transition in the first passage of a brownian process through a fluctuating boundary with implications for neural coding. *Proceedings of the National Academy of Sciences*.

[651] Tal, E., Oron, D., & Silberberg, Y. (2005). Improved depth resolution in video-rate line-scanning multiphoton microscopy using temporal focusing. *Optics letters*, 30(13), 1686–1688.

[652] Taub, A. H., Hogri, R., Magal, A., Mintz, M., & Shacham-Diamand, Y. (2012). Bioactive anti-inflammatory coating for chronic neural electrodes. *Journal of Biomedical Materials Research Part A*, 100(7), 1854–1858.

[653] Taylor, J., Cappellaro, P., Childress, L., Jiang, L., Budker, D., Hemmer, P., Yacoby, A., Walsworth, R., & Lukin, M. (2008). High-sensitivity diamond magnetometer with nanoscale resolution. *Nature Physics*, 4(10), 810–816.

[654] Tian, N., Guo, Q., Wang, A., Xu, D., & Fu, L. (2011). Fluorescence ghost imaging with pseudothermal light. *Optics Letters*, 36(16), 3302–3304.

[655] Tillberg, P. W. (2013). Development of multiplexing strategies for electron and super-resolution optical microscopy. Master's thesis, Massachusetts Institute of Technology.

[656] Tonouchi, M. (2007). Cutting-edge terahertz technology. *Nature Photonics*, 1, 97–105.

[657] Tran, T. X. & Biancalana, F. (2009). An accurate envelope equation for light propagation in photonic nanowires: new nonlinear effects. *Optics Express*, 17(20), 17934–17949.

[658] Traxler, M. J., Boudewyn, M., & Loudermilk, J. (2012). What's special about human language? the contents of the "narrow language faculty" revisited. *Language and linguistics compass*, 6(10), 611–621.

[659] Treutlein, B., Gokce, O., Quake, S. R., & Südhof, T. C. (2014). Cartography of neurexin alternative splicing mapped by single-molecule long-read mrna sequencing. *Proceedings of the National Academy of Sciences*, 111(13), E1291–E1299.

[660] Triplett, J. W., Pfeiffenberger, C., Yamada, J., Stafford, B. K., Sweeney, N. T., Litke, A. M., Sher, A., Koulakov, A. A., & Feldheim, D. A. (2011). Competition is a driving force in topographic mapping. *Proceedings of the National Academy of Sciences*, 108(47), 19060–19065.

[661] Trübel, H. K., Sacolick, L. I., & Hyder, F. (2005). Regional temperature changes in the brain during somatosensory stimulation. *Journal of Cerebral Blood Flow & Metabolism*, 26(1), 68–78.

[662] Tsai, P. S., Kaufhold, J. P., Blinder, P., Friedman, B., Drew, P. J., Karten, H. J., Lyden, P. D., & Kleinfeld, D. (2009). Correlations of neuronal and microvascular densities in murine cortex revealed by direct counting and colocalization of nuclei and vessels. *The Journal of Neuroscience*, 29(46), 14553–14570.

[663] Tsia, K. K., Goda, K., Capewell, D., & Jalali, B. (2010). Performance of serial time-encoded amplified microscopy. In *Lasers and Electro-Optics (CLEO) and Quantum Electronics and Laser Science Conference (QELS), 2010 Conference on* (pp. 1–2).: IEEE.

[664] Tsien, R. Y. (2013). Very long-term memories may be stored in the pattern of holes in the perineuronal net. *Proceedings of the National Academy of Sciences*, 110(30), 12456–12461.

[665] Tsurugizawa, T., Ciobanu, L., & Le Bihan, D. (2013). Water diffusion in brain cortex closely tracks underlying neuronal activity. *Proceedings of the National Academy of Sciences*, 110(28), 11636–11641.

[666] Tucker, R. S. (2011). Green optical communications—Part II: Energy limitations in networks. *IEEE Journal of Selected Topics in Quantum Electronics*, 17(2), 261–274.

[667] Tucker, R. S. & Hinton, K. (2011). Energy consumption and energy density in optical and electronic signal processing. *IEEE Photonics Journal*, 3(5), 821–833.

[668] Tulino, A. M. & Verdú, S. (2004). Random matrix theory and wireless communications. *Foundations and Trends in Communications and Information Theory*, 1(1), 1–182.

[669] Turaga, S. C., Murray, J. F., Jain, V., Roth, F., Helmstaedter, M., Briggman, K., Denk, W., & Seung, H. S. (2010). Convolutional networks can learn to generate affinity graphs for image segmentation. *Neural Computation*, 22(2), 511–538.

[670] Turecek, J., Yuen, G. S., Han, V. Z., Zeng, X.-H., Bayer, K. U., & Welsh, J. P. (2014). Nmda receptor activation strengthens weak electrical coupling in mammalian brain. *Neuron*, 81(6), 1375–1388.

[671] Usami, M., Tanabe, H., Sato, A., Sakama, I., Maki, Y., Iwamatsu, T., Ipposhi, T., & Inoue, Y. (2007). A 0.05×0.05 mm² RFID chip with easily scaled-down ID-memory. In *International Solid-State Circuits Conference, 2007 IEEE* (pp. 482–483).

[672] Vacher, H., Mohapatra, D. P., & Trimmer, J. S. (2008). Localization and targeting of voltage-dependent ion channels in mammalian central neurons. *Physiological reviews*, 88(4), 1407–1447.

[673] Van der Linden, A., Verhoye, M., Van Meir, V., Tindemans, I., Eens, M., Absil, P., & Balthazart, J. (2002). In vivo manganese-enhanced magnetic resonance imaging reveals connections and functional properties of the songbird vocal control system. *Neuroscience*, 112(2), 467–474.

[674] Van Hooser, S. D. (2007). Similarity and diversity in visual cortex: is there a unifying theory of cortical computation? *The Neuroscientist*, 13(6), 639–656.

[675] Vaziri, A. & Emiliani, V. (2012). Reshaping the optical dimension in optogenetics. *Current Opinion in Neurobiology*, 22(1), 128–137.

[676] Veeraraghavan, A., Genkin, A. V., Vitaladevuni, S., Scheffer, L., Xu, S., Hess, H., Fetter, R., Cantoni, M., Knott, G., & Chklovskii, D. (2010). Increasing depth resolution of electron microscopy of neural circuits using sparse tomographic reconstruction. In *Computer Vision and Pattern Recognition (CVPR), 2010 IEEE Conference on* (pp. 1767–1774).: IEEE.

[677] Velten, A., Willwacher, T., Gupta, O., Veeraraghavan, A., Bawendi, M. G., & Raskar, R. (2012). Recovering three-dimensional shape around a corner using ultrafast time-of-flight imaging. *Nature Communications*, 3, 745.

[678] Venkatachalam, V., Brinks, D., Maclaurin, D., Hochbaum, D., Kralj, J. M., & Cohen, A. E. (2014). Flash memory: photochemical imprinting of neuronal action potentials onto a microbial rhodopsin. *Journal of the American Chemical Society*.

[679] Vetter, R. J., Williams, J. C., Hetke, J. F., Nunamaker, E. A., & Kipke, D. R. (2004). Chronic neural recording using silicon-substrate microelectrode arrays implanted in cerebral cortex. *Biomedical Engineering, IEEE Transactions on*, 51(6), 896–904.

[680] Villasana, L. E., Klann, E., & Tejada-Simon, M. V. (2006). Rapid isolation of synaptoneurosomes and postsynaptic densities from adult mouse hippocampus. *Journal of neuroscience methods*, 158(1), 30–36.

[681] Vincent, T. J., Thiessen, J. D., Kurjewicz, L. M., Germscheid, S. L., Turner, A. J., Zhilkin, P., Alexander, M. E., & Martin, M. (2010). Longitudinal brain size measurements in APP/PS1 transgenic mice. *Magnetic Resonance Insights*, 4, 19–26.

[682] Vučinić, D. & Sejnowski, T. J. (2007). A compact multiphoton 3d imaging system for recording fast neuronal activity. *PLoS ONE*, 2(8), e699.

[683] Wakin, M. B., Laska, J. N., Duarte, M. F., Baron, D., Sarvotham, S., Takhar, D., Kelly, K. F., & Baraniuk, R. G. (2013). Compressive imaging for video representation and coding. In *Picture Coding Symposium*.

[684] Wally, V., Murauer, E. M., & Bauer, J. W. (2012). Spliceosome-mediated trans-splicing: the therapeutic cut and paste. *Journal of Investigative Dermatology*, 132(8), 1959–1966.

[685] Walsh, C. & Cepko, C. L. (1992). Widespread dispersion of neuronal clones across functional regions of the cerebral cortex. *Science*, 255(5043), 434–440.

[686] Wang, D. O., Martin, K. C., & Zukin, R. S. (2010). Spatially restricting gene expression by local translation at synapses. *Trends in neurosciences*, 33(4), 173–182.

[687] Wang, H. H., Isaacs, F. J., Carr, P. A., Sun, Z. Z., Xu, G., Forest, C. R., & Church, G. M. (2009). Programming cells by multiplex genome engineering and accelerated evolution. *Nature*, 460(7257), 894–898.

[688] Wang, J., Wagner, F., Borton, D. A., Zhang, J., Ozden, I., Burwell, R. D., Nurmikko, A. V., van Wagenen, R., Diester, I., & Deisseroth, K. (2012a). Integrated device for combined optical neuromodulation and electrical recording for chronic in vivo applications. *Journal of neural engineering*, 9(1), 016001.

[689] Wang, X.-J. (2013). The prefrontal cortex as a quintessential "cognitive-type" neural circuit.

[690] Wang, Y., Markram, H., Goodman, P. H., Berger, T. K., Ma, J., & Goldman-Rakic, P. S. (2006). Heterogeneity in the pyramidal network of the medial prefrontal cortex. *Nature neuroscience*, 9(4), 534–542.

[691] Wang, Y. M., Judkewitz, B., DiMarzio, C. A., & Yang, C. (2012b). Deep-tissue focal fluorescence imaging with digitally time-reversed ultrasound-encoded light. *Nature Communications*, 3(928).

[692] Ward, M. P., Rajdev, P., Ellison, C., & Irazoqui, P. P. (2009). Toward a comparison of microelectrodes for acute and chronic recordings. *Brain research*, 1282, 183–200.

[693] Wasserstrom, A., Adar, R., Shefer, G., Frumkin, D., Itzkovitz, S., Stern, T., Shur, I., Zangi, L., Kaplan, S., Harmelin, A., et al. (2008). Reconstruction of cell lineage trees in mice. *PLoS One*, 3(4), e1939.

[694] Wee, T.-L., Tzeng, Y.-K., Han, C.-C., Chang, H.-C., Fann, W., Hsu, J.-H., Chen, K.-M., & Yu, Y.-C. (2007). Two-photon excited fluorescence of nitrogen-vacancy centers in proton-irradiated type ib diamond. *The Journal of Physical Chemistry A*, 111(38), 9379–9386.

[695] Wei, B., Dai, M., & Yin, P. (2012). Complex shapes self-assembled from single-stranded dna tiles. *Nature*, 485(7400), 623–626.

[696] Wei, Y. & Koulakov, A. A. (2012). An exactly solvable model of random site-specific recombinations. *Bulletin of mathematical biology*, 74(12), 2897–2916.

[697] Wei, Y., Tsigankov, D., & Koulakov, A. (2013). The molecular basis for the development of neural maps. *Annals of the New York Academy of Sciences*, 1305(1), 44–60.

[698] Weibel, D. B., Garstecki, P., Ryan, D., DiLuzio, W. R., Mayer, M., Seto, J. E., & Whitesides, G. M. (2005). Microoxen. *Proceedings of the National Academy of Sciences of the United States of America*, 102(34), 11963–11967.

[699] Weiler, N., Wood, L., Yu, J., Solla, S. A., & Shepherd, G. M. (2008). Top-down laminar organization of the excitatory network in motor cortex. *Nature neuroscience*, 11(3), 360–366.

[700] Wessberg, J., Stambaugh, C. R., Kralik, J. D., Beck, P. D., Laubach, M., Chapin, J. K., Kim, J., Biggs, S. J., Srinivasan, M. A., & Nicolelis, M. A. L. (2000). Real-time prediction of hand trajectory by ensembles of cortical neurons in primates. *Nature*, 408.

[701] White, J. G., Southgate, E., Thomson, J. N., & Brenner, S. (1986). The structure of the nervous system of the nematode caenorhabditis elegans. *Philosophical Transactions of the Royal Society of London. B, Biological Sciences*, 314(1165), 1–340.

[702] Wickersham, I. R. & Feinberg, E. H. (2012). New technologies for imaging synaptic partners. *Current Opinion in Neurobiology*, 22(1), 121–127.

[703] Widder, E. A., Latz, M. I., Herring, P. J., & Case, J. F. (1984). Far red bioluminescence from two deep-sea fishes. *Science*, 225(4661), 512–514.

[704] Wieduwilt, T., Brückner, S., & Bartelt, H. (2011). High force measurement sensitivity with fiber bragg gratings fabricated in uniform-waist fiber tapers. *Measurement Science and Technology*, 22(7), 075201.

[705] Wiesinger, F., Van de Moortele, P.-F., Adriany, G., De Zanche, N., Ugurbil, K., & Prüssman, K. P. (2006). Potential and feasibility of parallel MRI at high field. *NMR in Biomedicine*, 19, 368–378.

[706] Wilson, J. M., Dombeck, D. A., Díaz-Ríos, M., Harris-Warrick, R. M., & Brownstone, R. M. (2007). Two-photon calcium imaging of network activity in XFP-expressing neurons in the mouse. *Journal of Neurophysiology*, 97(4), 3118–3125.

[707] Wilt, B. A., Burns, L. D., Wei Ho, E. T., Ghosh, K. K., Mukamel, E. A., & Schnitzer, M. J. (2009). Advances in light microscopy for neuroscience. *Annual Review of Neuroscience*, 32(1), 435–506. PMID: 19555292.

[708] Wilt, B. A., Fitzgerald, J. E., & Schnitzer, M. J. (2013). Photon shot noise limits on optical detection of neuronal spikes and estimation of spike timing. *Biophysical Journal*, 104(1), 51–62.

[709] Witzel, T., Lin, F.-H., Rosen, B. R., & Wald, L. L. (2008). Stimulus-induced rotary saturation (sirs): A potential method for the detection of neuronal currents with mri. *Neuroimage*, 42(4), 1357–1365.

[710] Wolf, P. D. (2008). *Thermal Considerations for the Design of an Implanted Cortical Brain–Machine Interface (BMI) In: Reichert WM, editor. Indwelling Neural Implants: Strategies for Contending with the In Vivo Environment.* Boca Raton (FL): CRC Press.

[711] Wood, L. (2013). Personal Communication.

[712] Woodruff, A. R., McGarry, L. M., Vogels, T. P., Inan, M., Anderson, S. A., & Yuste, R. (2011). State-dependent function of neocortical chandelier cells. *The Journal of Neuroscience*, 31(49), 17872–17886.

[713] Wu, F., Zhang, X., Cheung, J. Y., Shi, K., Liu, Z., Luo, C., Yin, S., & Ruffin, P. (2006). Frequency division multiplexed multichannel high-speed fluorescence confocal microscope. *Biophysical journal*, 91(6), 2290–2296.

[714] Wyss, R., König, P., & Verschure, P. F. J. (2006). A model of the ventral visual system based on temporal stability and local memory. *PLoS biology*, 4(5), e120.

[715] Xu, T.-B., Siochi, E. J., Kang, J. H., Zuo, L., Zhou, W., Tang, X., & Jiang, X. (2013). Energy harvesting using a PZT ceramic multilayer stack. *Smart Materials and Structures*, 22, 065015.

[716] Yablonovitch, E. (2008). Replacing the transistor: searching for the milli-volt switch.

[717] Yamagata, M. & Sanes, J. R. (2012). Transgenic strategy for identifying synaptic connections in mice by fluorescence complementation (grasp). *Frontiers in molecular neuroscience*, 5.

[718] Yamamori, T. (2011). Selective gene expression in regions of primate neocortex: implications for cortical specialization. *Progress in neurobiology*, 94(3), 201–222.

[719] Yamazaki, T. & Tanaka, S. (2007). The cerebellum as a liquid state machine. *Neural Networks*, 20(3), 290–297.

[720] Yáñez, I. B., Muñoz, A., Contreras, J., Gonzalez, J., Rodriguez-Veiga, E., & DeFelipe, J. (2005). Double bouquet cell in the human cerebral cortex and a comparison with other mammals. *Journal of Comparative Neurology*, 486(4), 344–360.

[721] Yang, Y. & Zador, A. M. (2012). Differences in sensitivity to neural timing among cortical areas. *The Journal of Neuroscience*, 32(43), 15142–15147.

[722] Yatabe, Y., Tavaré, S., & Shibata, D. (2001). Investigating stem cells in human colon by using methylation patterns. *Proceedings of the National Academy of Sciences*, 98(19), 10839–10844.

[723] Yin, P., Hariadi, R. F., Sahu, S., Choi, H. M., Park, S. H., LaBean, T. H., & Reif, J. H. (2008). Programming dna tube circumferences. *Science*, 321(5890), 824–826.

[724] Yin, S. (2006). Frequency division multiplexed fluorescence confocal microscopy. *BIOPHOTONICS INTERNATIONAL*, 13(12), 38.

[725] Yook, C., Druckmann, S., & Kim, J. (2013). Mapping mammalian synaptic connectivity. *Cellular and Molecular Life Sciences*, 70(24), 4747–4757.

[726] York, A. G., Chandris, P., Dalle Nogare, D., Head, J., Wawrzusin, P., Fischer, R. S., Chitnis, A., & Shroff, H. (2013). Instant super-resolution imaging in live cells and embryos via analog image processing. *Nature methods*.

[727] Yosef, I., Goren, M. G., & Qimron, U. (2012). Proteins and dna elements essential for the crispr adaptation process in escherichia coli. *Nucleic acids research*, 40(12), 5569–5576.

[728] Yoshimura, Y. & Callaway, E. M. (2005). Fine-scale specificity of cortical networks depends on inhibitory cell type and connectivity. *Nature neuroscience*, 8(11), 1552–1559.

[729] Yu, X., Glen, D., Wang, S., Dodd, S., Hirano, Y., Saad, Z., Reynolds, R., Silva, A. C., & Koretsky, A. P. (2012). Direct imaging of macrovascular and microvascular contributions to BOLD fMRI in layers IV–V of the rat whisker-barrel cortex. *NeuroImage*, 59(2), 1451–1460.

[730] Yue, K., Guduru, R., HongJeongmin, Liang, P., Nair, M., & Khizroev, S. (2012). Magnetoelectric nano-particles for non-invasive brain stimulation. *PLoS ONE*, 7(9), e44040.

[731] Yuste, R. & Bonhoeffer, T. (2001). Morphological changes in dendritic spines associated with long-term synaptic plasticity. *Annual review of neuroscience*, 24(1), 1071–1089.

[732] Yuste, R., MacLean, J. N., Smith, J., & Lansner, A. (2005). The cortex as a central pattern generator. *Nature Reviews Neuroscience*, 6(6), 477–483.

[733] Zadeh, J. N., Steenberg, C. D., Bois, J. S., Wolfe, B. R., Pierce, M. B., Khan, A. R., Dirks, R. M., & Pierce, N. A. (2011). Nupack: analysis and design of nucleic acid systems. *Journal of computational chemistry*, 32(1), 170–173.

[734] Zador, A. M., Dubnau, J., Oyibo, H. K., Zhan, H., Cao, G., & Peikon, I. D. (2012). Sequencing the connectome. *PLoS Biology*, 10(10), e1001411.

[735] Zamft, B. M., Marblestone, A. H., Kording, K. P., Schmidt, D., Martin-Alarcon, D., Tyo, K., Boyden, E. S., & Church, G. (2012). Measuring cation dependent DNA polymerase fidelity landscapes by deep sequencing. *PLoS ONE*, 7(8), e43876.

[736] Zhang, S., Block, K. T., & Frahm, J. (2010). Magnetic resonance imaging in real time. *Journal of Magnetic Resonance Imaging*, 31(1), 101–109.

[737] Zheng, T., Yang, Z., Li, A., Lv, X., Zhou, Z., Wang, X., Qi, X., Li, S., Luo, Q., Gong, H., et al. (2013). Visualization of brain circuits using two-photon fluorescence micro-optical sectioning tomography. *Optics express*, 21(8), 9839–9850.

[738] ZHENG, X. & BEVILACQUA, P. C. (2004). Activation of the protein kinase pkr by short double-stranded rnas with single-stranded tails. *Rna*, 10(12), 1934–1945.

[739] Ziv, Y., Burns, L. D., Cocker, E. D., Hamel, E. O., Ghosh, K. K., Kitch, L. J., El Gamal, A., & Schnitzer, M. J. (2013). Long-term dynamics of CA1 hippocampal place codes. *Nature Neuroscience*, 16, 264–266.

[740] Zorzos, A. N., Boyden, E. S., & Fonstad, C. G. (2010). Multiwaveguide implantable probe for light delivery to sets of distributed brain targets. *Optics Letters*, 35(24), 4133–4135.

[741] Zorzos, A. N., Scholvin, J., Boyden, E. S., & Fonstad, C. G. (2012). Three-dimensional multiwaveguide probe array for light delivery to distributed brain circuits. *Optics Letters*, 37(23), 4841–4843.